The University Of Sheffield.

High Frequency Permanent Magnet Generator for Pulse Density Modulating Converters

By

Bo Jiang

A thesis submitted in partial fulfilment of the requirements for the degree of Doctor of Philosophy

The University of Sheffield

Faculty of Engineering

Department of Electronic and Electrical Engineering

March 2020

Abstract

This thesis describes an investigation of high frequency permanent magnet generators for use in a novel power generation system for aerospace applications. The system consists of a high frequency generator (in the 10s of kHz range) which feeds a full-wave rectifier to produce to a high frequency pulse train as input to a pulse-density modulated soft-switched converter.

Various topologies of flux-switching, flux-reversal and Vernier machines are investigated using electric-circuit coupled finite element analysis. Having demonstrated the limitations of these topologies, a comprehensive design study into a single-phase, surface mounted permanent magnet machine based on a single turn serpentine winding is described. This study covers both internal and external rotor machines with pole numbers of 192 and 96 which correspond to generator fundamental frequencies of 32kHz and 16kHz at the rated speed of 20,000rpm. Several aspects of the machine design are optimised through extensive use of finite element modelling, including mechanical analysis of the rotor containment. This study includes a detailed consideration of iron loss, including consideration of iron powder based cores. This study has resulted in a down-selected design based on a low permeability but high resistivity powdered iron core.

The manufacture of a demonstrator is described including the need to re-design the machine to employ ultra-thin Nickel Iron laminations because of the difficulties encountered in the machining of a powdered iron core. The performance of this Nickel Iron variant is investigated and a final design established. The numerous challenges involved in manufacturing this novel machine are described.

Acknowledgements

I would like to express my deep sincere gratitude to my supervisor Professor Geraint Jewell. During this five years research, I have gone through a lot of challenges, difficulties and failures. Without his patience, invaluable help and guidance, I cannot have courage to complete this project. More than that, I also would like to appreciate every professional suggestion and idea he made. It's truly helpful in each step of research.

I would like to acknowledge all my colleagues in Rolls-Royce Sheffield University Technique Centre (UTC), especially Jason and Steve. Also, I would like to acknowledge technical staff in workshop, especially Clive, Sam, Karl and David. All of them gave me a lot of support and advice during my research.

Particularly, I would like to thank two women in my life. One is my mother. She had shown her great characteristic of brave, strong and optimistic even in her last time while suffering cancer. That leads me overcome frustration and setback throughout these years during research. Another one is my wife. Her encourage and support bring faith and confidence back to me and give me strength and courage.

Further, I would like to thank my friends and all other family members for their care and support, which I really appreciate. I would like to thank the Electrical Machine Drive Group for delight, warmly working environment.

Last but not least, I am indebted to previous research in this area. I would like to thank the architecture of electrical machine research that makes it possible to give me a chance to stand in frontier of science.

Contents

List of symbols

Symbol	Explanation	Unit
t_s	Simple time	**s**
f_{pulse}	DC pulse frequency	Hz
f_s	PDM switching frequency	Hz
f_{ac}	Machine side AC frequency	Hz
V_{dc}	Rectified voltage in average value	V
I_{dc}	Rectified current in average value	A
Ts	Number of small teeth	
sp	Split ratio	
σ_{max}	Maximum stress	Pa
δ_c	Containment mass density	kg/m^3
ω	Angular speed	rad/s
ν_c	Poisson ratio of containment	
d_{co}	Outer diameter of the containment	mm
d_{ci}	Inner diameter of the containment	mm
m_{eq}	Equivalent dead mass acting on the containment	kg
r_{meq}	Equivalent radius of the dead mass	mm
d_{mo}	Magnet outer diameter	mm
d_{mi}	Magnet inner diameter	mm
α	Magnet pole arc	degree
δ_m	Magnet mass density	kg/m^3
δ_{ip}	Inter-pole material mass density	kg/m^3
R_t	Ratio of rotor teeth (depth/width)	
ag	Airgap length	mm
br	Magnet bridge thickness	mm
SH	Stator hub ratio (stator hub diameter/machine outside diameter)	
B	Flux density	T
f	frequency	Hz
δ_{Fe}	Iron mass density	kg/m^3

σ	Conductivity	S/m
d	Lamination thickness	mm
T	Period of one cycle	s
K_h		
K_{exe}		
K_{cl}	Steinmetz coefficient	
α		
β		
K_{loop}	Coefficient of hysteresis minor loop	
pk	Slot area packing factor	
ρ	Electrical resistivity	μΩcm

Chapter 1 Introduction

1.1 More electric aircraft

In common with many other transport sectors, aerospace is gradually moving towards increased electrification. In the short to medium term future, it is unlikely that full-electric propulsion will be realised in anything other than very small, short-range, personal mobility platforms such as those in [1-3]. Hybrid-propulsion which uses a conventional gas-turbine to drive a generator to provide electrical power for distributed electrical propulsors may emerge in the medium term for smaller passenger aircraft. Larger aircraft are likely to focus on the concept of a 'more-electric aircraft' (MEA) to reduce fuel consumption, limit emissions and improve controllability by replacing mechanical, pneumatic or hydraulic power systems with electrical counterparts [4-10]. The most prominent commercial example of an MEA is the Boeing 787 which contains some, but by no means all, of the features proposed for a MEA. The 787 is equipped with main engine electrical starters and has adopted a bleed-less architecture in which the environmental control system (ECS) is powered electrically rather than from engine bleed-air [11]. Despite it being a significant change compared to previous commercial aircraft, it still has conventional oil and fuel pumps on the engine and the aircraft flight control surface and many other actuators remain hydraulic systems.

The mechanical, hydraulic and pneumatic systems on a modern aircraft have many drawbacks compared to electrical alternatives in terms of low efficiency, low reliability, high noise and high maintenance cost [5, 8]. Converting these systems to electrical power offers many advantages providing the electrical systems are competitive in terms of mass and cost and can achieve the very high levels of reliability required in aerospace systems. Given the potential benefits, increasing numbers of research and government/commercial projects have focused on the MEA concept over past decades [4, 5]. As components of this concept, numerous advanced power electronic converter [12-14] and electrical machines [9, 10] have been developed for aircraft. The main research area in MEA technologies have been categorized in [8], as shown in Figure 1.1.

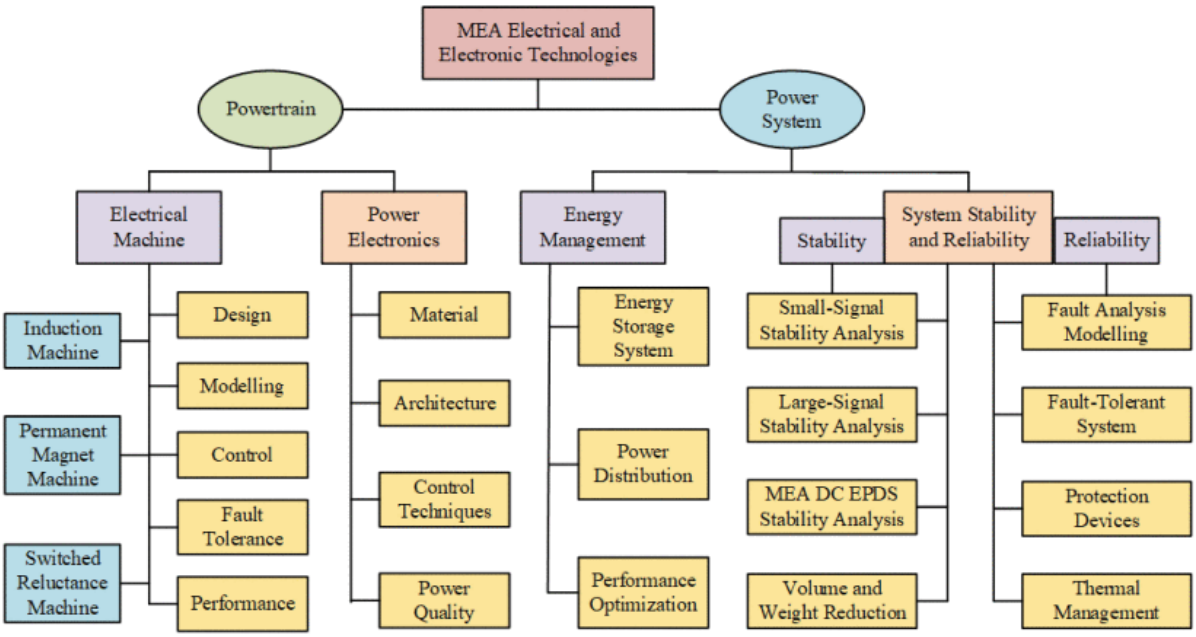

Figure 1.1 The main research area in MEA technologies (Source: [8])

The ultimate goal of a truly MEA is towards using electrical system to replace all the mechanical, pneumatic or hydraulic power, called 'All Electric Aircraft' (AEA). In the future, an increasing number of electrified technologies is likely to be adopted in aircraft such as electric environmental control systems [15, 16], electric taxi equipment [2, 3], and electro-mechanical or electro-hydraulic systems on flight surface control [17-19].

The adoption of more electrical systems on an aircraft will inevitably increase, the electrical load which will also increase the complexity of the electrical distribution network [20]. This places greater demands further increases in main engine generator capacity [21]. Figure 1.2 has shown the evolution of single generator power rating over year for commercial aircraft.

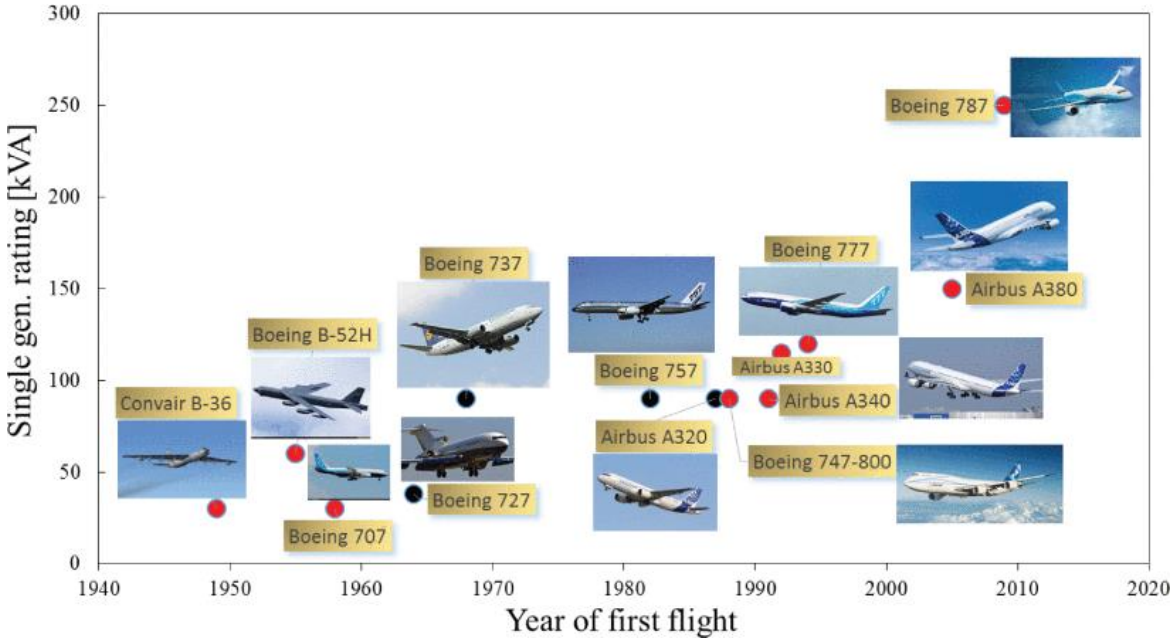

Figure 1.2 Single main generator power rating over years (Source: [10]). (Red dots indicate medium to long haul aircraft; black dots indicate short to medium haul aircraft)

The increasing power capacity and complex of power distribution also demand consideration of higher voltage in power distribution systems [22], in order to ensure competitive cable mass. In this regards, 270V DC distribution system is already accepted by MIL-STD-704F standard, furthermore, 540V DC distribution systems (based often on ±270V) is being adopted [22].

Permanent magnet machines offer the highest levels of power density of electrical machines, particularly for high-speed generators up to 250kW or so, and significant weight savings can be made by replacing wound-field generators (which are the dominant incumbent technology) with equivalent permanent magnet machines, at least at the machine level. However, some form of controlled power converter is necessary in order to interface a permanent magnet generator to a power network. In order to optimise overall system mass, there is a need to consider generator types that are able to operate with converters that offer advantages in weight and efficiency when compared to more conventional power converters [23].

The power distribution network also affects the design of power converters in terms of increased power density, higher temperature capability and wider switching frequency range [24, 25]. The switching of power electronics converters contributes electromagnetic interference and compromises power quality delivered by the generator to the electrical

network [26, 27]. To limit interference and distortions, the increased switching frequency of power electronics devices are preferred [28, 29].

1.2 Proposed system concept

1.2.1 System architecture

This thesis is concerned with an in-depth investigation into a novel electrical generation architecture proposed by Rolls-Royce [30]. Comparing the conventional generation system with controller shown in Figure 1.3, the key novelty in this concept is the combination of a high frequency output generator (up to tens of kHz) with a diode rectifier acting as input to a soft-switched pulse density modulation (PDM) converter, shown in Figure 1.6. Soft-switching in power converters generally involves switching the individual power switches when the voltage across them is zero, thus in principle eliminating switching losses. This improves converter efficiency and reduces cooling requirements at a particular frequency and allows a high switching frequency to be used (which has advantages for example in reducing filter size) without large increases in converter loss. In order to achieve soft-switching in a three-phase six-switch converter it is necessary for the input voltage applied to the converter 'link' to be periodically zero (or very close to zero) so that soft-switching can take place. Soft-switching of converters from a varying link is a well-established concept which has previously been based on generation of a so-called resonant DC link. Converter configurations of this type are not capable of bi-directional power flow and are hence limited to motoring or generating operation.

A block diagram showing a traditional approach to a soft-switched power converter operating in a generating system is shown in Figure 1.3: the more widely used system for PWM control and the soft switching PDM control system. It is worth noting that the vast majority of studies have considered their use as motor drives operating in motoring mode. The soft switching control strategies of Zero-voltage-switching (ZVS) or zero-current-switching (ZCS) allow the almost complete elimination switching loss and can also prove useful in reducing electromagnetic interference emission. [31 - 33]. Pulse Density Modulation (PDM) is a control strategy applied to drive DC/AC converters which operate with soft switching. Under the direction of a digital controller, the converter power switches either pass or block each input pulse in a pattern which adjusts average

output voltage or current. Compared to the far more widely Pulse Width Modulation (PWM), then PDM offers the ability to achieve soft switching under all load conditions [34], with further advantages in high efficiency, good dynamic response and low interference emission [26, 35, 36].

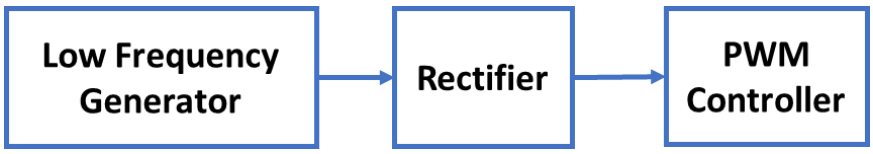

(a) Conventional generation system for PWM control

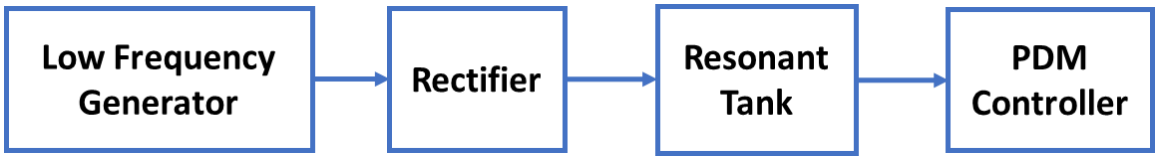

(b) Conventional generation system for PDM control

Figure 1.3 Conventional generation system with controller

A key element in the system of Figure 1.3 is the so-called resonant tank which uses a combination of a power switch and an LC network to generate the fluctuating input to the converter stage. A schematic representation of a typical three-phase resonant link converter is shown in Figure 1.4 in which the resonant tank elements are clearly evident on the input side of the circuit.

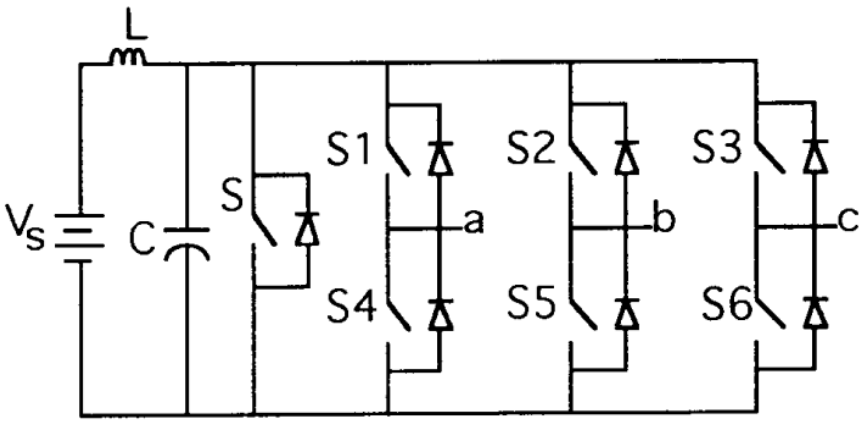

Figure 1.4 Basic voltage-fed resonant link converter (Source: [37])

The resonant tank is controlled to produce a high frequency fluctuating input voltage to the converter which oscillates between zero and a defined peak voltage at a frequency of many 10s of kHz [37] as shown schematically in Figure 1.5. The L-C network will exhibit the desired resonance effect when the switching frequency is equal to the resonance frequency. When switch S is in Figure 1.4 closed, all the capacitance is shorted while the inductance L draws energy from the supply Vs. When the current in inductance L has reached a particular value, switch S turns off, which results in the capacitor being charged by the current in the inductor. The voltage at the converters input increases sinusoidally. By switching S on and off periodically, the pulse train shown in Figure 1.5 will be generated at the converter input. Using the same principle, more complex resonant circuits [38-46] with different inductance-capacitor networks and even the combination passive and active components have been used to produce zero voltage across inverter devices. The control circuit of PDM converter includes a phase-locked loop that locks on to this resonant input voltage to ensure that the inverter switches at zero voltage switching [34] thereby reducing the switching loss to almost zero.

This applied input voltage can then be used by the converter to generate a controlled output voltage using a switching control strategy known as pulse density modulation (PDM). The mathematical basis of this modulating strategy is discussed in chapter 2, but in effect it controls the average voltage at the output by controlling the proportion of the voltage pulses at the input that are applied to the load. In order to have reasonable resolution of control over the output voltage, it is essential that the input voltage frequency is much higher than the fundamental frequency of the desired output voltage. Although it has been demonstrated that the performance of the converter stage itself can be improved by PDM soft-switching, the volume, mass and loss of the resonant tank have proved to be major drawbacks.

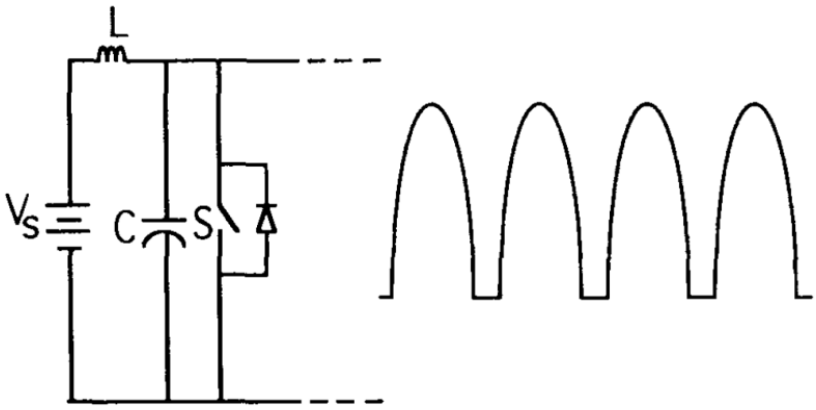

Figure 1.5 Basic principle of resonant L-C network (Source: [37])

In order to overcome the penalty of a resonant-tank, the system studies in this thesis dispenses with the resonant tank as shown in the block diagram of Figure 1.6. In this case the rectified output of the high-frequency genertor directly produces a high frequency voltage waveform which is similar to that shown previously in Figure 1.5 by the resonant tank, although there is no controlled dead- time at zero volts. It is worth noting that the generator does need to be a 3-phase generator in this system. Indeed, a normal 6 pulse, 3-phase rectifier would not produce the voltage zero conditions required at the input to the PDM converter and a single-phase machine is preferable as otherwise the power channels would need to be split.

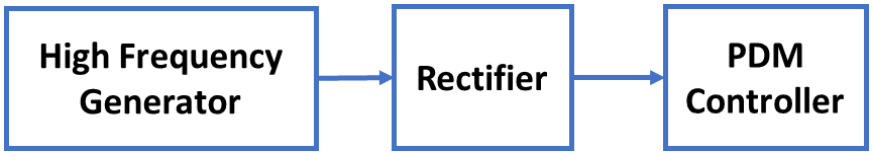

Figure 1.6 Proposed generator system architecture with high frequency generator and soft-switched converter

The design of the machines and the soft-switching PDM converter are strongly coupled, in particular the influence of the fundamental electrical frequency of the machine on the converter performance. In order establish the generator output frequency required in a particular application, it is necessary to understand the operation of the switching strategy and its effect on converter power quality.

1.2.2 Top-level performance requirements

The design of the machine and its associated power converter is strongly coupled, in particular the influence of the fundamental electrical frequency of the machine on the converter performance. In order to optimise overall system mass of the proposed generation system, there is a need to consider machine types that are able to operate with converters that offer advantages in weight and efficiency when compared to more conventional power converters [23]. The key to realising the system in Figure 1.6 are machines that can directly generate high frequency output power that can be fed to PDM converters following a rectification. This allows the mass of resonant circuit to be eliminated reducing the whole system weight. However, achieving a high frequency output may involve a compromise in the mass of the machine itself. They key to this research is whether an overall system mass benefit can be achieved, including recognising that converter efficiency is important because of the system wide mass penalty of removing the heat. Typical requirements for machine that would provide this functionality are:

- Single phase output
- High frequency – at least 20 kHz and ideally 30-40 kHz
- Low impedance in order to possible operate with an uncontrolled full-wave rectifier
- Competitive power densities with more conventional machine types such as permanent magnet brushless DC machines

The research has been performed within the context of aerospace generators, in which power ratings of several 10s of kW, standard aerospace voltages, i.e. 115Vrms phase voltage, rotational speeds of 20,000rpm are required and rotor diameters of 100-150mm are likely to be required.

In all aircraft, generators and any associated power conversion electronics which connect to the main bus need to meet standards such as MIL-STD 704 series. In many older aircraft, three phase 115V RMS at a fixed frequency of 400Hz AC power is used as main load supply and 28V DC power bus is used for avionics and battery system [4, 5]. In more recent aircraft (e.g. Boeing 787), power buses with variable frequency (350Hz to 800Hz) AC power supply many loads and are supplemented by 540V DC sub-bus

(±270VDC) [4, 5]. Since the proposed system concept includes a power converter it is able to supply both variable frequency or fixed frequency output. In order to establish filter parameters in chapter 2, an 115V 400Hz AC power bus was adopted as the target application. The requirements for an 115V 400Hz AC power bus as set out in MIL-STD 704 are shown in Table 1.1 while Figure 1.6 distortion amplitudes of AC operations at 400Hz.

Table 1.1 AC normal operation characteristics –for 400 Hz operation

(as set out in - MIL-STD-704F)

Steady state characteristics	Limits
Steady state voltage	108.0 to 118.0 Volts, RMS
Voltage unbalance	3.0 Volts, RMS maximum
Voltage modulation	2.5 Volts, RMS maximum
Voltage phase difference	116° to 124°
Distortion factor	0.05 maximum
Distortion spectrum	Figure 1.
Crest factor	1.31 to 1.51
DC component	+ 0.10 to - 0.10 Volts
Steady state frequency	393 to 407 Hz
Frequency modulation	4 Hz

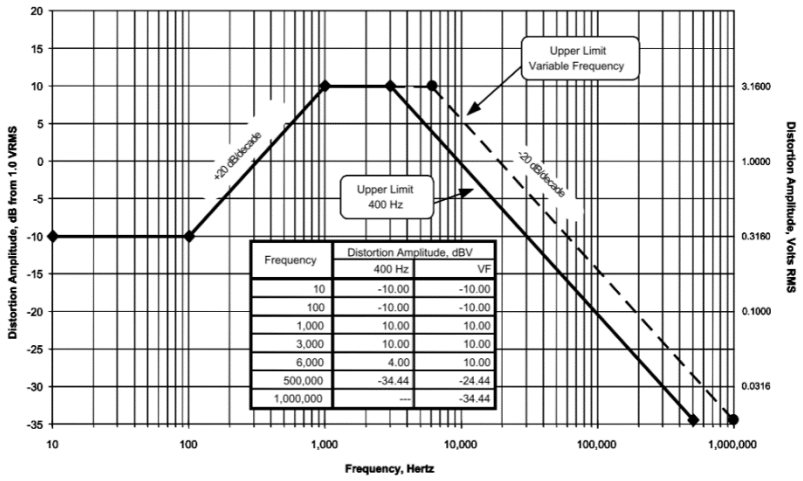

Figure 1.7 Distortion amplitudes of AC operations at 400Hz (source: MIL-STD-704F)

1.3 Review of candidate electrical machine topologies

The machine topologies which may be suitable for this application need to exhibit several generic features that are required in all electrical machines for aerospace generators, i.e. high power density, high efficiency and low reactance. However, the key requirement for any machine for feeding a soft-switched converter with an appropriate input voltage

waveform is a large multiplier between the mechanical frequency (determined by rotational speed) and electrical frequency. For example, in order to generate 20 kHz from a machine rotating at 20,000rpm, a 60-fold increase is required. When full wave rectified, this would give 40,000 pulses per second. In a conventional machine, this would require 60 pole-pairs on the rotor. Although such high pole numbers are common in very large, low-speed direct-drive wind generators [47] such pole numbers are not used in medium and high speed machines, and hence there is very little, if any, published literature on permanent magnet machines with output frequencies in the tens of kHz range.

A number of potential machines are reviewed in this section in terms of the features that could be used to generate output frequencies in the tens of kHz range. These different machines can meet several requirements, but not all of them in some cases. The merits and drawbacks of each machine topology are discussed in the context of the unusual demands of this particular application.

1.3.1 Conventional surface mounted permanent magnet machines

The merits of surface mounted permanent magnet (PM) machines, and example of which is shown in Figure 1.8, are well recognized and hence they have been widely adopted in a vast range of applications and power ratings. In conventional surface mounted PM machines, S pole and N pole magnets are arranged alternately on the surface of the rotor directly facing the working airgap.

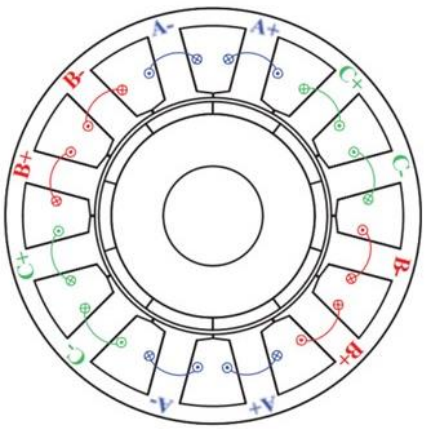

Figure 1.8 Typical arrangement of a conventional surface-mounted PM machine [48]

In order to achieve a high frequency output in the 10s of kHz range, a very high pole number would need to be used in surface mounted PM machines. Although generally the range of pole number in this kind of machines is wide, the high pole number would require a corresponding increase in the number of stator teeth, which would be prohibitive in most medium powered machines. For example, a 120 pole rotor with a conventional 1.5 slots per pole, 3-phase winding would require 180 slots. Even a single-phase machine would require 120 slots, a number that would be challenging to accommodate around a stator bore with a diameter of ~100-150mm and lead to very narrow slots. Hence, alternative machine topologies were explored with various features that machine can produce output frequencies which are many multiples of the rotational speed.

1.3.2 Flux-switching PM machines

Various types of so-called flux switching permanent magnet (FSPM) machines have a long history of development over 60 years or so [49]. Many developments have occurred with the progress of power electronics in more recent times. FSPM machines combine the benefit of surface mounted PM machines and switched reluctance machines, i.e. FSPM machines have the high airgap flux density of surface mounted PM machines and the robust rotor of switched reluctance machines [50]. There are many different types of FPSM but they all have the same basic double salient structure which is shown in Figure 1.9.

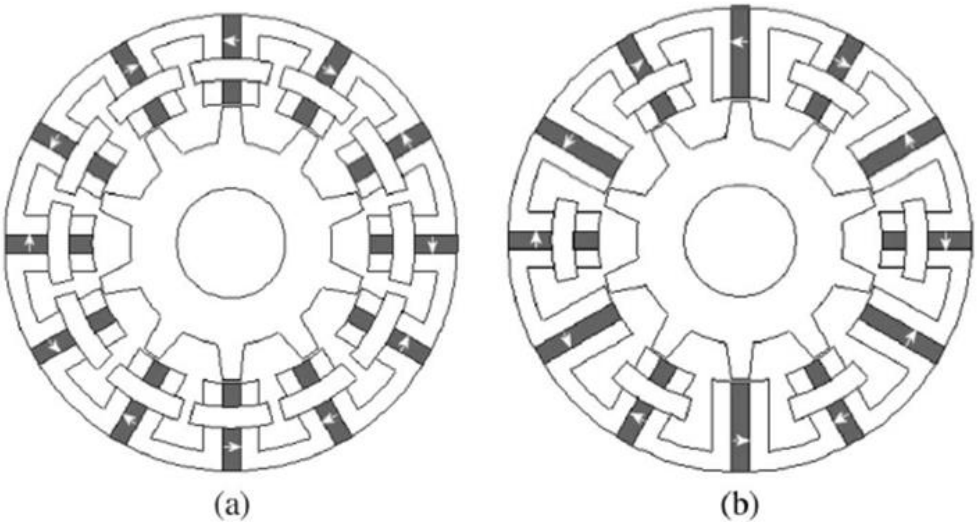

Figure 1.9 Flux switching PM machines:
(a) all poles wound (b) alternative poles wound [51]

The stator contains both coils and permanent magnets, with the permanent magnets embedded within the stator teeth. The rotor has a simple and rugged salient construction, with the number of teeth determining the multiplier between mechanical frequency and electrical frequency.

The most conventional FSPM machines are so-called 'all-poles wound' machines, also called double layer machines, where all stator poles are wound with coils. An example is shown in Figure 1.9 (a). The all poles wound FSPM machines have short end winding, giving slightly lower copper losses, and high power factor [52]. At same time, the mutual inductance between each coil is often cited as a reason for using a C core structure, which means higher magnetic coupling.

In [51], alternative poles wound FSPM machines were investigated. In this type of machine, stator poles are wounded alternately as shown in Figure 1.9 (b). Although the end winding length is increased, one attractive feature is lower mutual inductance between coils. In some other structures, further reductions of inductance have been realised, e.g. the fault tolerance FSPM machines [53-54], shown in Figure 1.10. This type of machine has modularised stator cores, in which each coil is isolated from the remaining coil other both electrically and magnetically, which makes in turn reduces the effective synchronous inductance.

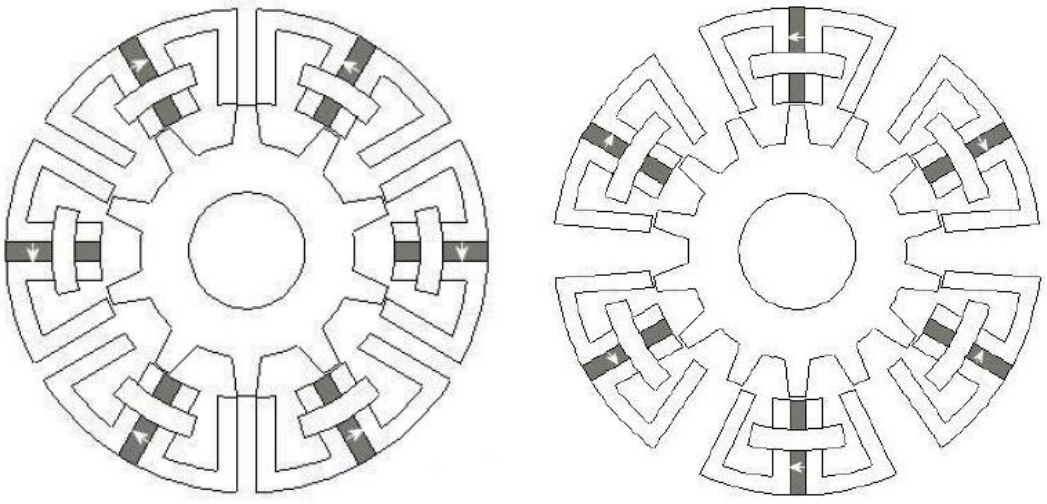

Figure 1.10 Fault tolerance FSPM machines investigated from [53]

1.3.3 Flux-reversal machines

Another machine topology which may be well suited to high frequency output are the various types of Flux Reversal (FR) machines. These have a similar salient rotor to switched reluctance machines, but employ a pair of alternate pole permanent magnets on the stator teeth, as shown in Figure 1.11. Comparing to the conventional PMSM machines, the attractive benefits of FR machines are simple rotor structure, low self- and mutual inductance, high torque density and high fault tolerance [55-57].

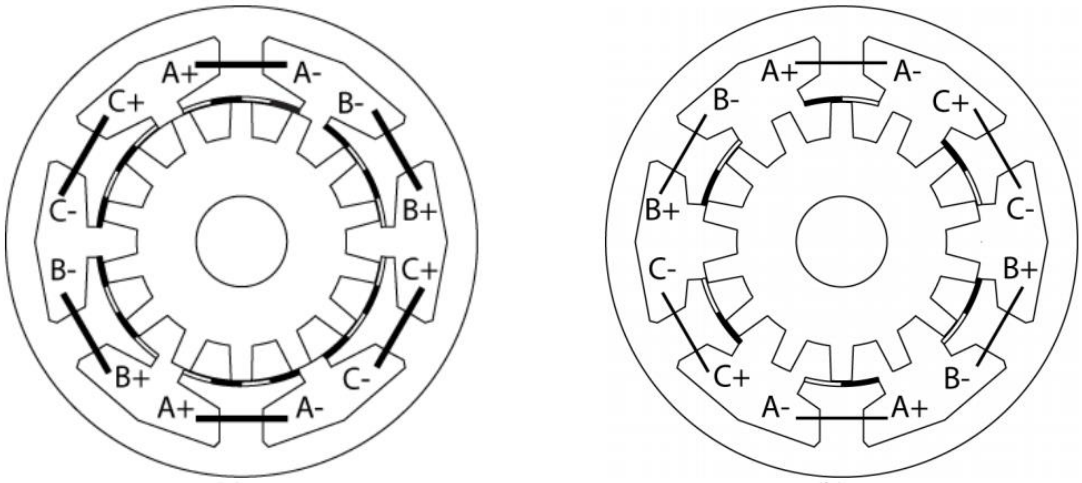

Figure 1.11 Flux Reversal Machines in different topologies (Source: [56])

As shown in Figure 1.11, a number of permanent magnets are mounted on the surface of each stator tooth. The number of PM poles on each stator tooth can exceed two (e.g. the 4 magnet poles in the left hand example of Figure 1.11). Hence, the number of PM pole-pairs on each tooth have can be high, which in turn dictates that the ratio of the number of PM pole pairs and the number of stator teeth number can be high. A high rotor pole number is essential in order to realise a high frequency generator output, which is well suited to the requirements of the application considered in this thesis.

The operating principles of FR machines can be seen in the machine on the left of Figure 1.11. Taking phase C as an example, the rotor teeth are aligned with N pole magnet in one stator teeth and another aligned to S pole magnet. When the rotor has rotated one magnet pitch, the flux through this path will be reversed.

A series of three phase FR machines were analysed in [55] which demonstrated that FR machines have good performance in high speed or high frequency applications. Low self-inductance and mutual inductance (due to the large effective airgap caused in the presence of the stator magnets) is useful for extracting power at high frequency, with some capability for fault tolerance. Pellegrino et al [56] observed that a high number of PM poles in each tooth can yield benefits in magnetic loading and shear stress, but at the expense of a decrease in the power factor.

1.3.4 Magnetically geared machines

Many flux modulating machines rely on a highly salient rotor to modulate the flux produced by a series of permanent magnets in the stator. These machines produce unipolar variations in the coil flux. There are many different types, including the topology described previously in section 1.3.2 and section 1.3.3. A mechanically complex type has been proposed in [58-60] and is shown in Figure 1.12. This magnetically geared (MG) machines, has several claimed advantages including high torque, high power density, low PM content and low weight. The flux distribution in the air gap is affected by the flux modulator. In this type of MG machine, there are three elements i.e. high pole number rotor, flux modulator and armature, although various topologies have proposed that some element, can be combined as a single assembly to form various flux modulation machines [60].

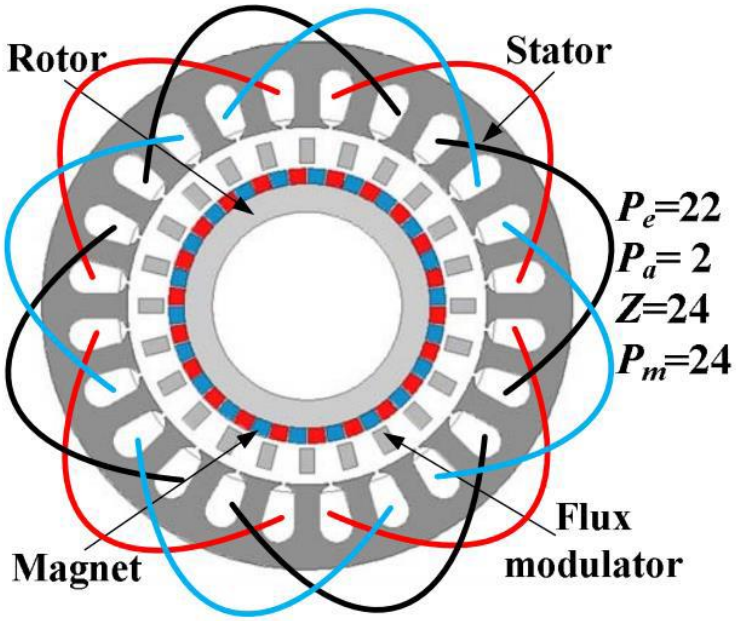

Figure 1.12 A kind of magnetically geared (MG) machine (Source: [60])

As shown in Figure 1.12, the pole number of the field exciter and flux modulator are necessarily different, which make the machine act in some respects like a magnetic gear. This gearing can be used in generate a high frequency output with is many multiples of the rotational speed.

A useful review of the various flux modulation machine types [60] also shows the relationship between flux reversal machines and flux switching machines, as well as magnetically geared machines and Vernier machines, as shown in Figure 1.13 and Figure 1.14. In flux reversal machines, the excitation coil and permanent magnet can be interchanged, so that the machine evolves into doubly-salient PM machine, where flux barriers are incorporated into the stator teeth to reduce the flux leakage. If the flux barriers are replaced by permanent magnet, the machine becomes a flux switching machine. Similarly, in magnetically geared machines, if the airgap between flux modulator and stator teeth is removed, then this topology changes to Vernier machines. These illustrate that these various flux modulation machine types have much in common in terms of their operating principles. Table 1.2 has compared advantage and disadvantage among FS, FR and Vernier machines.

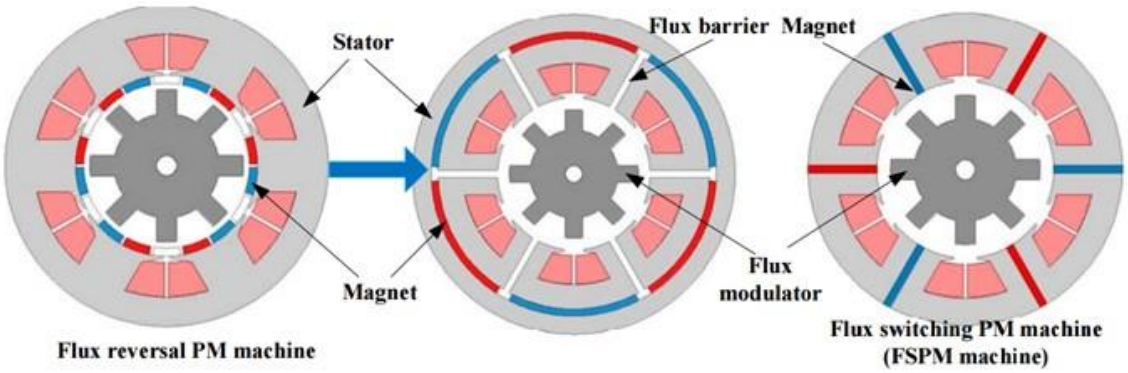

Figure 1.13 Machine topologies evolution from FR machine to FS machine [60]

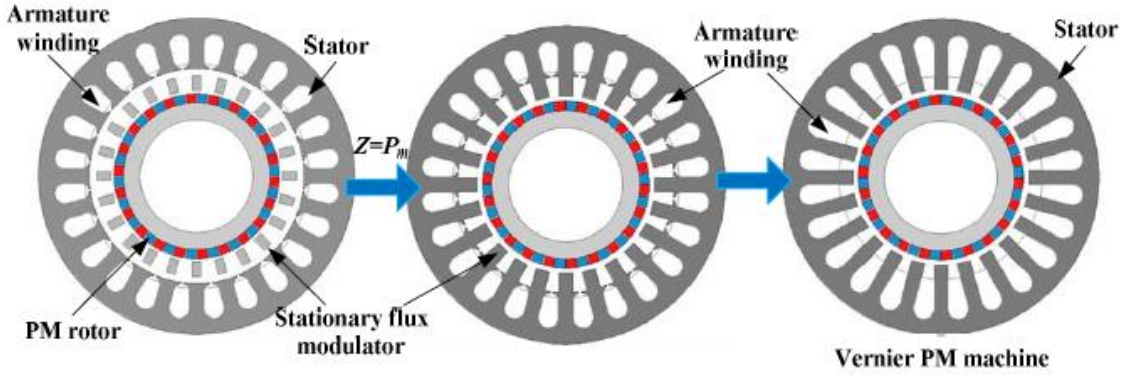

Figure 1.14 Machine topologies evolution from MG machine to Vernier machine [60]

Table 1.2 Comparison of FS, FR and Vernier machines

	Switched-flux	Flux-reversal	Vernier
Torque density	High	Medium	Good
Power density	High	Medium	Good
PM consumption	High	Low	Medium
PM immunity	High	Low	Low
Copper area	Low	Good	Good

1.3.5 Hybrid stepper machines

Hybrid stepper machines are widely used as motors in many applications, as they can provide high accuracy open-loop positioning without a sensor or any other feedback control [61, 62]. This ability to generate a small mechanical step from a single applied

pulse of current, in principle can be exploited in generation mode to produce a high frequency pulse-train from continuous rotation. In many hybrid stepper machines, a high number of small teeth are incorporated into both the stator and rotor which results in a step pitch in a range of 0.6° to 1.8° [61]. An axially magnetised permanent magnet ring is incorporated in the rotor between two rotor-cores with multiple teeth that force the flux go from one lamination stack to another. The two lamination stacks are rotated relative to each other by half pitch of small teeth as shown in Figure 1.15.

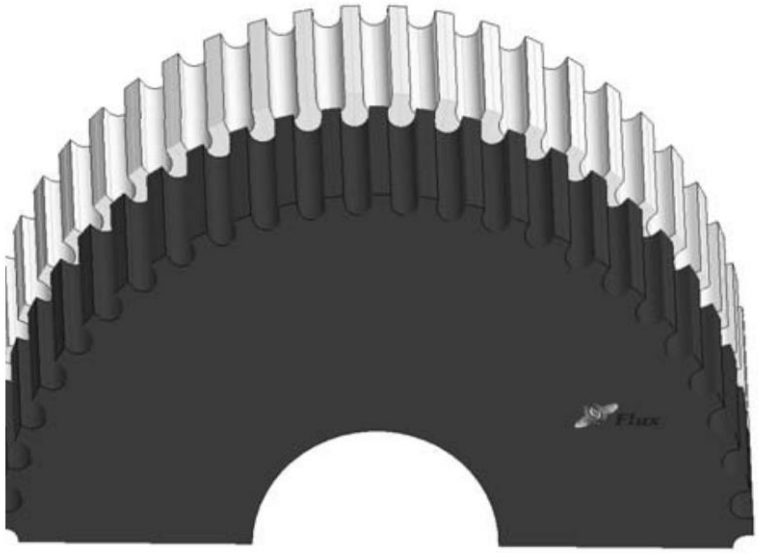

Figure 1.15 the rotor structure of a hybrid stepper motor [62]

Hybrid stepper machines have some features that may be useful in the application in this thesis. However, there are some significant challengers for use as a generator, the main one being the high reactance which would limit output power. Even when used as a motor at modest speeds (i.e. a few thousands of rpm) the high inductance tends to limit performance.

1.4 Research methodology

1.4.1 Overall research aims

The overall aim of this thesis is to assess the feasibility of the generator system architecture concept shown previously in Figure 1.6. The core of the research is the

development of machine designs which are capable of producing output frequencies in the tens of kHz with competitive power densities and to evaluate their performance in detail. The requirements of this application are very different from the majority of permanent magnet generator applications and hence several non-standard machine types and extreme operating conditions are explored. In order to assess the performance of different machine high output frequency machine types in a consistent manner, a set of baseline overall dimensions were selected and the performance of each different design predicted. Figure 1.16 shows a schematic representation of the various research activities undertaken during this research.

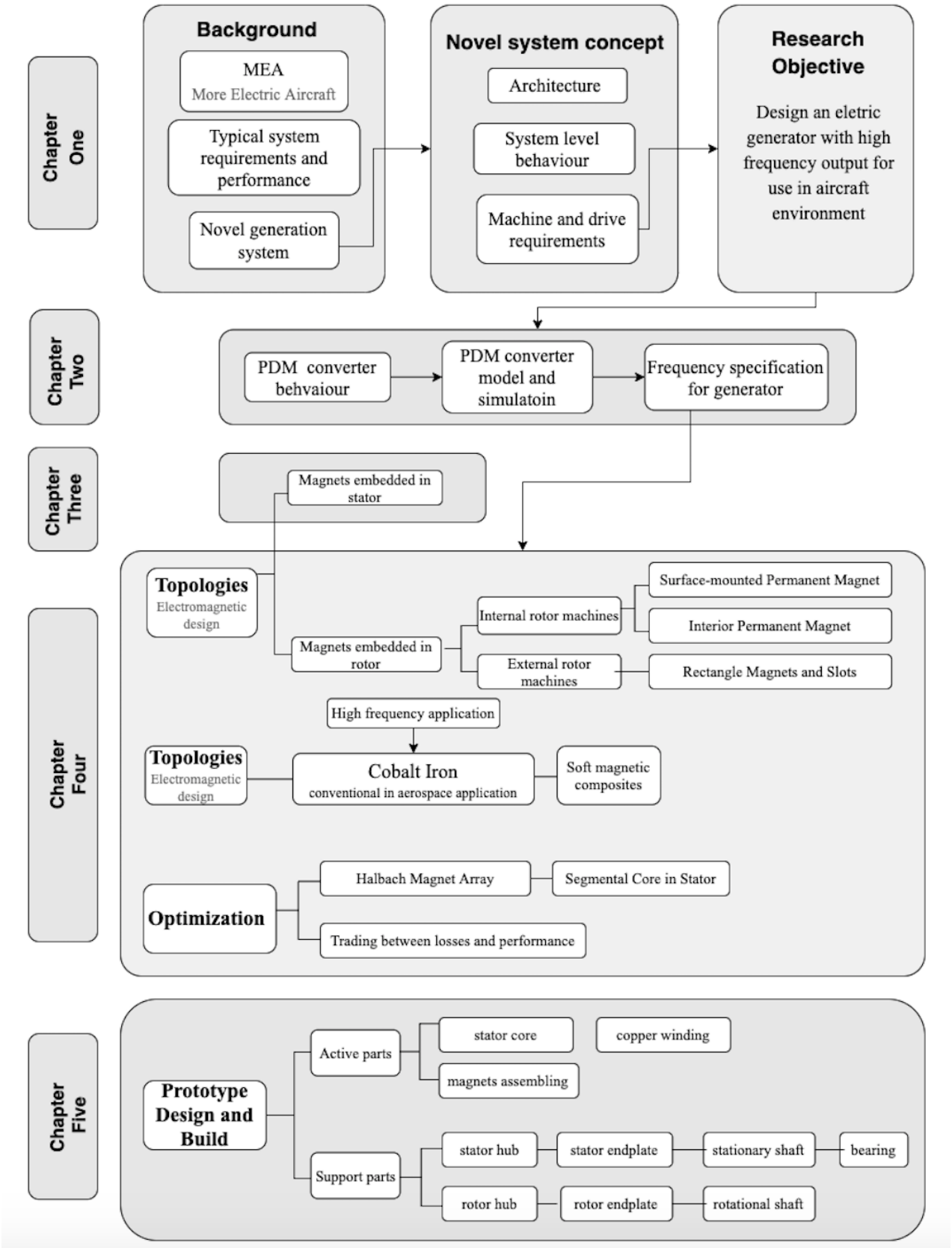

Figure 1.16 Summary of research activities

1.4.2 Baseline reference design of conventional brushless DC machine

The baseline dimensions were based on an existing 3-phase, 10-pole brushless PM machine design with surface mounted magnets which was developed in [63]. The machine has a machine outer diameter of 160mm, active axial length of 50mm and a rotor outer diameter of 118mm (more detailed dimensions will be shown in chapter 3). A cross-section through the machine is shown in Figure 1.17. The machine was designed to operate in generating mode only in combination with a three-phase uncontrolled rectifier. When generating 50kW output power via an uncontrolled rectifier into a purely resistive load, the machine has a stator current density of 14A/mm^2 rms. It is worth noting that this baseline machine has a fundamental frequency of 1.667 kHz at its maximum operating speed of 20,000rpm. Hence, it provides a useful baseline in terms of power density against which to judge high different machine topologies and designs, but does not have the high frequency output capability required. Further details of this machine are presented in chapter 3.

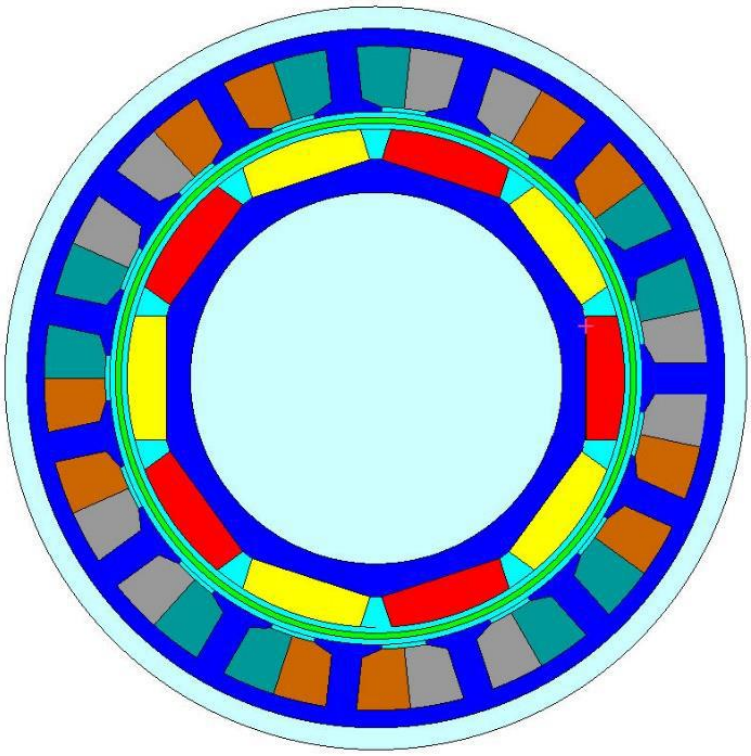

Figure 1.17 Reference machine design

1.4.3 Modelling tools

A series of different modelling tools were used to undertake the research described in this thesis.

- Electromagnetic finite element modelling, including electric circuit-coupled simulations, were undertaken using the OPERA package from Cobham.
- For the calculation of iron loss in chapters 4 and 5, OPERA was combined with an existing in-house developed finite element post-processing tool.
- The mechanical stress modelling reported in chapter 4 was undertaken using ANSYS.
- SIMULINK was used with various toolkits to simulate the converter performance in chapter 2.

1.5 Thesis outline

This thesis describes a series of design studies on a variety of different machine types to suit the unusual demands of the target application. These studies span electromagnetic, thermal and mechanical aspects of machine performance and address many manufacturing challenges and issues. Although focused on the machine design and manufacture, a chapter is devoted to the modelling of the converter as this provides valuable information in terms of setting the output frequency specification for the generator. The thesis is structured as follows:

Chapter 1 describes the system concept and reviews potential machine types.

Chapter 2 describes the SIMULINK modelling of PDM converter with a view to understanding the output frequency requirements for a generator design

Chapter 3 explores several alternative machine topologies, including various flux switching, flux modulating and hybrid stepper type structures. The chapter concludes by identifying a preferred topology.

Chapter 4 describes an extensive and detailed study into the performance of the preferred topology and considers numerous variants and design features. It includes a detailed consideration of the likely stator core is on preferred topology

Chapter 5 reports on the build of a prototype machine, including a re-design with Nickel iron laminations, and preliminary testing

Chapter 6 Conclusions and Future Research.

1.6 References

[1] A. W. Schäfer, S. R. H Barrett, K. Doyme, L. M. Dray, A. R. Gnadt, R. Self, A. O'Sullivan, A.P. Synodinos, J. Torija, 'Technological, economic and environmental prospects of all-electric aircraft', Nature Energy volume 4, pp. 160–166 (2019).

[2] A. Teo, K. Rajashekara, J. Hill, and B. Simmers, "Examination of aircraft electric wheel drive taxiing concept," in Proc. SAE Power Syst. Conf., 2008, pp. 1–5.

[3] F. Re, "Viability and state of the art of environmentally friendly aircraft taxiing systems," in Proc. IEEE Conf. Elect. Syst. Aircr. Railway Ship Propul., 2012, pp. 1–6.

[4] A. Boglietti, A. Cavagnino, A. Tenconi, and S. Vaschetto, "The safety critical electric machines and drives in the more electric aircraft: A survey," in Industrial Electronics, 2009. IECON '09. 35th Annual Conference of IEEE, 2009, pp. 2587-2594.

[5] B. Sarlioglu and C. T. Morris, "More Electric Aircraft: Review, Challenges, and Opportunities for Commercial Transport Aircraft," Transportation Electrification, IEEE Transactions on, vol. 1, pp. 54-64, 2015.

[6] T. Feehally and J. Apsley, "The doubly-fed induction machine as an aero generator," in Energy Conversion Congress and Exposition (ECCE), 2014 IEEE, 2014, pp. 1340-1347.

[7] T. Sebastian and G. R. Slemon, "Operating limits of inverter-driven permanent magnet motor drives", IEEE Trans. on Industry Applications, Vol. IA-23, No.2, pp. 327-333, March/April, 1987.

[8] K. Ni et al., "Electrical and Electronic Technologies in More-Electric Aircraft: A Review," in IEEE Access, vol. 7, pp. 76145-76166, 2019.

[9] W. Cao, B. C. Mecrow, G. J. Atkinson, J. W. Bennett, D. J. Atkinson, "Overview of electric motor technologies used for more electric aircraft (MEA)", IEEE Trans. Ind. Electron., vol. 59, no. 9, pp. 3523-3531, Sep. 2012.

[10] V. Madonna, P. Giangrande, M. Galea, "Electrical power generation in aircraft: Review challenges and opportunities", IEEE Trans. Transport. Electrific., vol. 4, no. 3, pp. 646-659, Sep. 2018.

[11] M. Sinnett, “787 No-Bleed Systems: saving fuel and enhancing operational efficiencies,” Boeing Aero Mag., vol. 4, pp. 6–11, 2007.

[12] A. Trentin, P. Zanchetta, P. Wheeler, J. Clare, "Performance evaluation of high-voltage 1.2 kV silicon carbide metal oxide semi-conductor field effect transistors for three-phase buck-type PWM rectifiers in aircraft applications", IET Power Electron., vol. 5, no. 9, pp. 1873-1881, Nov. 2012.

[13] A. Nawawi, C. F. Tong, S. Yin, A. Sakanova, Y. Liu, Y. Liu, M. Kai, K. Y. See, K. J. Tseng, R. Simanjorang, C. J. Gajanayake, "Design and demonstration of high power density inverter for aircraft applications", IEEE Trans. Ind. Appl., vol. 53, no. 2, pp. 1168-1176, Mar./Apr. 2017.

[14] Y. Liu, K. Y. See, S. Yin, R. Simanjorang, C. F. Tong, A. Nawawi, J. S. J. Lai, "LCL filter design of a 50-kW 60-kHz SiC inverter with size and thermal considerations for aerospace applications", IEEE Trans. Ind. Electron., vol. 64, no. 10, pp. 8321-8333, Oct. 2017.

[15] M. J. Cronin, “All electric environmental control system for advanced transport aircraft,” U.S. Patent 4 523 517, Jun. 18, 1985.

[16] H. Saito, S. Uryu, N. Morioka, and H. Oyori, “Study of VCS design for energy optimization of non-bleed electric aircraft prerequisite conditions to replace ACS,” SAE Tech. Pap. 2014-01-2225, 2014.

[17] A. R. Behbahani and K. J. Semega, “Control strategy for electromechanical actuators versus hydraulic actuation systems for aerospace applications,” SAE Tech. Pap. 2010-01-1747, 2010.

[18] D. R. Trainer and C. R. Whitley, “Electric actuation–Power quality management of aerospace flight control systems,” in Proc. IET Int. Conf. Power Electron. Mach. Drives, 2002, pp. 229–234.

[19] M. Liu and Y. Zhou, “The reliability prediction of an electro-mechanical actuator of aircraft with the hybrid redundant structure,” in Proc. IEEE Veh. Power Propul. Conf., 2008, pp. 1–5.

[20] T. Nelson, 787 Systems and Performance, Dec. 2017, [online] Available: http://myhres.com/Boeing-787-Systems-and-Performance.pdf.

[21] I. Moir, "More-electric aircraft-system considerations," in Electrical Machines and Systems for the More Electric Aircraft (Ref. No. 1999/180), IEE Colloquium on, 1999, pp. 10/1-10/9.

[22] J. Brombach, T. Schröter, A. Lücken, D. Schulz, "Optimized cabin power supply with a +/− 270 V DC grid on a modern aircraft", Proc. 7th Int. Conf.-Workshop Compat. Power Electron. (CPE), pp. 425-428, 2011.

[23] J. J. Pierro and J. E. Phillips "Investigation of High-Frequency Power Conversion and Generator Techniques", IEEE Transactions on Aerospace (Volume: AS-3, Issue: 2), June 1965, pp411-422

[24] R. Raju, “Silicon carbide high voltage, high frequency conversion,” in Proc. NIST High Megawatt Variable Speed Drive Technol. Workshop, 2014, pp. 5–8.

[25] H. Zhang and L. M. Tolbert, “Efficiency impact of silicon carbide power electronics for modern wind turbine full scale frequency converter,” IEEE Trans. Ind. Electron., vol. 58, no. 1, pp. 21–28, Jan. 2011.

[26] Pimentel, D., M.B. Slima, and A. Cheriti. Power Control for Pulse-Density Modulation Resonant Converters. in Industrial Electronics, 2006 IEEE International Symposium on. 2006.

[27] M. Nakaok, H.Yonemori, and K. Yurugi, "Zero-Voltage soft-switched PDM three phase AC-DC active power converter operating at unity power factor and sinewave line current" Proc. of PESC'93, 24th Annual IEEE 20-24 June 1993 pp. 787-794

[28] R. Li, D. Xu, "A zero-voltage switching three-phase inverter", IEEE Trans. Power Electron., vol. 29, no. 3, pp. 1200-1210, 2014.

[29] M. C. Cavalcanti, E. R. da Silva, D. Boroyevich, Wei Dong, C. B. Jacobina, "A feasible loss model for IGBT in soft-switching inverters", Power Electronics Specialist Conference 2003. PESC '03. 2003 IEEE 34th Annual, vol. 4, pp. 1845-1850, 4, June 2003.

[30] E.Chong, Internal Rolls-Royce correspondence, 2014.

[31] T.S. Wu, M.D. Bellar, A. Tchamjdou, J. Mahdavi, and M. Ehsani, “A review of soft-switched DC-AC converters”, in Proceedings of the IEEE IAS, 1996, pp. 1134-1144.

[32] K.M. Smith and K.M. Smedley, “A comparison of voltage mode soft switching methods for PWM converters,” in Proceedings of The IEEE APEC, 1996, pp. 291-298.

[33] F.T. Wakabayashi and C.A. Canesin, “A new HPF-PWM boost rectifier,” in Proceedings of the COBEP (Brazilian Conference on Power Electronics), 1999, pp. 417-422.

[34] H. Fujita, H. Akagi, "Control and Performance of a Pulse-Density-Modulated Series-Resonant Inverter for Corona Discharge Process", IEEE Transactions on Industry Applications, vol. 35, no. 3, pp. 621-627, May/June 1999.

[35] Wei Liu, Jiasheng Zhang, Rong Chen, "Modelling and control of a novel zero-current-switching inverter with sinusoidal current output", Power Electronics IET, vol. 9, no. 11, pp. 2205-2215, 2016.

[36] Chandan Suthar, Jeemut B. Sangiri, Suman Maiti, Chandan Chakraborty, "A Pulse density modulated LLC resonant converter based battery charger for HEV/PHEV application", Electrical Computer and Communication Technologies (ICECCT) 2019 IEEE International Conference on, pp. 1-7, 2019.

[37] J. B. Bell and R. M. Nelms, "Speed Control of a Brushless DC Motor Using Pulse Density Modulation and MCTs", IEEE-APEC, pp. 356-362, 1994

[38] D. M. Divan, "The Resonant dc Link Converter - A New Concept in Static Power Conversion", Annual Meeting IEEE Ind. Appl. Soc., pp. 648-655, 1986

[39] D. M. Divan and G. Skibinski, “Zero switching loss inverters for high power applications,” in Proc. IEEE IAS Conf. Rec., 1987, pp. 627–634.

[40] J. He, N. Mohan, and B. Wold, “Zero voltage switching PWM inverter for high frequency DC-AC power conversion,” IEEE Trans. Ind. Appl., vol. 29, pp. 959–968, Sep./Oct. 1993.

[41] J. G. Cho, H. S. Kim, and G. H. Cho, "Novel soft switching PWM converter using a new parallel resonant dc-link," in Proc. IEEE Power Electron. Spec. Conf., 1991, pp. 241–247.

[42] Q. Li, J. Wu, and H. Jiang, "Design of parallel resonant dc-link soft switching inverter based on DSP," in Proc. World Congr. Intell. Control Autom., 2004, pp. 5595–5599.

[43] Z. Y. Pan and F. L. Luo, "Transformer based resonant dc-link inverter for brushless DC motor drive system," IEEE Trans. Power Electron., vol. 20, no. 4, pp. 939–947, Jul. 2005.

[44] H. Hucheng, D. Jingyi, C. Xiaosheng, and L. Weiguo, "Three-phase soft switching PWM inverter for brushless DC motor," in Proc. IEEE Ind. Electron. Appl., pp. 3362–3365, May 2009.

[45] A. Sikorski and T. Citko, "Quasi-resonant parallel DC link circuit for high-frequency DC-AC inverters," in Proc. Eur. Conf. Power Electron. Appl., 1993, pp. 174–177.

[46] L. Malesani, P. Tenti, P. Tomasin, and V. Toigo, "High efficiency quasiresonant DC link three-phase power inverter for full-range PWM," IEEE Trans. Ind. Appl., vol. 31, no. 1, pp. 141–148, Jan./Feb. 1995.

[47] R. S. Semken, M. Polikarpova, P. Roytta, J. Alexandrova, J. Pyrhonen, J. Nerg, A. Mikkola1, J. Backman "Direct-drive permanent magnet generators for highpower wind turbines: Benefits and limiting factors," IET Renewable Power Generation, vol. 6, no. 1, pp. 1–8, Jan. 2012.

[48] D. Wu; Z. Q. Zhu "Influence of Slot and Pole Number Combinations on Voltage Distortion in Surface-Mounted Permanent Magnet Machines with Local Magnetic Saturation", IEEE Transactions on Energy Conversion (Volume: 30, Issue: 4), 05 June 2015, pp 1460 – 1471

[49] S. E. Rauch and L. J. Johnson, "Design principles of flux-switching alternators," AIEE Trans., vol. 74III, pp. 1261–1268, 1955.

[50] A.S. Thomas, Z.Q. Zhu, R.L. Owen, G.W. Jewell, and D. Howe, "Multiphase Flux-Switching Permanent-Magnet Brushless Machine for Aerospace Application," IEEE Trans. Ind. Appl, vol. 45, no. 6, pp. 1971-1981, Nov./dec. 2009.

[51] J. T. Chen, and Z. Q. Zhu, "Comparison of all and alternate poles wound flux-switching pm machines having different stator and rotor pole numbers," Proc. IEEE Energy Conversion Congress and Exposition (ECCE2009), San Jose, USA, 20-24 September, 2009, pp. 1705-1712.

[52] G. Li, J. Ojeda, E. Hoang, and Gabsi, "Double and single layers flux- switching permanent magnet motors: fault tolerant model for critical applications," in Proc. Int. Conf. Elec. Mach. Syst., Aug. 2011, pp. 1-6.

[53] R. Owen, Z.Q. Zhu, A. Thomas, G. W. Jewell, and D. Howe, "Fault tolerant flux switching permanent magnet brushless AC machines," IEEE Trans. Ind. Appl., vol. 46, no. 2, pp. 790-797, 2010.

[54] T. Rominosoa and Chris Gerada, "Fault tolerant winding technology comparison of flux switching machine," in Proc. Int. Conf. Elec. Mach., Sep. 2012, pp.1-6.

[55] C. Wang, S. A. Nasar, and I. Boldea, "Three phase flux reversal machine (FRM)," IEEE Trans. Electr. Power Appl., vol. 146, no. 2, pp. 139–146, Mar. 1999.

[56] Gianmario Pellegrino and C. Gerada, " Modelling of Flux Reversal Machines for direct drive applications " Power Electronics and Applications (EPE 2011), Proceedings of the 2011-14th European Conference on Sept. 1 2011

[57] R. P. Deodhar, S. Anderson, I. Boldea, and T. J. E. Miller, "The flux reversal machine: A new doubly salient permanent magnet machine," IEEE Trans. Ind. Appl., vol. 33, no. 4, pp. 925–934, Jul./Aug. 1997.

[58] W. Fu and S. Ho, "A flux-modulated low-speed motor with an improved structure and its performance analysis using finite-element method," in Electromagnetic Field Computation (CEFC), 2010 14th Biennial IEEE Conference on, p. 1, may 2010.

[59] Fu, W N; Ho, S L, "A Quantitative Comparative Analysis of a Novel Flux-Modulated Permanent-Magnet Motor for Low-Speed Drive" IEEE Transactions on Magnetics46.1 (Jan. 2010): 127-134.

[60] D. Li, R. Qu, and J. Li, "Topologies and Analysis of Flux-Modulation Machines" Energy Conversion Congress and Exposition (ECCE), 2015 IEEE, Sept. 2015, pp2153 – 2160

[61] M. Bodson, J. N. Chiasson, R. T. Novotnak, R. B. Rekowski, "High performance nonlinear feedback control of a permanent magnet stepper motor," IEEE Transactions on Control Systems Technology, vol. 1, no 1, pp. 5 –14, Mar. 1993.

[62] A. Oswald and H.G. Herzog, "Investigation of the usability of 2D- and 3D-FEM for a hybrid stepper motor," in Proc. 6th IEEE Int. Elect. Mach. Drives Conf., Miami, FL, USA, May 3–6, 2009, pp. 535–542.

[63] M. Shortte, 'Electro-thermal optimisation of a 50kW synchronous permanent magnet generator for aerospace application'. PhD thesis, University of Sheffield, 2016.

Chapter 2 Modelling of a Pulse Density Modulation Converter

2.1 Introduction

The basic principles, benefits and challenges of a soft-switching power electronic converter with a fluctuating DC link were discussed in chapter 1. The main focus of this thesis is the electromagnetic design of the generator and not the detailed design and control of a power converter. However, since the switching frequency of the converter is fixed by the rectified output frequency of the generator, there is a need to establish a suitable converter switching frequency in order to set a pole number for the generator design. Establishing a generator output frequency and hence converter switching frequency involves a trade-off between selecting a lower frequency to reduce the machine core loss and converter switching loss and selecting a higher switching frequency to provide greater resolution of control, improved power quality or reduced filter size [1-9]. This chapter focusses on the modelling of a three-phase bridge to operate in the system outlined in Chapter 1, in particular on establishing an understanding of the electrical output frequency specification for a generator. In addition, given that the converter output needs to meet an amplitude specification set by industry standards, the converter model provides a means of estimating the amplitude of the converter input produce a given output amplitude with account of the modulating effect of the converter and the attenuation in the filter. It does not consider detailed aspects of closed loop control or converter switching loss.

2.2 Simulink model of PDM inverter fed with a full-wave rectified

A top level block diagram of the PDM inverter system model is shown in Figure 2.1. A model representing this block diagram was developed in SIMULINK, including extensive use of elements and sub-systems from the Simscape Electrical Library. The overall SIMULINK model is made up from a number of sub-systems which are described in the next section.

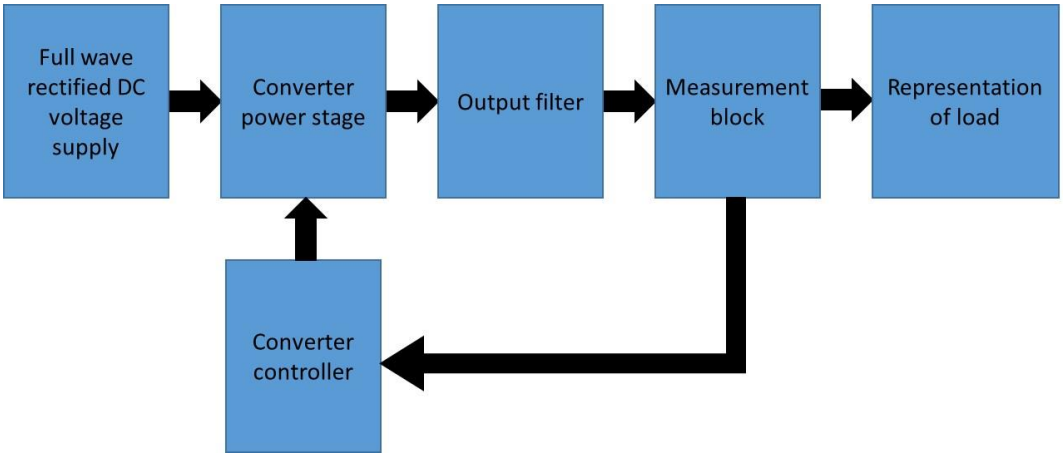

Figure 2.1 Block diagram of a PDM converter model

2.2.1 Voltage source and full wave rectifier

This simple sub-system models an idealised representation of the generator and its rectifier. It is based on a sinusoidal AC source with zero output impedance. An AC sinusoidal voltage source (with user settable magnitude and frequency) is connected to a full wave bridge rectifier consisting of diodes which have a fixed forward voltage drop of 1 V but are otherwise ideal. The SIMULINK implementation of this sub-system is shown in Figure 2.2, while Figure 2.3 shows typical output generated by this model for the case of a 520V, 32 kHz sinusoidal supply.

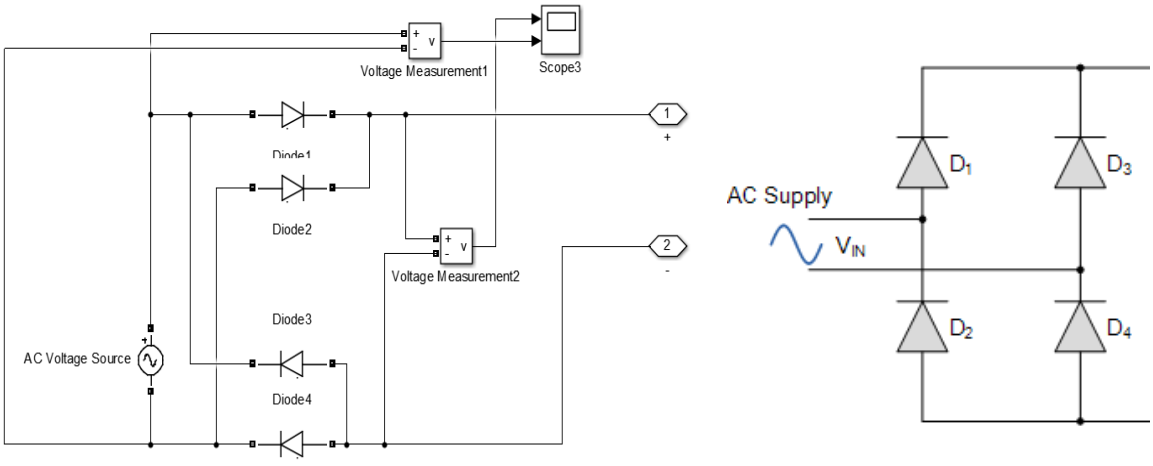

(a) MATLAB model (b) Principle model

Figure 2.2 SIMULINK sub-system for zero output impedance source

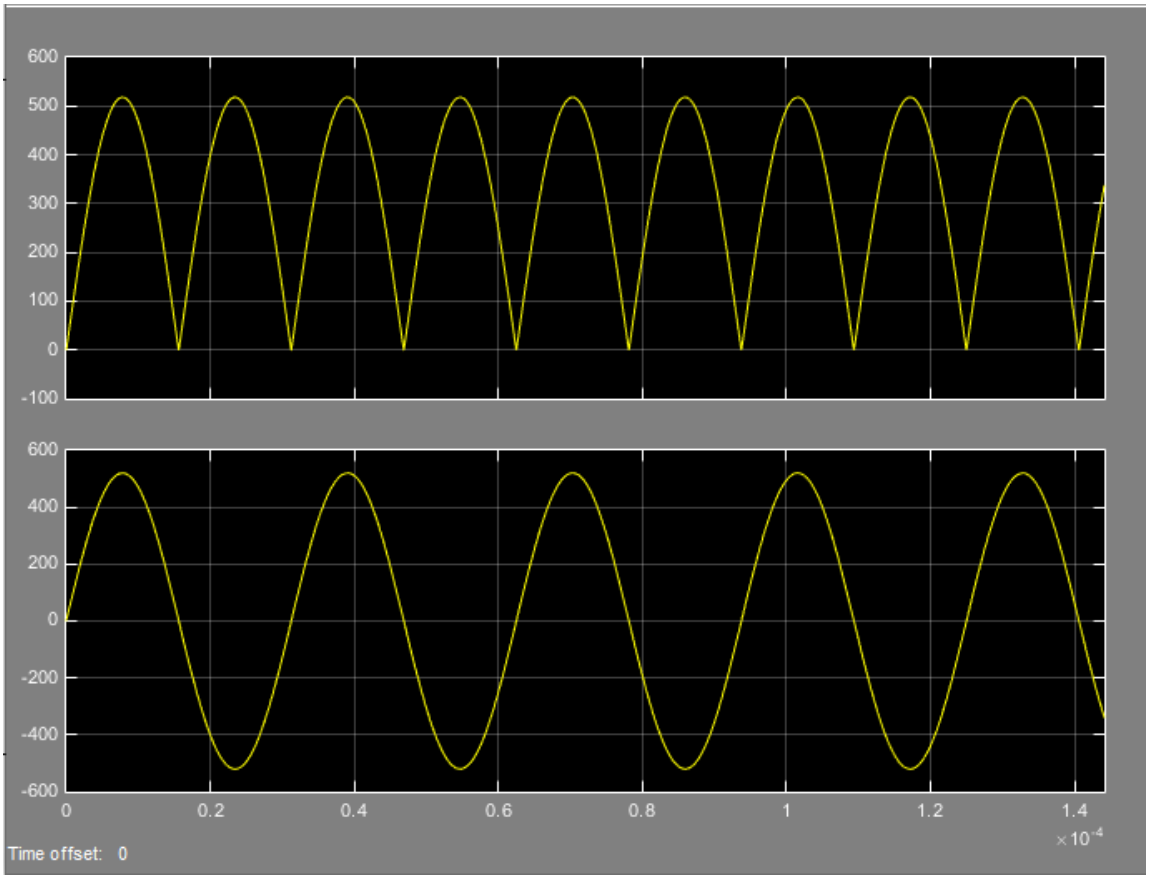

Figure 2.3 SIMULINK generated waveform of rectified DC pulses (upper) and AC source (lower) for a 520V peak, 32kHz sinusoidal supply

2.2.2 Converter power stage

This sub-system model implements a standard three-phase IGBT converter with clamping diodes using the Universal Bridge block from the SIMULINK SIMSCAPE Electrical Library. The SIMULINK block is shown in Figure 2.4. The 6 gate signals are provided via a single bus (labelled g) and control the individual switches in the bridge. The converter input supply voltage (which in this case is the full-rectified output from the source shown previously in Figure 2.2) is connected via the ports labelled + and –, and the three phase outputs are labelled as A, B and C. The elements within this block are also shown in Figure 2.4. The individual switches are IGBTs (with ideal switching behaviour) and the clamping diodes also have ideal switching behaviour and have a forward voltage drop of 1V.

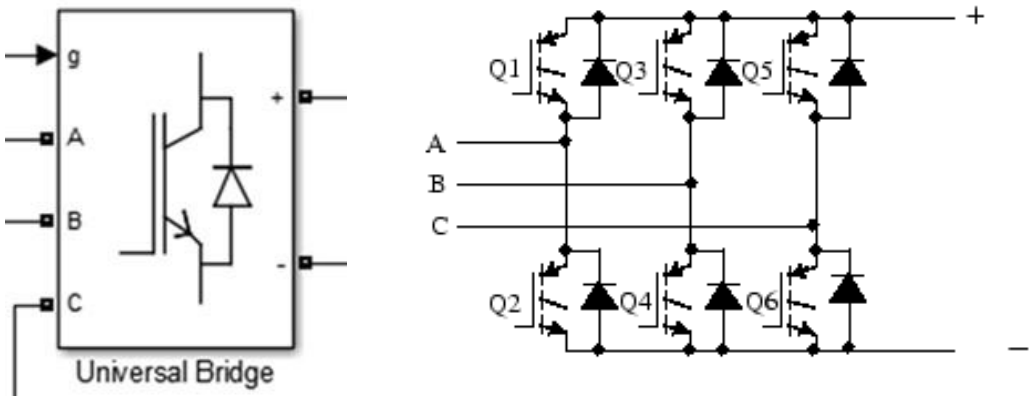

(a) Top level block (b) Detailed layout of block elements

Figure 2.4 SIMULINK model of converter power stage

2.2.3 Converter controller

As introduced in chapter 1, pulse density modulation (PDM) is based on regulating the converter output voltage by controlling the proportion of the converter input voltage pulses that are allowed to pass to the output [10-13]. The converter switching is synchronised to the zero voltage intervals of the input voltage in order to ensure soft switching of the main power devices. The core of the controller are the sub-systems which generate the synchronised gate signals to control the six switches in the three-phase power stage of the converter.

The SIMULINK implementation of the sub-system which generates the gate drive signals for one phase leg is shown in Figure 2.5. The full model consists of three of these sub-systems, one for each phase. The input to this gate signal generator is a reference sine wave (with the reference sine waves for the other two phases being shifted by 120° and 240°). It is worth noting that a practical controller for a PDM system would also include features such as closed loop control of the output voltage and not simply an open-loop reference signal as used in this simplified representation of a controller. The output of sub-system is pair of complementary digital outputs which control the upper and lower power switches of the phase leg.

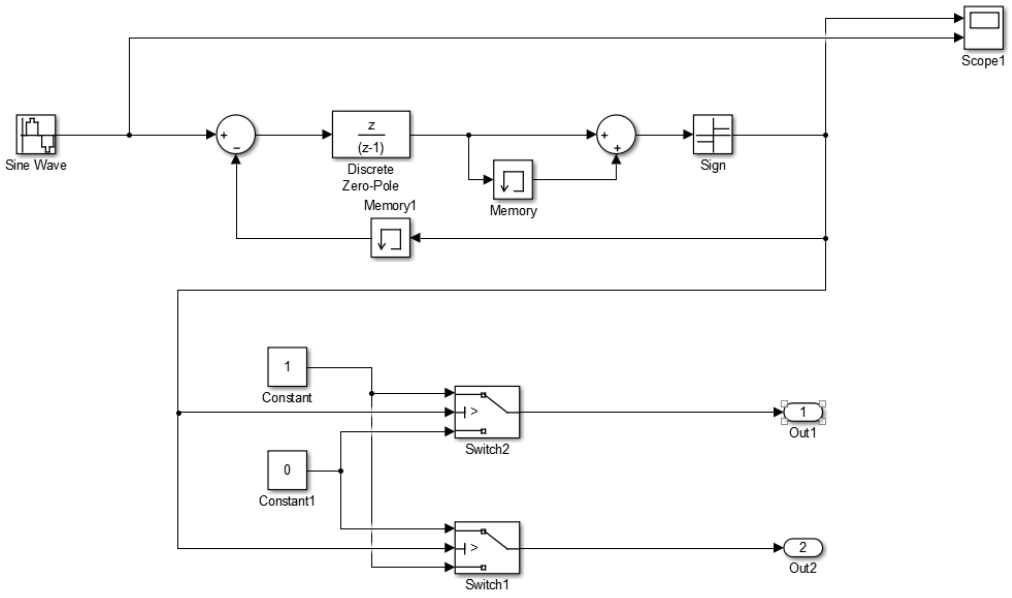

(a) MATLAB model

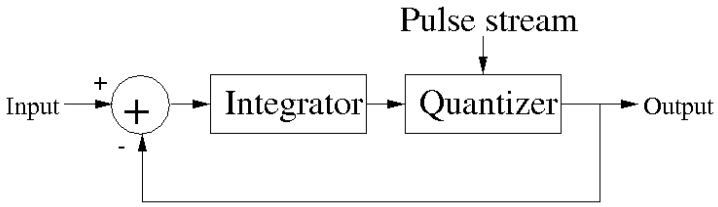

(b) Principle model

Figure 2.5 SIMULINK implementation of the PDC control subsystem

To generate the PDM switching pattern for a given phase-leg, the reference signal is modulated to generate a binary stream using delta-sigma modulation [14-17]. In this particular analogue to digital conversion process, a single bit quantizer produces a 1 or 0 bit stream. An output of 1 or 0 is generated based on amplitude of the input analogue signal [18]. As shown, the modulator incorporates a feedback loop to limit error between binary signal and analogue signal. In delta-sigma modulator, the Z-transform has been used for input and output signals in discrete time and discrete frequency domain, giving X(z) and Y(z) respectively. The delta-sigma modulation can be represented as:

$$Y(z) = E(z) + [X(z) - Y(z)z^{-1}]\left(\frac{1}{1 - z^{-1}}\right) \quad (2.\ 1)$$

where E(z) is the frequency-domain quantization error.

The memory element in the system model of Figure 2.5 introduces a delay (Z^{-1}) and the discrete zero pole element acts as a high pass filter. The two block outputs (labelled as Out1 and Out2 in Figure 2.5) are complementary signals which drive the upper and lower switches in a phase leg of the power stage. In this control system, the reciprocal of discrete simple time (t_s) represents maximum switching frequency, so that the discrete simple time (t_s) in the model needs to be set to reciprocal of frequency of DC rectified pulses ($1/f_{pulse}$). Figure 2.6 and Figure 2.7 shows a typical gate drive signals generated from modulation of a 400Hz sinusoidal reference signal with rectified DC pulses at 64 kHz and 32 kHz respectively.

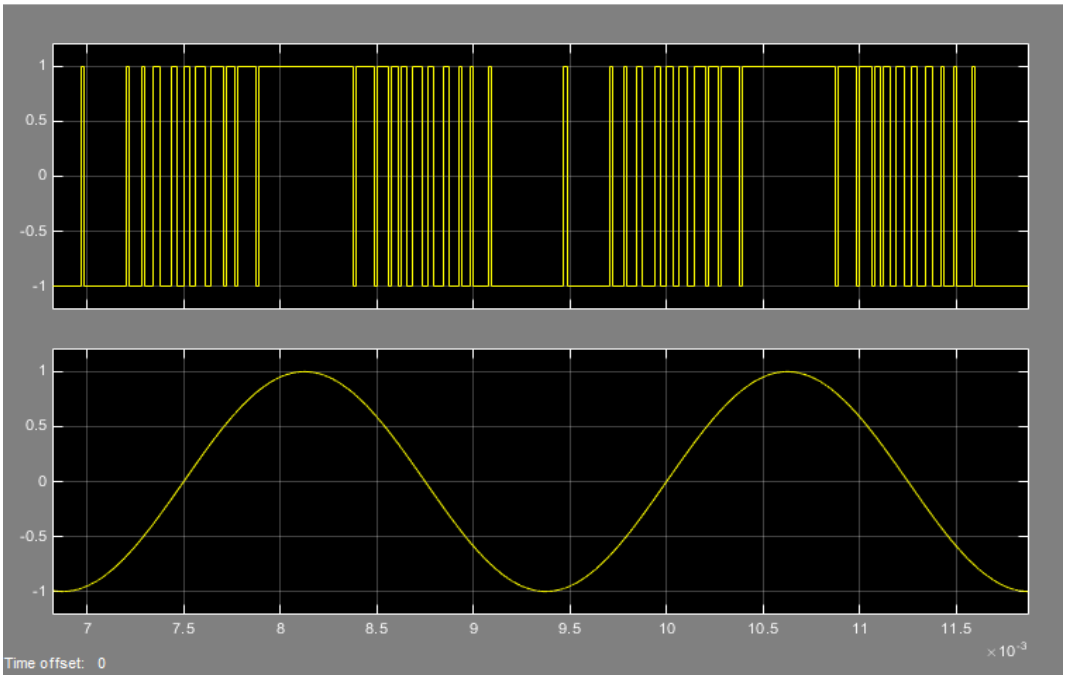

Figure 2.6 Switching signal (upper) and reference signal (lower) from subsystem. Conditions: 400Hz fundamental reference signal and rectified pulse rate of 64 kHz (corresponds to a generator AC output frequency of 32kHz)

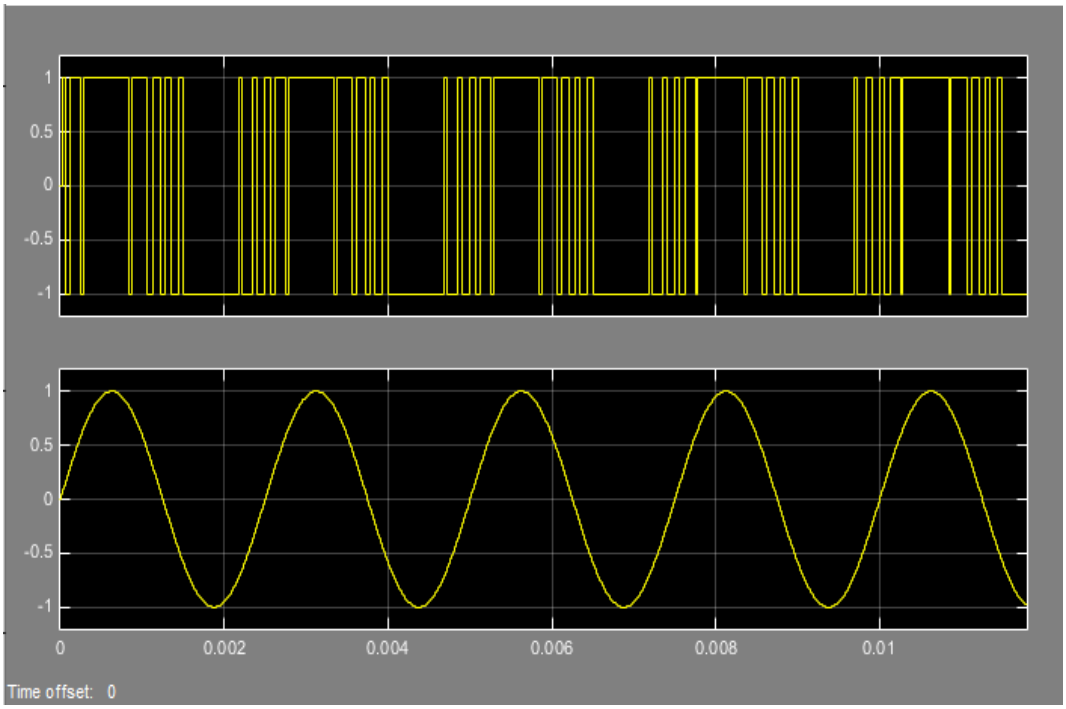

Figure 2.7 Switching signal (upper) and reference signal (lower) from subsystem. Conditions: 400Hz fundamental reference signal and rectified pulse rate of 32 kHz (corresponds to a generator AC output frequency of 16kHz)

2.2.4 Load and converter output filter

The three-phase load connected to the converter output is an entirely passive and simplified representation of the wider network of loads that the PDM converter would feed in an actual aerospace application and consists simply of a star connected arrangement of resistors with a floating star point. The output voltage filter in the first instance are simply standard filter blocks from the SIMULINK library which filter the measured phase voltages across the load resistors. These filters therefore provide a good indicator of the voltage waveforms that could be achieved with a particular power filter design but do not represent physical power filters directly. The SIMULINK implementation of these elements is shown in Figure 2.8, in which first and second order filters are used to filter the phase voltage of phase A. The two second order filters have different damping ratio (0.3 and 0.707) but the same corner frequency and provide a means of establishing the influence of the filter damping.

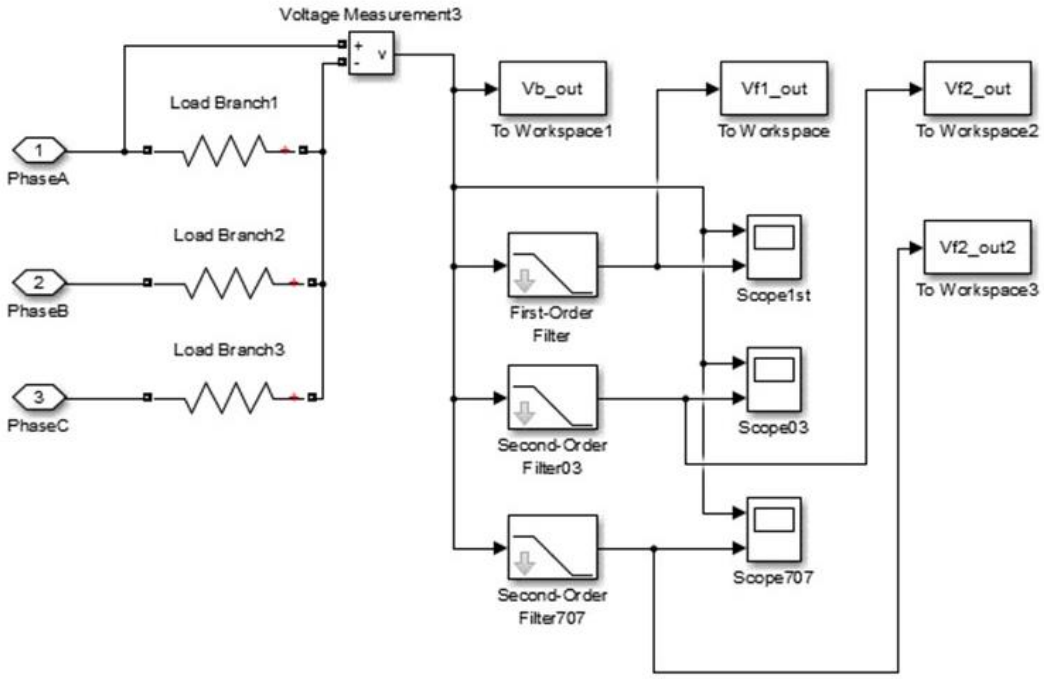

(a) MATLAB model

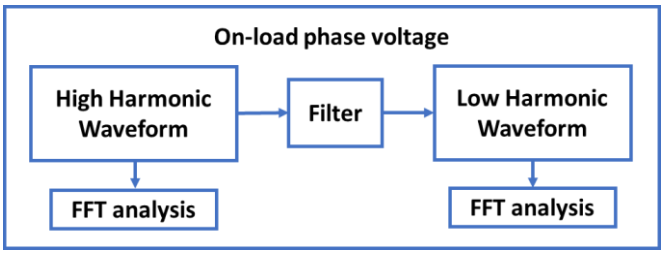

(b) Principle model

Figure 2.8 SIMULINK implementation of output voltage filters and converter load

2.3 Simulated converter performance

This section presents the simulated performance of a PDM converter for various combinations of output filter and switching frequency, with a particular focus on understanding the effect on power quality of the frequency of the DC rectified input to the converter and the frequency of the sinusoidal reference voltage. The filtered output voltage needs to meet the aerospace AC power standards described previously in chapter 1. Although there many factors in these standards, the particular focus in these simulations was voltage distortion of the load voltage. In the initial simulations, the load

resistances were set to 1MΩ to provide open-circuit voltage characteristics of the converter.

2.3.1 Unfiltered performance

Figure 2.9 shows the converter power stage output voltage waveform, i.e. prior to the actions of any filtering, and the normalised reference sinusoid which acts as the input to the PDM modulator, in this case for a 64kHZ rectifier output pulse train. Figure 2.10 shows a zoomed in plot of the same waveform in which the rectified DC link voltage is more evident in each pulse.

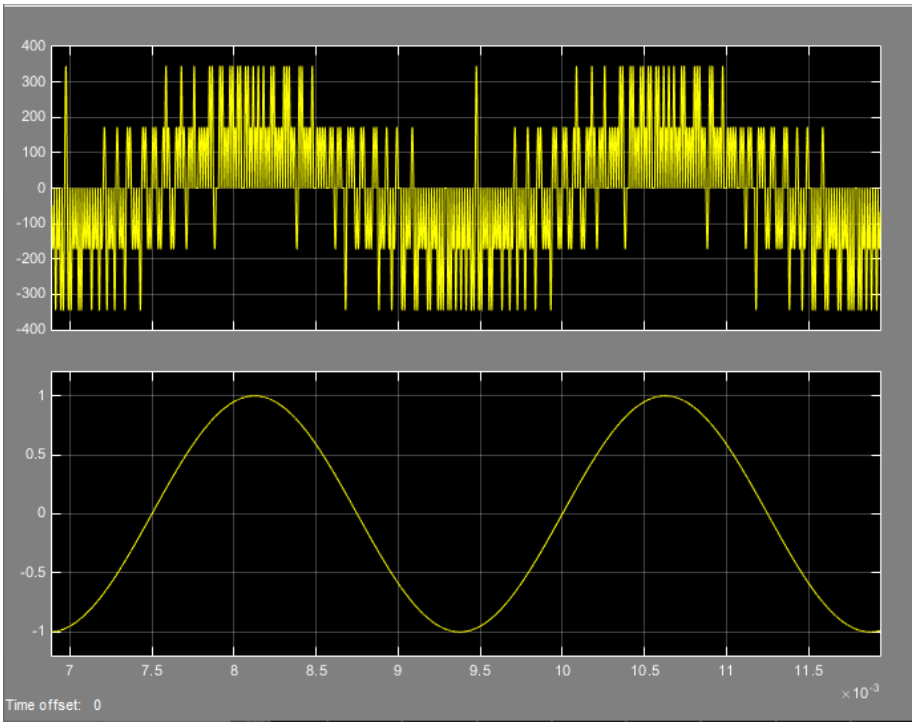

Figure 2.9 Waveform of un-filtered phase voltage (upper) and reference signal (lower) Conditions: 400Hz fundamental reference signal and rectified pulse rate of 64 kHz (corresponds to a generator AC output frequency of 32 kHz)

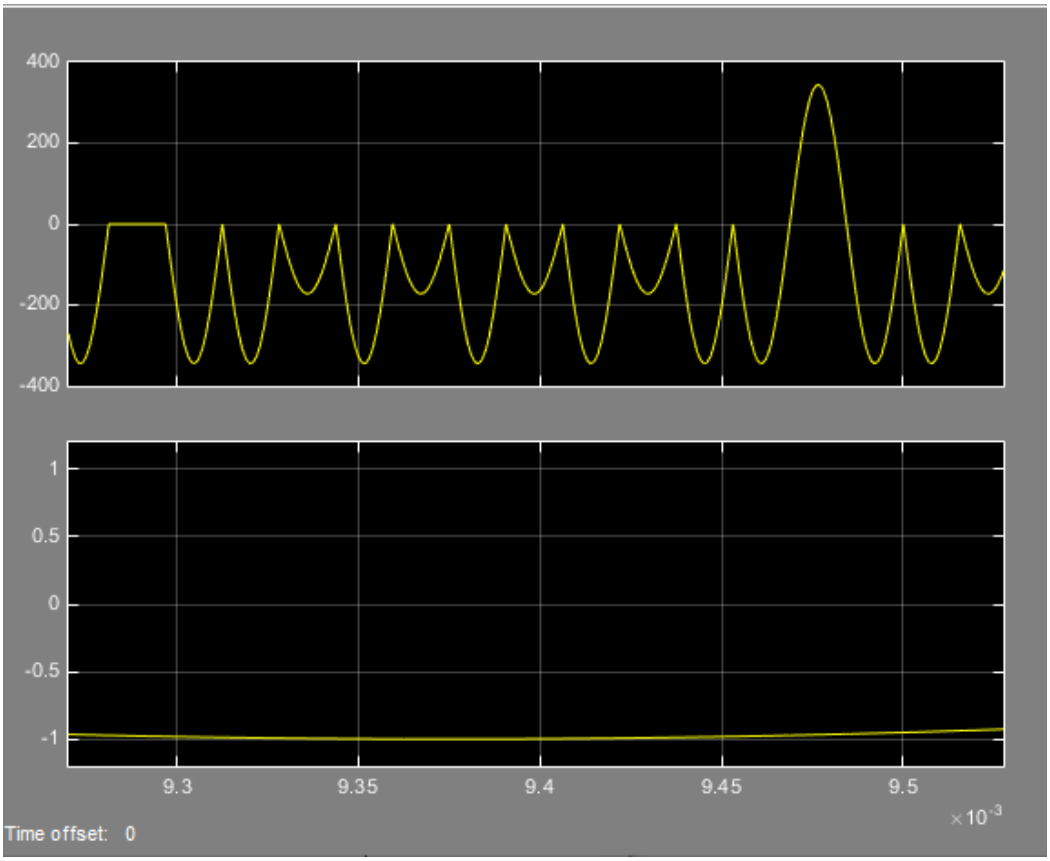

Figure. 2.10 Close up of waveforms of Figure 2.9 from 9.3 to 9.5ms

The Fast Fourier Transform of this unfiltered waveform is shown in Figure 2.11 which, as would be expected, contains many prominent harmonics. The overall total harmonic distortion (THD) is 108.05%, which significantly exceeds that permissible by the aerospace standards. A particular interesting feature is the very high harmonic at 64 kHz. Whereas normal switching converters have prominent harmonics around the switching frequency, the fact that their voltage pulses are square waves mean that the resulting spectrum is somewhat spread out across numerous harmonics of the switching frequency. However, in a PDM waveform, the sinusoidal shape of the individual pulses tends to concentrate the switching harmonics. A corresponding FFT for a reduced rectifier pulse train output of 32 kHz (equivalent to a generator AC output frequency of 16 kHz) is shown in Figure 2.12. In this reduced input frequency case, the THD is marginally reduced at 106.7% but still nearly two orders of magnitude outside acceptable limits. As would be expected there are prominent related harmonics at 32 kHz. A further halving of the generator AC frequency to 8kHz (16kHz pulse train from the rectifier) yields the FFT spectrum shown in Figure 2.13 with a THD of 106.8% while Figure 2.14 further having of the generator frequency to 8kHz (16kHz pulse train from the rectifier).

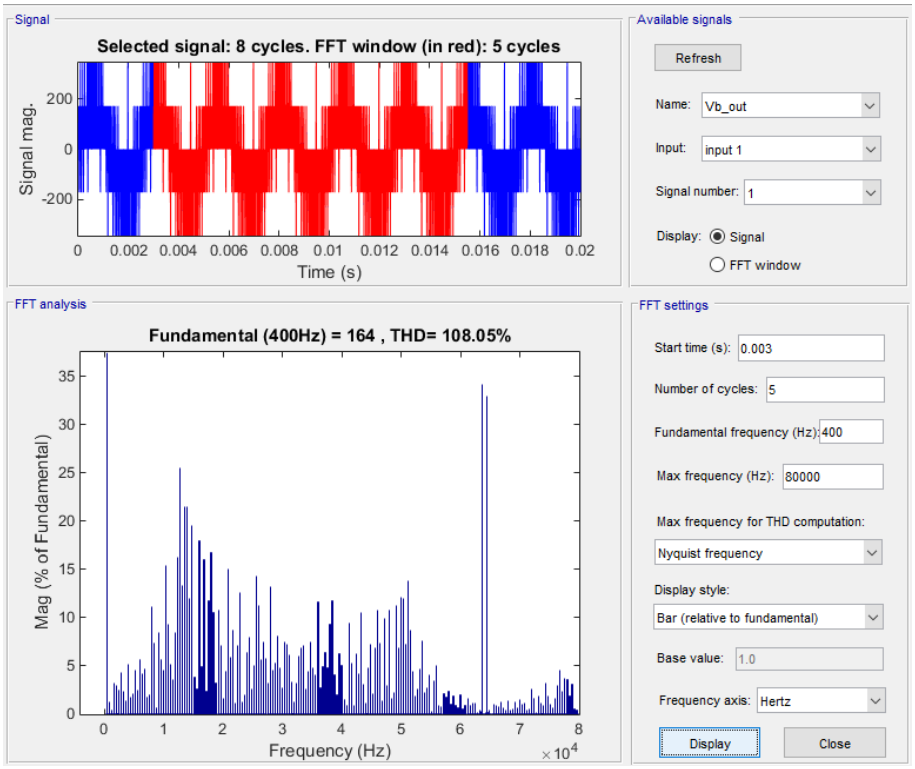

Figure 2.11 FFT analysis of waveform of phase voltage
Conditions: 400Hz fundamental reference signal and rectified pulse rate of 64 kHz
(corresponds to a generator AC output frequency of 32 kHz)

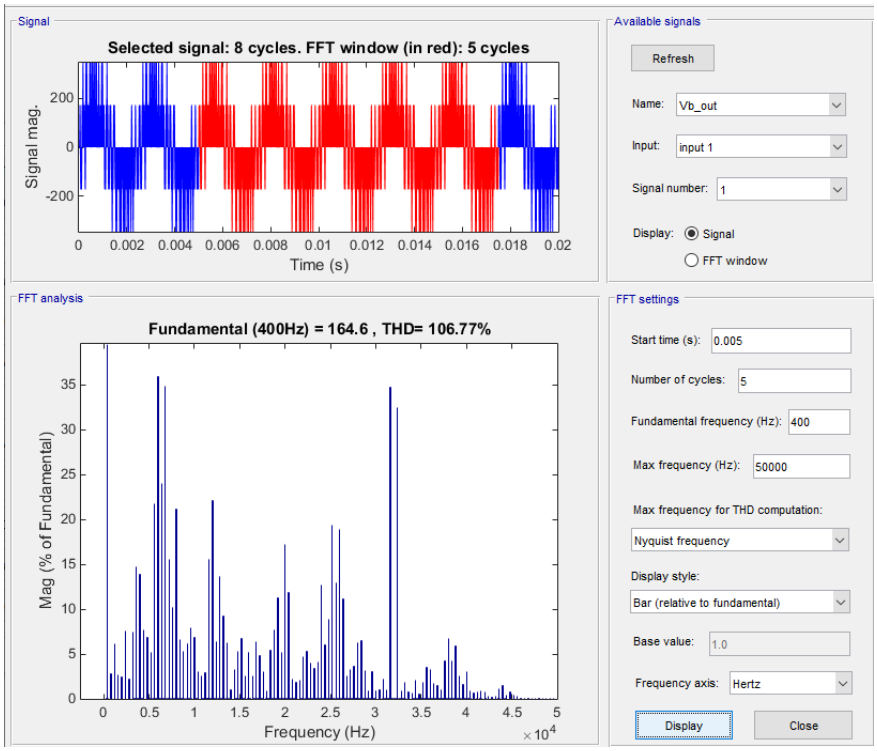

Figure 2.12 FFT analysis of waveform of phase voltage
Conditions: 400Hz fundamental reference signal and rectified pulse rate of 32 kHz
(corresponds to a generator AC output frequency of 16 kHz)

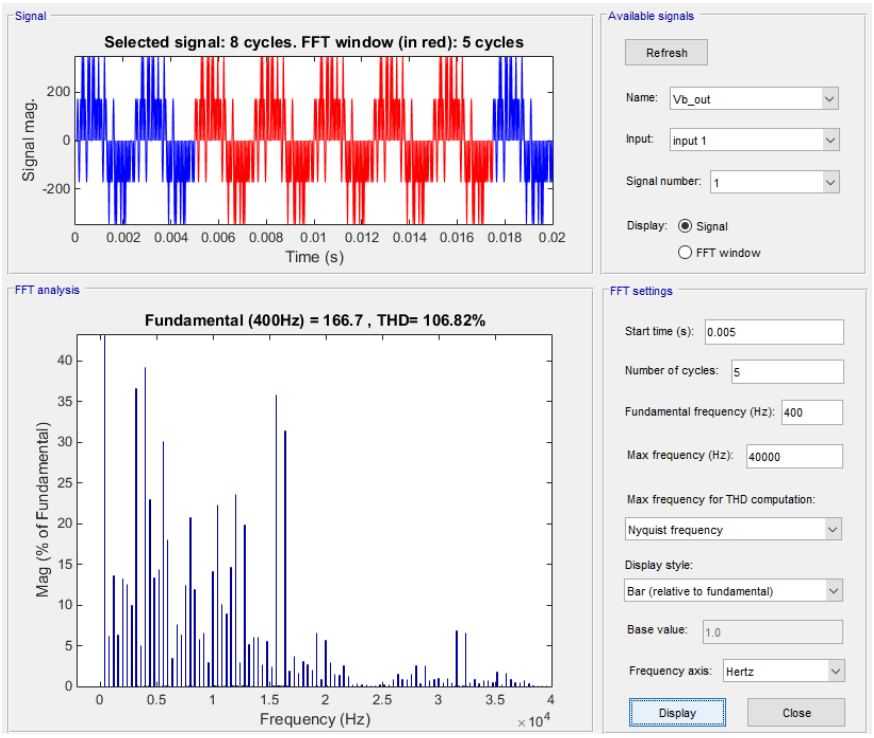

Figure 2.13 FFT analysis of waveform of phase voltage
Conditions: 400Hz fundamental reference signal and rectified pulse rate of 16 kHz
(corresponds to a generator AC output frequency of 8 kHz)

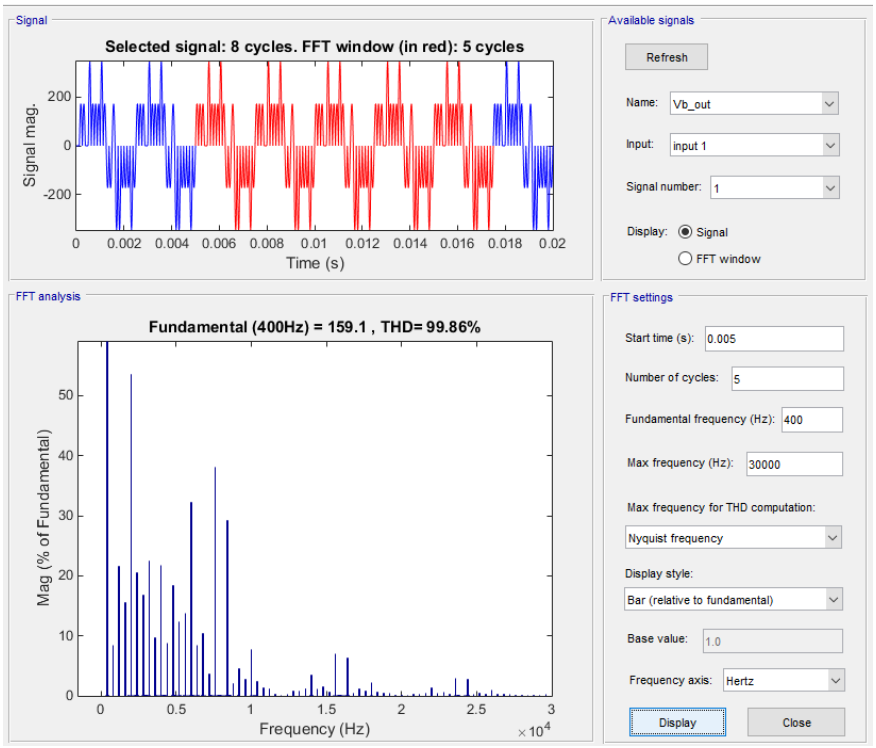

Figure 2.14 FFT analysis of waveform of phase voltage
Conditions: 400Hz fundamental reference signal and rectified pulse rate of 8 kHz
(corresponds to a generator AC output frequency of 4 kHz)

2.3.2 Performance with first-order filter

In order to improve the quality of the output voltage to even approach the requirements of aerospace standards is essential to add an output filter. The simplest form of passive filter which can be applied to the output of the PDM converter is a simple first-order low-pass filter. This would be realised in practice by a combination of a series resistance and parallel capacitor. The initial investigation of first-order filter performance was done with the built-in first-order filter block in SIMULINK Simscape. In this block, the filter is specified simply in terms of a time constant and hence cut-off frequency (also referred to as corner frequency or -3dB frequency) rather than a particular combination of resistance and capacitance. The selection of the cut-off frequency involves establishing a compromise between placing the cut-off frequency too low so that it starts to significantly attenuate the fundamental and too high so that it does not attenuate some key harmonics sufficiently. It is common practice in many power filters to place a significant separation between the fundamental and the switching frequencies. However, as shown by the FFTs shown previously in Figure 2.11, there are significant harmonics in the sub kHz range of unfiltered waveforms when producing a 400Hz fundamental output for many of the switching frequencies simulated in section 2.3.1.

Figure 2.15 shows a series of typical voltage waveforms produced with a first order filter, in this specific case for a 400Hz sinusoidal demand reference, a generator AC output frequency of 32kHz and a series of first order filter cut-off frequency over the range 400Hz to 1000Hz. As will be apparent, several of these filter designs results in significant residual harmonics in the voltage waveforms, with appreciable attenuation of the voltage with the first-order filter having a cut-off frequency of 400Hz. Since this cut-off frequency corresponds to the fundamental of the reference waveform, then the -3dB attenuation is to be expected.

400Hz cut-off frequency

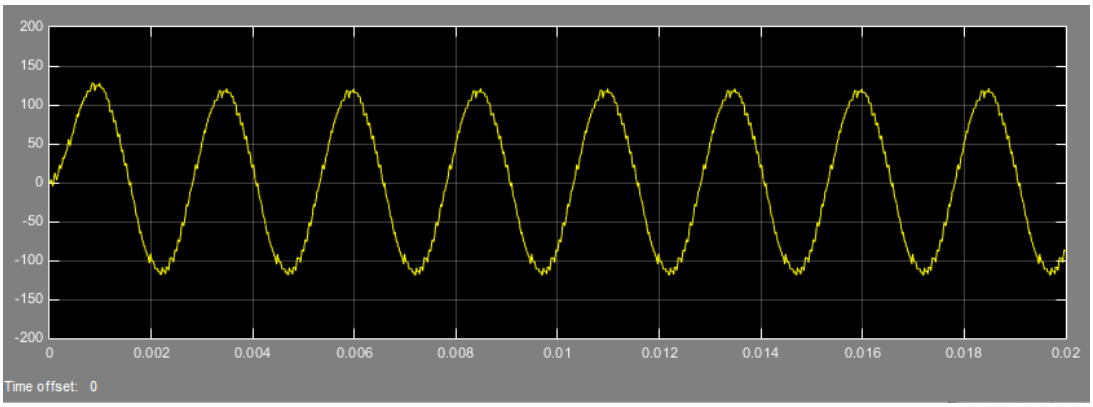

600Hz cut-off frequency

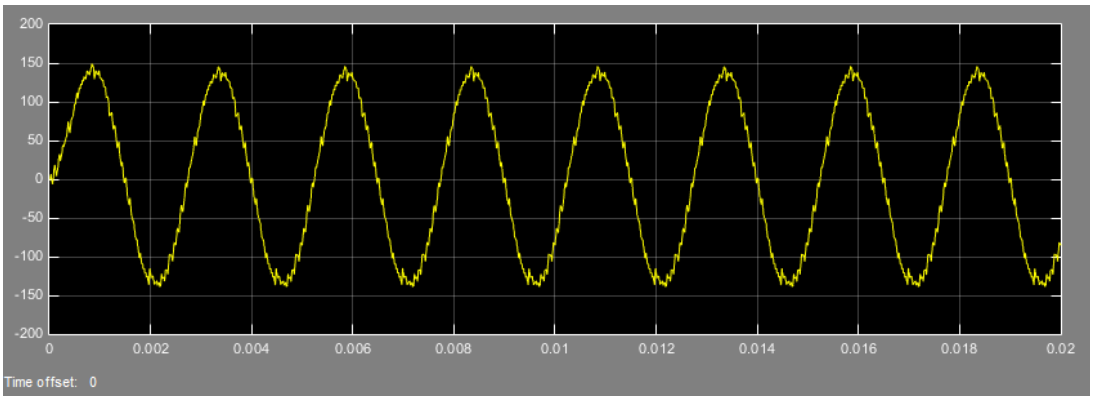

800Hz cut-off frequency

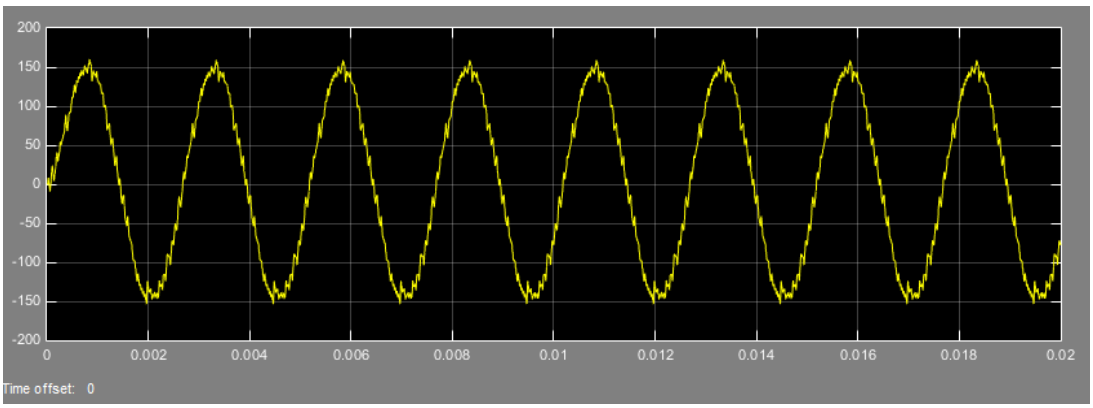

1000Hz cut-off frequency

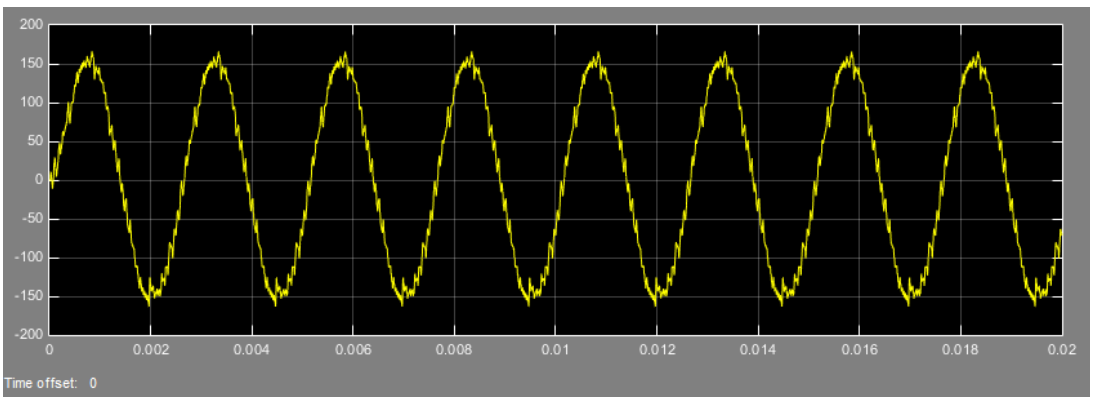

Figure 2.15 Simulated filtered output voltages for various first-order filter designs with a generator AC output frequency of 32 kHz

An FFT was performed on each output voltage waveform in Figure 2.15 to determine the magnitude of the fundamental and the total harmonic distortion (THD), with a sampling window spanning 5 cycles and taken after 5ms in order to eliminate the influence of any start-up transients. By way of examples, Figure 2.16 and Figure 2.17 show FFTs for a generator AC output frequency of 32kHz (i.e. a rectified pulse rate at the input of the converter of 64kHz) for the case of first-order filters with cut-off frequencies of 400Hz and 1000Hz.

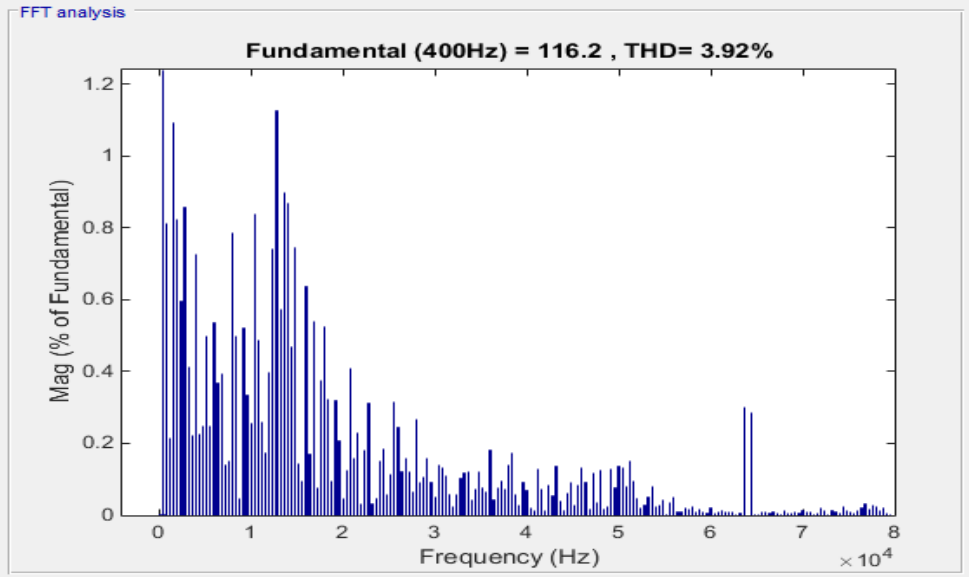

Figure 2.16 Predicted FFT with a first-order filter with a cut-off frequency of 400Hz

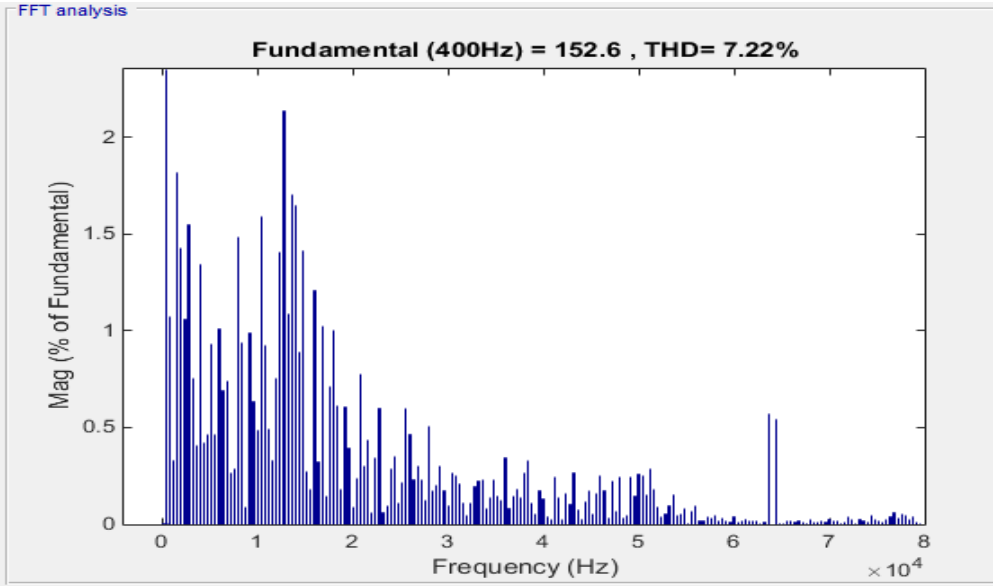

Figure 2.17 Predicted FFT with a first-order filter with a cut-off frequency of 1000Hz

As would be expected with the higher cut-off frequency filter, there are significantly more prominent harmonics in the spectrum of Figure 2.17 in the low kHz range than in Figure 2.16 (noting the different axis scales). A summary of the predicated performance for a range of generator AC output frequency range from 8 kHz to 32 kHz in combination with various first-order filter designs is shown in Table 2.1. As will be apparent, almost all combinations in Table 2.1 exceed the THD limit of 5% required to meet one element on the MIL-STD-704 standard (many by a great distance) with only two combinations (32 kHz input frequency with either a 400Hz or 600Hz cut-off frequency) meeting the 5% limit. However, both of these involve significant attenuation of the fundamental.

Table 2.1 Summary of predicted first-order filter performance

	Generator AC output frequency							
	4kHz		8kHz		16kHz		32kHz	
Filter cut-off frequency	Fundamental (V peak)	THD (%)	Fundamental (V peak)	THD (%)	Fundamental (V peak)	THD (%)	Fundamental (V peak)	THD (%)
400Hz	112.5	21.56	117.9	13.94	116.5	8.17	116.2	3.92
600Hz	132.4	26.58	138.7	17.31	137.1	10.26	136.8	4.95
800Hz	142.3	31.69	149.1	20.83	147.3	12.51	147	6.07
1kHz	147.8	36.52	154.8	24.32	152.9	14.80	152.6	7.22
1.2kHz	151	40.96	158.2	27.68	156.3	17.09	155.9	8.39
1.4kHz	153	44.97	160.3	30.89	158.4	19.34	158.1	9.55
No filter	159.1	99.86	166.7	106.82	164.5	106.76	163.6	108.03

2.2.3 Performance with second order filters

In the design of second order power filters it is common to select a low damping factor (order of 0.2-0.3) in order to maintain a reasonable filter efficiency. However if the filter natural frequency is close to the fundamental, then some resonant behaviour can occur with a net increase in the voltage occurring due to the action of the filter. On the other hand, a higher level of damping such as 0.7 results in a less pronounced resonant peak

around the natural frequency (i.e. higher Q factor) but at the expense of increased filter losses. Figure 2.17 shows a series of predicted output voltages for a series of second-order filter designs (all with a damping factor of 0.3 in this case) for a 400Hz fundamental reference waveform and an AC rectifier input frequency of 32kHz.

Adopting the same approach as the first-order filters, an extensive series of simulations and subsequent FFTs were performed on output voltage waveforms with second-order filters for different combinations of rectifier input frequencies, filter cut-off frequencies, and damping factors. Table 2.2 and Table 2.3 summarise the predicted performance of a range of filters for damping factors of 0.3 and 0.707 respectively. As will be apparent, there are many more combination of filter parameters and switching frequencies which satisfy the <5% THD threshold. However, with the damping factor of 0.3 there is some degree of resonant behaviour with the filters that have natural frequencies close to the 400Hz fundamental. This is evident in the significant increase in the magnitude of the fundamental from the ~160V of the unfiltered cases. As an example, Figure 2.19 shows the voltage waveforms for a generator output frequency of 32kHz and a second-order filter with a natural frequency of 600Hz and a damping ratio of 0.707. As will be apparent, there is significant evidence of resonance in this case, which ultimately could lead to stability issues. Finally, it is worth noting that the THD for a given combination of rectifier input frequency and output filter natural frequency is lower with the higher damping factor.

400Hz cut-off frequency

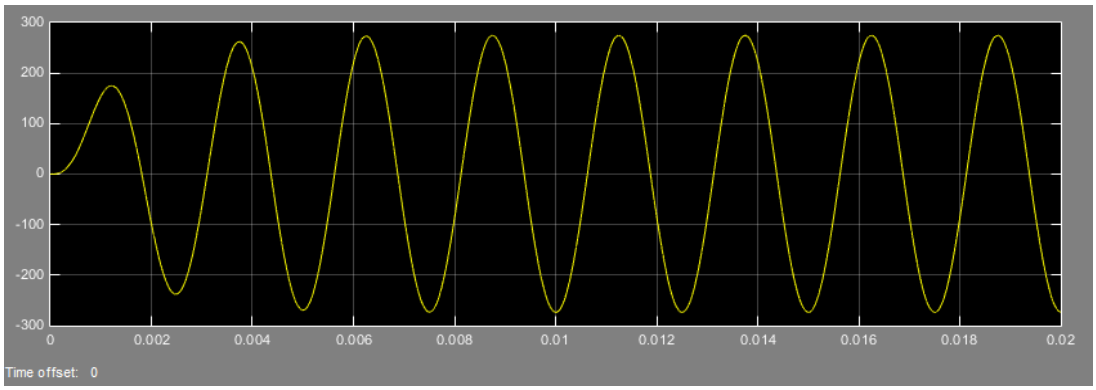

600Hz cut-off frequency

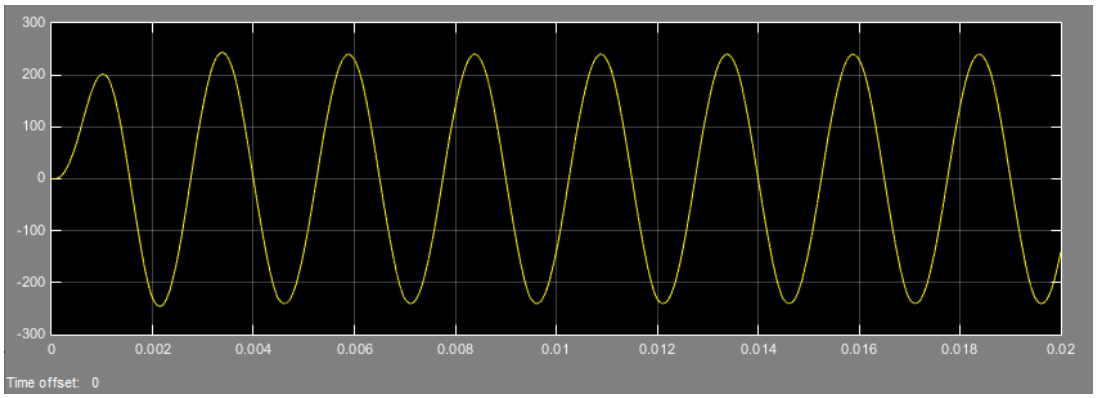

800Hz cut-off frequency

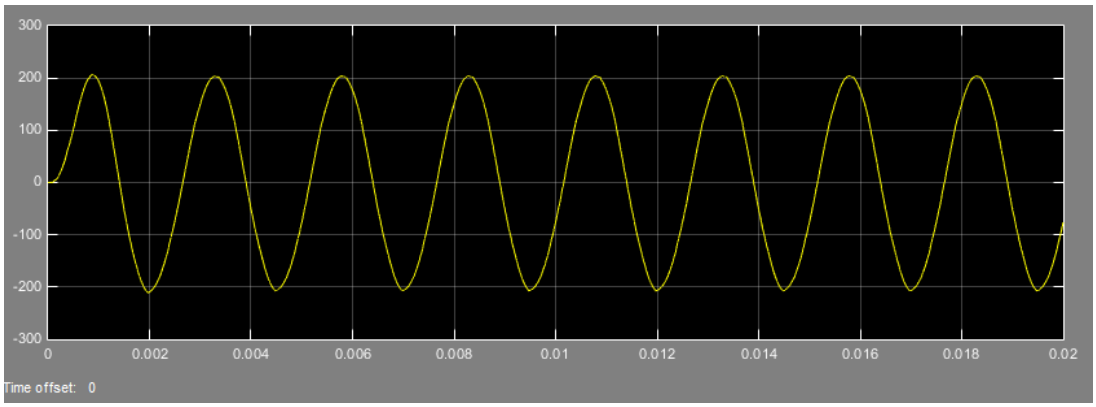

1000Hz cut-off frequency

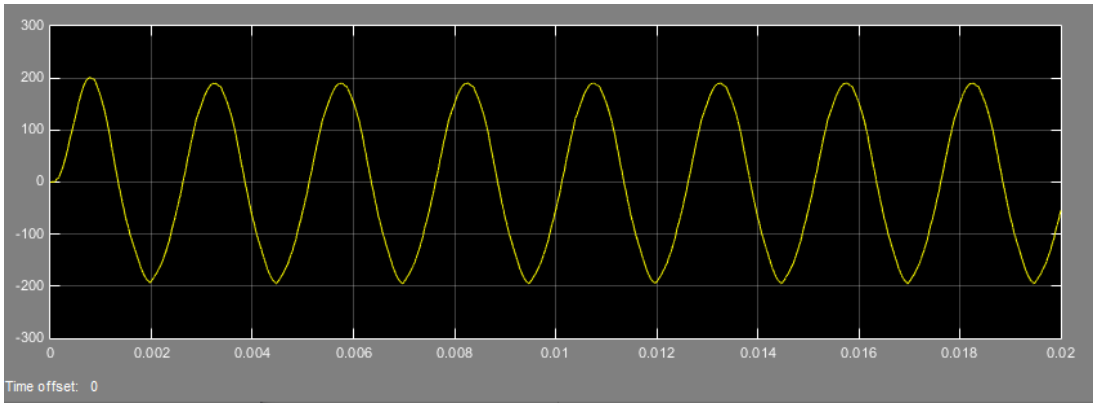

Figure 2.18 Simulated filtered output voltages for various second-order filter designs with an AC rectifier input frequency of 32kHz – all filters with a damping ratio of 0.3

Table 2.2 Summary of predicted second-order filter performance (damping factor of 0.3)

	Generator AC output frequency							
	4kHz		8kHz		16kHz		32kHz	
Filter natural frequency	Fundamental (V peak)	THD (%)	Fundamental (V peak)	THD (%)	Fundamental (V peak)	THD (%)	Fundamental (V peak)	THD (%)
400Hz	264.7	2.73	277.4	1.73	274.1	0.81	273.5	0.46
600Hz	232.4	8.06	243.5	5.11	240.6	2.29	240.1	0.92
800Hz	197	18.52	206.4	11.68	203.9	5.24	203.5	2.04
1kHz	182.2	30.65	190.8	18.13	188.5	8.09	188.2	2.75
1.2kHz	174.7	44.67	183	24.91	180.8	11.03	180.4	3.75
1.4kHz	170.3	56.71	178.5	28.68	176.3	12.49	176	5.25
No filter	159.1	99.86	166.7	106.82	164.5	106.76	163.6	108.03

Table 2.3 Summary of predicted second-order filter performance

(damping factor of 0.707)

	Generator AC output frequency							
	4kHz		8kHz		16kHz		32kHz	
Filter natural frequency	Fundamental (V peak)	THD (%)	Fundamental (V peak)	THD (%)	Fundamental (V peak)	THD (%)	Fundamental (V peak)	THD (%)
400Hz	112.5	5.67	117.9	3.38	116.5	1.52	116.3	0.60
600Hz	145.4	9.52	152.4	5.60	150.5	2.51	150.2	0.98
800Hz	154.4	14.91	161.8	8.53	159.8	3.82	159.5	1.48
1kHz	157.1	20.99	164.6	11.63	162.7	5.20	162.3	2.04
1.2kHz	158.2	27.26	165.7	14.70	163.7	6.57	163.4	2.64
1.4kHz	158.6	33.42	166.2	17.68	164.2	7.93	163.8	3.27
No filter	159.1	99.86	166.7	106.82	164.5	106.76	163.6	108.03

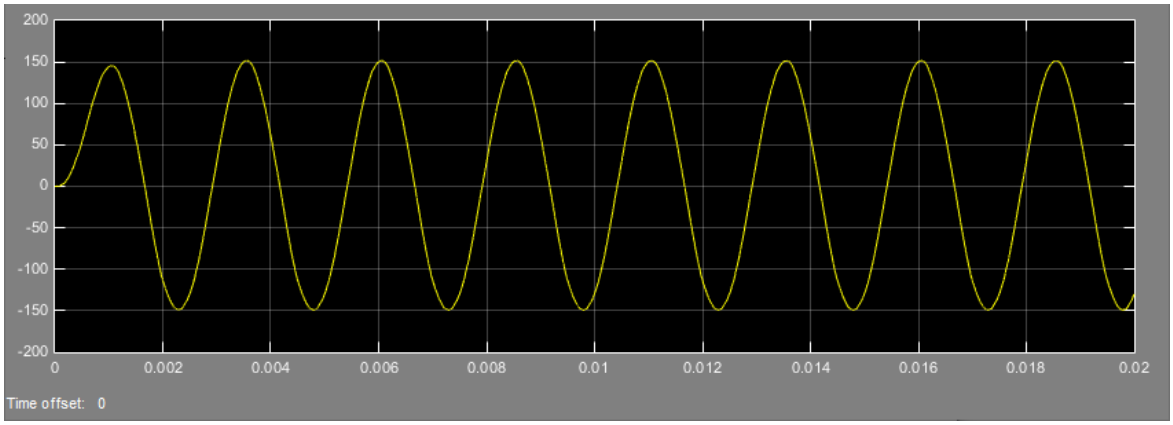

Figure 2.19 Simulated voltage waveform for a generator output frequency of 32kHz and a second-order filter with a natural frequency of 600Hz and a damping ratio of 0.707

As noted at the beginning of this chapter, the main aim of the converter modelling described in this chapter was to provide a basis for selecting a switching frequency of PDM converters then an output frequency for the generator design rather than the development of converter control algorithms or extensive characterisation at different power levels and with different loads. The predicted performance of the various filters demonstrate that second-order filters are likely to be preferred to first-order filters in this case. This is consistent with practice in many commercial drives where second or even higher order filters are used. To aid the selection of a generator frequency, Table 2.4 provides a summary of filter performance from which it can be seen that in order to both meet a 5% THD limit on voltage distortion (on no-load) and maximise the gap between the filter natural frequency and the 400Hz fundamental, a generator AC output frequency of 32kHz is preferable and indeed is the minimum frequency of those considered that can meet these two selection criteria.

Table 2.4 Summary of converter and filter performance

Generator AC output frequency	Highest natural frequency* for second order filter with a THD <5%		Magnitude of 400Hz fundamental for selected filter	
	0.3 damping	0.707 damping	0.3 damping	0.707 damping
4kHz	400	N/A	264.7	N/A
8kHz	400	400	277.4	117.9
16kHz	600	800	240.6	159.8
32kHz	1200	>1400	180.4	163.8

* 200Hz increments

2.4 Conclusions

This chapter has developed and employed a simplified model of a PDM converter in order to provide a quantitative basis for selecting a generator output frequency as a pre-cursor to its electromagnetic design in subsequent chapters. The analysis presented has established a well-founded basis for setting an initial generator output frequency of 32kHz. This is well beyond the electrical frequencies adopted in conventional machines and requires a significant departure from normal design practice and guidelines as discussed later in chapters 3 and 4.

2.5 References

[1] T. W. Ching and K. U. Chan, "Review of soft-switching techniques for high-frequency switched-mode power converters," 2008 IEEE Vehicle Power and Propulsion Conference, Harbin, 2008, pp. 1-6.

[2] G. Hua and F. C. Lee, "Soft-switching techniques in PWM converters," in IEEE Transactions on Industrial Electronics, vol. 42, no. 6, pp. 595-603, Dec. 1995.

[3] A. Mertens, "Design of a 20 kva resonant dc link igbt inverter on the base of experimental device evaluation," in European Conference on Power Electronics and Applications Conf. Proc., pp. 4.172-4.177, 1991.

[4] J. Dudrik, and J. Oetter, "High-Frequency Soft-Switching DC-DC con-verters for Voltage and Current DC Power Sources," Acta Polytechnica Hungarica, Vol. 4, No. 2, 2007.

[5] Krogemann, Markus, "The parallel resonant DC link inverter: a soft-switching inverter topology with PWM capability." PhD thesis, University of Nottingham. 1997

[6] Xiao Yao, "The method for designing the third order filter," 8th International Conference on Harmonics and Quality of Power. Proceedings (Cat. No.98EX227), Athens, Greece, 1998, pp. 139-142 vol.1.

[7] R. W. Erickson, "Optimal single resistors damping of input filters," APEC '99. Fourteenth Annual Applied Power Electronics Conference and Exposition. 1999 Conference Proceedings (Cat. No.99CH36285), Dallas, TX, USA, 1999, pp. 1073-1079 vol.2.

[8] D. M. Divan, "The resonant de-link converter- a new concept in power conversion" IEEE Trans on Industrial Applications, Volume 25, Issue 2, March-April 1989 Page(s):317-325

[9] D. M. Divan and G. Skibinski, “Zero switching loss inverters for high power applications,” in Proc. IEEE IAS Conf. Rec., 1987, pp. 627–634.

[10] J. Essadaoui et al., "Power Inverter Control for Induction Heating by Pulse Density Modulation with Improved Power Factor", IEEE Canadian Conference on Electrical and Computer Engineering-Toward a Caring and Human Technology, May 2003.

[11] D. Pimentel, M.B. Slima, and A. Cheriti. Power Control for Pulse-Density Modulation Resonant Converters. in Industrial Electronics, 2006 IEEE International Symposium on. 2006.

[12] M. Nakaok, H.Yonemori, and K. Yurugi, "Zero-Voltage soft-switched PDM three phase AC-DC active power converter operating at unity power factor and sinewave line current" Proc. of PESC'93, 24th Annual IEEE 20-24 June 1993 pp. 787-794

[13] A. Sandali, A. Chériti, P. Sicard, "Comparison of the Various PDM Control Modes", IEEE International Conference on Industrial Technology, 2004.

[14] O. Feely, "Theory of lowpass and bandpass sigma-delta modulation," IEE Colloquium on Oversampling and Sigma-Delta Strategies for DSP, London, UK, 1995, pp. 7/1-7/8.

[15] S. Dai, A. von Jouanne, A. Wallace and G. C. Temes, "Delta-sigma modulation applications in neutral-point clamped inverters," 38th IAS Annual Meeting on Conference Record of the Industry Applications Conference, 2003., Salt Lake City, UT, USA, 2003, pp. 678-683 vol.1.

[16] A. Mertens, "Performance analysis of three-phase inverters controlled by synchronous delta-modulation systems," in IEEE Transactions on Industry Applications, vol. 30, no. 4, pp. 1016-1027, July-Aug. 1994.

[17] J. Nieznanski, "Performance characterization of vector sigma-delta modulation," IECON '98. Proceedings of the 24th Annual Conference of the IEEE Industrial Electronics Society (Cat. No.98CH36200), Aachen, Germany, 1998, pp. 531-536 vol.1.

[18] K.C. Pohlmann, Principles of Digital Audio, 3rd ed., McGraw-Hill, 1995

Chapter 3 Alternative concept studies on different topologies

3.1 Introduction

The conventional low frequency generators connected in generation system for the PDM control shown previously in Figure 1.3 (b) are usually perfered 3 phase surface mounted permanent magnet machines (SPM) with fractional slot concentrated winding (FSCW). This kind of machine earned lots of attention recently because of some significant benefits such as high power density, high efficiency, low loss (both in copper and iron) and fault-tolerance [1-9]. However, with the same topology it is impossble to generate high frequency suitable for the input of PDM converter, because in most time, the pole pair number is way too low in conventional machine. For the most machine topology, when the pole pair numbers increased to a high value like several tens or a hundred, the power capacity of machine will declined dramaticilly, for the reason of flux leakage and high self impedance. In this chapter, numbers of topologies have been studied to compare their potential advantages especially in power output. All high frequency designs attempt to have competitive power capacity and power density, even compared with conventional low frequency generator in similar usage situation.

3.2 Baseline machine design

The starting point for the concepts studies was an existing design of a conventional SPM derived from [10]. A cross-section through this machine is shown in Figure 3.1 while Table 3.1 summarises the key dimensions and parameters. This reference machine was designed to be connected to a 270V DC bus through a three-phase uncontrolled diode bridge rectifier and a DC/DC converter. This machine is an oil-cooled permanent magnet synchronous generator with 15 stator slots and 10 rotor poles, equipped with surface mounted loaf shaped rotor magnets. The machine direct flood oil of the stator allows a high electric loading to be used (equivalent to a conductor current density of 12A/mm^2 rms). The stator is manufactured with high performance 49% Cobalt iron in both stator and rotor core. As noted in chapter 1, although not capable of producing the high frequency output required in the application considered in this thesis, it provides a useful benchmark in terms of power density.

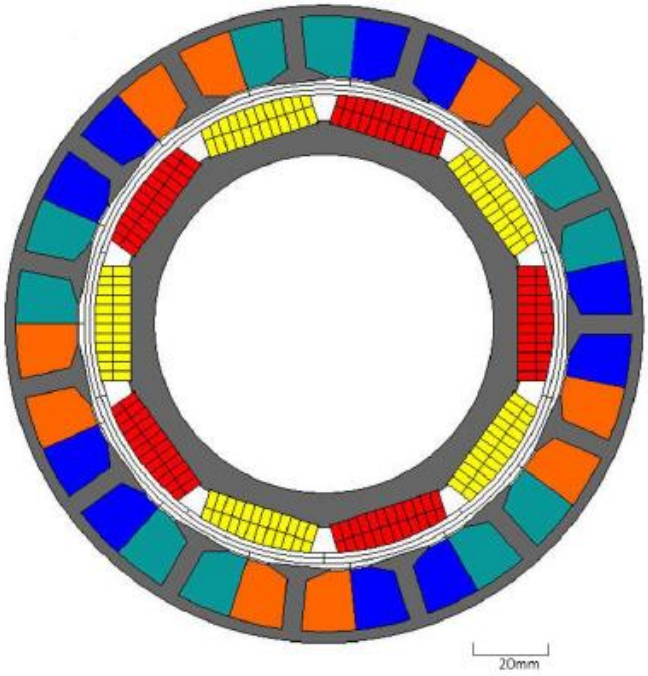

Figure 3.1 Cross –section of 15-10 baseline SPM machine (Source: [10])

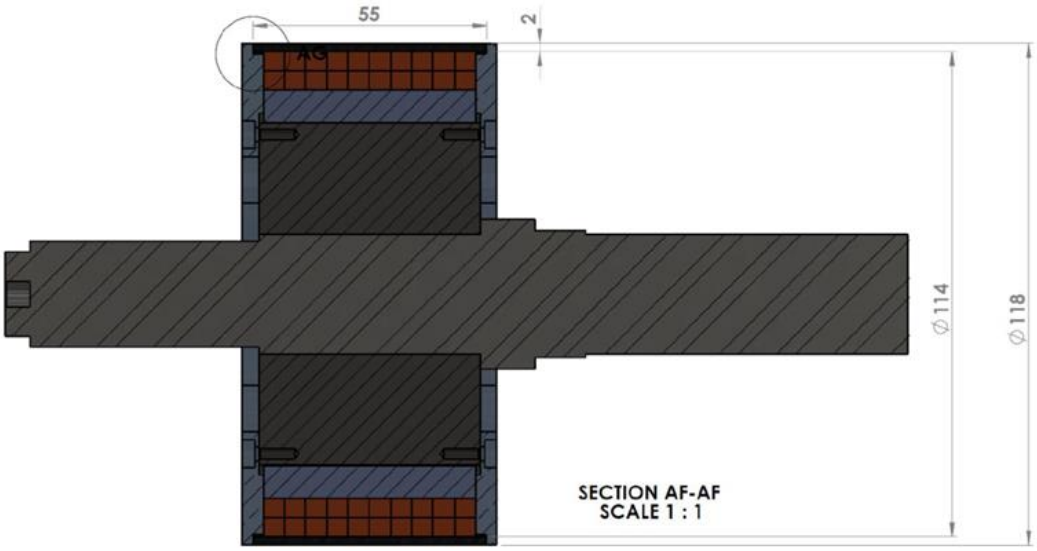

Figure 3.2 Side-view of rotor for the 15-10 baseline design

Table 3.1 Design parameters of the MS's design [10]

Stator Dimensions	**Value (mm)**
Number of stator slots	15
Stator outer diameter	160
Stator bore diameter	122
Effective magnetic air-gap	4.0
Stator back iron thickness	2.8
Stator bore coolant retention sleeve thickness	1.0
Tooth body width	4.9
Tooth tip height	0.5
½ Slot area (mm_2)	174
Stator slot packing factor	0.5
Turns per coil	5
Series connected coils per phase	5
Machine active length	50
Resistance per coil (mΩ)	1.38
Inductance per coil (Including End-winding)	6.97μH
Rotor Dimensions	**Value**
Number of poles	10
Magnet height (from centre)	9
Containment thickness	2
Rotor outer diameter (include containment)	118
Rotor inner diameter	85
Active weight (kg)	**4.77**

The rated power capability of this machine was 50kW at 17,000rpm achieved with an RMS current density of 12A/mm^2. The use of flooded oil cooling of the stator allows a compact stator winding to be produced. As a consequence of the high stator current density, this machine has a relatively high split ratio for an SPM of 0.7125 (based on the rotor magnet outer diameter to stator outer diameter).

The machine design of Figure 3.1 has an active mass of 4.77kg (i.e. excludes casing, shaft and rotor hub) and hence an active power density of 10.57kW/kg. The various contributions to the overall mass are summarised in Table 3.2.

Table 3.2 Mass breakdown of baseline machine design [10]

Component	Density (kg/m^3)	Mass (kg)
Stator lam	8120	1.18
Rotor lam	8120	0.75
Magnets	8400	1.00
Windings	8940	1.84
Total		**4.77**

3.3 Modified baseline design for assessment of alternative topologies

Whereas the baseline machine of Figure 3.1 provides a useful starting point in terms of overall dimensions and power density, the split ratio is higher than the typical optimal split ratios identified for various flux switching / reversal machines and indeed many SPMs. To provide a more direct comparison for subsequent investigations at a topology level the starting design in Figure 3.2 was modified to achieve a split ratio of 0.6, by increasing the stator outer diameter to 196.6mm and leaving the rotor diameter at 118mm. This modified design will become the principal baseline in this chapter where alternative topologies are considered. However, the original design (stator outer diameter of 160mm) from [10] will feature as the baseline in Chapter 4 for comparison with the preferred topology in terms of power density and performance.

A cross-section though the baseline design for this chapter (based on a split ratio of 0.6 and stator outer diameter of 196.6mm) is shown in Figure 3.3, while the leading parameters are summarized in Table 3.3. The pole and slot numbers were kept at 10-15 and the rotor diameter maintained at 118mm. The increase in outer diameter required to realise the new split ratio of 0.6 was achieved by simply increasing the slot depth, keeping the back iron thickness fixed at 2.8mm. This results in an increase of the active mass from 4.77kg for the original baseline machine of Figure 3.1 to 8.33kg for this modified baseline.

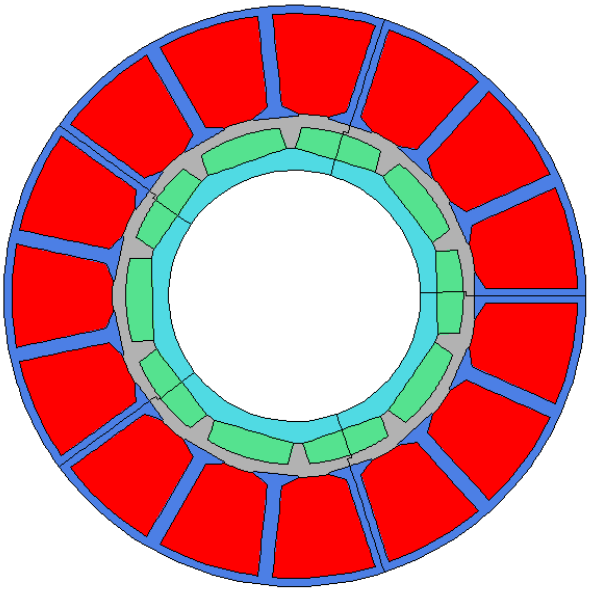

Figure 3.3 Cross-section through modified baseline machine

Table 3.3 Design parameters of the modified baseline machine

Stator Dimensions	**Value (mm)**
Number of stator slots	15
Stator outer diameter	196.6
Stator bore diameter	122
Effective magnetic air-gap	4.0
Stator back iron thickness	2.8
Tooth body width	4.9
Tooth tip height	0.5
½ Slot area (mm^2)	468
Turns per coil	5
Series connected coils per phase	5
Machine active length	50
Rotor Dimensions	**Value**
Number of poles	10
Magnet height (from centre)	9
Rotor outer diameter	118
Rotor inner diameter	85

3.3.1 Performance predictions for original and modified baseline designs

The performance of the modified 196.6mm baseline designs was predicted using an electric-circuit coupled finite element simulation in OPERA and compared with that of the 160mm original baseline. Three cases were considered:

- The original baseline machine with rotor outside diameter 160mm from [10] at 17,000rpm (its nominal rated speed). This provided a means of comparing the calculated average load voltage versus current characteristics with those published in [10].
- The original baseline machine with rotor outside diameter 160mm from [10] at a speed of 20,000rpm which is the rated speed for the proposed generation system.
- The modified baseline machine with rotor outside diameter 196.6mm at a speed of 20,000rpm which is the rated speed for the proposed generation system.

Figure 3.3 shows electric-circuit coupled finite element predicted average load voltage versus average load current characteristics for the three cases listed above along with a 50kW power contour. Also shown in Figure 3.3 is the corresponding curve for the original bassline taken directly from [10] which provides some correlation between the models used (FLUX2D in [10]). The modified baseline with the 196.6mm diameter stator has a reduced power envelope compared to the original 160mm baseline design at the

same speed since it has the same rotor but deeper stator slots. Although these deeper slots would allow a lower current density to be achieved, they increase the reactance of the machine and do not increase the flux-linkage due to the permanent magnets and hence the power capability is reduced.

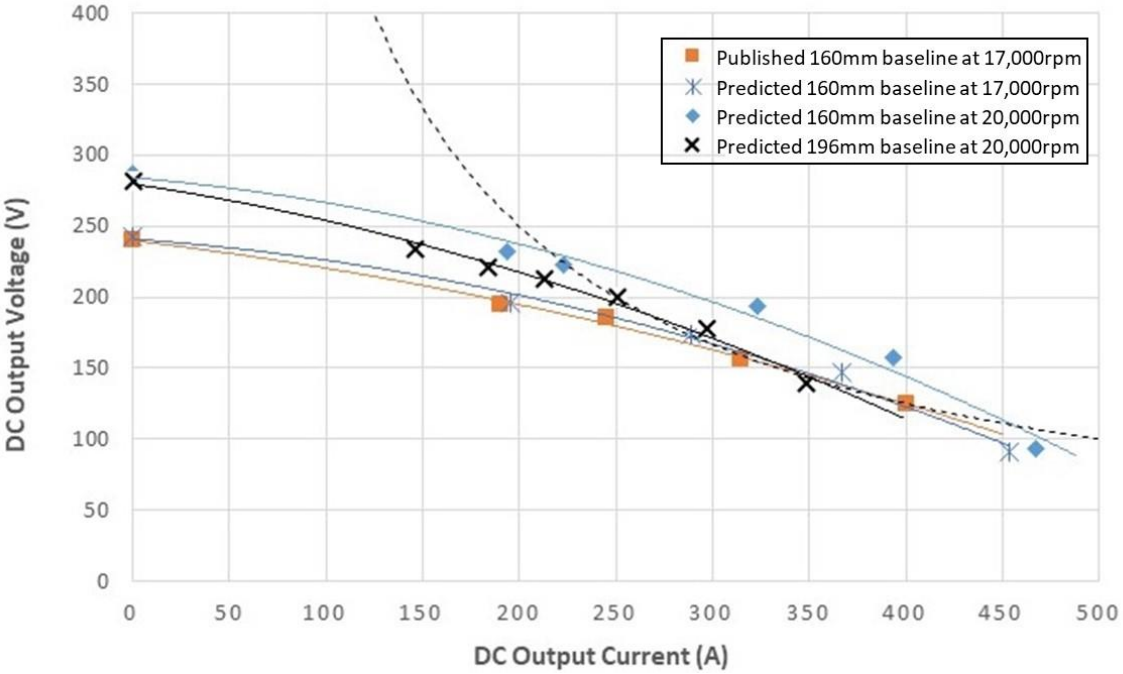

Figure 3.4 Simulated Current-Voltage characteristics of reference machine and modified baseline machine

3.4 Methodology for evaluation of different topologies

In order to provide some consistency in the comparison of competing topologies, the following specifications and constraints were applied:

- All machine topologies analysed in this chapter have the same overall stator outer diameter of 196.6mm and axial length of 50mm as the modified baseline design.
- The material in the stator and rotor core is assumed to be VacoFlux 50 Cobalt Iron manufactured by Vacuumschmelze. The magnetisation curve for this material is shown in Figure 3.5 below. Also shown in Figure 3.5 are the corresponding magnetisation characteristics for competing soft magnetic materials which are often used in high performance electrical machines. As will be apparent, the main benefit of adopting

Vacoflux 50 is its high flux saturation level of 2.35T [11]. It also exhibits low core loss compared to many other laminated soft magnetic materials.

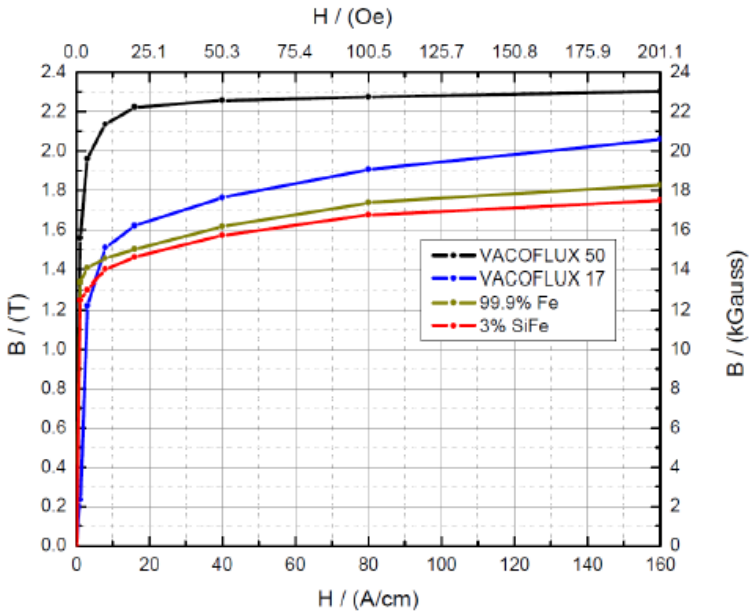

Figure 3.5 Comparison of the BH curves of soft magnetic material (Source: [11])

- The rotor permanent magnet material was assumed to be Vacomax 225 Sm_2Co_{17} magnets, also produced by Vacuumschmelze [12]. The demagnetisation characteristic of this material at a series of temperatures is shown in Figure 3.6. Because of its linear behaviour of demagnetisation in the working area (fourth quadrant) in wide temperature range, this kind of magnet is suitable for high temperature, heavy load applications. For the purposes of this design study, a magnet operating temperature of 150◦C was assumed, resulting in a remnant flux density for use in the electromagnetic modelling of 1.075T.

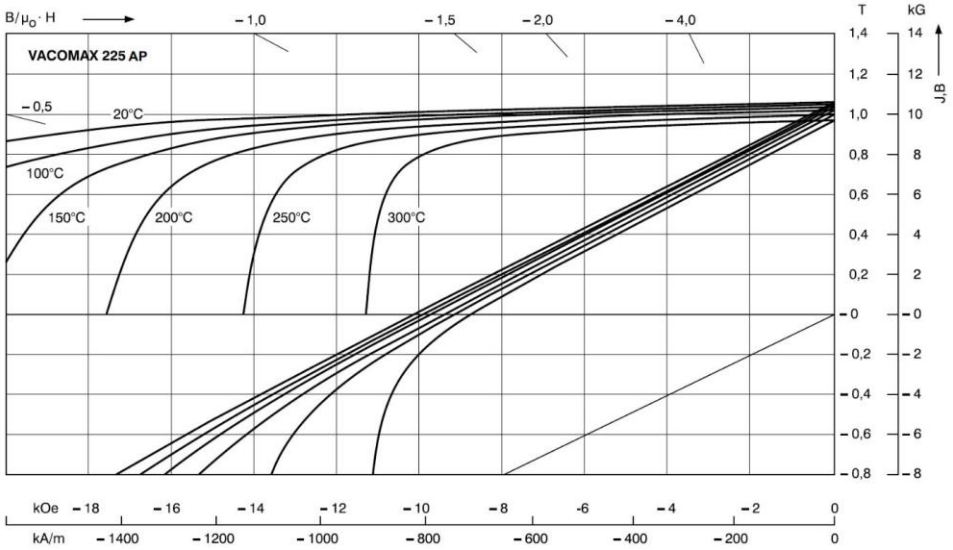

Figure 3.6 Demagnetisation curves of Vacomax-225 Samarium Cobalt magnets at a range of operating temperature (Source: [12])

3.5 Topologies of machines analysed

Five topologies of single-phase permanent magnet machines were considered in the initial phase of this investigation, all potentially being suitable for very high pole numbers. They are all variants of flux modulation machines. All the topologies, which are shown in Figure 3.7, are all based on salient rotors which contain no magnets. The permanent magnets are located at various positions in the stator and the rotating salient rotor has the effect of modulating the permanent magnet flux linking the multi-phase stator winding. The specific topologies considered were:

- Vernier PM Machines (VPMM)
- Flux Switching Machines (FSM);
- Flux Reversal Machines (FRM);
- Flux Reversal Machines B type (FRMB)
- Flux Reversal Machines (FRM) with core modifications

In this first phase of design, all the machines were based on stator split ratio of 0.6 and a stator outer diameter of 196.6mm, i.e. the same combination as the modified baseline design of Figure 3.2. Each machine topology was equipped with a salient rotor having 96 teeth, with the rotor tooth slots having both width of the slots in the salient stator were set to 1.9mm, a value which yields a rotor tooth width to slot pitch ratio of 0.5, as shown Figure 3.7 (f).The rotor slot depth in all cases was

set to the same 1.9mm. The remaining dimensions of each design were established by application of standard machine design practice, e.g. ensuring that the stator core has sufficient cross-section throughout to avoid magnetic saturation. In this preliminary design phase, the radial airgap between the stator and rotor was set to 0.2mm. It was recognised that realising this in a prototype and in a production environment would be extremely challenging, but it was adopted to provide an indication of the upper limit of the electromagnetic performance of these machine topologies. Cross-sections through the resulting designs are shown in Figure 3.7.

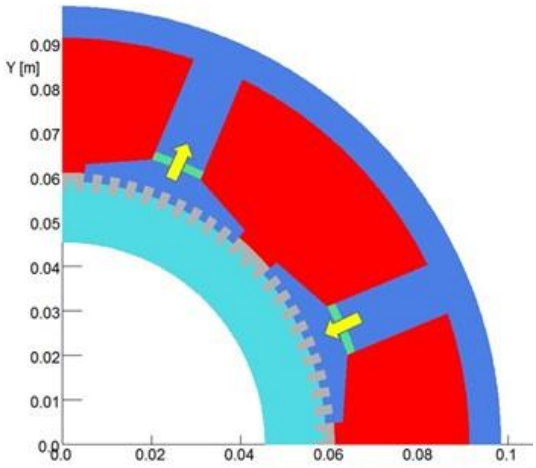

(a) Flux Modulation Machines

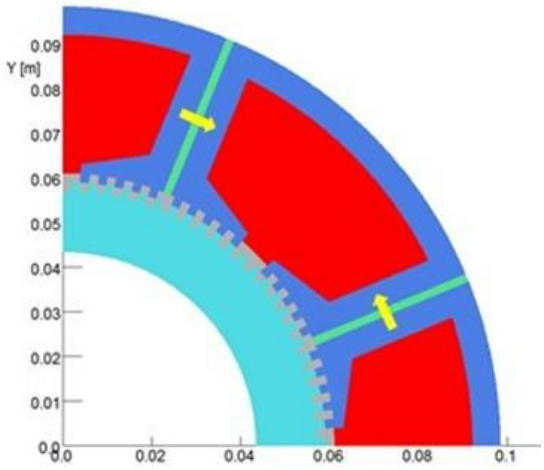

(b) Flux Switching Machines

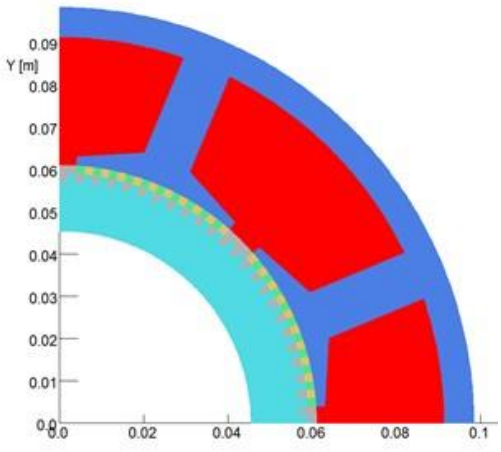

(c) Flux Reversal Machine-Type A

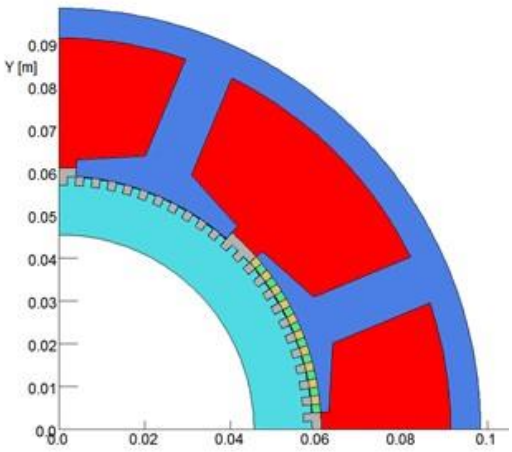

(d) Flux Reversal Machines–Type B

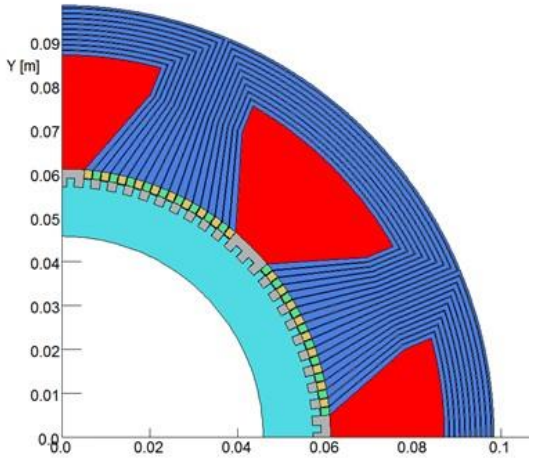

(e) Flux Reversal Machines with oriented laminations

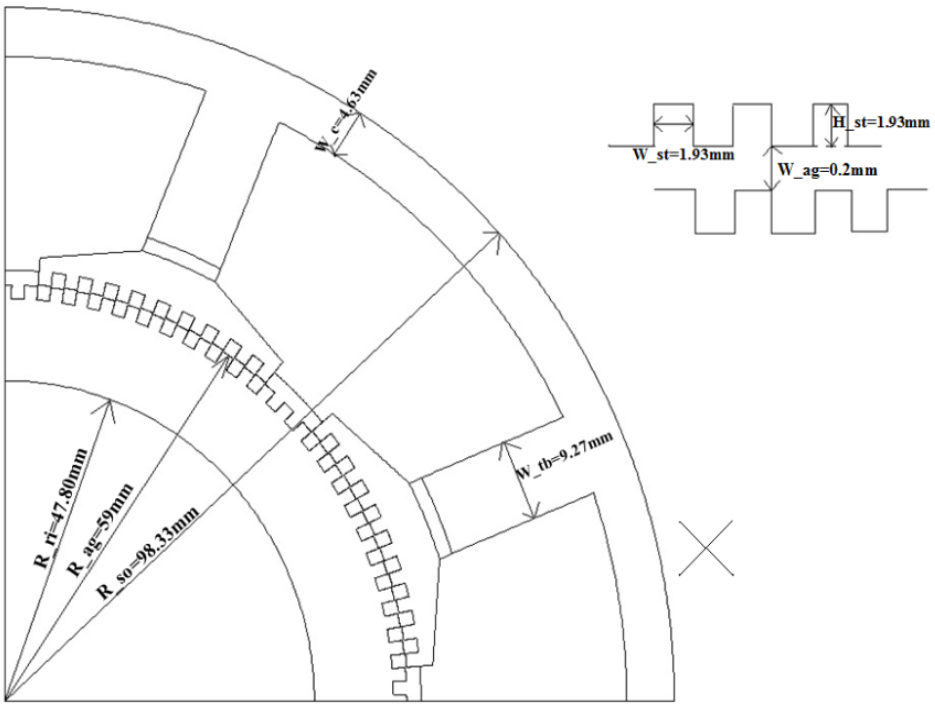

(f) Example dimension detail of Vernier PM Machines

Figure 3.7 Cross-section through machine topologies considered in design study

The VPMM in Figure 3.7 (a), has eight main teeth in the stator. Each tooth has a single embedded permanent magnet of alternating polarity which are magnetised in a radial direction as shown. On each stator main tooth, there are ten smaller teeth which modulate

the flux produced by permanent magnet. The width of the smaller stator matches the pitch of the rotor teeth and hence come into alignment simultaneously. This is achieved by setting the width of main slot opening between the 8 large teeth to be an odd integer number of the width of the smaller slots, in this particular case. When the rotor and stator teeth are aligned the coil flux linkage due to the permanent magnet will increase. When the rotor rotates to unaligned position, with the reluctance in the flux path increased, the flux linkage will be reduced. There is no change in the polarity of the coil flux-linkage, simply a modulation about some mean value.

The FSM in Figure 3.7 (b) shares many features with VPMM of Figure 3.7 (a), except that the permanent magnet is located in the middle of main stator tooth. When the rotor rotates, the flux will switch direction in main teeth like conventional flux switching machines. However, compared to a conventional flux switching machine, in this machine the small teeth increase the output frequency.

The Type A FRM shown in Figure 3.7 (c), has the same rotor and main teeth structure as the VPMM. However, the permanent magnets are not embedded in the main teeth, but mounted on the surface teeth. On each main tooth, there are ten S poles and ten N poles. When the rotor teeth align to S poles on one main tooth, they will align to N poles on another main tooth. The flux will reverse in the main teeth with the rotor rotation.

The Type B FRM (FRMB) shown in Figure 3.7 (d) is similar to the FRM, but only half of main teeth are equipped with PMs, saving half volume of PM material. The main teeth without magnets are aligned to rotor teeth all the time.

The main drawback of both FRMs is the small pole-pitch of the permanent magnets mounted on the stator teeth, which leads to significant leakage flux. One concept which was developed and investigated in an attempt to address this is shown in Figure 3.7 (e). The stator core includes a large number of narrow gaps (0.2mm wide in the designs analysed) which attempt to direct the magnet flux to link with the stator coils. The practicality of this stator core is questionable, but it nevertheless provides an interesting electromagnetic option.

3.6 Performance evaluation of different machine types

3.6.1 Finite element modelling of flux linkage variation in different machine topologies

The first performance assessment undertaken was to employ two-dimensional finite element analysis to predict the variation in flux linkage with rotor angular position for all the machine designs in Figure 3.7. In order to provide some degree of generality, the predicted variation in flux-linkage was normalised on a per tooth and per turn basis with the values shown being for a core axial length of 50mm in all cases. The resulting predicted variations in flux-linkage are shown in Figure 4.1. The waveforms in Figure 4.1 which correspond to the VPMM when initially calculated contains a significant DC offset of 0.000565Wb. This DC offset has been removed in Figure 3.8 to aid a direct comparison.

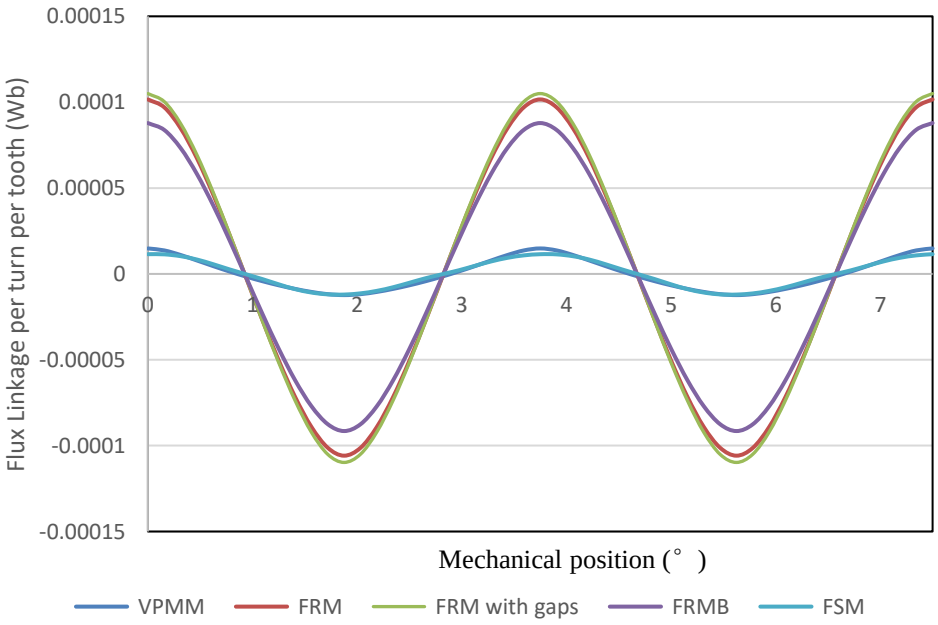

Figure 3.8 Flux linkages versus rotor mechanical position comparing the average flux for each machine in open circuited

As shown in Figure 3.8, the various flux reversal machines produce a much larger variation in flux linkage with amplitudes that are some 4-5 times higher those for the FSM or VPMM. The main reason for the poor performance of VPMM and

FSM is the very small size of the teeth which results in a significant leakage and hence a small variation in the reluctance between the aligned position and unaligned positions.

As discussed above, to reduce the flux leakage between reversed PM in FRM, a series of complex airgaps were introduced into the main teeth as shown in Figure 3.7 (e). The increase in flux linkage amplitude produced by this stator core is only some 3%-5% higher than the normal FRM. This modest increase in unlikely to be sufficient to justify the manufacturing difficulties of incorporating these gaps into an FRM.

3.6.2 Influence of number of rotor teeth

The small size of the rotor teeth and the magnet poles in the FRM designs dictates that leakage in an important factor in limiting performance. It would be expected that the performance of FRMs would improve in terms of the magnitude of the flux change if the number of rotor teeth was reduced. As series of finite element simulations were performed for variations on the FRM design in Figure 3.7(c) for a range of rotor teeth between 48 and 192. In all cases, the main dimensions such as rotor diameter and radial thickness of the magnets were kept fixed. Figure 3.9 shows the resulting variation in flux linkage with rotor angular displacement. As will be seen, although the flux change does increase with 48 teeth compared the 96 tooth designs previously, the rate of change of flux with angular position is lower. As shown, the rate of change of flux linkage keeps improving marginally with increasing numbers of rotor teeth.

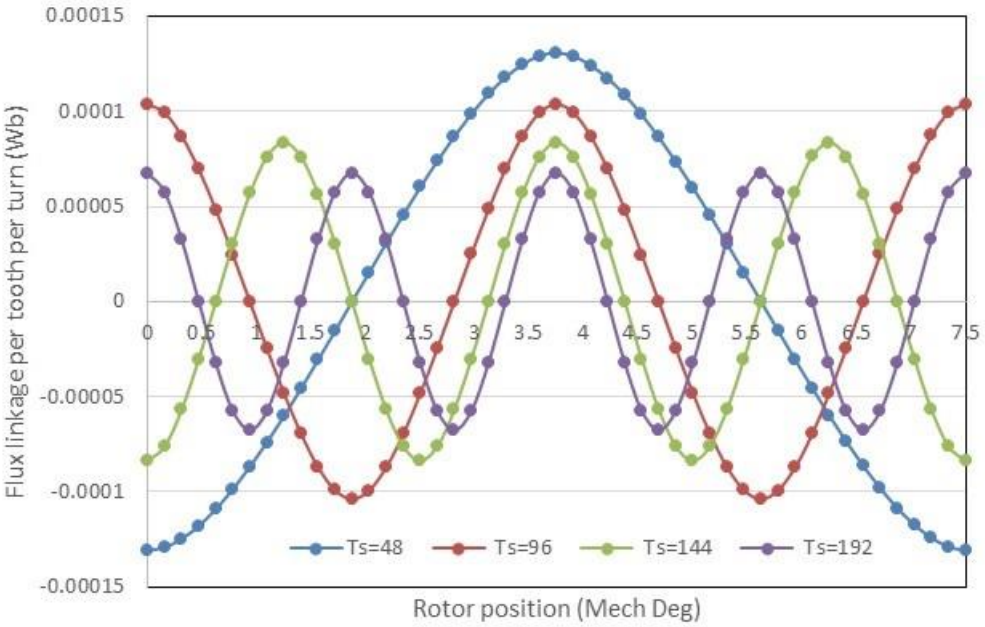

Figure 3.9 Influence of the number of rotor teeth on flux-linkage variation in an FRM reference design

A similar analysis was performed for the VPMM reference design as shown in Figure 3.7 (a). The resulting variations in flux-linkage with rotor angular displacement is shown in Figure 3.10. In this type of machine, there is a significant benefit in reducing the number of rotor teeth, but even with 48 teeth, both the change in flux-linkage and the rate of change of flux-linkage are much lower than the FRM designs.

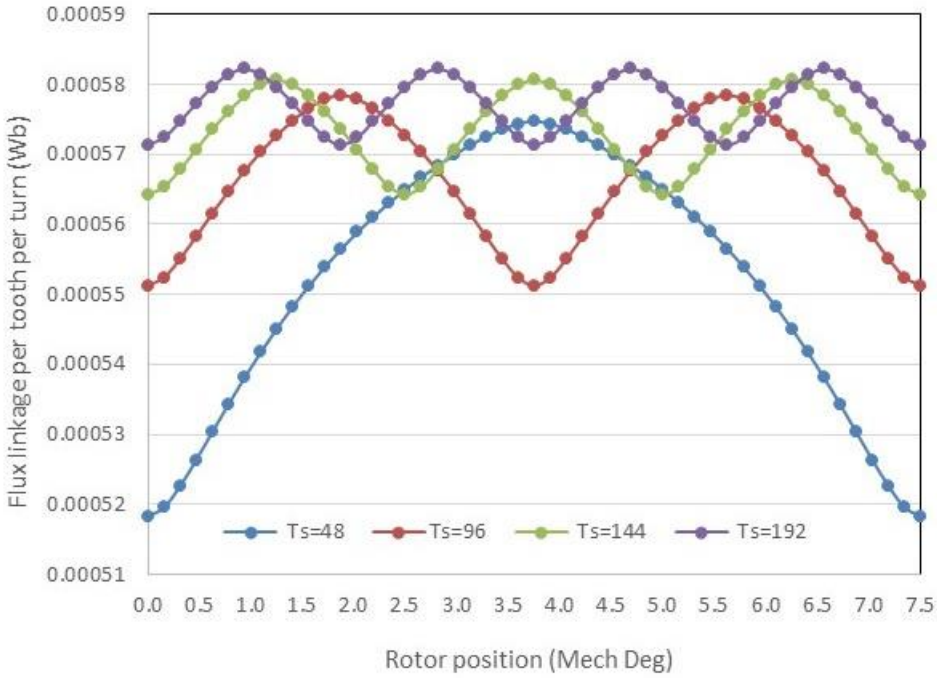

Figure 3.10 Influence of the number of rotor teeth on flux-linkage variation in an VPMM reference design

3.6.3 Finite element analysis of regulation and power curves

It has been shown that for the high pole numbers required in this application, FRMs tend to have superior performances in terms of open-circuit flux variations compared to VPMM and FSM topologies. FRMs were therefore selected for further analysis. The output power capability of various FRM designs was predicted using an electric circuit-coupled finite element simulation using the Opera 2D RM analysis for a standard FRM with 96 rotor teeth. The electric coupled circuit used in these finite element simulations is shown in Figure 3.11. The coils which couple into the finite element model are connected to a full wave diodes bridge rectifier consisting of four uncontrolled rectifier diodes (D1, D2, D3 and D4) with a fixed forward voltage drop set to 1 V. The load resistor on the rectifier output (R1) can be varied to set different current operating points.

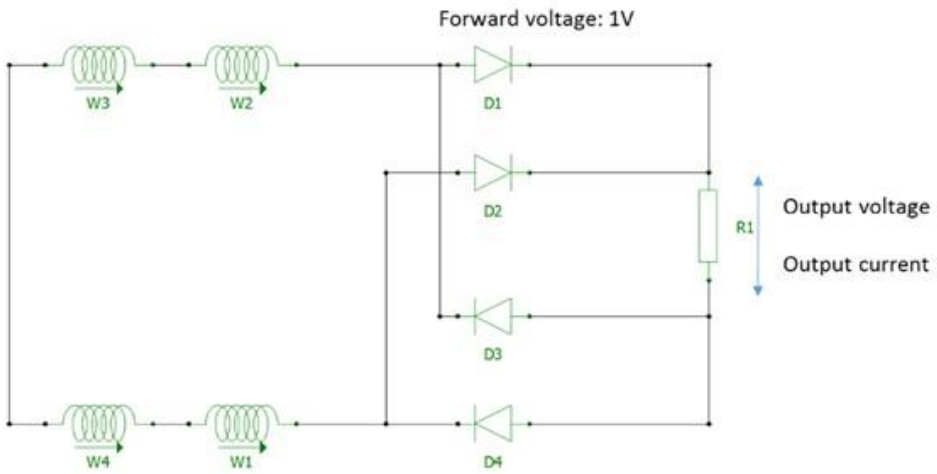

Figure 3.11 Coupled electric circuit used in finite element simulations

In all following simulations in this chapter, the rotational speed was set to 20,000 rpm which results in a generator AC output electrical frequency of 32kHz for the 96 rotor teeth. The number of series turns per coil was initially selected as 2 in order to maintain an output voltage below 270 V (as was the case in the reference 3-phase brushless machine design shown previously in Figure 3.1). Initial simulations were performed for a split ratio of 0.6. The predicted electrical output power as a function of average load current is shown in Figure 3.12.

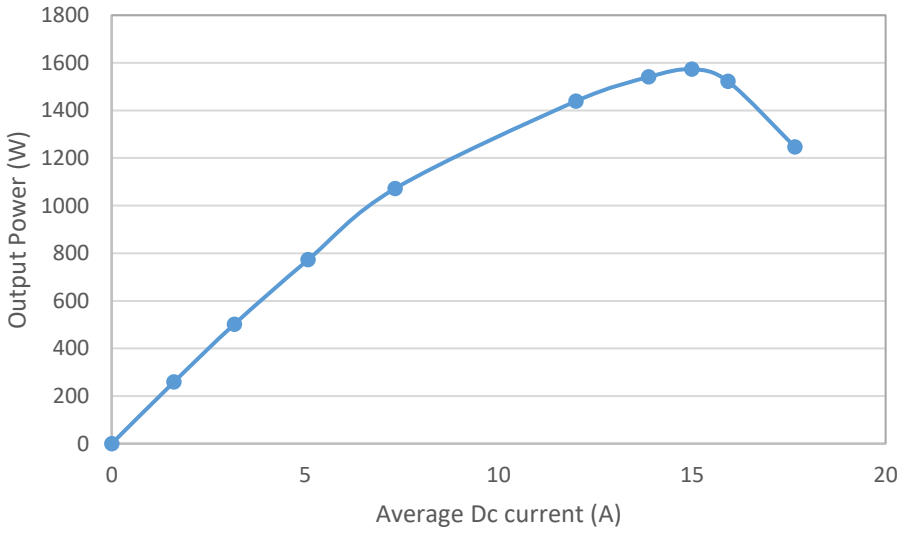

Figure 3.12 Finite element predicted output power characteristic for a reference FRM design with a split ratio of 0.6

As can be seen from this characteristic, the power level is very modest compared to the 50kW that can be achieved by the reference brushless machine design at 20,000rpm when

operating with a 3-phase rectifier. There are two main factors which contribute to this very significant power shortfall. Firstly, the open circuit emf is low due to leakage effects and secondly the high reactance of this type of machine. The maximum currents that can be produced in this design with an active rectifier are low (due to electromagnetic not thermal considerations). This would suggest that the split ratio is too low for this type of machine. Increasing the split ratio will both increase the open-circuit emf and make better use of the stator volume in terms of pushing up the current density.

The power curves shown in Figure 3.13 were predicted for a series of split ratios from 0.65 to 0.8 for the same configuration as the reference FRM design (96 rotor teeth and 8 main stator teeth). As will be apparent, there is a significant improvement in output power capability with increasing the split ratio, but the performance even with a split ratio of 0.8 is very modest when compared to the reference conventional brushless machine, with a maximum electromagnetic power limit of only ~3.9kW.

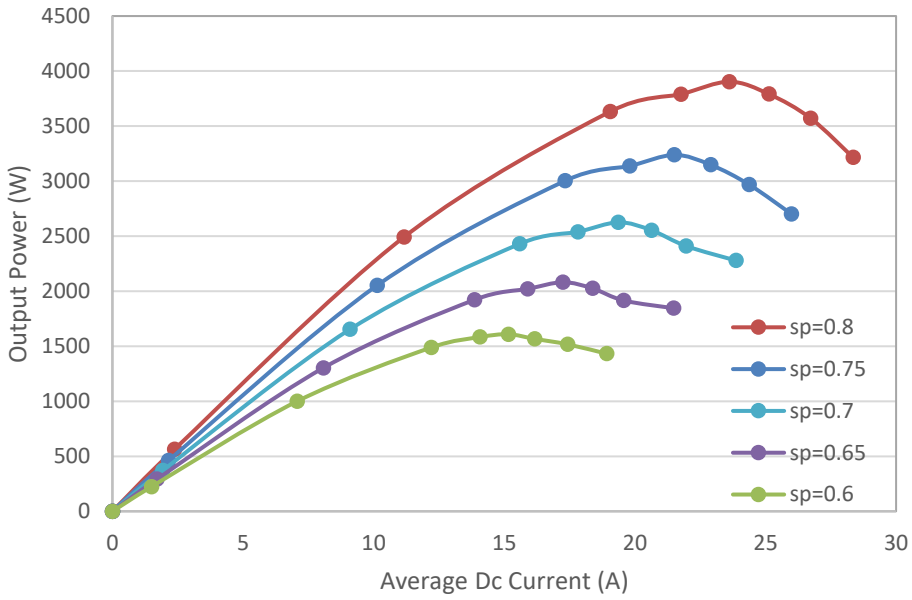

Figure 3.13 Power curves for FRM designs with increasing split ratios (sp)

3.6.4 Influence of magnet geometry on performance

Up to this point in the design and analysis, a fixed magnet radial thickness of 1.9mm was employed. For an FRM with a split ratio of 0.8 and 12 magnet poles per main tooth, the width of the individual magnet poles is ~1.9mm. The magnet poles considered up to this point are also 1.9mm in the radial direction which gives a radial height to width ratio for

the poles of 1.0. Increasing the height of the magnet in the radial direction will tend to decrease the reactance (by virtue of a larger effective magnetic airgap) but may reduce the change in magnet flux. For the design with a split ratio of 0.8, the magnet height to width ratio was varied between 0.10 (a magnet thickness of only 0.2mm) up to the original value of 1.0. The predicted variations in the maximum power for each of these designs is shown in Figure 4.7. As can be seen, the maximum output power can be increased up to 7.4kW with the optimum magnet proportions. However, this is a very thin magnet of thickness of 0.25mm which would be prone to demagnetisation.

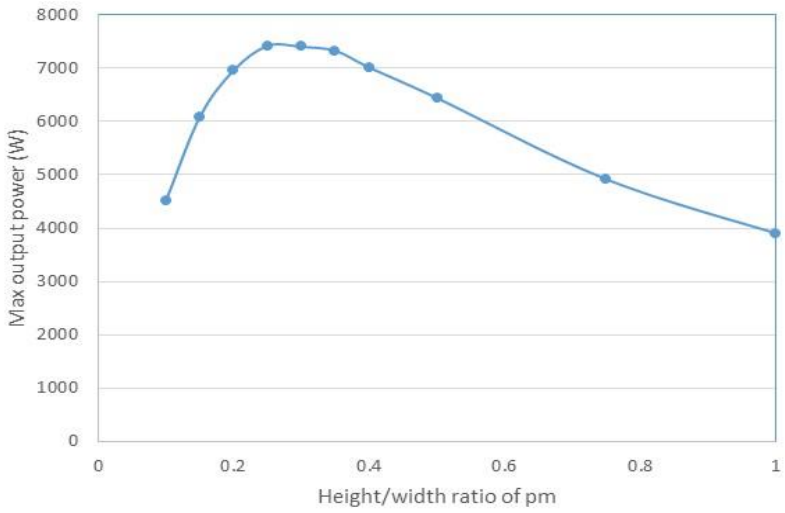

Figure 3.14 Variation in maximum output power with aspect ratio for an FRM design with 96 rotor teeth, a split ratio of 0.8 of magnet width of 1.9mm per pieces

A cross-section through the optimised design up to this point is shown in Figure 3.15. For the 50mm axial length, this design has an active mass (cores, coils, magnets, Aluminium hub and shaft but excluding casing) of 6.95kg, which gives a power density for active mass of 1.07kW/kg. Although still a long way short of the baseline oil-cooled brushless machine, this is starting to be competitive with many other machine types, particularly given the requirement for a high frequency output.

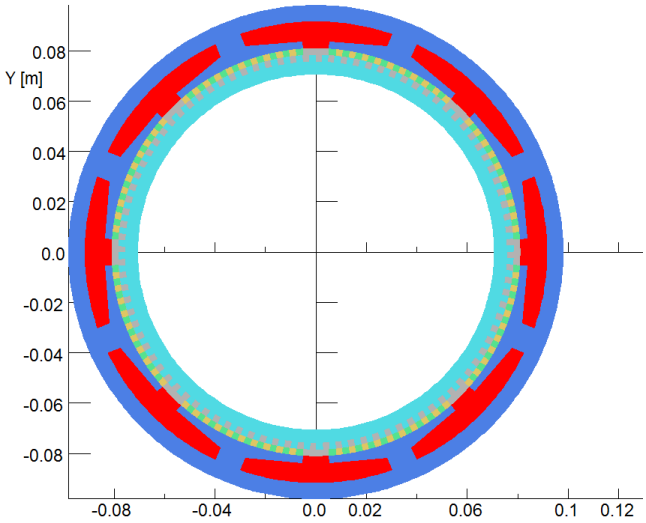

Figure 3.15 Cross-section through 96 tooth optimal design with a split ratio of 0.8 (axial length of 50mmm)

3.7 Conclusions

This chapter has considered several machine types which would appear to offer a high multiplier between mechanical rotation speed and electrical output frequency. Even though significant optimisation has resulted in some improvements in performance, the maximum power capability of the machine of Figure 3.15 is still much lower at 7kW than the 50kW achieved for the baseline SPM design. Furthermore, the airgap required in this machine for it small at 0.2mm.

Overall, this type of machine with a low number of coils (and hence a large coil inductance per turn) and significant inter-polar magnet leakage flux will always struggle to be competitive as a high power density generator. This type of machine does nevertheless provide the functionality of high frequency output with a simple coil structure.

3.8 References

[1] N. Bianchi, S. Bolognani and P. Frare, "Design criteria of high efficiency SPM synchronous motors," IEEE International Electric Machines and Drives Conference, 2003. IEMDC'03., Madison, WI, USA, 2003, pp. 1042-1048 vol.2.

[2] A. M. El-Refaie, "Fractional-Slot Concentrated-Windings Synchronous Permanent Magnet Machines: Opportunities and Challenges", IEEE Transactions on Industrial Electronics, vol. 57, no. 1, pp. 107-121, Jan. 2010.

[3] Massimo Barcaro, "Analysis and Tests of a Dual Three-Phase 12-Slot 10-Pole Permanent-Magnet Motor", IEEE Transactions on Industry Applications, vol. 46, no. 6, November/December 2010.

[4] D. Wu and Z. Q. Zhu, "Influence of Slot and Pole Number Combinations on Voltage Distortion in Surface-Mounted Permanent Magnet Machines With Local Magnetic Saturation," in IEEE Transactions on Energy Conversion, vol. 30, no. 4, pp. 1460-1471, Dec. 2015.

[5] J. Cros, P. Viarouge, "Synthesis of high performance PM motors with concentrated windings", IEEE Trans. Energy Convers., vol. 17, no. 2, pp. 248-253, Jun. 2002.

[6] F. Magnussen and C. Sadarangani, "Winding factors and Joule losses of permanent magnet machines with concentrated windings," IEEE International Electric Machines and Drives Conference, 2003. IEMDC'03., Madison, WI, USA, 2003, pp. 333-339 vol.1.

[7] I. E. K. Koukouvini, C. T. Krasopoulos and A. G. Kladas, "Fault tolerant design of fractional slot concentrated winding PM motor for electric traction," 2017 IEEE 11th International Symposium on Diagnostics for Electrical Machines, Power Electronics and Drives (SDEMPED), Tinos, 2017, pp. 181-187.

[8] B. Sen and J. Wang, "Stator inter-turn fault detection in SPM machines using PWM ripple current measurement," 7th IET International Conference on Power Electronics, Machines and Drives (PEMD 2014), Manchester, 2014, pp. 1-6.

[9] H. Kang, L. Zhou, J. Wang and X. Peng, "Investigation of multiphase modular stator SPM with fault tolerance," 2014 17th International Conference on Electrical Machines and Systems (ICEMS), Hangzhou, 2014, pp. 1572-1575.

[10] M. Shortte, 'Electro-thermal optimisation of a 50kW synchronous permanent magnet generator for aerospace application'. PhD thesis, University of Sheffield, 2016.

[11] R.Boll "Soft Magnetic Materials: Fundamentals, Alloys, Properties, Products, Applications: The Vacuumschmelze Handbook", Heyden 1979, ISBN: 3800912724.

[12] Vacuumschmelze GmbH & Co., "Rare-Earth Permanent Magnets," vol. 3, no. 1, 2010.

Chapter 4 Design and analysis of a single-phase permanent magnet machines

4.1 Introduction

Chapter 3 focussed on machine topologies which employ various types of flux modulation to achieve high frequency output with a relatively low number of stator coils. These produce an output frequency equivalent to that of a 96 pole-pair machine, i.e. 32 kHz at 20,000rpm. However, this approach resulted in machines with low power density, due to the combination significant inter-polar flux leakage and high reactance. This chapter is concerned with more conventional machine topologies in which the number of stator coils equals the number of rotor pole-pairs, as is the case in a standard single-phase permanent magnet machine. These are very high pole number variants of standard surface-mounted and interior and exterior rotor permanent magnet machines, although they are unusual in that they have single-phase outputs. The very high number of stator slots which must be accommodated around the stator periphery, inevitably means that the slots and teeth are very narrow. The single-phase stator winding in this type of machine could be realised with a simple serpentine coil as shown schematically in Figure 4.1. As will be shown in this chapter, the number of turns required in each slot could be as low as one, allowing a rectangular section Litz wire to be used.

Throughout this chapter, a consistent numbering system has been used to identify machine designs. A full list of these design numbers is included as Appendix A of this thesis.

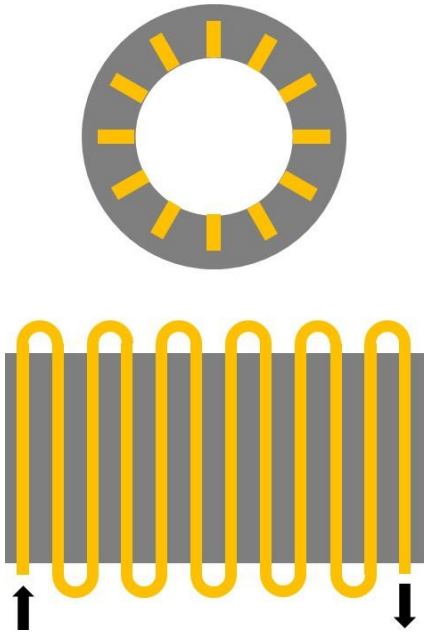

Figure 4.1 Schematic of a stator with a single phase serpentine winding (end-on and unrolled views of 12 slot variant)

4.1 Design of internal rotor machine

4.1.1 Surface mounted PM machine topology designs

The starting design in this chapter is a single-phase, inner rotor, surface-mounted permanent magnet machine with a stator outer diameter of 160mm, 96 permanent magnet pole-pairs and 192 stator teeth which generates a machine output frequency of 32 kHz at 20,000rpm (which would generate a 64 kHz pulse train when rectified). For this high number of poles, each PM pole pitch will be only ~2mm wide and each coil slot is likely to be 1-2mm wide. In order to ensure competitive airgap flux densities, it is necessary to employ a radial magnetic airgap which is several times smaller than the magnet pole pitch. In order to determine the upper limit on the electromagnetic capability of this type of machine the radial length of the effective magnetic airgap for the first series of designs was set to 0.2mm despite the inevitable mechanical challenges that this would present.

A key feature of any electrical machine initial sizing and design is the selection of the machine split ratio, i.e. the ratio of the rotor diameter to the overall stator diameter. For many medium power (10s of kW) SPMs reported in literature, split ratios of 0.55-0.65 are commonly used as these are claimed to generally offer optimum torque density [1]. However, these tend to have much lower number of stator teeth than in this application,

particularly for concentrated wound machines. When a very high pole number is used such as the 192 considered here, the aspect ratio of the teeth, the shape of the slot and the back-iron thickness become extreme (and likely impractical) and split ratios below 0.8 or so. As an example, Figure 4.2 shows a close-up of a pair of slots for 192 pole machine designs with a stator outer of 160mm. As will be apparent, the more 'sensible looking' design are those at high split ratios. Although the lower end of the split ratio range may cause practical difficulties and have poor electromagnetic performance due to slot-leakage and hence higher reactance, as shown in Table 4.2, these were still modelled to establish the variation in performance with split ratio. The initial set of designs shown in Figure 4.2 all include tooth tips which enhance the capture of rotor magnet flux. In all these designs, the ratio of stator tooth tip angle to stator tooth pitch is 0.8 while the ratio of stator tooth body width to stator tooth tip width is 0.6.

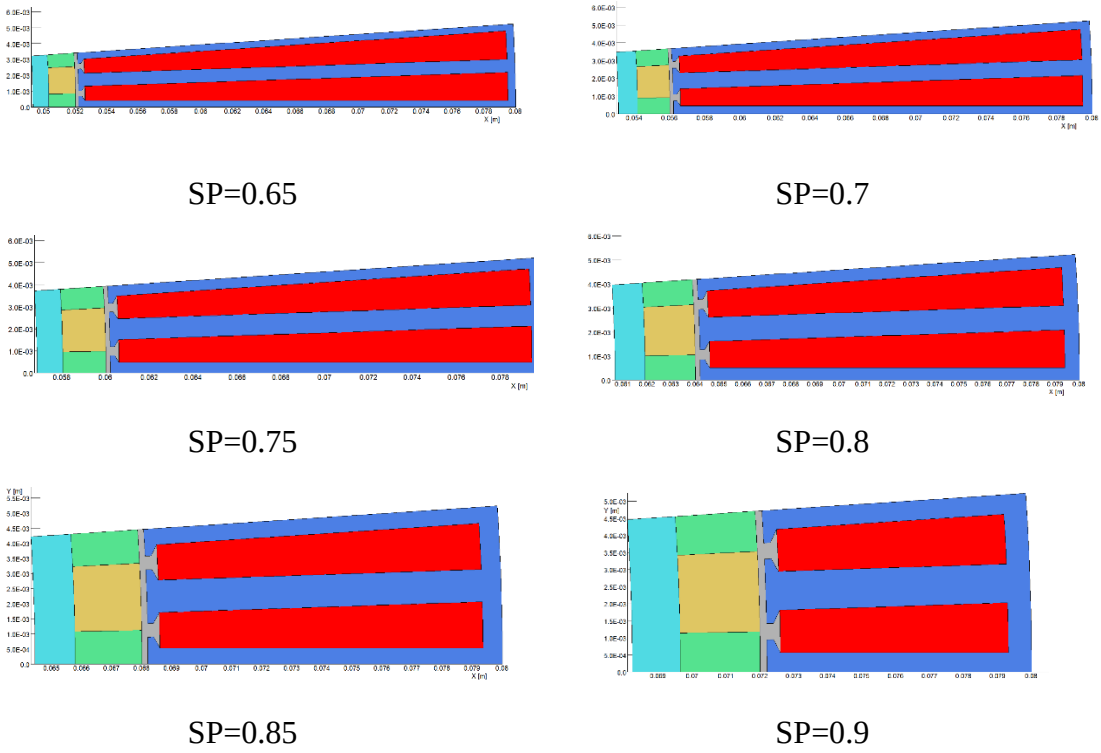

Figure 4.2 Surface mounted PM machine with split ratio from 0.65 to 0.9 (design 4.1.1) (Colour key: Blue – stator core; Red – stator coil; Green – rotor permanent magnet N pole; Yellow – rotor permanent magnet S pole.)

The leading dimensions of the initial designs which were analysed are summarised in Table 4.1. The magnetic materials used in these machines are same with that in chapter

3, i.e. stator and rotor core of VacoFlux 50 Cobalt Iron [2] and the permeant magnets are Vacomax 225 Sm_2Co_{17} [3].

Table 4.1 Leading dimensions of designs analysed (design 4.1.1)

	Split ratio						
	0.60	0.65	0.70	0.75	0.80	0.85	0.90
Stator outer diameter (mm)	160	160	160	160	160	160	160
Stator inner diameter (mm)	96.4	104.4	112.4	120.4	128.4	136.4	144.4
Rotor outer diameter (mm)	96	104	112	120	128	136	144
Magnet pole pitch (mm)	1.571	1.702	1.833	1.963	2.094	2.225	2.356
Stator tooth width (mm)	0.757	0.820	0.883	0.946	1.008	1.071	1.134
Stator slot depth (mm)	33.12	29.21	25.30	21.40	17.49	13.58	9.676
Available slot area (mm2)	41.46	36.10	30.73	25.34	19.94	14.52	9.082

As would be expected given the high frequencies involved in these machines, the winding impedance is dominated by the winding reactance. Table 4.2 shows the per-slot calculated resistance and reactance in designs with split ratios from 0.6 to 0.9 (based on a packing factor of 0.75 and a 20% increase in overall conductor length for end-windings). As will be apparent, at 32 kHz, the coil reactance completely dominates the impedance, being three order of magnitude greater than the resistance. Indeed, in all the design in this chapter the coil impedance is dominated by its reactance, and hence the resistance component (which in any case will be dependent on the packing factor that can be achieved) can be neglected in terms of predicting electromagnetic performance with no meaningful error.

Table 4.2 Summary comparison for SPM in different split ratio (design 4.1.1)

Split ratio	Inductance/slot (μH)	Area of conductor for each slot (mm^2)	Resistance per slot (μΩ)	Reactance per slot at 32kHz(mΩ)
0.60	0.57	41.46	32.4	114.6
0.65	0.53	36.10	37.2	106.6
0.70	0.48	30.73	43.7	96.5
0.75	0.42	25.34	53.0	84.4
0.80	0.35	19.94	67.4	70.4
0.85	0.28	14.52	92.6	56.3
0.90	0.21	9.082	148	42.2

The symmetry in these machines allows a single pair of stator teeth to represent the finite problem domain. The finite element coupled electric circuit employed to simulate machine performance is shown in Figure 4.3. The symmetry and associated scaling set up in the finite element model means that the circuit element W1 represents a series connection all 96 positively oriented conductors. Similarly, W2 represents a series connection of the 96 negative oriented conductors. The machine windings are connected to a full wave bridge rectifier and a pure resistive load. The diodes in the model have a fixed on-state voltage drop of 1V. This is typical of the voltage drop of a power diode. The voltage regulation and power curves for a particular design are generated by running a series of simulations with various values of load resistance.

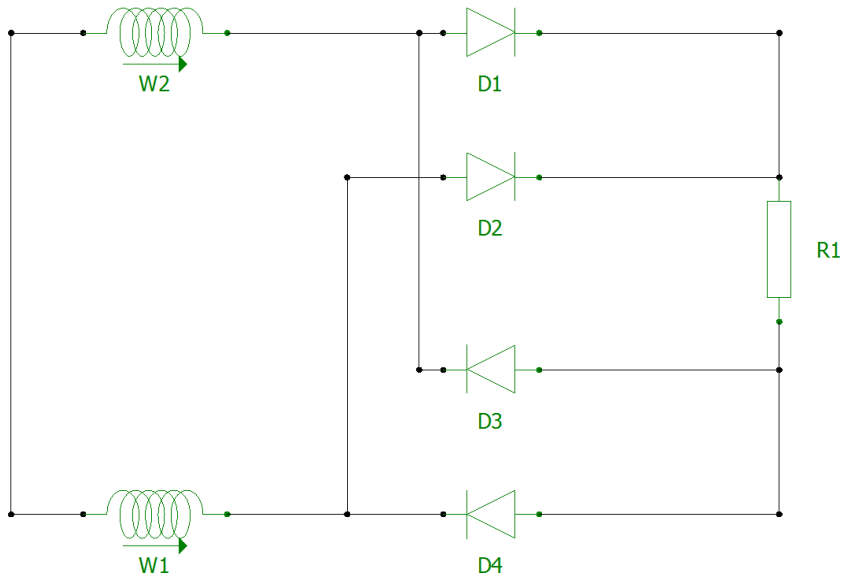

Figure 4.3 Finite element coupled electric circuit for a generator connected to a full-wave rectifier bridge and load resistance

The finite element predicted flux linkage per tooth per turn under open-circuit conditions is shown in Figure 4.4. As would be expected, the increased rotor radius which follows from a higher split ratio increases the stator flux linkage per tooth by increasing magnet volume and reducing magnetic reluctance. A finite element predicted field distribution under open-circuit conditions for a split ratio of 0.9 is shown in Figure 4.5.

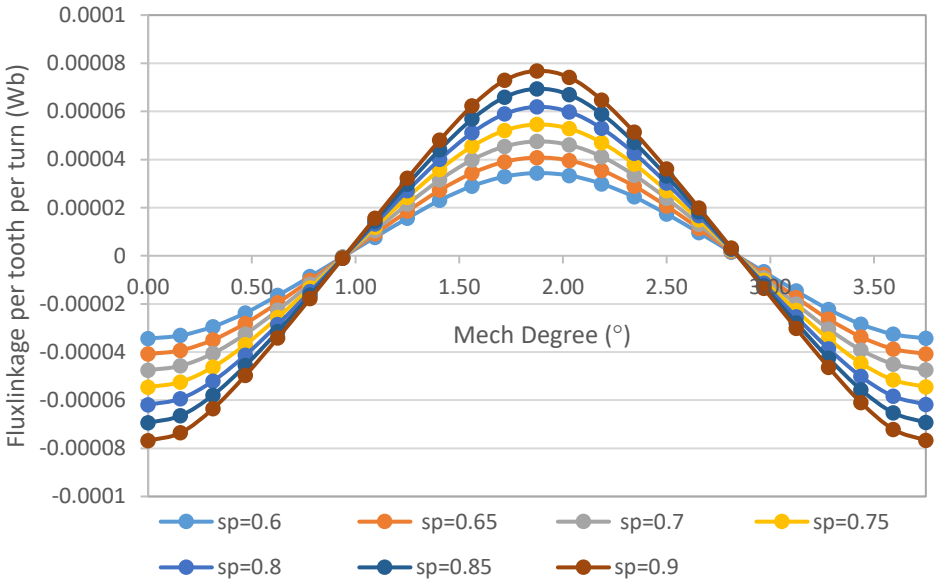

Figure 4.4 Open-circuit flux linkage per tooth per turn as a function of rotor angular position (design 4.1.1)

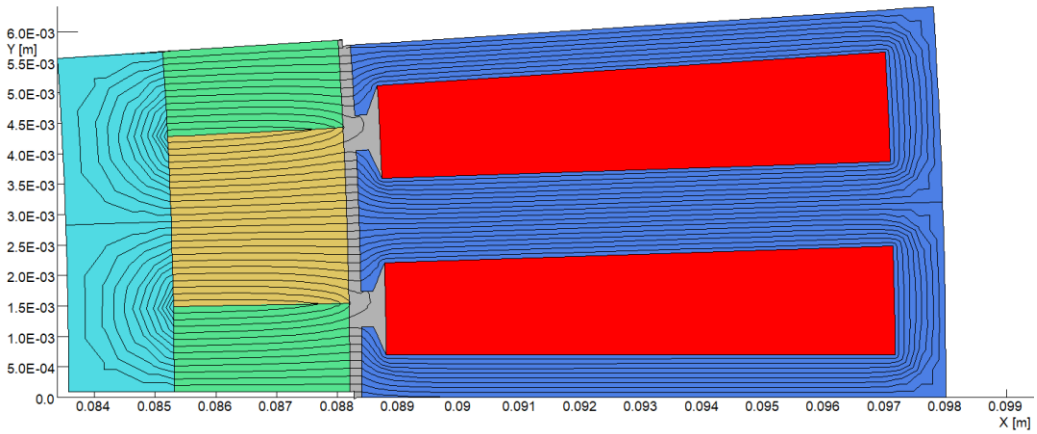

Figure 4.5 Finite element predicted field distribution under no-load conditions (design 4.1.1) (Blue – stator core; Red – coil; Light blue – rotor core; Yellow – magnet N pole; Green – magnet S pole)

A single phase machine with the same number of rotor poles and stator teeth will generate a large cogging torque as all the poles come into alignment with the teeth at the same

time. Figure 4.6 shows the no-load cogging torque predicted for the machine design with a split ration of 0.90 whose leading dimensions were shown previously in Table 4.1. As shown, the peak cogging torque of 12.1Nm which is ~50% of the rated torque of 23.9Nm (which corresponds to 50kW at 20,000rpm). In many applications where a maximum cogging torque forms part of the specification, this level would be regarded as excessive. However, there is in general no cogging torque specification for aerospace generators of this type since they are generally driven from a very high power and high moment of inertia prime-mover and hence this high cogging torque is not a problem in this case.

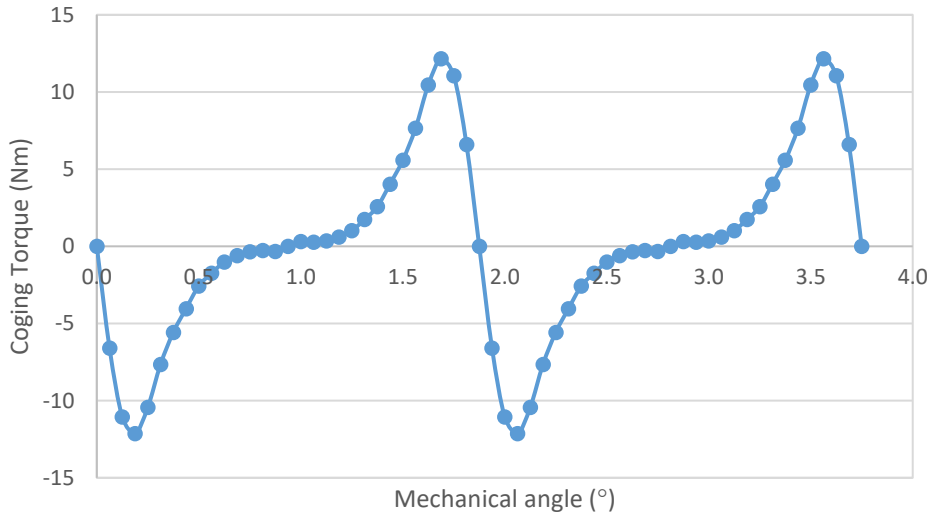

Figure 4.6 Finite element predicted no-load cogging torque for the machine (design 4.1.1)

The initial set of machine designs was based on a single serpentine wound coil, which resulted in a series connection of the conductors in all slots. At this stage in the design process, the serpentine coil has a single turn, i.e. only one effective series connected conductor per slot (although this would be made up from several multiple parallel strands). As will be demonstrated in this chapter, even a single turn results in an open-circuit EMF in the 700V+ range for some design. In a practical machine for an aerospace application it is likely that the stator would need to be wound in two or more sectors which are then connected in parallel to achieve an appropriate output voltage, e.g. of the order of 300V peak.

Providing the resistance can be neglected, the electromagnetic performance of a particular design can be established without specifying a coil packing factor (i.e. the

proportion of each stator slot which is occupied by conductor rather than insulation, gaps etc.). However, the viability of a machine in terms of delivering the maximum electromagnetic power with a sustainable power loss and acceptable efficiency, is dependent on the achievable packing factor. The parallel sided slots and the use of a single turn serpentine coil should enable a high packing factor to be achieved particularly if a rectangular rolled rectangular section Litz wire is matched to the slot shape. Figure 4.7 shows published manufacturer guidance on fill factor of compacted rectangular Litz wire. This suggests an overall packing factors in the range 0.6-0.8 depending on the Litz type used, the slot-liner thickness and the fit to the slot dimensions of the bundle profile. For the rest of this chapter, conductor current densities are quoted for both packing factors of 0.6 and 0.8 which should cover the range that can be realised in practice.

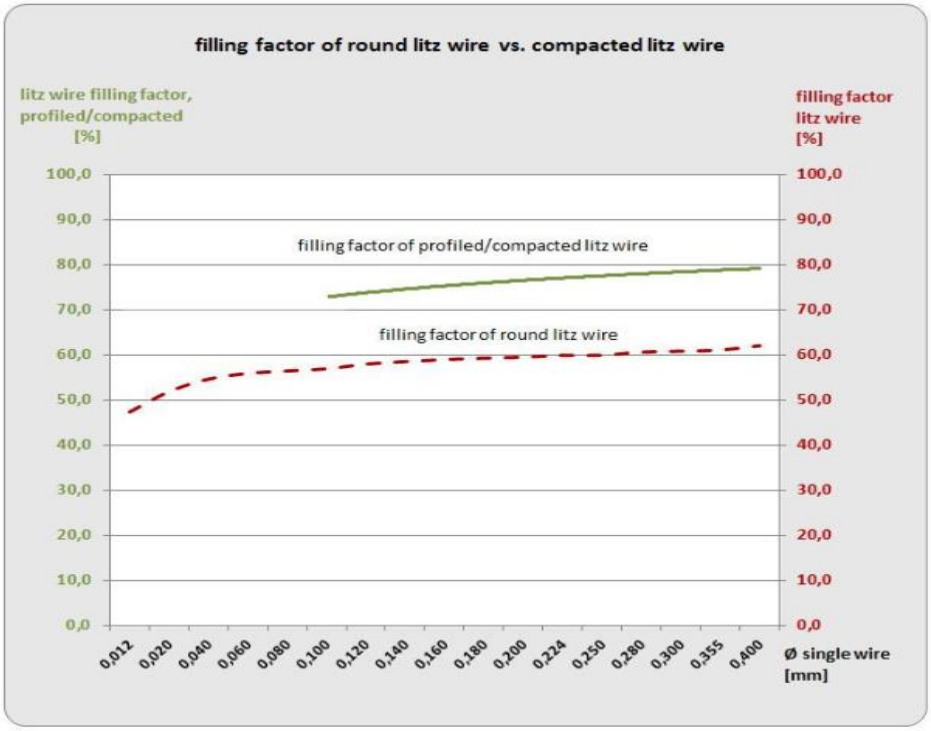

Figure 4.7 Published manufacturer design guidelines for rectangular (profiled) compacted Litz wire (Source: [4])

A series of electric-circuit coupled finite element simulations were performed using the rectifier circuit shown previously in Figure 4.3. For a particular machine design, the load resistance was decreased in steps to gradually increase the average load current. The predicted variations in the average load voltage as a function of the average load current is shown in Figure 4.8a. Figure 4.8b shows the corresponding predicted variations in the average load power. As shown, the electromagnetic output power capability of the

machine with split ratio in 0.6 is only ~4.1kW. However, with the split ratio increased to 0.9, the average output power capability increases to 43.4kW. This is due to a combination of increased magnet flux from the larger rotor and the reduced reactance of the shallower slots which improves the load regulation.

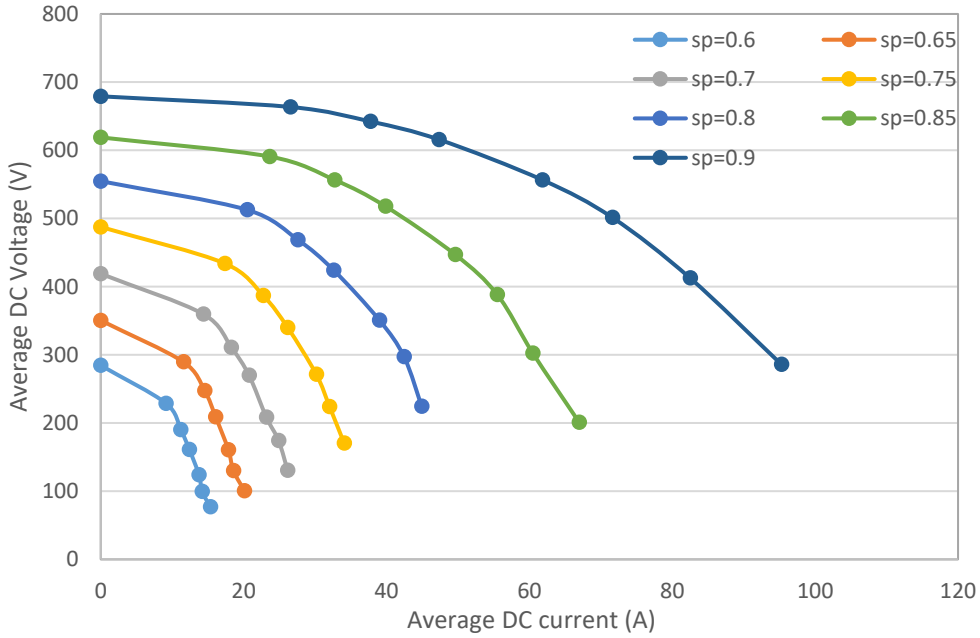

(a) Output V-I curve of the machine in different split ratios at 20,000rpm

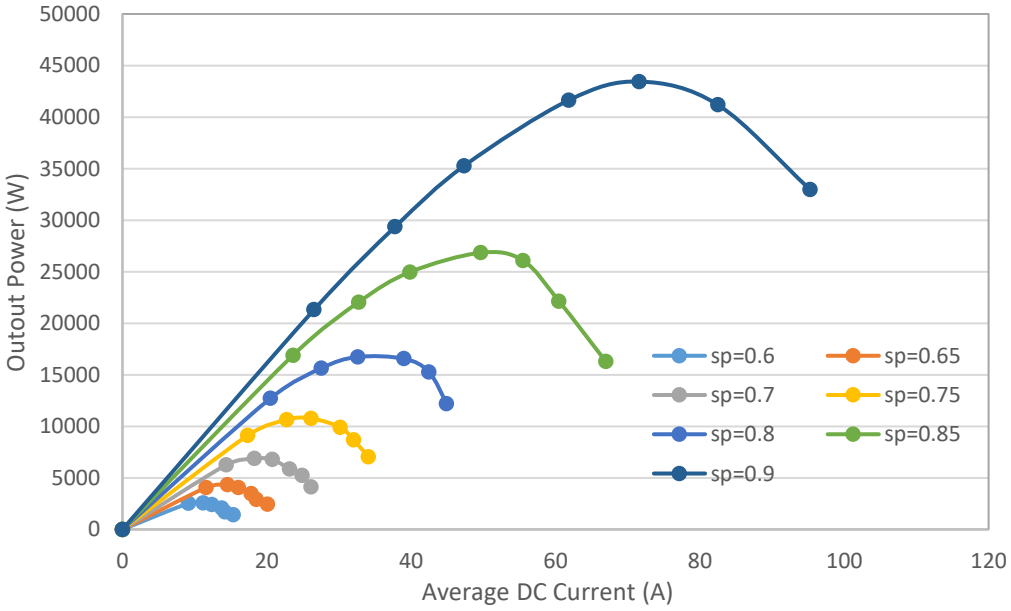

(b) Output power in different split ratios at 20,000rpm

Figure 4.8 Output performance of the machine in different split ratios (design 4.1.1)

It is important to recognise that this increased electromagnetic power capability does not necessarily mean that this power level could be sustained from a thermal point of view. It will be shown later in this chapter, that iron loss is a critical factor in terms of thermal behaviour, but at this point it is useful to focus on the copper loss. In the case of the design with a split ratio of 0.9, the peak power corresponds to a DC average load current of 71.6A. This design has a slot area of 9.08mm^2. For a coil packing factor of 0.8, this would result in a current density in the conductor of 10.9A/mm^2 rms at the 43.4kW operating point, increasing to 14.6A/mm^2 if a packing factor of only 0.6 could be achieved. Setting the rms current density limit of 10A/mm^2 rms which is a value typical of an indirect liquid cooled machine (i.e. cooled with a water or oil jacket) would result in an output power of 42kW for a packing factor of 0.8, dropping to ~37kW for a packing factor of 0.6. It is worth noting that the relatively shallow optimum in the power curves shown in Figure 4.8b mean that a useful reduction in current density and hence copper loss can be obtained with only a small reduction in power by selecting an operating point below just below the optimum. Figure 4.9 shows a predicted load current from the finite element coupled electric circuit simulations for the design with a split ratio of 0.9 at the maximum power point. As well as offering greater electromagnetic power capability, an increased split ratio also reduces the active mass of the machine as shown in Table 4.3.

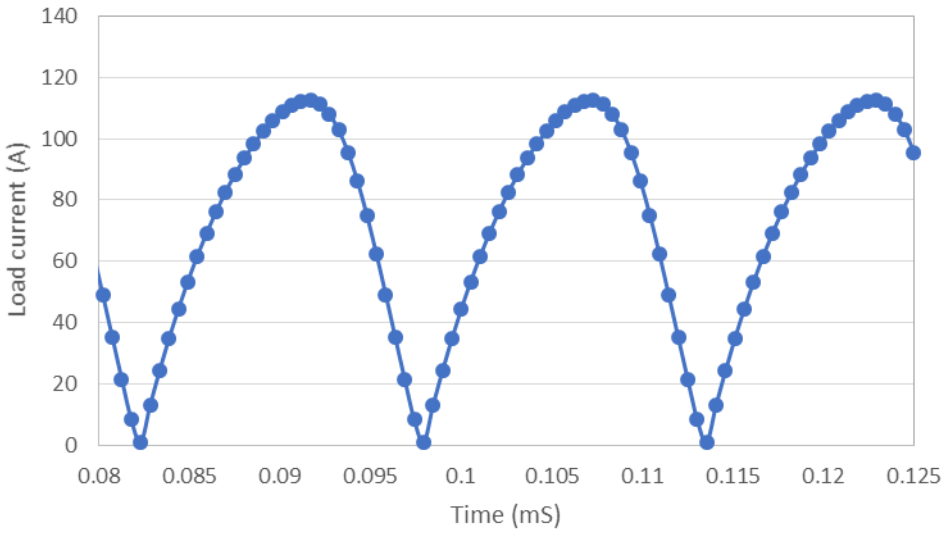

Figure 4.9 Load current waveform for (design 4.1.1) with a split ratio of 0.9 at maximum power operating point (initial transient interval not shown)

Table 4.3 Calculated active mass of the machine designs (neglects rotor shaft, rotor hub and stator casing) (design 4.1.1)

Split ratio	**0.60**	**0.65**	**0.70**	**0.75**	**0.80**	**0.85**	**0.90**
Active mass (kg) - packing factor 0.8	5.09	4.69	4.24	3.76	3.24	2.69	2.10
Active mass (kg) - packing factor 0.6	4.39	4.07	3.72	3.33	2.90	2.44	1.94

The machine designs shown previously in Figure 4.2 have stator cores with tooth tips. Although these tooth tips will tend to increase the induced emf from the permanent magnet field they will also increase the reactance of the stator winding and hence degrade the load regulation. Eliminating the tooth tips to produce open and parallel stator slots will tend to reduce the stator reactance of the machine but at the expense of a reduced emf. Other effects include making the machine easier to manufacture but at the expense of exposing the windings to an increased field from the rotating permanent magnet fields hence potentially increasing AC losses in the winding.

In order to determine whether removing the tooth tips would increase the power capability of this type of machine, a further series of electric-circuit coupled finite element simulations were performed on the machine designs shown in Figure 4.10, which again have split ratios from 0.6 to 0.9. As was the case with the versions with tooth tips, the stator winding was a single serpentine winding with one turn per slot. In the machine with the tooth-tips the winding is retained to some degree by the tooth tips although a trapezoidal shaped slot-wedge could be incorporated to fully retain the winding. In the case of stator teeth with no tips, a region of the slot at the slot opening was left with no coil as shown in Figure 4.5 and 4.6 to allow for either resin potting and/or a slot wedge to retain the winding. The depth of this void was set to 0.4mm (twice the length of the airgap). The slot areas quoted in this analysis and for calculation of losses does not include this void, i.e. the packing factor is applied to the red region only in Figure 4.5 and Figure 4.6 for example.

However, the width of the magnet poles was reduced to reflect the reduced flux capture capability of the parallel-sided tooth. The predicted variations in average load voltage and average load power as a function of average load current are shown in Figure 4.11(a)

and Figure 4.11(b) respectively. As would be expected, there is reduction in the open-circuit output voltage compared to the equivalent machine with tooth tips, e.g. from 679V to 659V for a split ratio of 0.9. Although there is some improvement in the load regulation, overall the absence of tooth tips results in a lower electromagnetic power capability, with a maximum of ~40kW.

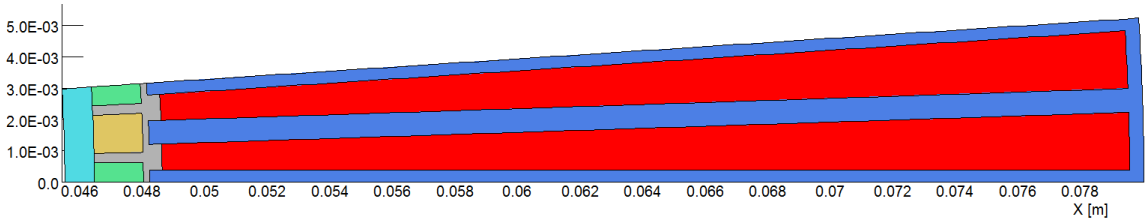

Figure 4.10 Machine designs with no tooth tips (design 4.1.2) (example shown has a split ratio of 0.6)

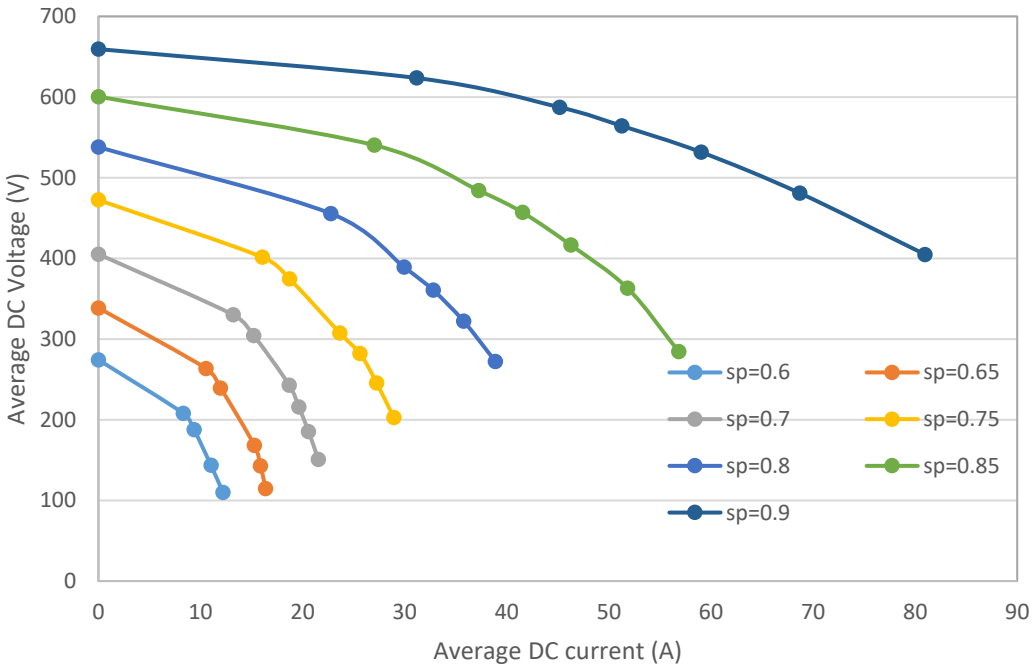

(a) Output V-I curve of the machine in different split ratios at 20,000rpm

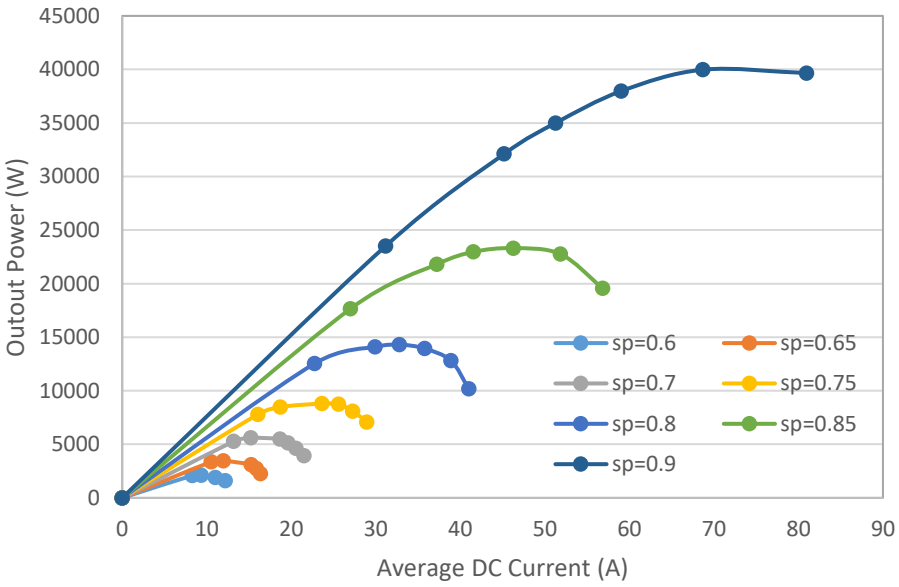

(b) Output power in different split ratios at 20,000rpm

Figure 4.11 Finite element predicted output performance of the machine in different split ratios (design 4.1.2)

Although these SPM machines have shown some useful potential in terms of the electromagnetic power capability, particularly at the higher split ratio, these are based on a 0.2mm airgap which is likely to prevent a practical containment sleeve from being employed to the retain the rotor magnets against the influence of centrifugal loading. An estimate of the containment thickness required to retain the magnets in the designs of Figures 4.2 can be obtained using analytical stress calculation formulae from [5].

Taking a worst-case assumption that the magnets act as a dead-weight on the containment sleeve (i.e. neglecting the effect of an adhesive bond between the individual magnets and the rotor core) then the containment sleeve can be analysed as a homogenous rotating thick-walled cylinder. If the inner and outer diameters and the pole arc being defined as d_{mo}, d_{mi}, and α, as well as d_{co} and d_{ci} of the containment sleeve, the maximum hoop stress σ_{max} in a containment sleeve at a rotational speed of ω is given by:

$$\sigma_{\max} = \frac{\delta_c \omega^2}{8}\left[(3+\nu_c)\left(\frac{d_{co}^2}{2}+\frac{d_{ci}^2}{4}\right)-(1+3\nu_c)\frac{d_{ci}^2}{4}\right]+\left(\frac{d_{ci}^2+d_{co}^2}{d_{co}^2-d_{ci}^2}\right)\left(\frac{m_{eq} r_{meq} \omega^2}{\pi\, d_{mo}}\right) \tag{4.1}$$

Where δ_c and ν_c presents the mass density and the Poisson's ratio of the containment, and the effective mass and radius of the arc shaped magnet pieces are given by:

$$m_{eq} = \frac{\pi}{4}\left(d_{mo}^2 - d_{mi}^2\right)\left(\frac{\alpha\delta_m}{180} + \left(1 - \frac{\alpha}{180}\right)\delta_{ip}\right)$$

$$r_{meq} = \frac{\sqrt{2}}{2}\sqrt{\frac{(d_{mo}^4 - d_{mi}^4)}{4(d_{mo}^2 - d_{mi}^2)}}$$

These analytical formulae from [5] were used to calculate the stress in a range of different containment sleeves. Table 4.4 shows the calculated stresses for split ratios for a nominal sleeve thickness of 0.5mm and the containment sleeve thickness required to limit the stress to 1GPa which is at the upper end of the stress capability of filament-wound carbon fibre sleeves. As shown by Table 4.4, there is a significant increase in stress with increasing split ratio. This is due to a combination of increased rotor radius and increased magnet radial thickness and hence mass since the individual magnet poles were all based on a 1:1 aspect ratio between radial thickness and pole pitch. The calculated values in Table 4.4 show that a minimum a sleeve thickness of 0.65mm would be required for a split ratio of 0.9 (and thicker if a greater safety margin than that with 1GPa was required). When added to a minimum mechanical clearance of ~0.2mm, this would result in an effective magnet airgap of 0.8-0.9mm for this split ratio. It is worth noting that in terms of mechanical analysis, the split ratio is setting the rotor diameter and hence the results in Table 4.4 suggest that a smaller diameter but axially longer machine might be a viable option. However, the reduced pole pitch and hence the increased leakage would work against a machine with a smaller rotor diameter. This option of changing the aspect ratio was not considered further, since the design study was focussed on a direct comparison with the reference design. The issue of aspect ratio could be returned to in a future study.

Table 4.4 Analytically predicted containment sleeve performance at 20,000rpm for a series of machine design from Figure 4.2 with different split ratios

	SP = 0.6	SP=0.75	SP=0.9
Containment hoop stress for 0.5mm thick containment sleeve	408MPa	737MPa	1.20GPa
Containment sleeve thickness for a maximum stress of 1GPa	0.153mm	0.330mm	0.65mm

In order to understand the electromagnetic impact of increasing the gap between the surface of the magnets and the stator bore, a further series of finite element simulations were performed for a machine design with tooth tips and a split ratio of 0.9 for magnetic airgaps of 0.4mm, 0.6mm and 0.8mm. Figure 4.12 shows magneto-static finite element predicted field distributions for the various airgaps. As would be expected, the inter-polar airgap leakage flux increases significantly with increasing airgap.

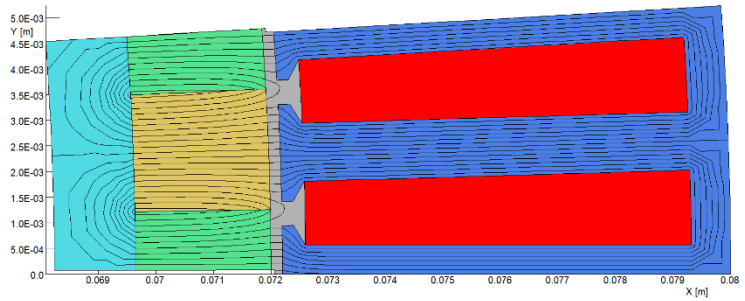

(a) Open circuit flux distribution in SPM machine with a radial airgap of 0.2mm

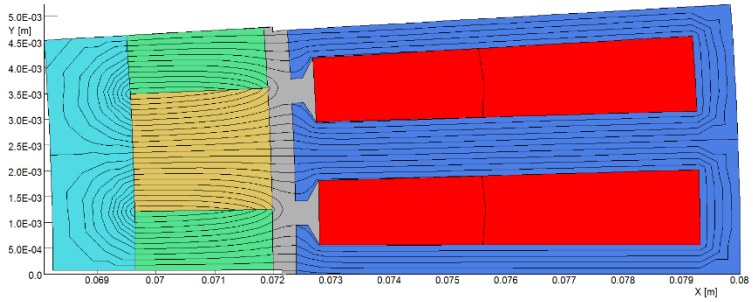

(b) Open circuit flux distribution in SPM machine with a radial airgap of 0.4mm

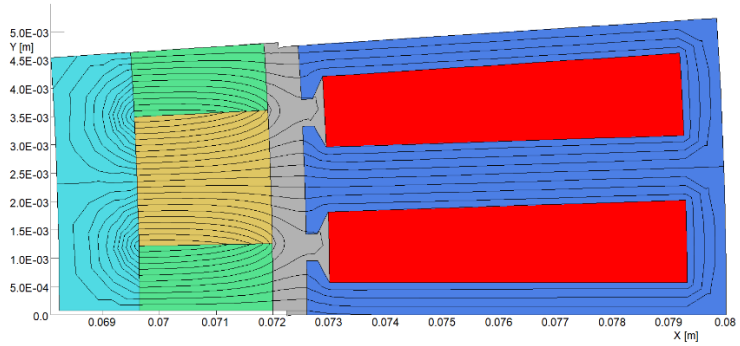

(c) Open circuit flux distribution in SPM machine with a radial airgap of 0.6mm

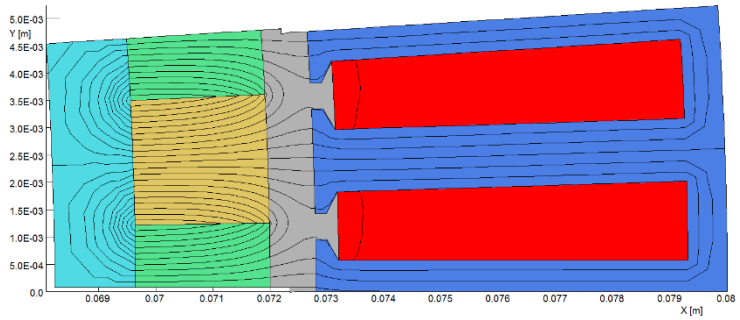

(d) Open circuit flux distribution in SPM machine with a radial airgap of 0.8mm

Figure 4.12 Open circuit Flux distribution in machine (design 4.1.1-ag) with different air gaps for machines with a split ratio of 0.9

Figure 4.13a shows the predicted variation in the average output voltage with increasing load current while Figure 4.13b shows the corresponding variation in the average output power for the various airgap lengths. As will be apparent, increasing the airgap even by a further 0.2mm to 0.4mm results in a dramatic reduction in the average output DC voltage and power. On the basis of the predictions of Figure 4.13b, it was concluded that a mechanically viable machine, i.e. an airgap of at least 0.8mm to accommodate a 0.65mm thick containment sleeve (operating at 1GPa), does not provide a competitive power output for the particular combination of speed and power.

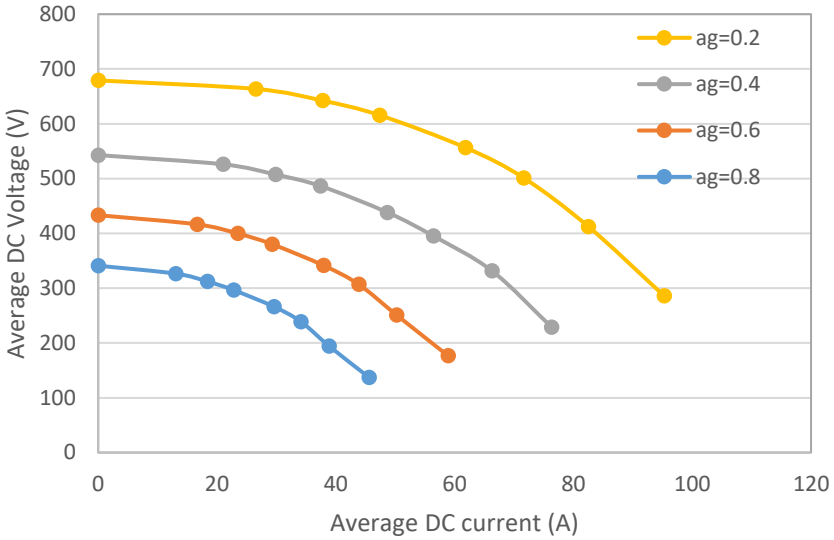

(a) Output V-I curve of a series of machines with different air gap width

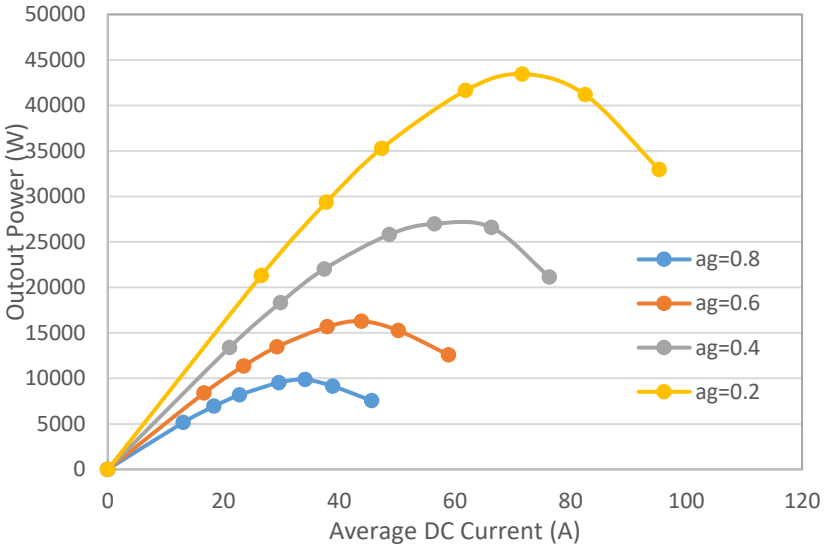

(b) Output power versus DC load current at a series of air gap lengths

Figure 4.13 Finite element predicted output performance of the machine in a series of air gap lengths (design 4.1.1-ag)

4.1.2 Interior permanent magnet rotor designs

One potential means for maintaining a competitive airgap flux density while accommodating larger airgaps is to use flux-focussing. This can be realised with internal rotor machines using so-called interior permanent magnet (IPM) machines. Figure 4.14 shows close-ups of one-pole pair of a series of designs with the same stator dimensions

but with a series of different rotor magnet dimensions. In each case, the green regions in the rotor represent circumferentially magnetised magnets of alternating polarity as shown while the light blue regions represent iron pole pieces. In principle, these iron pole pieces could be keyed into the non-magnetic rotor hub (grey region) to provide some mechanical retention although this could increase leakage flux around the inner edge of the magnets. The dimensions of each rotor design are defined in terms of the rotor magnet aspect ratio (R_t) which is defined as the ratio of radial depth of a magnet pole to its width. In all cases, the stator design remains fixed. The increasing magnet radial depth is accommodated by reducing the outer diameter of the non-magnetic rotor hub.

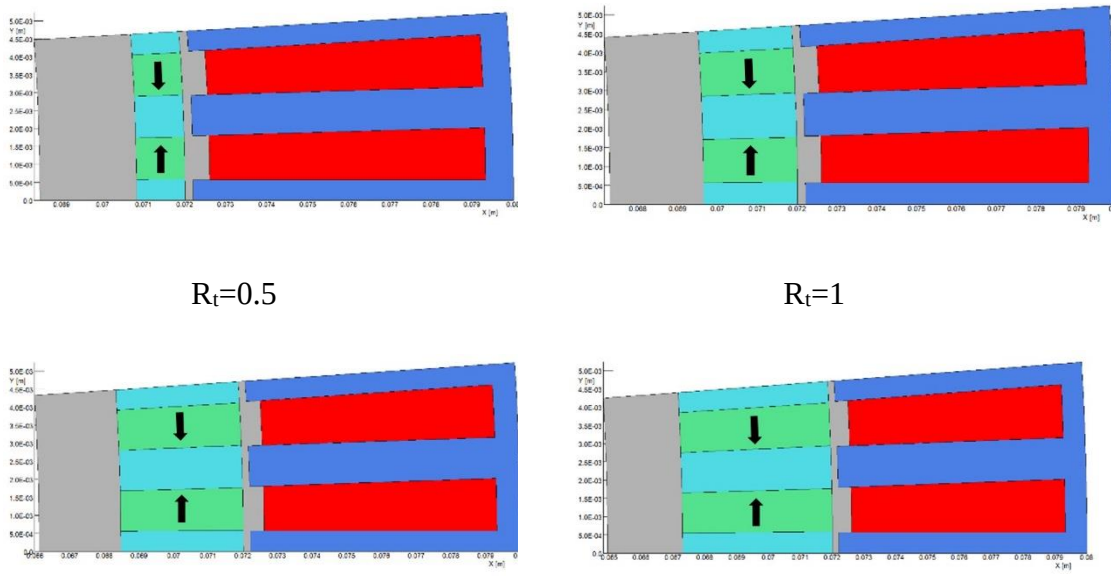

R_t=0.5 R_t=1

R_t=1.5 R_t=2

Figure 4.14 Inset PM Machine designs (design 4.2.1) (Darker blue – stator core; red – stator coil; green – rotor magnets; light blue – rotor core pole-pieces)

The finite element predicted field distribution under open circuit conditions is shown in Figure 4.15 for the case of R_t=2 and an airgap of 0.2mm. This demonstrates that although there is still some flux leakage at the inner edge of the rotor shaft, the majority of flux from magnet is focussed in to the stator teeth when the rotor iron inter-poles are aligned with the stator teeth. The benefit of increasing the ratio R_t in terms of increasing the stator flux-linkage is clearly shown in the flux density distributions of Figure 4.16 and Figure 4.17. As shown, the stator tooth bulk flux density is ~2T for Rt=2 compared to only ~1.2T for Rt=05.

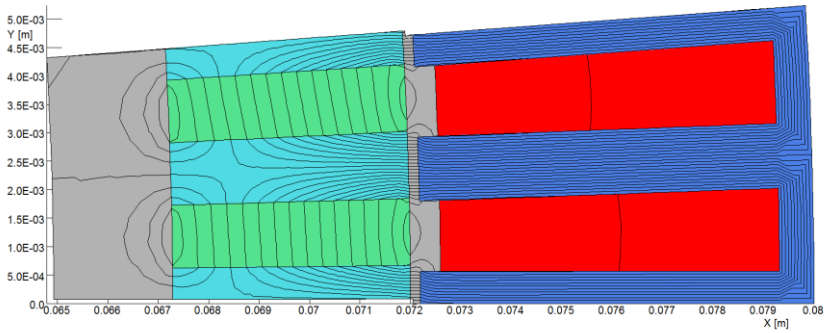

Figure 4.15 Open circuit field distribution in IPM machine with R_t = 2 and an airgap of 0.2mm (design 4.2.1)

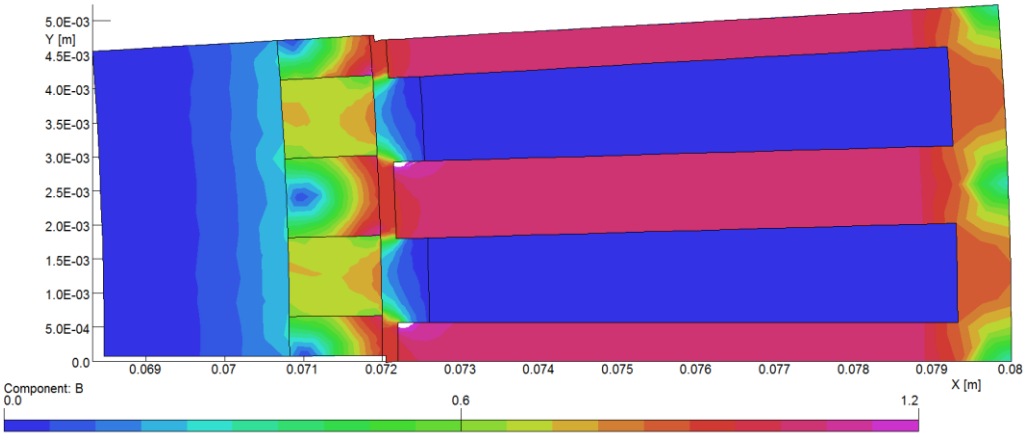

Figure 4.16 Open circuit flux density distribution in IPM machine with R_t=0.5 and airgap of 0.2mm (design 4.2.1)

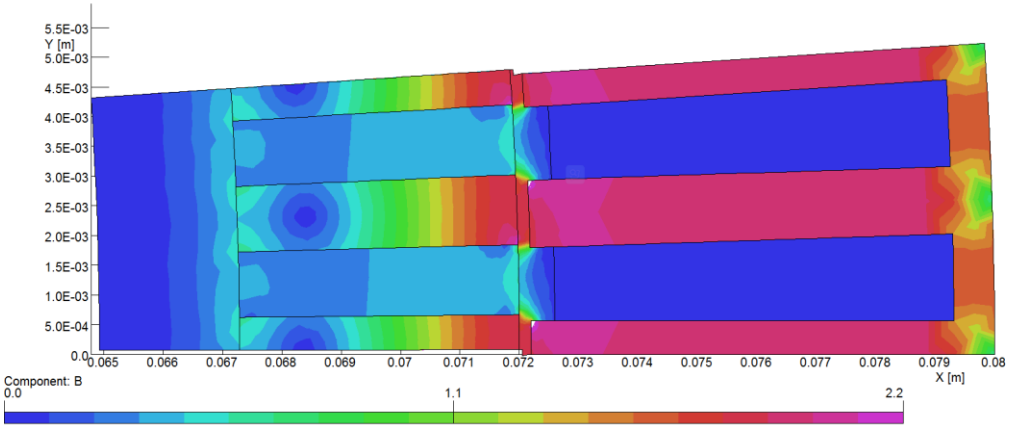

Figure 4.17 Open circuit flux density distribution in IPM machine with R_t=2 and airgap of 0.2mm (design 4.2.1)

The corresponding load voltage and power curves for designs which have identical stators but different values of R_t are shown in Figure 4.18(a) and Figure 4.18(b) respectively. As shown, for an R_t value of 2, the maximum output power output is ~135kW. This power is the electromagnetic limit and not necessarily realisable thermally on a steady-state basis. An indication of the practicality of these machines from a thermal perspective can be obtained by considering the current density in the stator conductors. As was the case for all the designs simulated previously in this chapter, for this particular stator, it is assumed that the conductors in all 192 slots (1 conductor per slot) are series connected. Each stator slot in this stator design has a cross-sectional area of 9.08mm^2. Assuming a coil packing factor of 0.8, the peak power of 11.5kW occurs at a DC average current of 118A for $R_t = 2$ corresponds to an average current density of 18.04A/mm^2 rms. A more pessimistic packing factor of 0.6, would increase this to 24.06A/mm^2 rms. Both of these values are likely to be higher than could be sustained in continuous operation. A reduction to 10A/mm^2 rms at a packing factor of 0.8 (equivalent to 13.3 A/mm^2 rms for a packing factor of 0.6) which is arguably more realistic in terms of a thermal performance corresponds to an average DC load current of 65.4A, still produces a load power of ~98kW.

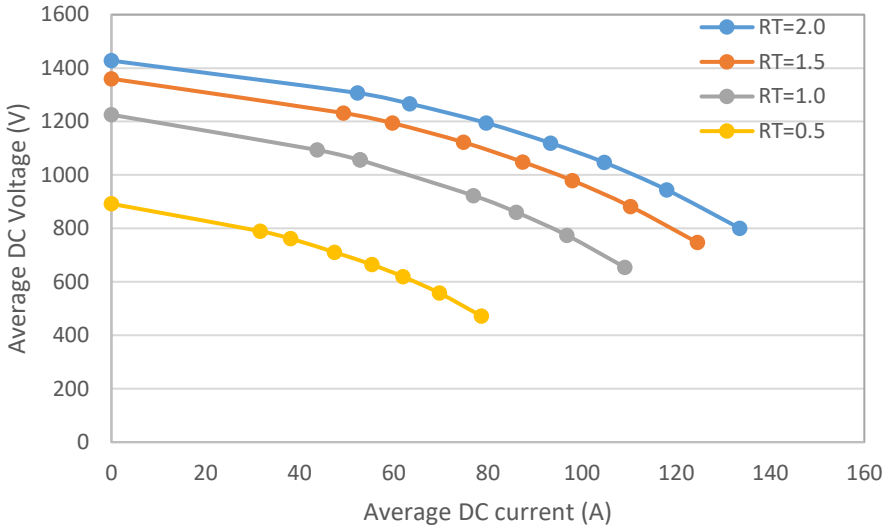

(a) Output V-I curve of the machine in different magnet depth/width ratio

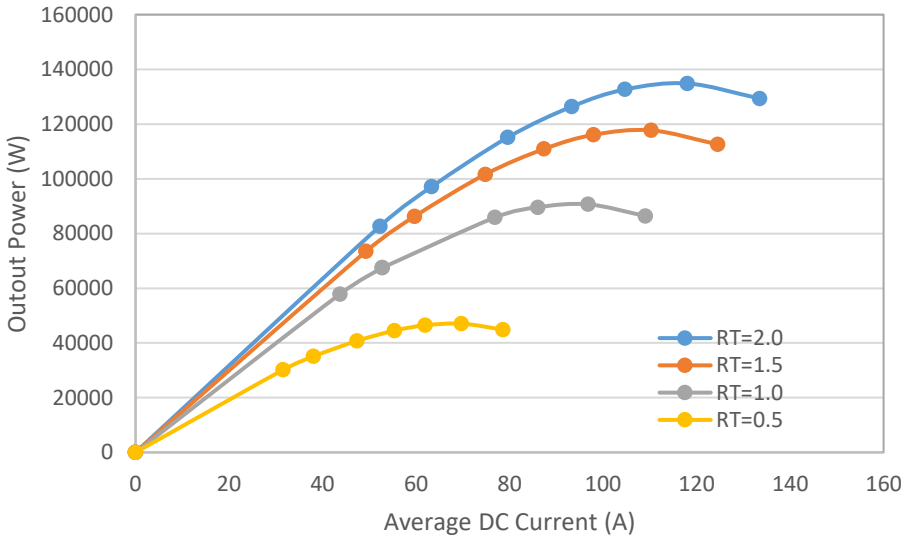

(b) Output power of the machine in different magnet depth/width ratio

Figure 4.18 Finite element predicted output performance of the machine in different magnet depth/width ratio (design 4.2.1)

Although the topology shown in Figure 4.14 with a value of Rt=2 provides excellent level of output power even with a reduced current density of 10A/mm^2 rms, it is still based on a very small airgap of 0.2mm. The large radial thickness of the magnet for Rt=2 is 4.71mm which inevitably means that retaining the magnets against centrifugal forces will require a potentially thick containment layer. It may be possible to incorporate some

retaining features on the inner surface of pole pieces which would lock into the non-magnetic rotor hub (e.g. fir-tree as in gas turbine blades [6]). However, this would not be possible for the magnets since they are very weak and their mechanical behaviour is unpredictable in tension. The thickness of a carbon fibre sleeve required to retain the magnets in the machine design of Figure 4.17 (which has a value of Rt=2) can be calculated using equation 4.1 shown previously. For a carbon fibre stress limit of 1GPa (which is at the upper end of the range that could be used), the thickness would vary between 0.51mm for loading by the magnet only (i.e. the pole pieces are completely retained by the mechanical retention feature into the hub) and 1.11mm assuming that both the magnets and the pole-pieces act as a deadweight on the containment sleeve.

The electromagnetic impact of such a thick non-magnetic sleeve was investigated by considering the impact of increasing the effective magnetic airgap from 0.2mm to 0.6mm. Figure 4.19 shows the open-circuit flux distribution for an airgap of 0.6mm which shows the significant leakage flux, both within the airgap and at inner edge of the magnet through the non-magnetic rotor hub. The resulting voltage versus current and load power versus current characteristics for different airgaps are shown in Figure 4.20. As will be apparent, there is a very significant reduction in performance with a non-magnetic containment sleeve even when it is only 0.6mm thick. Although even larger airgaps could have been considered, e.g. up to 1.2-1.4mmmm to accommodate the worst case of a 1.11 mm containment sleeve to contacting dead-weight iron pole-piece, the electromagnetic performance at 0.6 has deteriorated to the point where it is not a competitive solution.

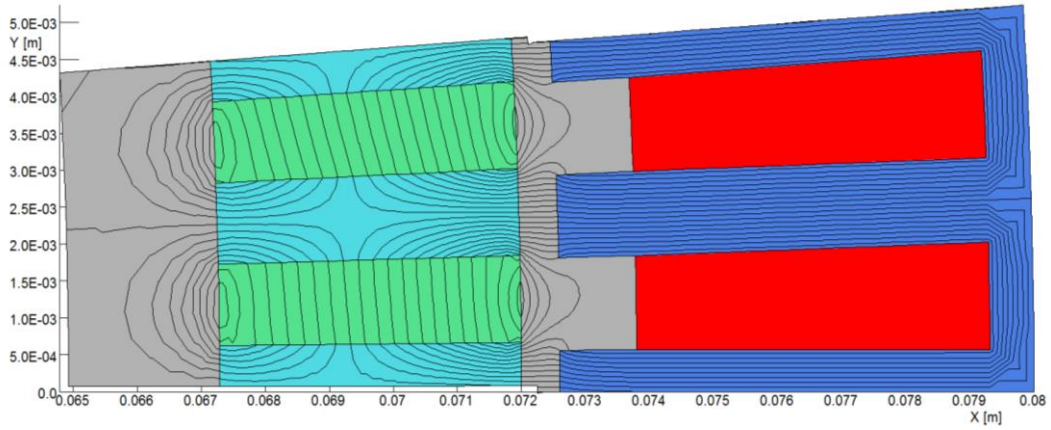

Figure 4.19 Finite element predicted field distribution in a design with an airgap of 0.6mm

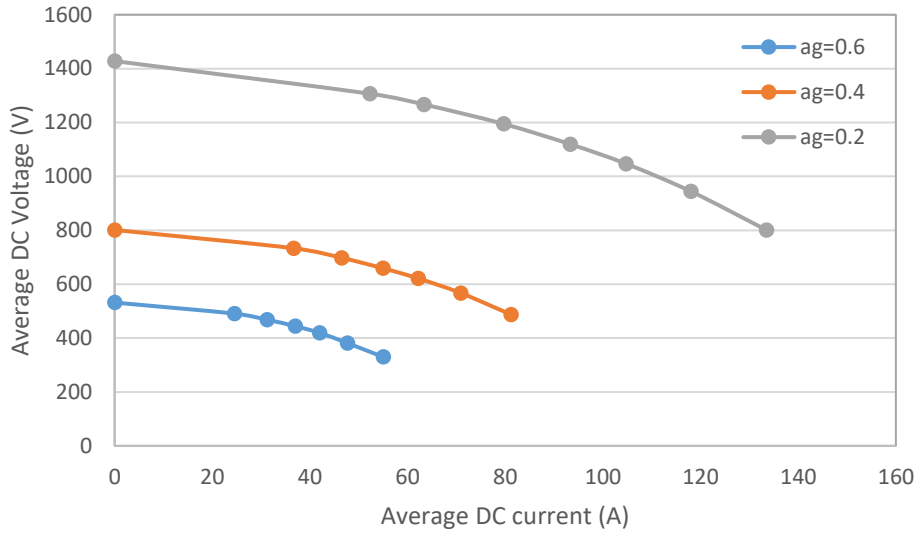

(a) Output V-I curve of a series of machines with different air gap lengths

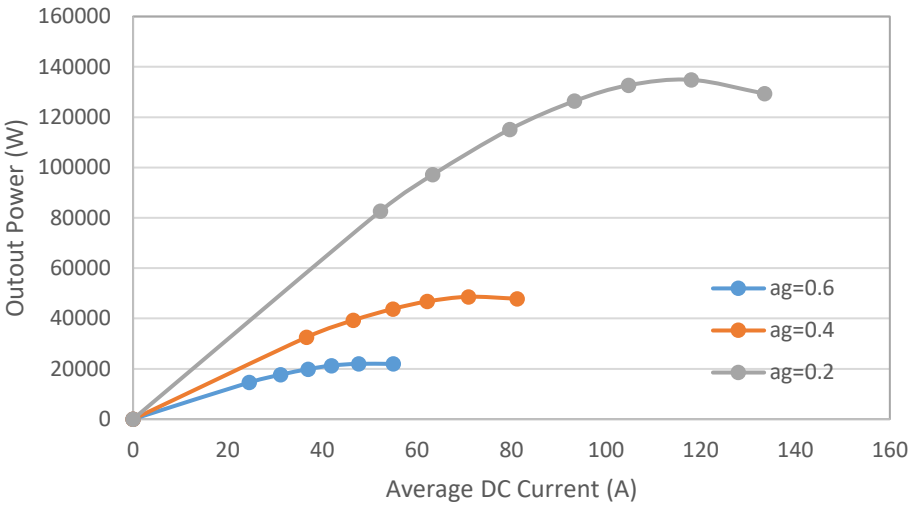

(b) Output power versus DC load current at a series of air gap lengths

Figure 4.20 Finite element predicted output performance of the machine in a series of air gap lengths (design 4.2.1-ag)

Rather than incorporating a separate sleeve to retain the magnets, the alternative rotor structure shown in Figure 4.21 was considered. This is an interior permanent magnet machine in which the rotor magnets are contained within the rotor core structure by bridges between the main rotor core pole-pieces, forming a single continuous rotor core. This type of rotor has the benefit of reducing the effective magnetic airgap to the permanent magnet flux passing across the airgap but at the expense of promoting leakage

flux within the bridge region outside each magnet. The bridge would need to be laminated because of slotting harmonics and would need to be high-strength soft magnetic material.

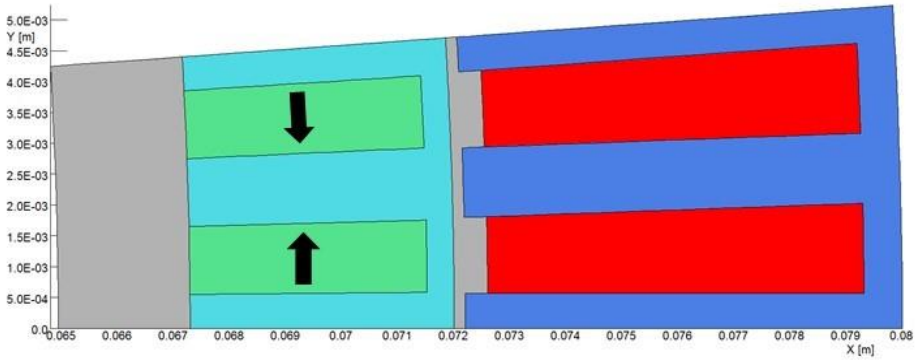

Figure 4.21 IPM topology with bridge structure (design 4.2.2 with bridge thickness of 0.48mm)

In selecting the radial thickness of the bridge region, there is a trade-off between mechanical strength and electromagnetic performance since the bridge acts as a magnetic short-circuit for some of the rotor magnet flux. Figure 4.22 shows magneto-static finite element predicted field distributions for bridge radial thickness of 0.16mm and 0.48mm which shows the tendency of significant magnet flux to pass through these regions rather than crossing the airgap and the high level of magnetic saturation that occurs in these bridge regions.

The corresponding flux density distributions are shown in Figure 4.23. The flux density in the stator tooth is a useful indication of the electromagnetic effectiveness of the rotor. As will be seen, with a bridge which is only 0.16mm thick, the bulk stator tooth flux density is ~ 1.5T under open circuit conditions, but this reduces to a corresponding value of 0.7T when the bridge thickness increases to 0.48mm. It is clear from Figure 4.21 that very high levels of flux density are encountered in the bridge sections in the rotor.

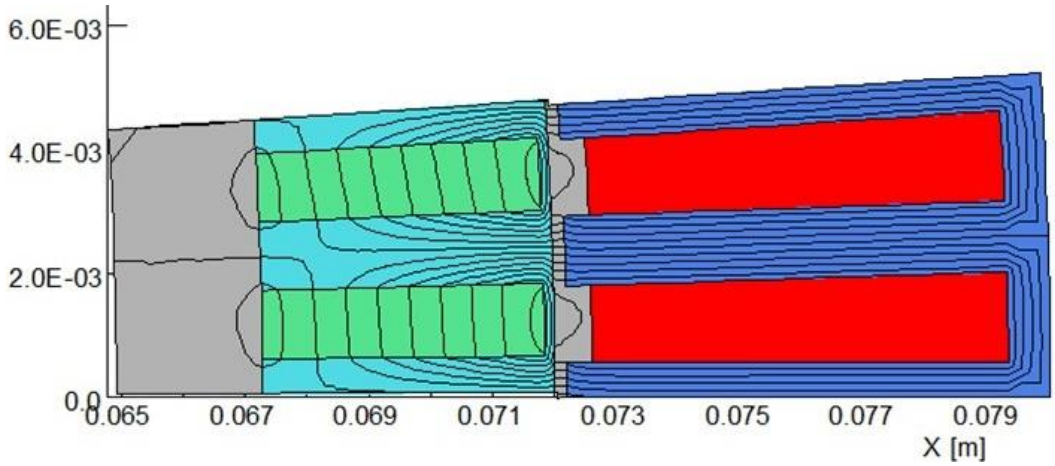

(a) Bridge thickness = 0.16mm

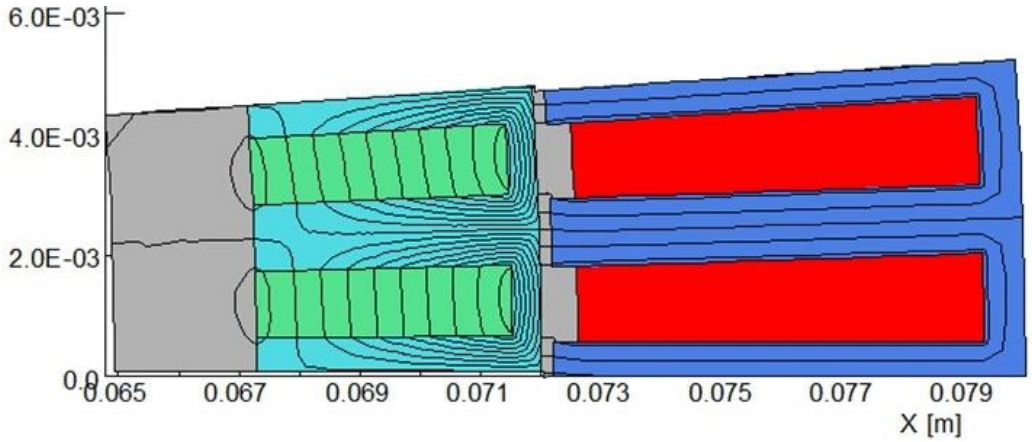

(b) Bridge thickness = 0.48mm

Figure 4.22 Finite element open-circuit predicted field distributions for an IPM design with bridge radial thicknesses of 0.16mm and 0.48mm (design 4.2.2)

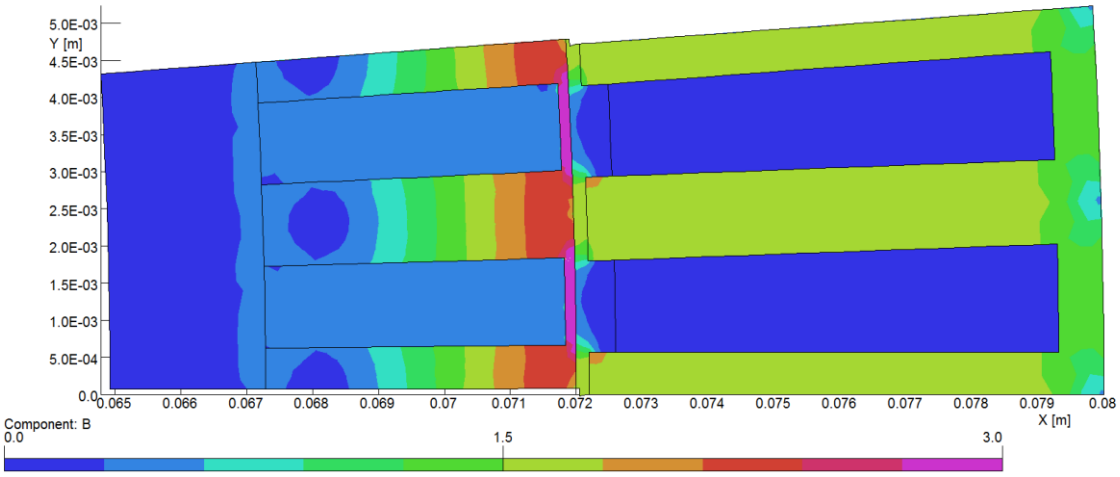

(a) Machine with 0.16 mm thick bridge

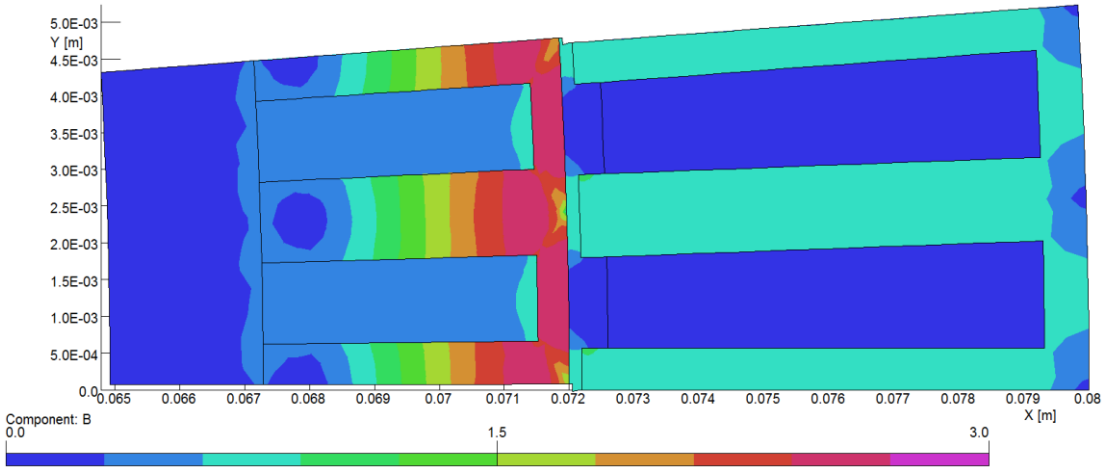

(b) Machine with 0.48 mm thickness bridge

Figure 4.23 Open circuit flux density in the machine (design 4.2.2)

The output voltage and power curves for a range of bridge thicknesses are shown in Figure 4.24. Although the machine is able to achieve a maximum load power output of greater than 50kW with a 0.32mm thick bridge, the power capability drops very significantly to 23kW for a modest increase in bridge thickness to 0.48mm.

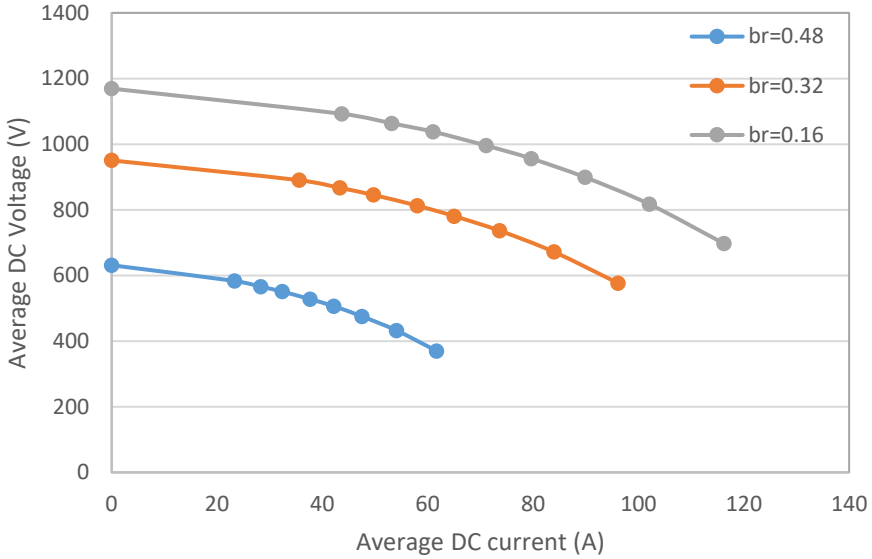

(a) Output V-I curve of a series of machines with different bridge thickness

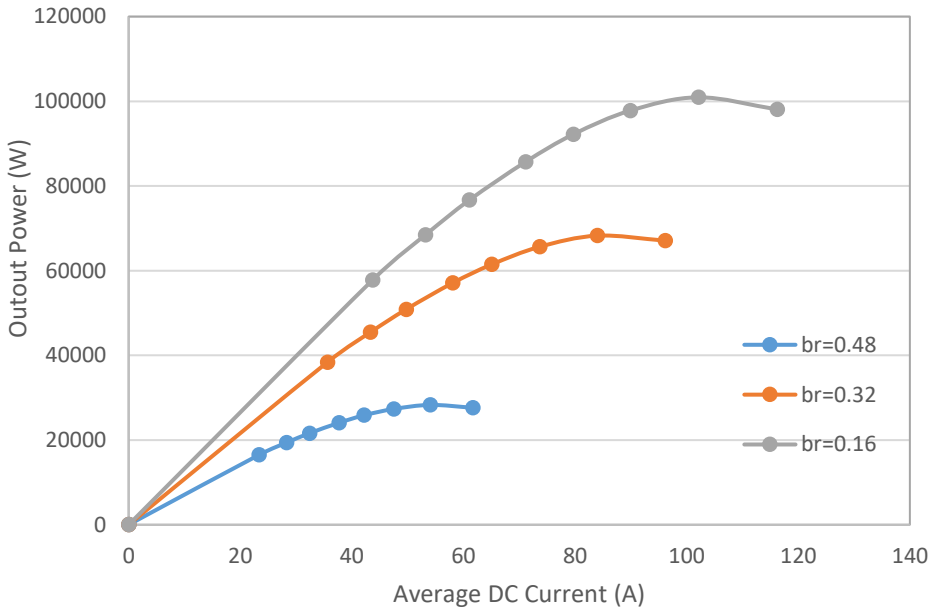

(b) Output power versus DC load current at a series of different bridge thickness

Figure 4.24 Finite element predicted output performance of the machine with different bridge thickness (design 4.2.2)

In an attempt to enhance the airgap flux density and hence maintain a competitive electromagnetic power density, a trapezoid magnet geometry was investigated. This geometry is shown in Figure 4.25 which used the same stator dimensions as that used in the designs of Figure 4.19. The main reason for using a trapezoidal magnet is to minimise

the flux linkage on the inner edge of the magnet. The open circuit magnetic field distribution and flux density variation in this machine are shown in Figure 4.25 and Figure 4.26, which shows that the trapezoidal magnet shape is effective in reducing the flux leakage through rotor hub. As a consequence, the flux density in both airgap and stator teeth were increased to competitive level compared with IPM with bridge.

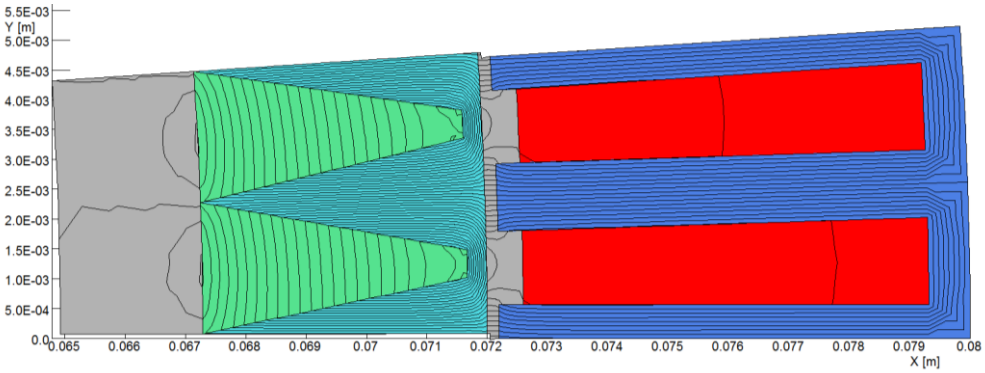

Figure 4.25 Open circuit flux distribution in Trapezoid magnet IPM machine

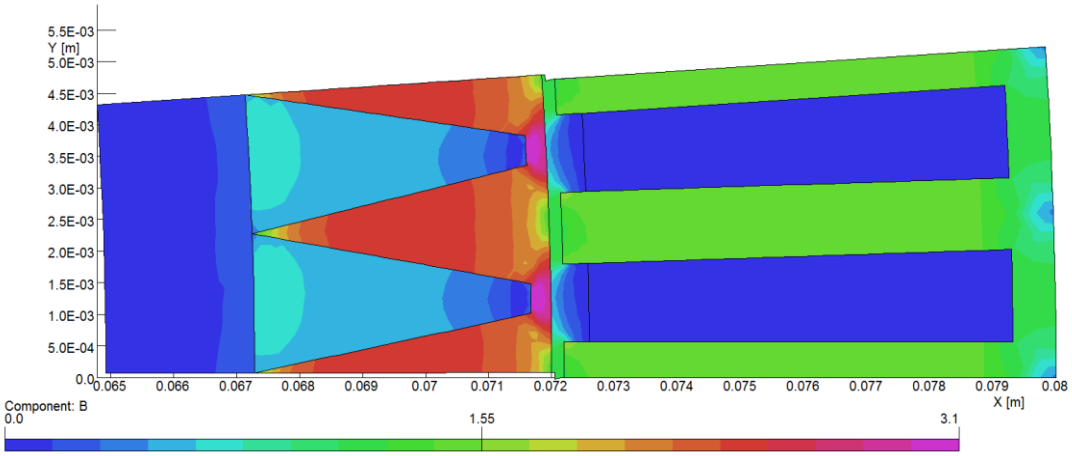

Figure 4.26 Open circuit flux density in Trapezoid magnet IPM machine (Br=0.32mm)

The corresponding output characteristics predicted with the electrical circuit coupled finite element model for this design are shown in Figure 4.27, again for the case of a single turn series wound coil. As will be apparent when Figure 4.27 is compared with Figure 4.22, the machine with trapezoidal magnets have a higher power capability than an IPM machine with the same bridge thickness, e.g. for a bridge thickness of 0.48mm, the maximum power capability increases from 83.4kW to 97.5kW. However, even with the trapezoidal magnets, when the bridge thickness is increased to 0.6mm, the output power capability falls dramatically to only 25kW.

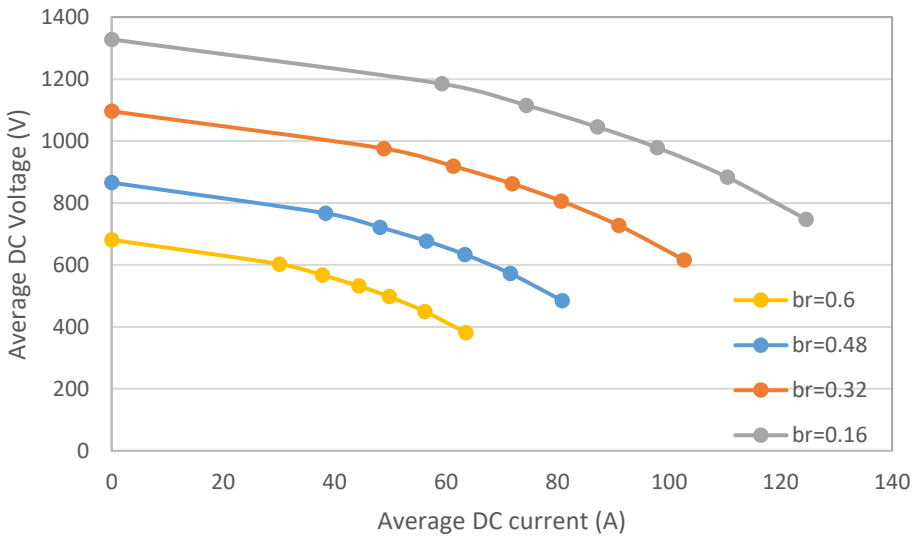

(a) Output V-I curve of the machine in different bridge thickness

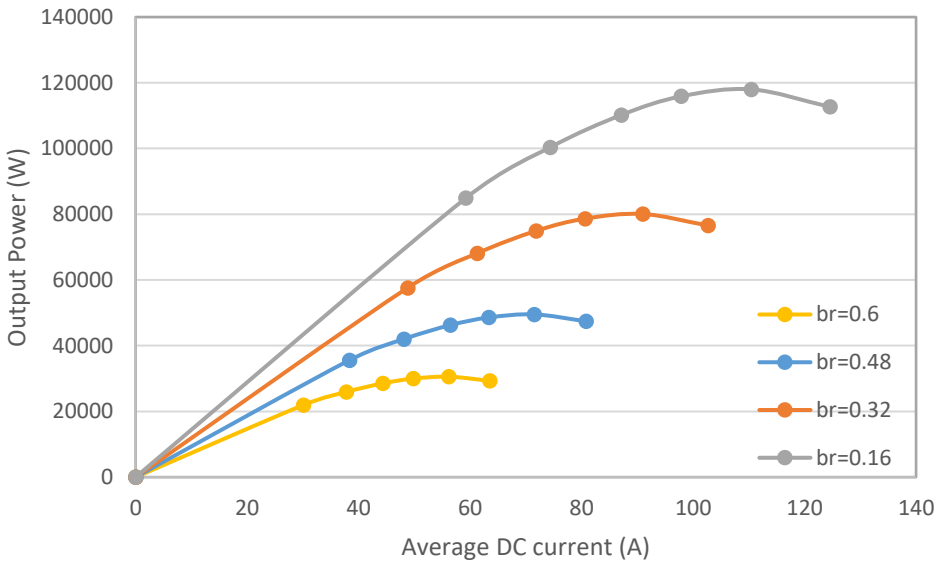

(b) Output power versus DC load current with different bridge thickness

Figure 4.27 Finite element predicted output performance of the machine with different bridge thickness (for trapezoid PM machine design 4.2.3)

The key to establishing the viability of an IPM machine in which Cobalt-Iron bridges retain the magnet is the stress in the bridge regions. In order to establish the mechanical viability of such thin bridge regions, a series of ANSYS simulations were performed at 20,000rpm for an IPM machine with trapezoidal magnets. The key mechanical properties

for Vacodur S+ Cobalt Iron which can be heat-treated to optimise the mechanical properties are shown in Table 4.5 which draws on published data from [7].

Table 4.5 Manufacturer data for physical properties of Vacodur S+ with heat-treatment to optimise mechanical properties

0.2% Yield strength	800MPa
Young's modulus	250GPa
Tensile strength	1200MPa

Initially the geometry shown previously in Figure 4.25 was modelled, but this resulted in very stress concentrations in the rotor core bridges around the outer corners of the trapezoidal magnets. To reduce the stress concentration a radius of 0.2mm was introduced into the narrow end of the magnet poles. The resulting Von-Mises stress distributions at 20,000rpm for 0.48mm and 0.60mm bridge thicknesses are shown in Figure 4.28. The maximum localised stress in all case occurs in the region of the rotor core near the outer edges of the magnets. It is interesting to note that the reduction in localised maximum stress from thickening the bridge is only from 596MPa to 560MPa, i.e. a 6% reduction in stress for a 25% increase in bridge thickness. Although the relative displacements of the rotor components are greatly exaggerated by scaling to aid clarity, the rotor hub and magnets would detach from the hub at these speeds. This could be eliminated by shrink-fitting the rotor core to the hub thus putting a significant compressive force on the magnets at standstill. If the correct level of pre-compression is applied, then this would result in the same stress levels in the rotor core bridges as shown in Figure 4.28 at 20,000rpm [5]. The predicted stresses in Figure 4.28 are well outside the capability of the rotor core material since the likely design stress in-service operation would be ~400MPa (based on a safety margin of ~2 applied to the 0.2% yield stress of 800MPa to allow for fatigue and manufacturing tolerances). Hence, this approach does not offer a viable solution from a mechanical perspective at 20,000rpm and also results in modest electromagnetic performance.

20°C

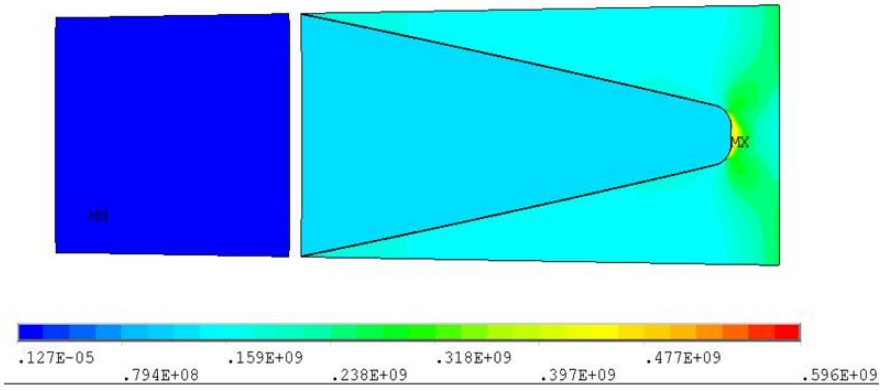

(a) 0.48mm thick rotor bridge

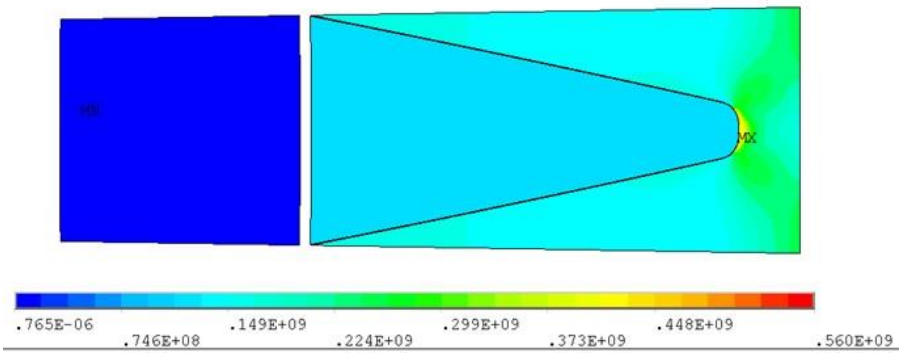

(b) 0.48mm thick rotor bridge

Figure 4.28 ANSYS finite element predicted Von-Mises mechanical stress in rotor at 20,000rpm.

Some of these interior rotor machines, when constrained to the same stator outer diameter of 160mm and axial length of 50mm, as the baseline SPM described in section 3.1, show superior electromagnetic power capability, e.g. 80-90kW, although this is for small airgaps of 0.2mm and/or narrow magnet bridge in 0.16mm. However, the electromagnetic power diminishes significantly with only small increases in the length of the airgap thickness of the bridging sections of the rotor cores, such that more practical mechanical arranges are not capable of meeting the 50kW output power specification. However, it is important when considering these designs to recognise that for the higher split ratio of 0.9 with the same 160mm stator outer diameter, the mass of the active elements is considerably lower than the baseline for the same axial length, e.g. 2.62kg in the case of a 192 pole machine with a split ratio of 0.9 compared to 4.77kg for the baseline. Hence, to provide a direct comparison, it would be reasonable to increase the axial length of the 0.9 split ratio machines from the 50mm of the baseline to 91mm to yield the same active mass. This would scale the powers obtained in Figure 4.28(b) for example by a

factor of 1.82. Applying this scaling to a machine with a 0.6mm thick bridge, increases the power capability to 55.6kW for a DC average load current of 56.2A which corresponds to a current density 8.6A/mm^2 rms for a packing factor of 0.8 increasing to 11.5/mm^2 rms for a packing factor of 0.6.

Despite the promising electromagnetic performance of many designs with an internal rotor, the need to increase the effective magnetic airgap to at least 0.6mm (and arguably greater to maintain a practical mechanical clearance in a high speed machine) results in a large reduction in performance. Hence, the focus on the design was shifted to external rotor machines.

4.2 Design of External rotor machine

The analysis in section 4.1 has shown that although the various internal rotor topologies investigated are capable of producing a rectified output power which exceed the power specification of 50kW, this is only realised with very small magnetic airgaps of <0.5mm. As discussed previously, the need to mechanically contain the rotor magnets with a sleeve means that this topology is unlikely to be a practical solution for high-speed machines of such high pole numbers. One potential solution to change to an external rotor topology in which the magnet containment is located outside the rotor and hence does not sit in the airgap. The containment sleeve thickness can then be dimensioned to contain the magnet reliably with an appropriate safety margin with no first-order electromagnetic implications. Figure 4.29 shows a typical design of a 96 pole-pair IPM machine with an external rotor, in this case with a split ratio of 0.9. It is worth noting that in this topology, the stator slot depth is not set by the split ratio (as is largely the case with an internal rotor machine). Hence, there is likely to be some optimisation of slot depth required in terms of a trade-off between mass, current density and stator reactance.

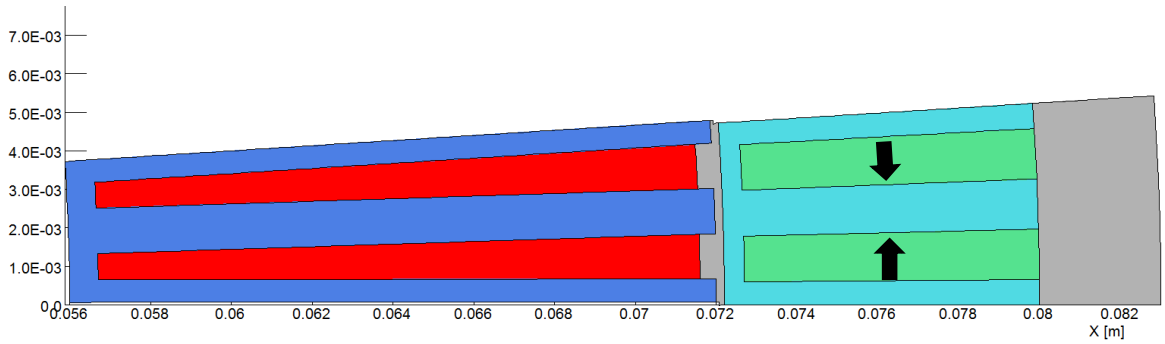

Figure 4.29 External rotor machine topology with an interior permanent magnet rotor geometry (design 4.3.1)

For the machine design shown in Figure 4.29, the split ratio (airgap diameter to outer rotor diameter) was maintained at 0.9. It is useful to define the rotor dimensions in terms of the stator hub ratio (inner stator diameter/ outer rotor diameter) and this was initially set to 0.7. The same grade of Cobalt Iron was used for the stator core. However, although the rotor iron does not need to counter the centrifugal force on the magnets, it may still be useful to have a bridge between the iron pole pieces to produce a single piece rotor core.

Four types of rotor structures were explored for this machine and are shown in Figure 4.30. Type A and type C employ rectangular iron pole pieces while type B and type D employ trapezoidal pole-pieces. As shown in Figure 4.30, rotor types A and B have a bridge adjacent to the airgap side, when type C and type D put bridge on outside edge of the rotor. In all cases, the bridge thickness was fixed at 0.5mm. The outer diameter of active section of the rotor was maintained at 160mm and the same axial length of 50mm was also maintained.

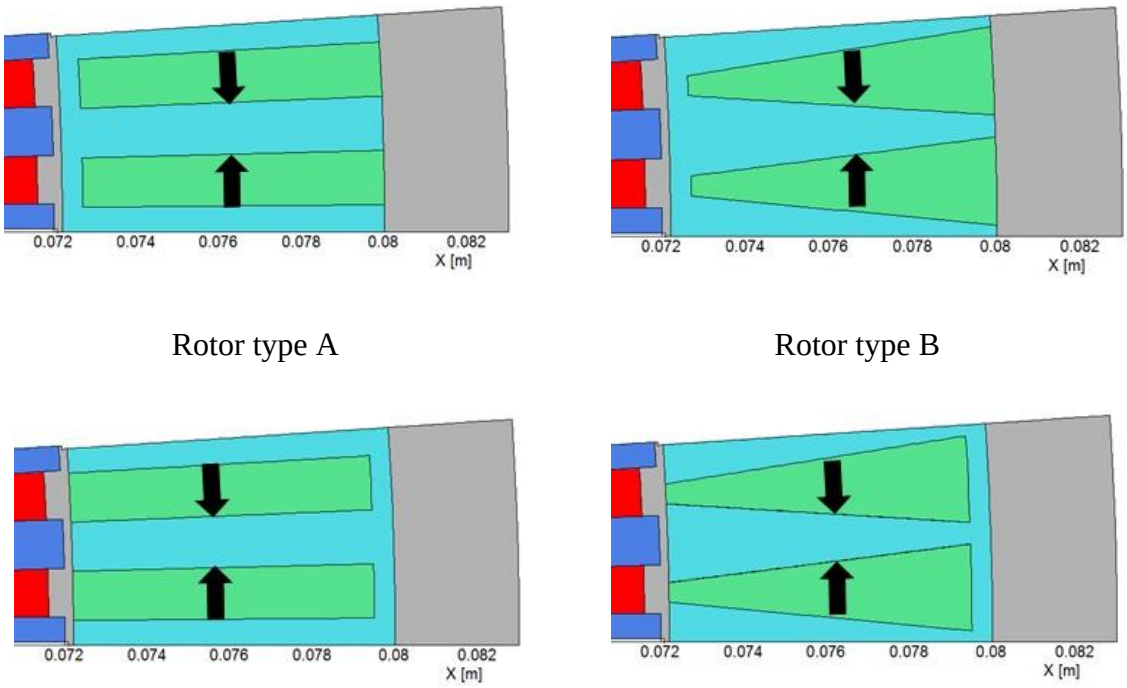

Figure 4.30 Four rotor structures considered in analysis (designated as design 4.3.1-4.3.4) – Stator core -dark blue; Rotor magnet - green; Stator coil - red; Rotor core – light blue; Rotor mechanical containment – grey)

The finite element predicted voltage and power curves for these four designs are shown in Figure 4.31, again with a single turn per slot. As will be seen, despite these designs having the same leading dimensions, the location of the soft magnetic bridge has a very significant effect on the power capability of the machines. Types C and D which employ bridges on the outer edge of the rotor provide competitive power even though these still provide a magnet flux short-circuit path.

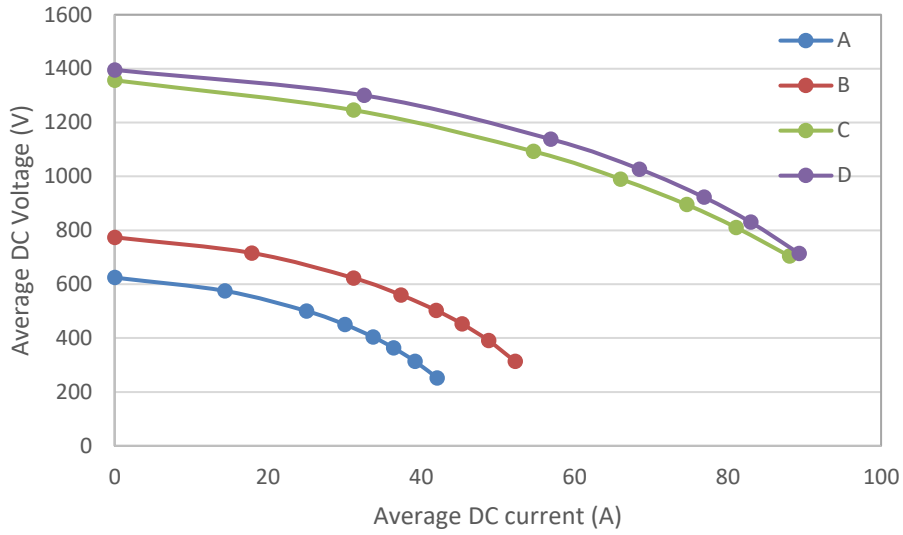

(a) Output V-I curve of the machine in different rotor type

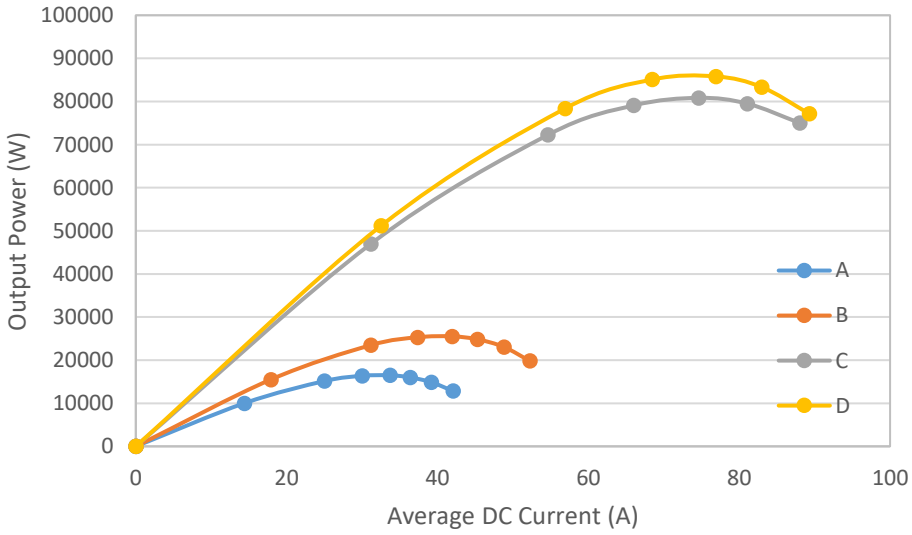

(b) Output power versus DC load current for the machine in different rotor type

Figure 4.31 Finite element predicted output performance of the machine (design 4.3.1-4.3.4 as shown in Figure 4.30)

The stator teeth in the external rotor design shown previously in Figures 4.29 and 4.30 are based on stator teeth with constant width. This results in a gradual narrowing of the slot with increasing slot depth. In order to accommodate rectangular rolled Litz wire into this type of a slot, it would be necessary to size the wire on the basis of the minimum slot width which would result in a gradually increasing triangular void in the slot. This under-utilisation of the slot would result in an increased copper loss. An alternative approach is

to design the stator with a fixed slot width. This is results in a gradual narrowing of the stator core tooth which it is recognised will increase the stator core loss. A stator design based on a parallel sided slot is shown in Figure 4.32, in this case for a stator hub ratio of 0.7.

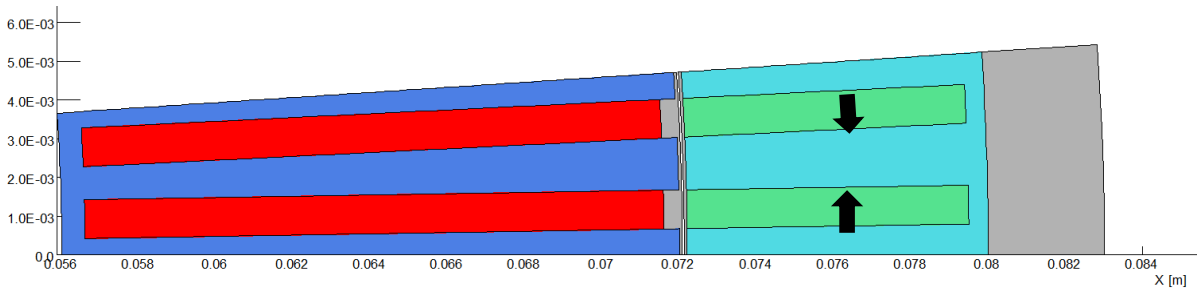

Figure 4.32 External rotor machine with a parallel sided stator slot (design 4.4.1). Stator core -dark blue; Rotor magnet - green; Stator coil - red; Rotor core – light blue; Rotor mechanical containment - grey

The stator also can also be optimised by varying the stator slot depth, which can be simply achieved by changing the stator hub ratio (i.e. the ratio of the stator hub diameter to the overall machine diameter) while keeping the airgap, rotor inner and outer diameter fixed. When the stator hub ratio is increased, the length of stator tooth and the hence the depth of the stator slot decreases. This has three advantages and one disadvantage:

- The cross-slot leakage flux will reduce, which reduce the stator self-inductance and hence the stator reactance which will improve the voltage regulation.
- If there is the any magnetic saturation in the stator core, reducing the flux path length will reduce the effect on the stator magnetic reluctance and so reducing the influence of magnetic saturation on the stator flux-linkage.
- It will tend to reduce the stator iron loss because of the reduced stator tooth volume.
- The reduced slot area will increase the current density and hence losses for a given stator ampere turns.

Figure 4.33 shows the electromagnetic performance of a series of machine designs with a range of different stator hub ratios from 0.7 (previous design shown in Figure 4.32) to 0.8, (denoted as design 4.4.1-4.4.3 in sequence).

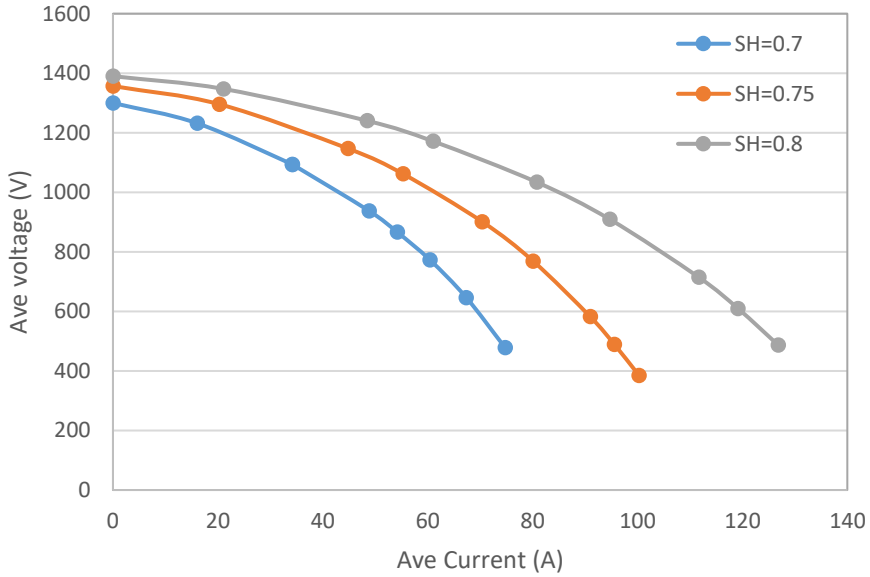

(a) Output V-I curve of the machine with a series of different stator hub ratio

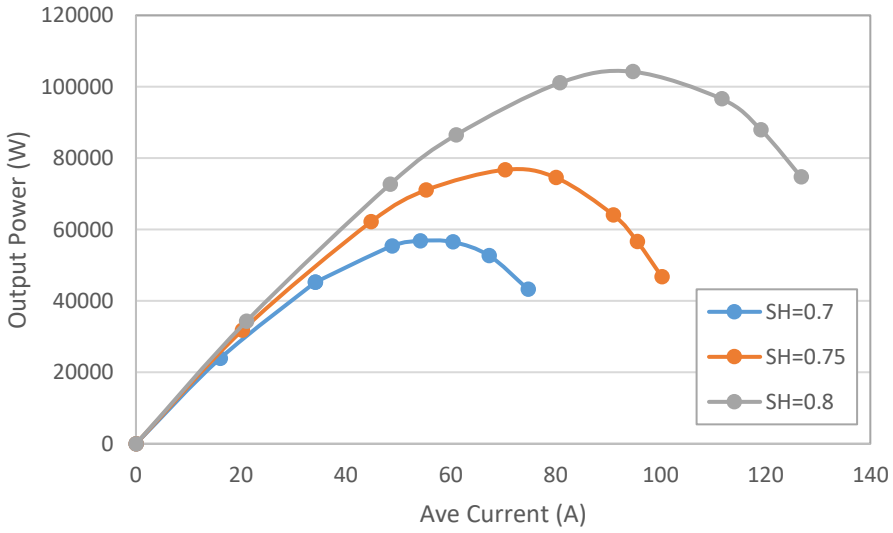

(b) Output power with different stator hub ratio

Figure 4.33 Finite element predicted output performance of the machine (design 4.4.1-4.4.3)

As shown in Figure 4.33, as the stator hub ratio increases from to 0.70 and 0.8, the maximum power increases from 56.8kW at a current of 54A to 104.2kW at a current of 94.7A respectively. However, due to combination of the higher current at the maximum power point and the shallower slots, there is a significant increase in the current density for the shaft hub ratio of 0.8. The slot depths are 15mm, 10.4mm and 6.4mm for stator

hub ratios of 0.7, 0.75 and 0.8 respectively). For a stator hub ratio of 0.7 operating at its maximum power point with a DC average output current of 54A (corresponds to an rms machine current of 60.0A) then at a packing factor of 0.8 the current density in the conductors is 5.0A/mm^2 rms. When the stator hub ratio is increased to 0.8 with a maximum operating point current of 95A, the rms current density in the machine for a packing factor of 0.8, increases to 20.6A/mm^2. The corresponding current densities at a coil packing factor of 0.6 are 6.7 A/mm^2 and 27.5A/mm^2 respectively. It is also worth noting however that a lower value of stator hub ratio leads to longer stator teeth and hence an increased core loss.

4.3 Evaluation of iron loss and candidate core materials

The analysis up to this point has been concerned with the electromagnetic power limit of the machines, which is determined predominantly by the combination of induced EMF and coil reactance, and some consideration of the current density in the stator coil. It has been shown that from a maximum power capability. However, it is also necessary to establish thermal limitations on the achievable power as these may well be lower than the electromagnetic limit. The combination of a very high fundamental frequency and high stator flux densities in the machines considered previously means that iron loss will be a particular concern. It is also worth noting that the use of a diode rectifier will lead to some distortion of the machine current.

Figure 4.34 shows a representative machine-side current waveform, in this case for design 563 at its peak power of 104.2kW at a DC average load current of 94.7A (corresponding to a peak AC machine current of 149Apk). The waveform of Figure 4.34 contains relatively little harmonic distortion and evidenced by an FFT which gives 3rd, 5th and 7the harmonic magnitudes of 2.26A, 1.83A and 0.42A. In the calculation of iron loss described later in this chapter, the use of a circuit-coupled finite element model ensures that these harmonics in the current waveform are included in the loss calculation.

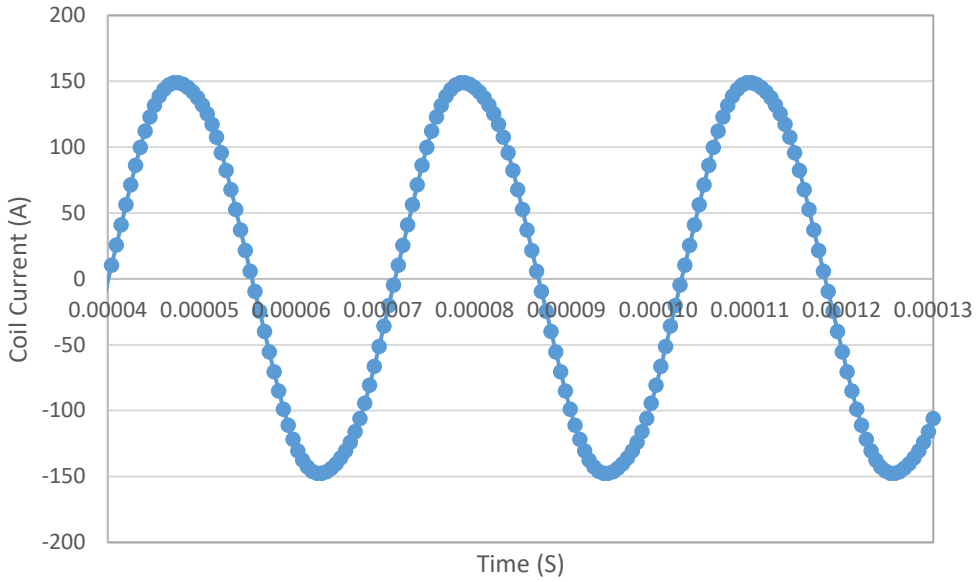

Figure 4.34 Predicted machine current waveform for design 4.4.3 at its peak power operating point of 104.2kW

The analysis presented up to this point in this chapter has been based on stator cores with Vacoflux 50 cores which is the same material as that used in the baseline machine design of chapter 3. As noted in chapter 3, this is a high performance soft magnetic material which is widely used in aerospace electrical machines because of its combination of low iron loss and high saturation flux density. This section describes the properties of several alternative soft magnetic materials that might be more suitable for the stator core in this high frequency application and predicts machine performance for the most promising materials.

In the high frequency applications, iron loss tends to be dominated by the eddy current component of loss. There are two fundamental approaches to reducing eddy currents in magnetic cores:

1. Modify the composition of the material to increase electrical resistivity, e.g. by add silicon or other alloying elements.
2. Modify the geometry of the individual soft magnetic elements, e.g. through the use of very thin laminations or the use of cores manufactured from electrically insulated powder particles.

Soft magnetic composites (SMCs) in which a ferromagnetic powder is bonded together to form a net-shape component is a technology which is well suited to high frequency

applications in which the losses are likely to be dominated by eddy current loss. Hence, the focus in this design optimisation was establishing either a soft magnetic composite which offers a lower loss than the Cobalt Iron baseline design.

4.3.1 Soft magnetic composites

In a soft magnetic composite (SMC), particles of very fine soft magnetic powders are bonded together with some form of binder to form a net-shape soft magnetic component. In some cases, this type of material is referred to as powdered-iron or powder cores. Although they have generated significant interest in recent years, they have been proposed for more than 100 years [8]. Whereas powdered iron cores with permeability of a few 10s have been around for many years, it is only since the 1990s that SMCs have been developed for electrical machines with permeabilities of several hundred [9]. Figure 4.35 shows a schematic representation of an SMC. It consists of an iron powder coated with organic insulation which are the pressed under a high pressure (typically up to 800MPa [10]) to achieve near full density (typically up to 98-99% dense). Careful control of the pressing and processing is required in order to maintain the insulation layer between iron powder particles (to retain a high electrical resistivity) while also ensuring near full density (in order to achieve a relative permeability of several hundreds).

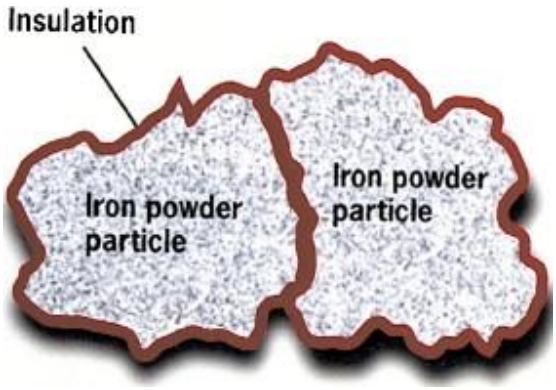

Figure 4.35 Schematic picture of component elements of SMC material (Source: [10])

The hysteresis loss in SMCs tends to be higher than in electrical steel laminations because of the significant mechanical stresses which are applied to the iron particles during pressing which cannot be relieved by annealing at high temperature as this would damage the binder. However, since the individual iron particles remain largely insulated from each other, the eddy current loss tends to be lower than a laminated electrical steel.

Figure 4.36 shows published guidance on the operating range of SMCs which demonstrates that they offer a greater useable frequency range that SiFe lamination, and potentially in the 10s of kHz range, albeit at lower flux densities [11] [12]. In this section, several SMC materials which offer a range of properties are reviewed, viz. Somaloy 130i 5P, CSC high flux 125µ and CSC mega flux 60µ.

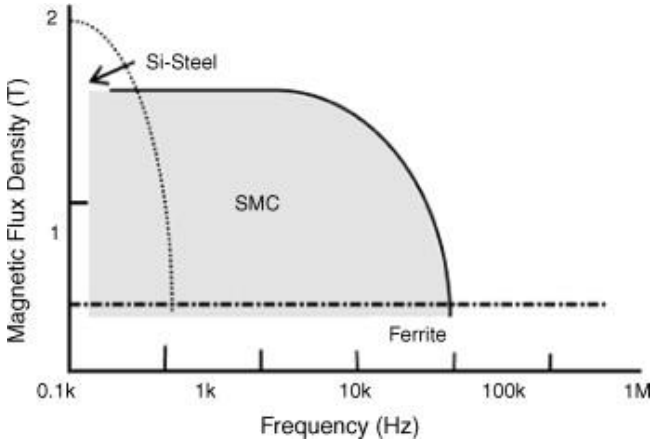

Figure 4.36 Manufacturer published operating range for SMCs (Source: [11])

4.3.1.1 Somaloy 130i 5p

Somaloy is a commercially produced family of grades of SMC material manufactured by Hoganas. It contains three product groups, in which Somaloy 5P materials has lowest iron losses [13]. One specific grade which is evaluated in this project is Somaloy 130i 5P which has a maximum relative permeability of 350 and a material bulk electrical resistivity of 20000 µΩm. This is highest electrical resistivity in the Somaloy product family (as of 2018) but this is gained at the expense of a reduced permeability compared to other grades which are better suited to lower frequency applications. Figure 4.37 shows manufacturers key performance data for Somaloy 130i 5P.

Somaloy material	Density [g/cm³]	Resistivity [µOhm m]	TRS ambient [MPa]	B@ 10000 A/m [T]	μ_{max}	Core losses [W/kg]				
						Cross-section 5x5 mm				15x15 mm
						100 Hz 1 T	1 kHz 1 T	5 kHz 0.5 T	10 kHz 0.1 T	1 kHz 1 T
Medium particles #100										
Somaloy 130i 5P	7.44	20000	35	1.47	350	8.0	93	205	24	94

Figure 4.37 Manufacturer published key magnetic data for Somaloy 130i 5P (Source: [13])

Figure 4.38 shows the manufacturer published magnetisation curve for Somaloy 130i 5P. The material is fully saturated at ~ 2T with the onset of significant saturation from ~1.5T

onwards. In the product data sheet for this material, the manufacturer provides a simplified loss estimation model for this material with accompanying material coefficient as shown in Figure 4.39.

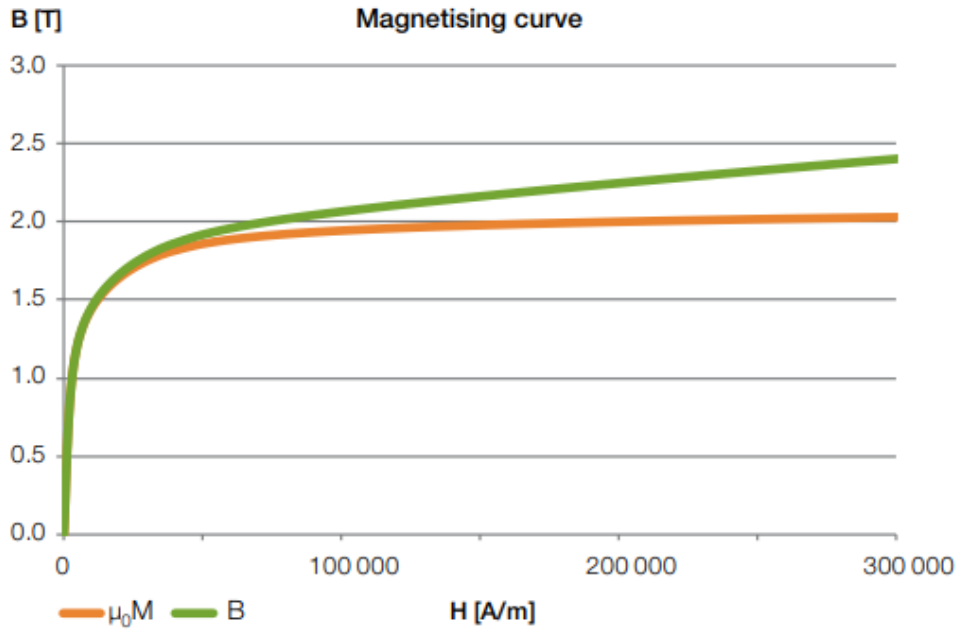

Figure 4.38 B-H curve of Somaloy 130i 5P material (Source: [13])

Loss model			
K_h	0.079	K_{ep}	0.000014

$$P_{tot} = K_h * f * B^{1.75} + K_{ep} * f^2 * B^2 + \frac{B^2 * f^2 * d^2}{1.8 * \rho * resistivity * 1000} \quad [W/kg]$$

Model is verified up to 0.5T-1.5T and 5000Hz.

K_h Hysterisis loss coefficient K_{ep} In particle eddy current coefficient

f Frequency [Hz] B Field strength [T]

ρ Density [g/cm3] resistivity [μΩm]

d Smallest cross section of component [mm]

Figure 4.39 Iron loss estimation model for Somaloy 130i 5P material (Source: [13])

4.3.1.2 CSC Powder Core High Flux 125u/Mega Flux 60u

An alternative type of soft magnetic composite cores are the various powder composites with more modest relative permeability (usually <200). These are manufactured in a

similar manner to the Somaloy composites, but with a lower pressing force. Hence, they do not achieve the same density and hence relative permeability as Somaloy but they do maintain better insulation integrity and hence have higher electrical resistivity. The Chang Sung Corporation (CSC) produce four types of soft magnetic composite cores: MPP (Ni-Fe-Mo powder); High Flux (Ni-Fe powder); Sendust (Fe-Si-Al powder); Mega Flux (Fe-Si powder). The main magnetic properties of these materials is summarised in Figure 4.40. Of the materials listed in Figure 4.40, High-Flux and Mega-Flux powder composites are the best fit in terms of electrical machine applications.

Comparison of Core materials

Materials		Perm. (μ_R)	Bs (G)	Core Loss	DC Bias	Relative Cost	Temp. Stability	Curie Temp (℃)
Powder	MPP	14-200	7,000	Lower	Better	High	Best	450
	High Flux	26-160	15,000	Low	Best	Medium	Better	500
	Sendust	26-125	10,000	Low	Good	Low	Good	500
	Mega Flux®	26-90	16,000	Medium	Best	Low	Better	700
	Iron	10-100	10,000	High	Poor	Lowest	Poor	770
Strip	Fe-si (Gapped)		18,000	High	Best	Lowest	Good	740
	Amorphous (Gapped)		15,000	Low	Better	Medium	Good	400
	Ferrite (Gapped)		4,500	Lowest	Poor	Lowest	Poor	100~300

Figure 4.40 Comparison of commercial powdered iron (Source: [14])

CSC High Flux is a series of Fe-Ni powder cores with a magnetic saturation level of ~1.5T (denoted as 15,000 Gauss in Figure 4.40). Of particular relevance to this application is that Mega Flux and High Flux are available in large circular cores up to 200mm or so in diameter which would allow a core for the candidate designs considered in this chapter to be manufactured from a single piece or a stack of cores, i.e. no segmentation within the cross-section. The values of relative permeability listed in Figure 4.40 span a large range to recognise that the permeability reduces significantly with DC magnetizing field strength as magnetic saturation starts to play a role as shown in Figure 4.41. The manufacturer published variation in core loss with flux density at a series of frequencies are shown in Figure 4.42. A key requirement for this application is the availability of commercial cores that are large enough to produce the stator core, ideally as a single piece. CSC High Flux 125μ is both the highest permeability product in this series and available in large toroidal cores suitable for machining a full stator core from a single piece.

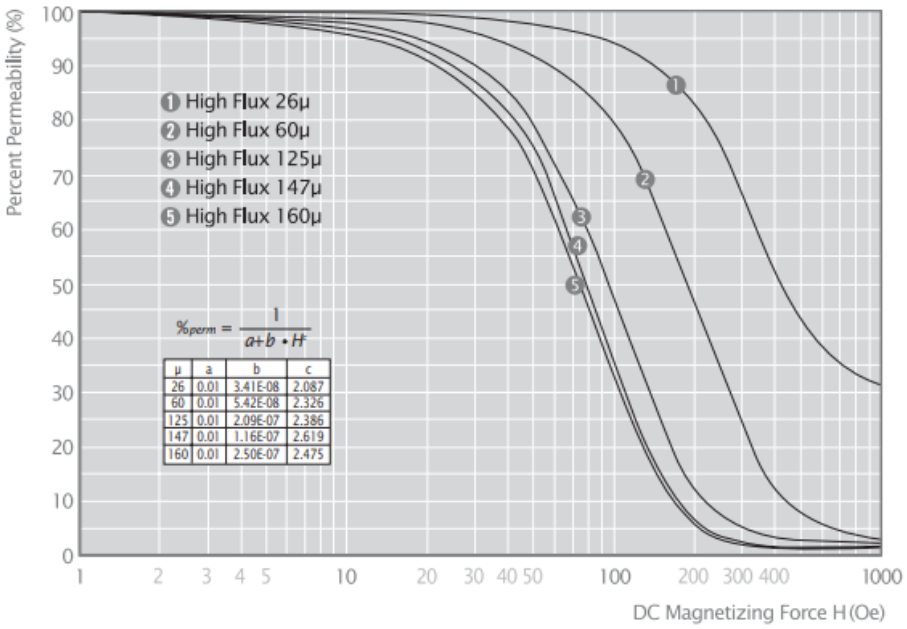

Figure 4.41 Manufacturer published permeability vs DC Bias Curves for High Flux 125µ powder core (Source: [14])

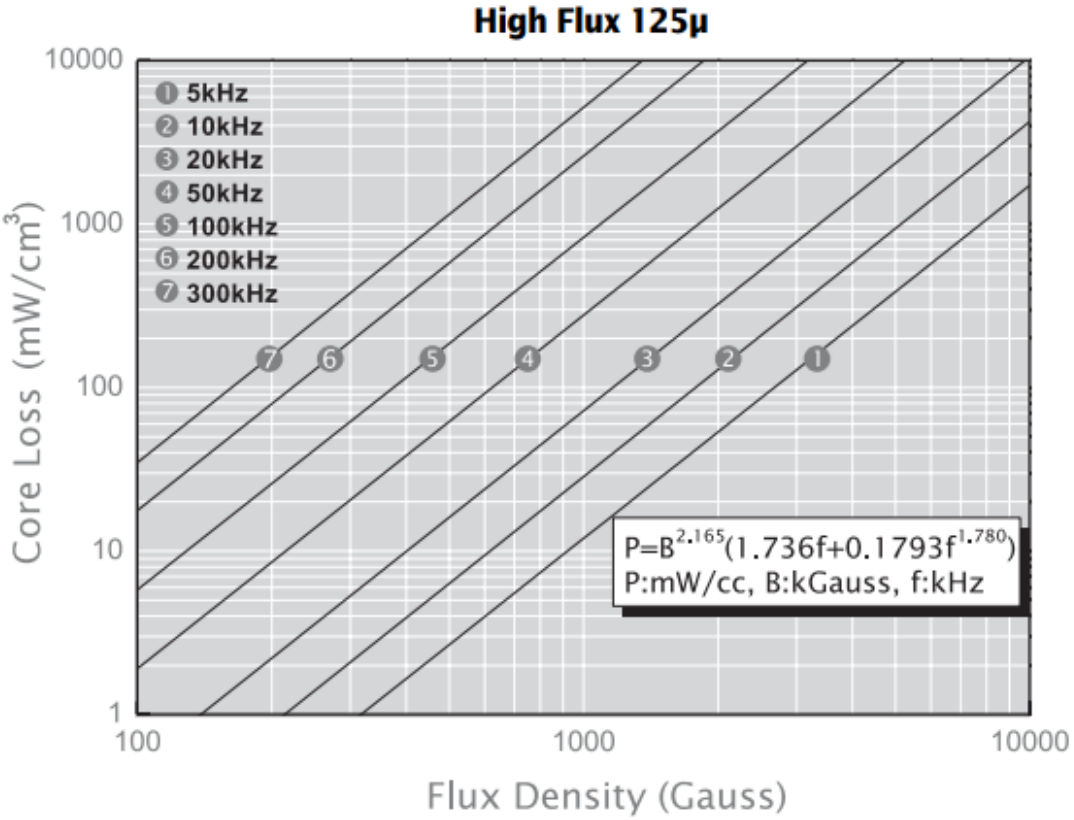

Figure 4.42 Manufacturer published variation in iron loss for High Flux 125µ powder core (Source: [14])

CSC Mega-Flux core is a series of core consisting of pressed Fe-Si alloy powder with non-organic insulation, which has higher flux saturation level of 1.6T (16,000 Gauss) and improved permeability compared to CSC High Flux cores. There are no thermal aging effects in this core, which gives it excellent thermal performance [14]. However, the iron loss performance of CSC Mega Flux is inferior to that of a corresponding CSC High Flux Core. CSC Mega Flux 60μ is the highest permeability product in this series which is available in the required size. Figures 4.43 and 4.44 show the corresponding permeability and iron loss characteristics for this material.

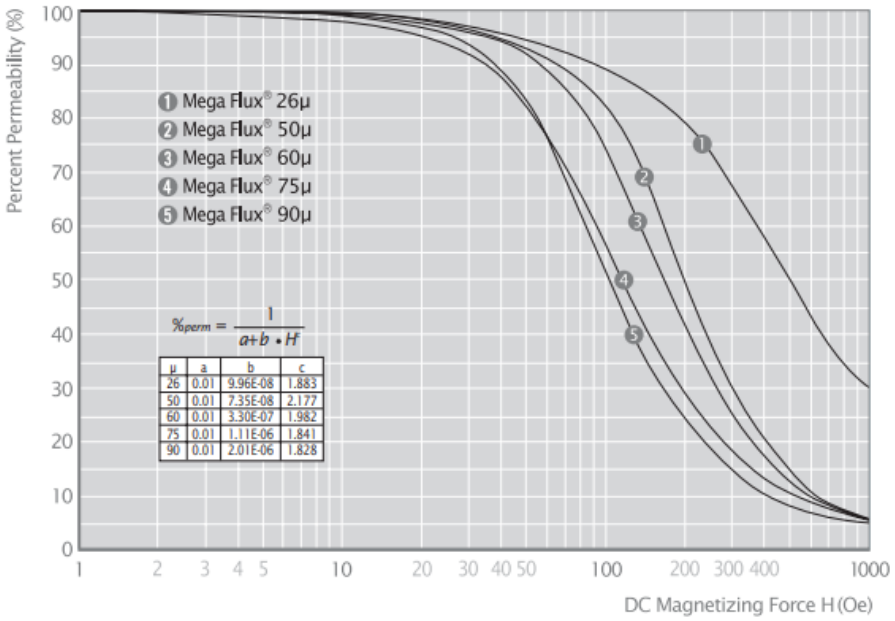

Figure 4.43 Manufacturer published permeability vs DC bias curves for PCMF (Mega Flux powder core) (Source: [14])

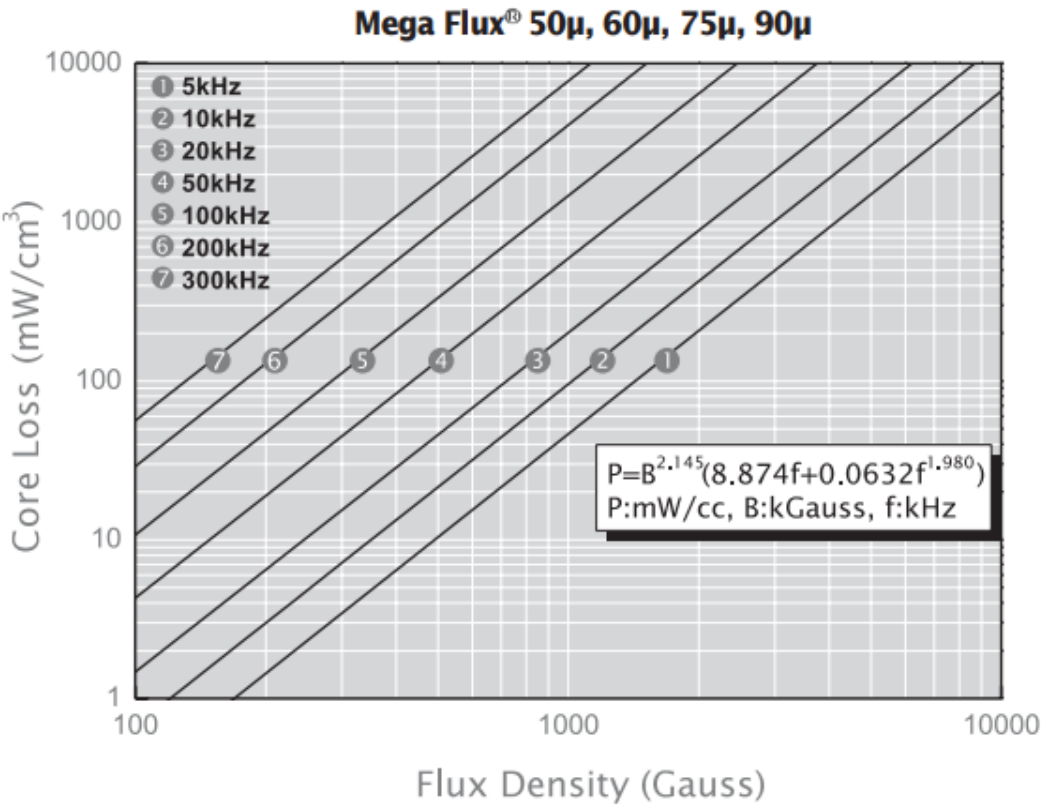

Figure 4.44 Manufacturer published variation in iron loss model for Mega Flux powder core (Source: [14])

4.3.2 Machine performance with SMC core materials

External rotor machine design 4.4.2 and 4.4.3 i.e. machines with stator hub ratio (SH) of 0.75 and 0.8 respectively, were modelled with a series of different stator core materials. The original designs for these designs, which were modelled previously in this chapter were based on Vacoflux 50 Cobalt Iron. All the designs were based on direct substitution of the stator core material with no modifications to dimensions to allow for any limitations of the various materials. The available area of one slot for stator hub ratios of 0.75 and 0.80 are 10.4mm^2 and 6.4mm^2.

The resulting variation in output power with 3 grades of SMC type material (Somaloy 130i5p, PCHF125 and PCMF60) are shown in Figure 4.45 along with the corresponding power curve for the original Vacoflux 50 design. In all cases, these characteristics are based on a single-turn in each slot. As would be expected given the direct substitution method adopted, there is reduction in the electromagnetic power capability with all of these materials, although at this stage no consideration has been given to iron loss. This

deterioration in performance results from a combination of a lower saturation flux density and/or lower permeability. It is worth noting that whereas the Somaloy 130i5p machine at SH=0.8 is capable of a maximum power of 80.0kW at a DC average load current of 103A at load, this is achieved at a current density of 22.4A/mm^2 rms and a copper loss of 427W for a winding temperature of 180°C and a packing factor of 0.8, increasing to 29.8A/mm^2 rms and 569W for a packing factor of 0.6. The shift of the peak power point to higher current is due to a combination of increased magnetic reluctance of the core which tends to reduce the core reactance and hence improves the voltage regulation. Similar behaviour is observed with PCHF125 and PCMF60 with current densities of 21.1A/mm^2 rms and 20.7A/mm^2 rms at the maximum power point respectively for a packing factor of 0.8.

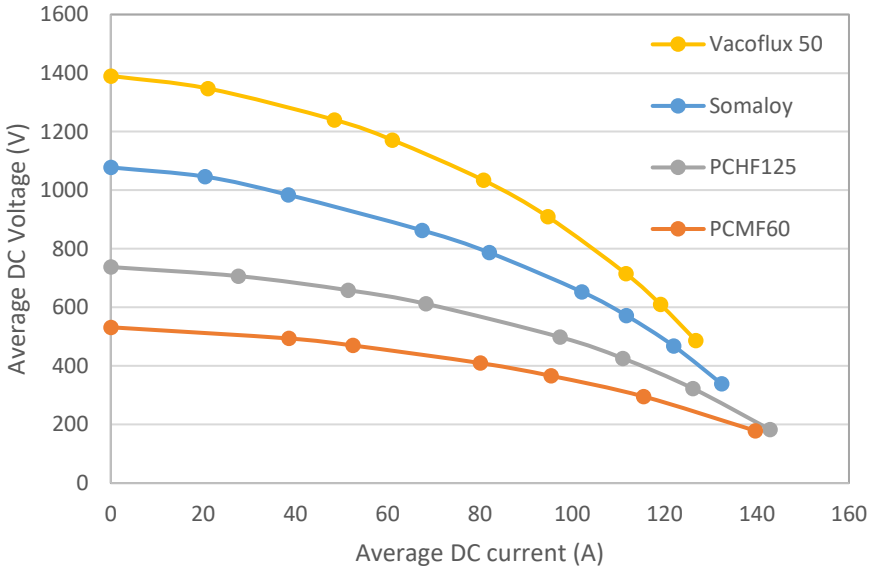

Figure 4.45 Finite element predicted output V-I curve of the machine with different stator materials (design 4.4.3 at SH=0.8)

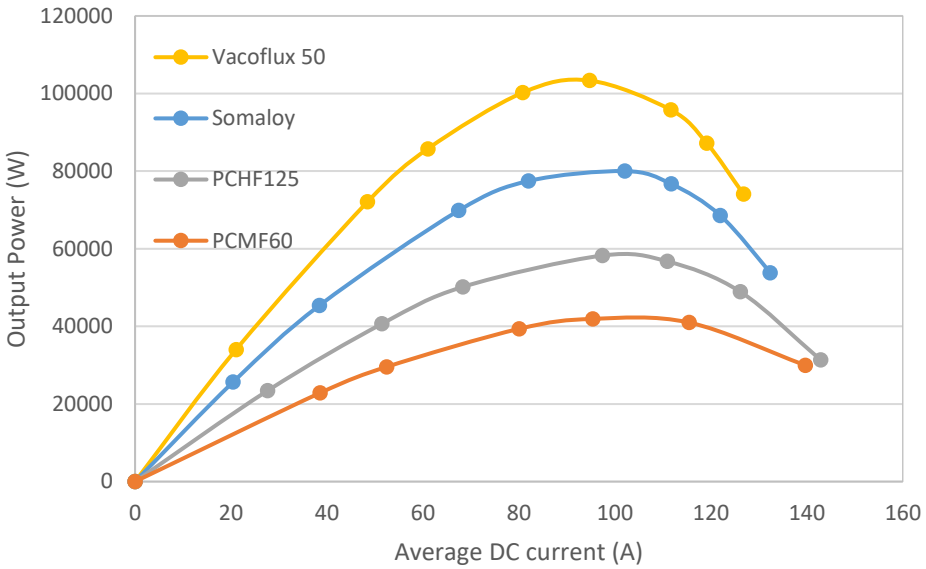

Figure 4.46 Finite element predicted output power characteristics with different stator materials (design 4.4.3 at SH=0.8)

The corresponding voltage and power curves for a stator hub ratio of 0.75 are shown in Figure 4.47 and 4.48. As will be apparent, the same trends are exhibited in terms of the reduction in no-load voltage with different stator core materials, with the powder iron cores showing the lowest performance in terms of load voltage and power capability.

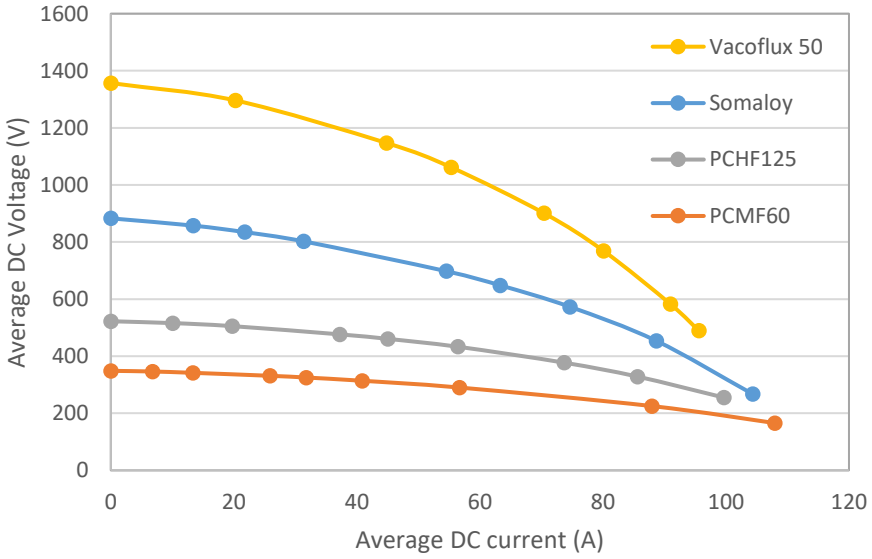

Figure 4.47 Finite element predicted output V-I curve of the machine with different stator materials (design 4.4.2 at SH=0.75)

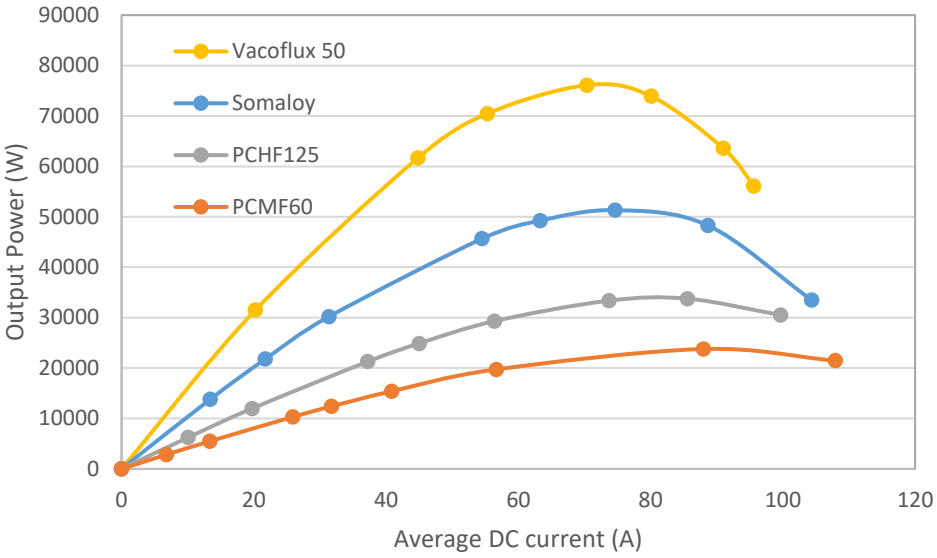

Figure 4.48 Finite element predicted output power characteristics with different stator materials (design 4.4.2 at SH=0.75)

As will be apparent, the increase in the slot depth from the reduced stator hub ratio results in a significant decrease in the electromagnetic power capability of the machine. This is due to increased stator reactance, recalling that the airgap diameter remains fixed with varying stator hub ratio. The combination of a reduced power capability and increased slot area results in a very significant reduction in the rms current density at the maximum power point as shown in Table 4.7, with several of the designs not achieving a 50kW operating point.

Table 4.7 Summary of key operating point performance for different core materials

Material	Somaloy®		PCMF60		PCHF125	
Stator hub ratio	0.75	0.80	0.75	0.80	0.75	0.80
Maximum power (kW)	51.3	80.0	23.8	41.9	33.7	58.2
Current density at maximum power (A/mm2 rms) *	10.0	22.3	11.7	20.7	9.8	21.1
Current density at 50kW operating point (A/mm2 rms)*	9.2	9.3	N/A	N/A	N/A	14.7

* - assuming 0.8 coil packing factor

4.4 Iron loss calculation for machine designs

As noted previously in the description of the various materials, material suppliers provide a number of different formulae for calculating iron loss at a range of frequencies and flux densities. These are often based on simple empirical curve fits to measured loss curves. These formulas are often quoted with operating ranges (combination of frequency and flux density) over which they remain valid. Although these manufacturer equations provide a useful indication of losses under sinusoidal conditions, in the calculation of iron loss for the various machine design and material combinations a well-established loss separation method was used. This is able to accommodate arbitrary non-sinusoidal flux density waveforms. This made use of an existing post-processing tool which takes in element-by-element time based flux density waveforms from a series of time-stepped finite element solutions and uses the standard equation below based on the model reported in [15] to predict loss:

$$P_{Fe} = k_h B^{\alpha+bB} f + \frac{\sqrt{\sigma}}{\delta_{Fe}} K_{exc} \frac{1}{T} \int_T \left|\frac{dB}{dt}\right|^{1.5} dt + K_{cl} \frac{1}{T} \int_T \left|\frac{dB}{dt}\right|^2 dt \quad (W\ kg^{-1}) \tag{4.2}$$

In the case of laminated materials, the coefficient associated with the classical eddy current component of the loss, K_{cl}, can be expressed in terms of conductivity, density and lamination thickness based on well-established analytical equation for eddy current loss in a 'thin' sheet, i.e. a sheet which is sufficiently thin so that no significant skin effect occurs [16].

$$K_{cl} = \frac{\sigma d^2}{12\delta_{Fe}} \tag{4.3}$$

Where σ, δ and d are the electrical conductivity, mass density and the thickness of the lamination respectively. The above equation is capable of calculating loss for arbitrary flux density waveforms and not just sinusoidal flux density waveforms. Although coefficients are available for various electrical steels and Cobalt Iron from published studies such as [17] [18]. These particular model parameters were not available for Somaloy, PCMF and PCHF. Although a series of experimental loss measurements could be performed from which to extract the coefficients, the equipment and suitable material samples were not available for this project. A method was used which combined the manufacturer supplied models to generate loss data as a function of flux density and frequency which was then fitted to produce the coefficients required for equation 4.2.

The resulting coefficients for the various materials considered are summarised in Table 4.8. In the case of the powder based materials, the classical eddy current coefficients are derived directly from the measurement while for the laminated Cobalt Iron, these are calculated on the basis of electrical conductivity and lamination thickness using equation 4.3.

Table 4.8 Iron loss coefficients for the materials considered

	Vacoflux 50	Somaloy 130i 5P	PCMF	PCHF
Kh	0.016	0.079	0.1737	0.0341
α	1.405	1.75	2.145	2.165
β	0.075	0	0	0
K_{loop}	0.65	0.65	0.65	0.65
Bulk Conductivity (S/m)	1.79×106	50	50	56
Lamination thickness (mm)	0.1	N/A	N/A.	N/A
Mass density	8120	7440	7131	7131
Kexc	3.7x10-5	N/A*	N/A*	N/A*
Kcl	1.86x10-7	7.07 x10-7	5.57x10-8	6.52x10-8

* - not accounted for in manufacturer model used to generate data

Figure 4.49 (a) to (c) show comparisons of the predicted loss variation with frequency for the three powder based materials based on equation 4.2 using coefficients above and manufacturer data for a peak flux density of 1T. As will be apparent, these combinations of coefficients provide a good fit over the range of frequencies considered.

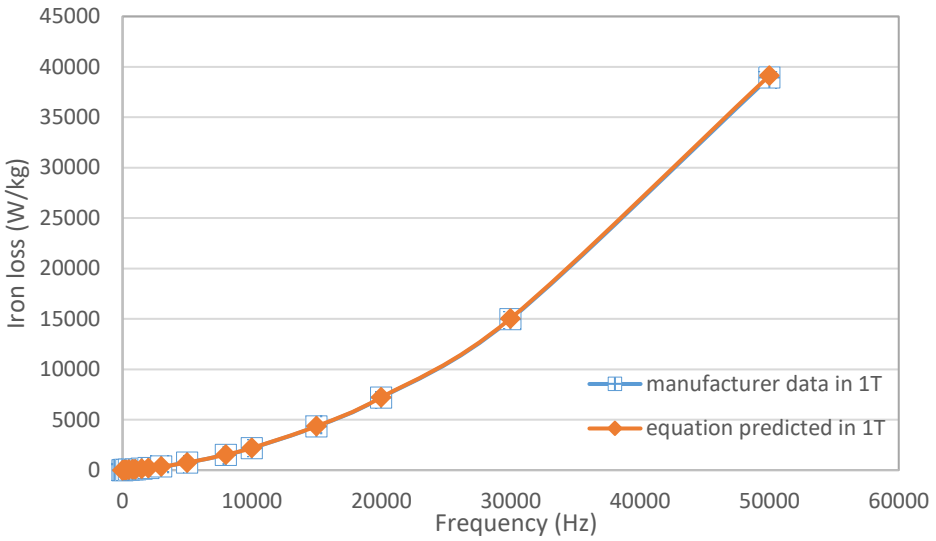

Figure 4.49 (a) Predicted variation in iron loss with frequency for Somaloy 130i 5P

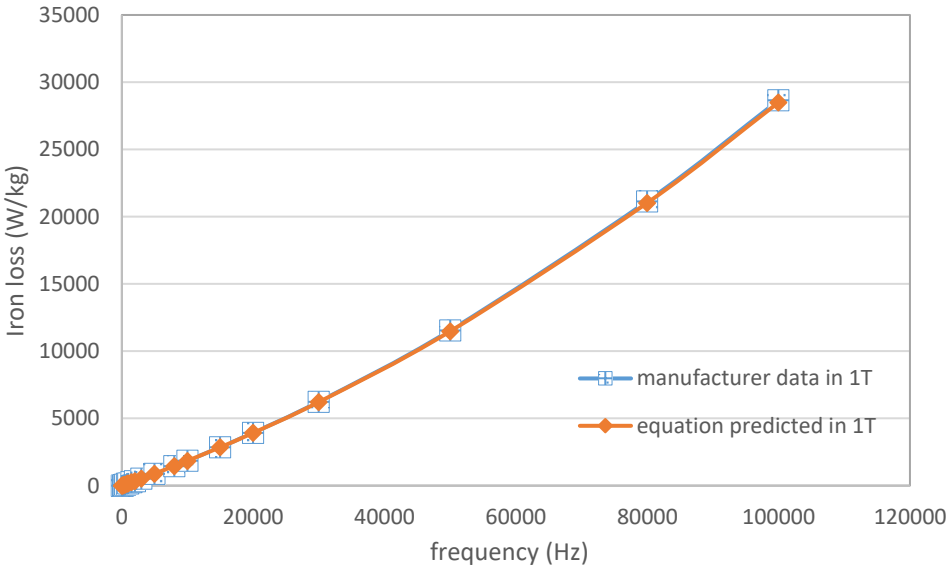

Figure 4.49 (b) Predicted variation in iron loss with frequency for PCMF

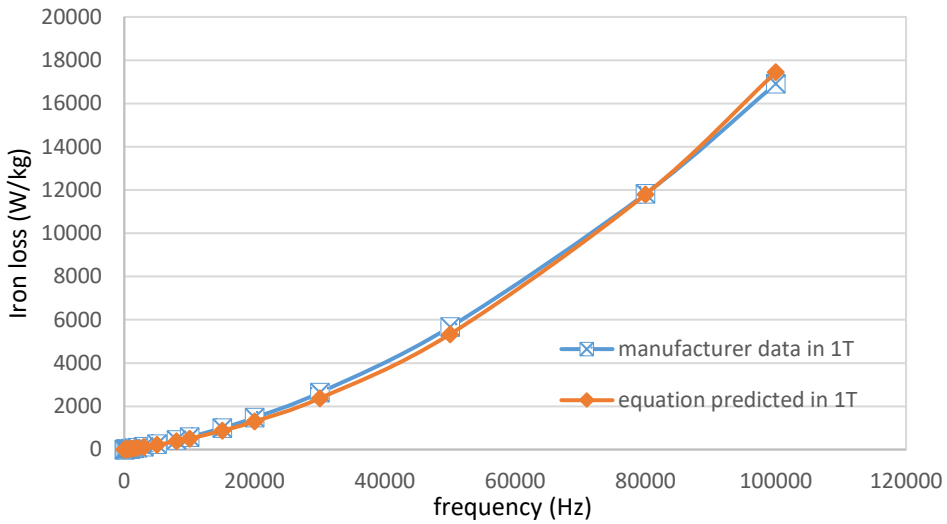

Figure 4.49 (c) Predicted variation in iron loss with frequency for PCHF

In addition to the contribution to the hysteresis loss from the major hysteresis loop (determined by positive and negative peaks of the flux density during one cycle) there will also be additional hysteresis loss from minor loops due to harmonics in the flux density waveforms. For this series of iron loss calculations, the minor loop loss was calculated within the post-processing tool using the method proposed by Lavers et al [19]. In this method, the additional loss from each minor loop excursion is scaled by a factor K_{loop}. In the absence of detailed minor loop loss data for the various materials, in this series of calculations K_{loop} was set to 0.65 for all materials. This value is the mid-point of the range 0.6-0.7 identified by Lavers in as covering most commercial soft magnetic materials.

4.4.1 Calculation of machine losses

Having established coefficients for each material, the time-stepped finite element simulation results for each material, specifically time variation of flux density in each individual element of the stator cores, were used as input to the core loss post processor. This existing post-processor implements equation 4.2 on an element-by-element basis to establish both instantaneous and average loss in each element, which can then be summed to provide overall average loss.

Figures 4.50 shows a typical example of post-processor output generated by this post-processor which shows the spatial distribution of core loss in a Vacoflux 50 Cobalt-Iron stator (design 4.4.3 with an SH ratio of 0.8) operating at its maximum power point of

103.4kW at a DC load current of 94.7A. The values of total loss in Figure 4.52 is for the problem domain shown (i.e. one-half of a stator tooth) and not the overall machines. In the case of this 96 pole-pair and hence 192 tooth design, this calculated loss must be scaled by 384 to establish the overall loss, i.e. 5,587W in this example.

The loss distribution plot demonstrates that there is a large variation in the loss density throughout the stator core, with particularly high levels near the front of the stator teeth. It is also worth noting that as shown in the plot of radial versus circumferential flux density variations that there are regions of significant rotational fields (the point taken being near the front of the stator tooth). It is also interesting to note the breakdown of the core loss with hysteresis, excess loss and eddy current loss contributing 10.6%, 6.4% and 83% respectively. As would be expected in this low hysteresis loss Cobalt Iron, the losses are dominated by eddy current losses in this case, despite the use of 0.1mm thick laminations. The corresponding breakdown of losses for Somaloy 130i 5P is 14.0%, 0.5% and 85.5%.

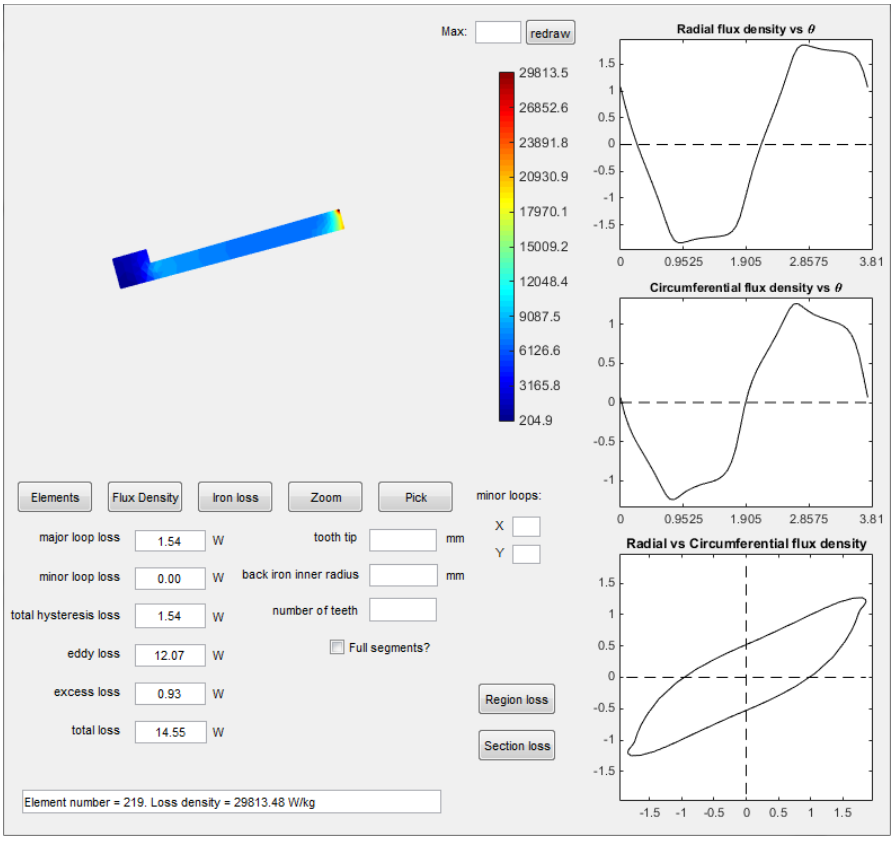

Figure 4.50 Output from iron loss post-processing tools for peak power point (103.4kW at 20,000rpm) for design 4.4.3 (SH=0.8) with core material Vacoflux 50 (Values shown are for half stator tooth and an axial length of 50mm). Colour scale refers to loss density in W/kg. Total machine loss is 5,587W.

Figure 4.51 shows the corresponding loss distributions for the various SMCs and powdered iron cores along with the loss distribution for the other Vacoflux 50 design (i.e. with SH=0.75). In all cases, these are losses at the maximum power operating point. As shown, there is a significant variation in the total losses, with the lowest loss for the PCHF cores. As will be apparent, the eddy current losses for the Somaloy cores (which as discussed previously make up 85% of the loss) are so high as to make this material not viable in this application.

It is recognised that there are several simplifications and approximations in this loss separation model, e.g. assumption of negligible skin effect within a single lamination which may be problematic at such high frequencies and no account of end-effects in the single-piece powder cores. However, despite these simplifications, the loss distributions and total losses in Figure 4.10 provides a useful indication of design viability and the relative merits of different materials.

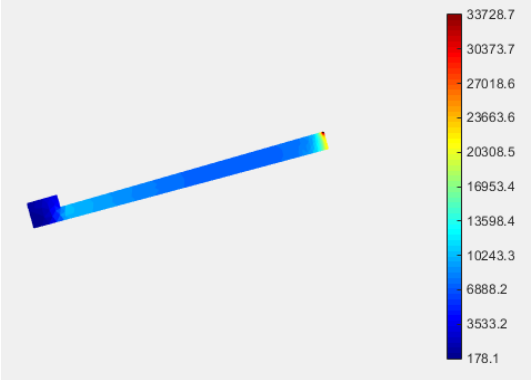

(a) Design 4.4.2 (SH=0.75) at 76.1kW / 20,000rpm with Vacoflux 50 core – total loss of 8,813W

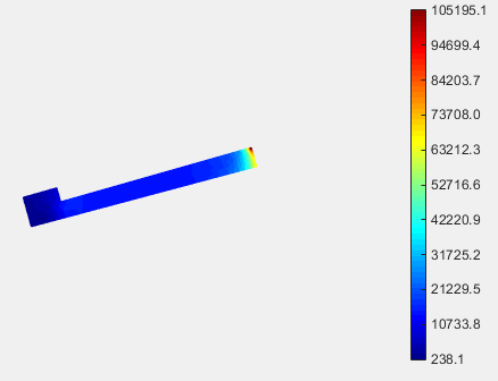

(b) Design 4.4.3-S (SH=0.8) 80.0kW / 20,000rpm with Somaloy 130i 5P core - total loss of 11,581W

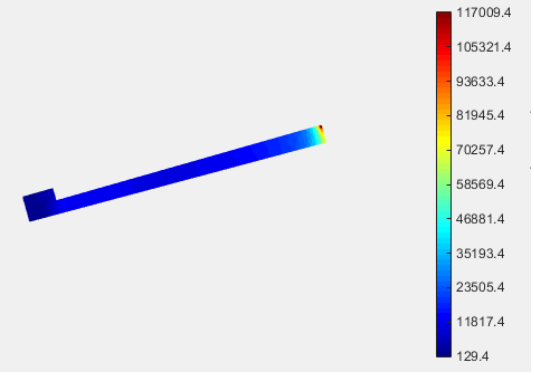

(c) Design 4.4.2-S (SH=0.75) at 51.3kW / 20,000rpm with Somaloy 130i 5P core – total loss of 14,991W

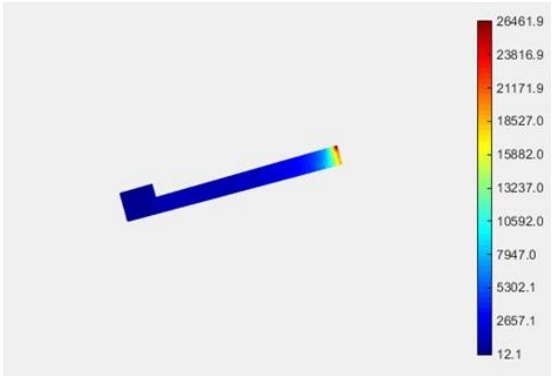

(d) Design 4.4.3-M (SH=0.8) at 41.9kW/20,000rpm with PCMF core – total loss of 1,778W

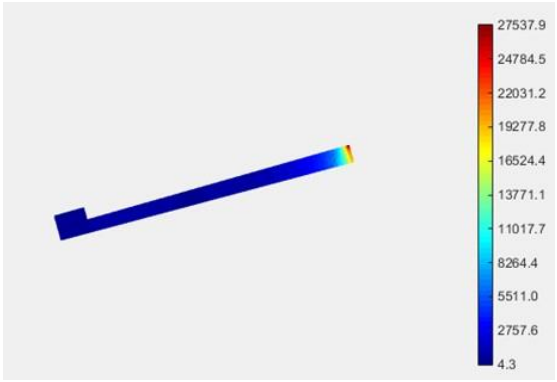

(e) Design 4.4.2-M (SH=0.75) at 23.7kW/20,000rpm with PCMF core – total loss of 1,809W

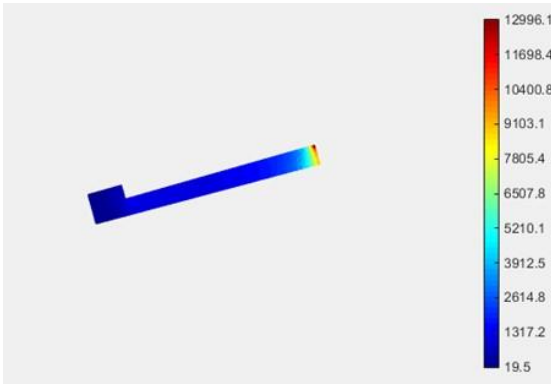

(f) Design 4.4.3-H (SH=0.8) at 58.2kW /20,000rpm with PCHF core – total loss of 1,160W

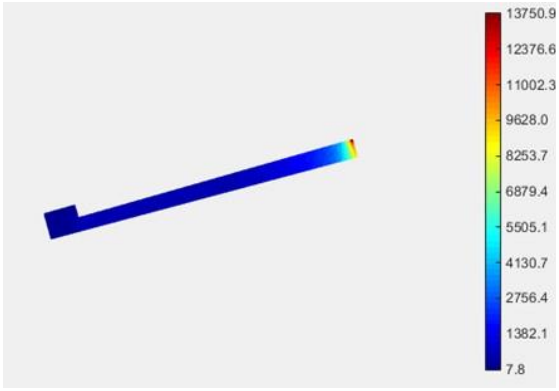

(g) Design 4.4.2-H (SH=0.75) at 33.8kW/20,000rpm with PCHF core – total loss of 1,171W

Figure 4.51 Finite element predicted core loss distributions in a series of machine designs.

A summary of the overall loss for various designs and materials is shown in Table 4.9, in each case at the individual maximum power operating point. The copper loss shown in Table 4.9 was calculated on the basis of a Litz wire packing factor of 0.8, as discussed in connection with Figure 4.7, and a temperature corrected value of resistance assuming a winding temperature of 180°C. In order to account for the small additional end-winding of a serpentine winding, the mean length per turn was calculated as 120% of the stator core length.

Table 4.9 Calculated loss performance for each machine at maximum power operating point

	Design number	Stator hub ratio	Output power at optimal load (kW)	DC load current at optimal load (A)	Stator Iron loss for entire stator (W)	Total copper loss * (W)	Efficiency at peak power operating point
Cobalt Iron	4.4.2	0.75	76.1	70.4	8,813	123	89.5%
	4.4.3	0.8	103.4	94.7	5,587	361	94.6%
Somaloy 130i 5P	4.4.2-S	0.75	51.3	74.6	14,911	138	77.3%
	4.4.3-S	0.8	80.0	102.0	11,581	419	87.0%
PCMF	4.4.2-M	0.75	23.7	88.0	1,809	192	92.2%
	4.4.3-M	0.8	41.9	95.4	1,778	366	95.1%
PCHF	4.4.2-H	0.75	33.8	85.6	1,171	181	96.2%
	4.4.3-H	0.8	58.2	97.4	1,160	382	97.4%

* - based on 0.8 packing factor and an assumed winding temperature of 180°C

In comparing the losses predicted for each material in Table 4.9, it is important to recognise that many of the designs with different materials produce more power than the 50kW baseline operating point. However, whereas reducing the output current to produce only 50kW will inevitably reduce the copper losses, the reduced armature reaction field in generating mode has the potential to increase the stator core loss. This was investigated by re-calculating the core loss for an operating point of 50kW for the 4 designs from Table 4.9 with a stator hub ratio of 0.8 whose maximum output power exceeds 50kW, i.e. design 4.4.3 with a Cobalt Iron core, design, design 4.4.3-S with a Somaloy 130i 5P core and design 4.4.3-H with a PCHF core. Since no PCMF designs were able to meet the 50kW operating point, these were not included in this further analysis.

Table 4.10 shows a comparison of the core loss for these two designs at their maximum power point and a 50kW operating point. As will be apparent, in both cases, there is a significant increase in the core loss at the 50kW operating point. A further series of core loss calculations were performed for these designs under open-circuit conditions. The open-circuit core losses are also shown in Table 4.10.

Table 4.10 Calculated losses in four selected designs with a stator hub ratio of 0.8 which are operating at 50kW operating point

	Design number	DC average current at 50kW	Stator Iron loss (W)	Total copper loss * (W)	Efficiency at peak operating point
Cobalt Iron	4.4.3	32.5A	9300	42.5	81.3%
Somaloy 130i 5P	4.4.3-S	42.3A	17833	72	64.2%
PCHF	4.4.3-H	68.3A	1452	188	96.7%

* - based on 0.8 packing factor and an assumed winding temperature of 180°C

High power density machines with efficiencies of <90% or so are very difficult, and likely impossible, to cool in terms of their loss per unit volume. Only the design with a PCHF core is meeting this criterion when producing 50kW. However, the average loss density throughout this PCHF core is still very high at 1927W/kg. Ultimately, the feasibility of any design will be determined by the ability of the cooling system employed to remove the predicted losses (both core loss and copper loss) from the stator core. There are reasonably well established design guides for setting current densities based on cooling [20] [21], e.g. 3-5 A/mm^2 for natural convection, 8-10A/mm^2 for liquid jacket cooling. However, in terms of removing overall loss, there are no such straightforward guidelines. One useful approach is to consider the likely ranges of heat-flux (i.e. heat removal per unit surface area) that can be removed. This approach was adopted by Yu [22] in which a constraint of a total stator loss heat flux of 25kW/m^2 was imposed at the back of the stator core. The basis of this value was not explored in any detail in terms of its viability, but was simply taken as the value for the baseline reference design used in the study. In order to assess the viability of the machine design 4.4.3, 4.4.3-S and 4.4.3-H in the table above in terms of overall loss, it is necessary to establish some basis for specifying a maximum heat-flux for the stator core.

It is worth noting that the balance between copper and core loss in these designs is very different from mainstream electrical machines. Taking the examples shown in Table 4.9, the predicted copper loss ranges between 1% and 25% of the overall loss. In many conventional electric machines, the copper loss is often around 50% of the total loss at

the rated power point, although it can form a higher proportion in machines operating with very aggressive current densities of >10A/mm^2 rms.

On the basis of the heat-flux calculations and the very intensive heating that will occur on the front edges of the teeth, the benefits of reducing the pole number by a factor of two was investigated. This should, at least in principle, lead to a reduction in core loss by a factor of up to four since the loss at high frequencies is likely to be dominated by the eddy current component of loss.

4.5 Design of a reduced pole number (96 poles) machine with material PCHF

To investigate the benefits of reducing the fundamental frequency a series of further external rotor machine designs with 96 poles (i.e. 48 pole-pairs) were established their performance predicted. These machines produce a machine output frequency of 16 kHz (and hence a rectified 32 kHz pulse train into the converter). As noted in chapter 2, this reduction in frequency would require an increase in the size and weight of the converter output filter. A machine design based on a reduced pole number is shown in Figure 4.52 in this case a split ratio of 0.9 and a stator hub ratio of 0.8 (design 574). The circumferential width of stator slot and magnet are both set to 2mm. The stator slot is 5.2mm deep. The stator core material is assumed to be PCHF which is same material that produced the lowest loss for the 192 pole design. The finite element predicted output voltage and power curves for this machine as a function of the load current is shown in Figure 4.53, in this case for a series connection of a single turn in each slot.

This 96 pole design shows a significant improvement in peak electromagnetic power capability compared to the equivalent 192 pole machine, with a maximum electromagnetic power capability of 139kW at an output average current of ~300A, which corresponds to a machine rms current of 334Arms. This compares with 58.2kW for a similar 192 pole design. The slot area available in this 96 pole design is 10.40mm^2, which results in an rms current density at this operating power of is 40.2A/mm^2 for a packing factor of 0.8, increasing to 53.6A/mm^2 for a reduced packing factor of 0.6. Both of these current densities are clearly unsustainable in terms of temperature rise in the winding. At the rated power of 50kW, the average output DC load current is 75.4A which corresponds to an rms current in the machine of 83.7Arms and hence an rms current

density of 10.1A/mm^2 rms for a packing factor of 0.8, increasing to 13.4A/mm^2 for a reduced packing factor of 0.6.

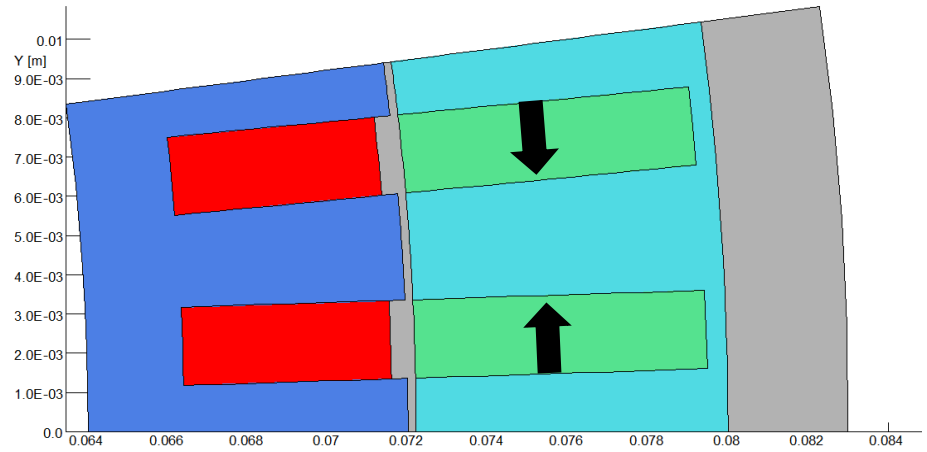

Figure 4.52 Cross-section though 96 pole external rotor machine with a split ratio of 0.9 and a shaft hub ratio of 0.8 (design 4.5.1)

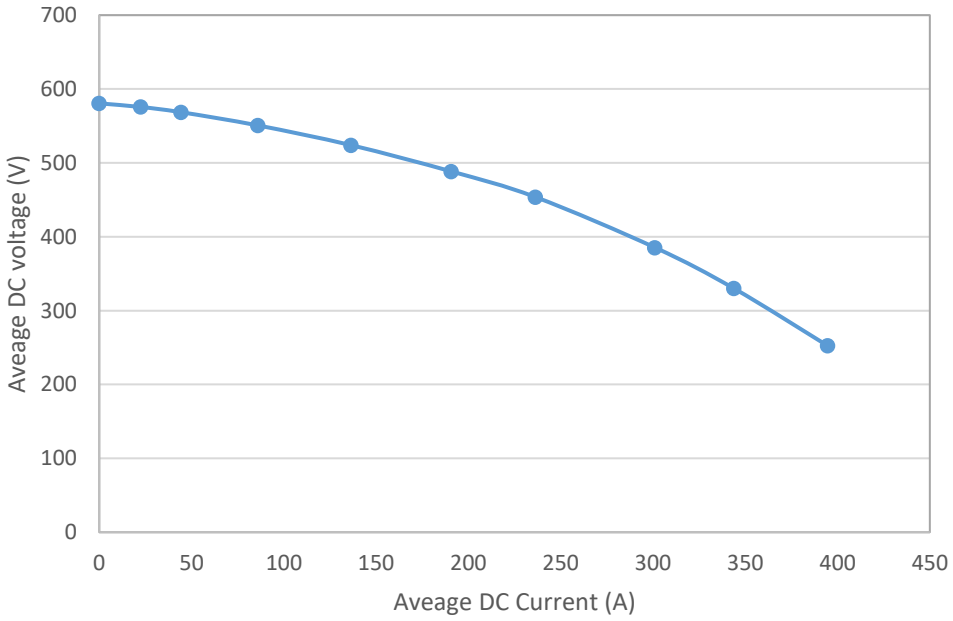

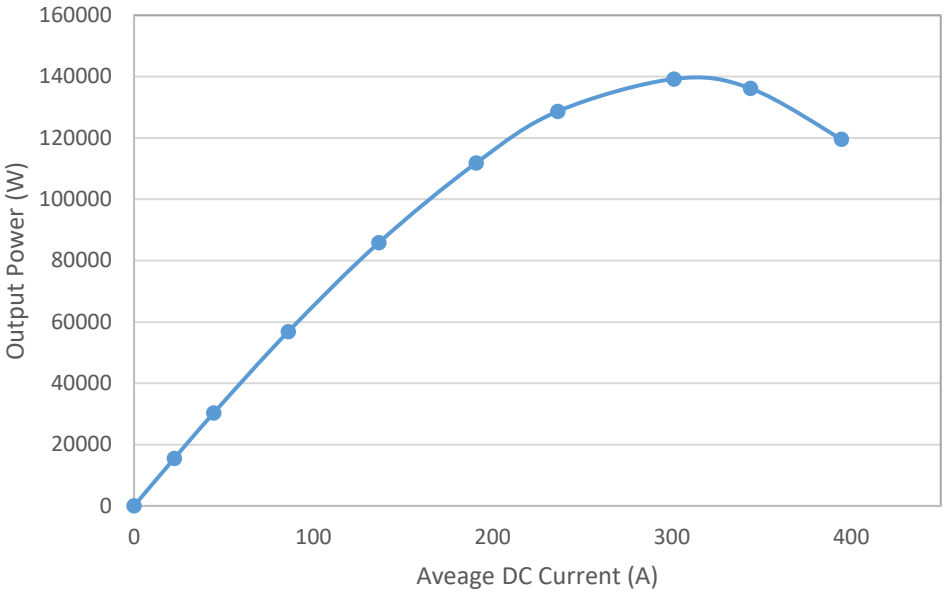

Figure 4.53 Finite element predicted variation in output voltage and power with current for 96 pole machine (design 4.5.1)

Figure 4.54 shows the output from the iron loss post-processor for this machine design at the 139kW operating point, which predicts an overall iron loss of 916W. When combined with the predicted copper loss of 2.23kW for a packing factor of 0.8 (increasing to 2.97kW for a packing factor of 0.6) the efficiency of this machine at this maximum power operating point is 97.8% (reducing to 97.2% for a packing factor of 0.6).

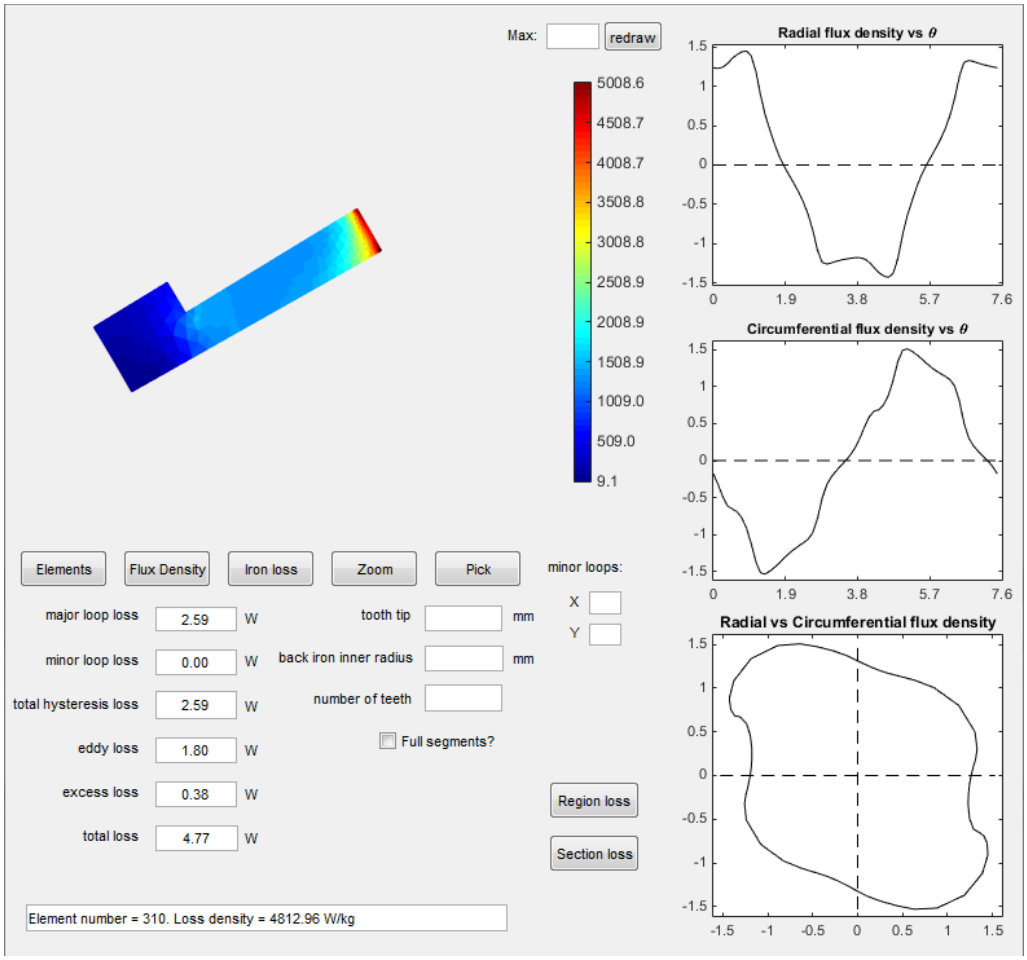

Figure 4.54 Output from iron loss post-processing tools for peak power point (139kW at 20,000rpm) for design 4.5.1 with core material PCHF (Values shown are for half stator tooth and an axial length of 50mm). Total machine iron loss of 916W.

When the load resistance is increased to operate the machine at an output power of 50kW, the machine and hence average DC load current is reduced to 75.4A. This results in a very significant reduction in the copper loss to 141W at a packing factor of 0.8 at 180°C (increasing to 188W for a packing factor of 0.6). However, as observed with the 192 pole machines, reducing the armature reaction field from the stator current tends to increase the iron loss. Figure 4.55 shows the output from iron loss post-processing tools for a 50kW operating point, with an overall machine loss of 1121W as compared to 916W at the 139kW maximum power point. This gives efficiencies of 97.5% for a packing factor of 0.8 reducing to 97.4% for a packing factor of 0.6. This compares favourably with the corresponding PCHF 192 pole design which had an iron loss at ~50kW operating point of 1452W and an efficiency of 96.7%.

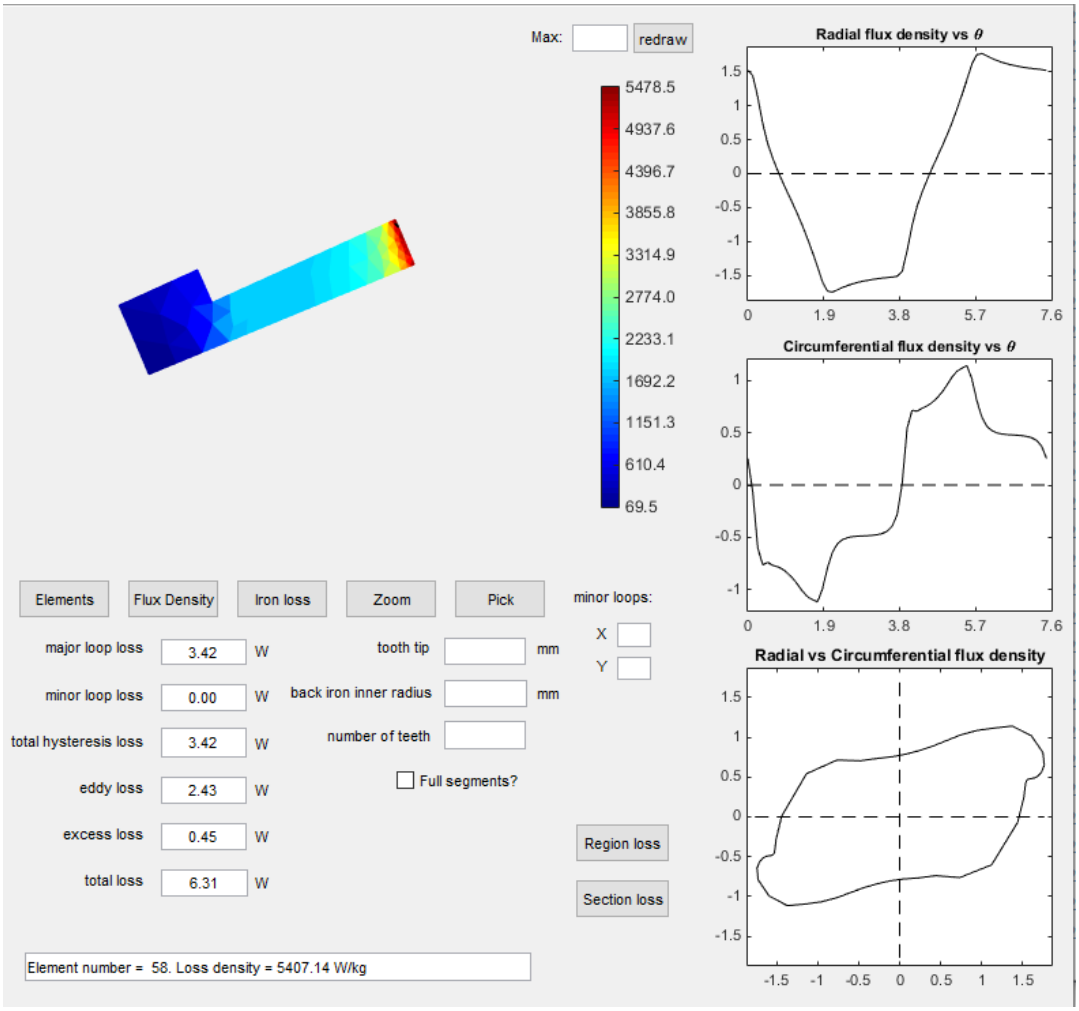

Figure 4.55 Output from iron loss post-processing tools for peak power point (~50kW at 20,000rpm) for design No.4.5.1 with core material PCHF (Values shown are for half stator tooth and an axial length of 50mm).

Although the 50kW working point brings the rms current density down to a more manageable value at ~10A/mm^2, the large electromagnetic power capability of this design provides an opportunity to optimise aspects of mechanical and thermal performance. Hence, a series of modifications were made to this design:

- The airgap was increased from 0.2mm to 0.5mm.
- A Halbach array magnet was used in the rotor.
- The magnet pole width of the Halbach array was increased from 2mm to 2.2mm.
- The stator slot width was also increased to 2.2 mm.

There are two different types of Halbach arrays as shown in Figure 4.56. A pure Halbach array is based on a continuous co-sinusoidal variation the direction of magnetisation

within a single magnet piece while the other type involves an approximation to a Halbach magnetisation pattern and is made up of a discrete series of segments, each of which has a single direction of magnetisation. Although a true Halbach magnetisation can be produced within an isotropic bonded magnet [23] such materials have modest magnetic properties and poor temperature resistance. Hence, the use of discrete magnet array using high performance sintered magnets is far more common [24] [25]. A Halbach array tends to produce a more sinusoidal airgap field compared to a normal radially magnetised set of magnets [26], which can lead to a reduced iron loss in stator. Additionally, a Halbach magnet array is almost entirely self-shielding and can eliminate the need for a back iron. Furthermore, the working point of the magnet in Halbach array is raised up the demagnetisation curve compared conventional radially magnetised magnet [27] and also the flux density variation due to stator slotting and armature reactance tends to be lower, which can reduce rotor magnet loss.

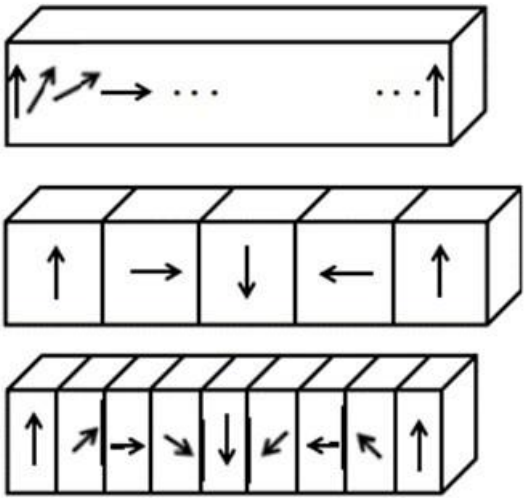

Figure 4.56 Halbach magnetic array with flux distribution (Source: [28])

Table 4.11 summarises the influence of these changes on the electromagnetic power capability. As shown by Table 4.11, a simple increase in the airgap with a conventional radially magnetised magnet array results in a very dramatic reduction in the electromagnetic power capability, although it still comfortably meets the 50kW requirement with maximum power operating point of 60.6kW. However, when this increase in airgap is combined with a two-piece Halbach array (the simplest and coarsest implementation of a Halbach array) the power capability recovers to 102.1kW which

demonstrates the usefulness of Halbach magnet arrays in directing flux and accommodating larger airgaps.

Table 4.11 Power capability resulting from design changes

Design number	EM power capacity (kW)	Description of design change
4.5.1	140.0	Interior magnet machine, airgap=0.2mm, width of stator slot=2mm
4.5.2	60.6	Interior magnet machine, airgap=0.5mm, width of stator slot=2mm
4.6.1	102.1	Two pieces per pole Halbach array magnet machine, airgap=0.5mm, width of slot=2.2mm

The four different types of Halbach magnet arrays shown in Figure 4.57 were considered further in this investigation. Each of these four designs has a stator hub ratio of 0.8. Two of the variants, (a) and (c), use two pieces per pole which result in a 90° change in magnetisation for successive magnet pieces. The other two variants, (b) and (d), use four pieces per pole which results in a 45° change in magnetisation for successive magnet pieces. In all 4 cases, the light grey structure around the outer edge of the rotor in a non-magnetic structural component. In Figure 4.57 (a) and (b), the magnets are located within a soft magnetic rotor frame, while in Figure 4.57 (c) and (d) the rotor frame is non-magnetic. Since rectangular magnets are used in both cases, the rotor frames incorporate thin triangular shaped separators between successive magnets, which are 0.1~0.2mm wide.

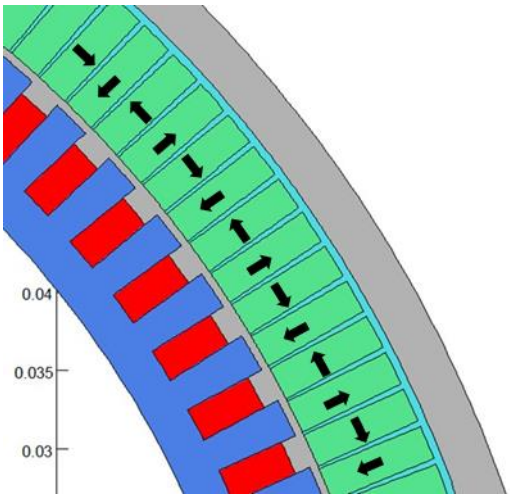

(a) Rotor with 2 pieces Halbach array magnet and magnetic frame

(design 4.6.1).

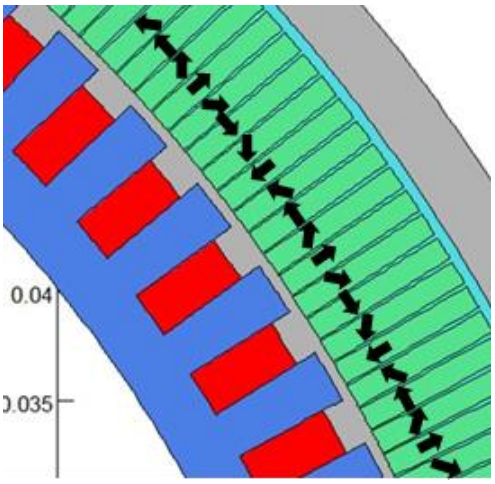

(b) Rotor with 4 pieces Halbach array magnet and magnetic frame

(design 4.6.2)

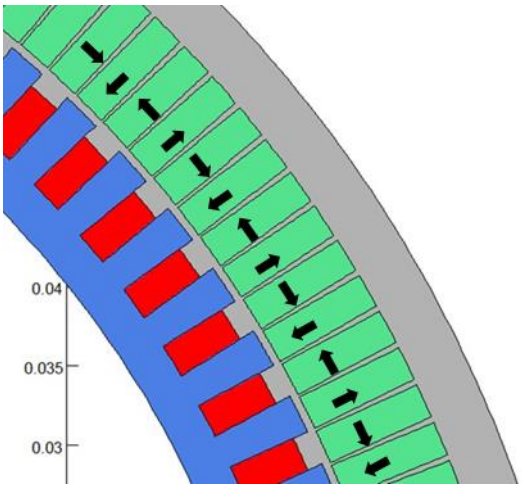

(c) Rotor with 2 pieces Halbach array magnet and non-magnetic frame

(design 4.6.3)

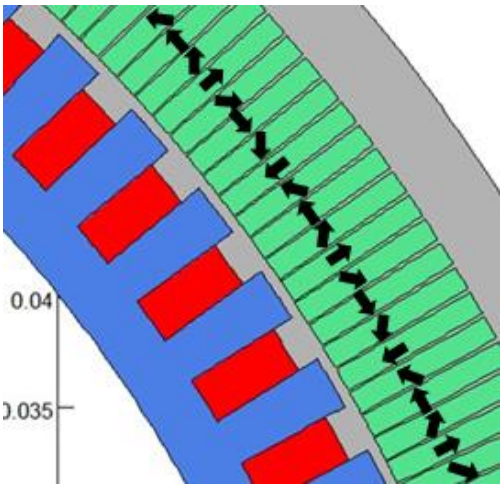

(d) Rotor with 4 pieces Halbach array magnet and non-magnetic frame

(design 4.6.4)

Figure 4.57 External rotor machines with Halbach magnet array (magnetic frame is light blue region between and around individual magnet pieces). All designs have a stator hub ratio of 0.8.

Figure 4.58 shows a comparison between open circuit finite elements predicted flux distribution for cases of two pieces per pole and four magnet piece pole Halbach magnet array with both magnetic and non-magnetic magnet frames.

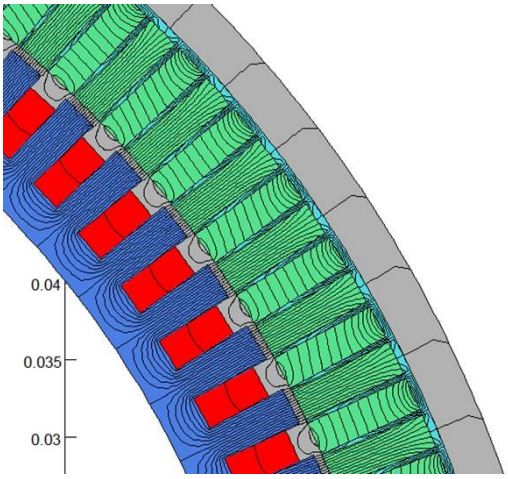

(a) Two pieces Halbach magnet array with magnetic frame (region in light blue)

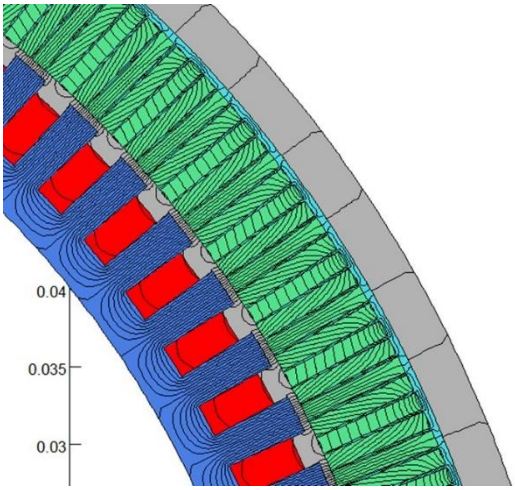

(b) Four pieces Halbach magnet array with magnetic frame (region in light blue)

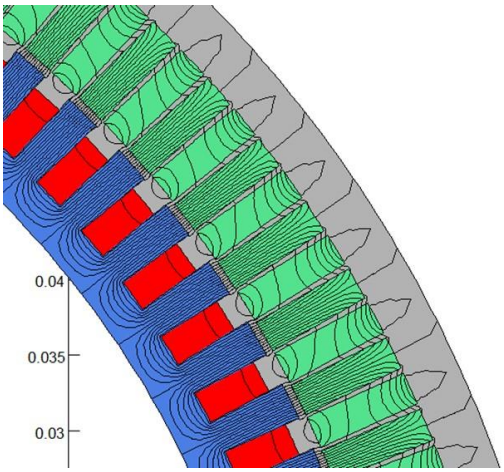

(c) Two pieces Halbach magnet array with non-magnetic frame

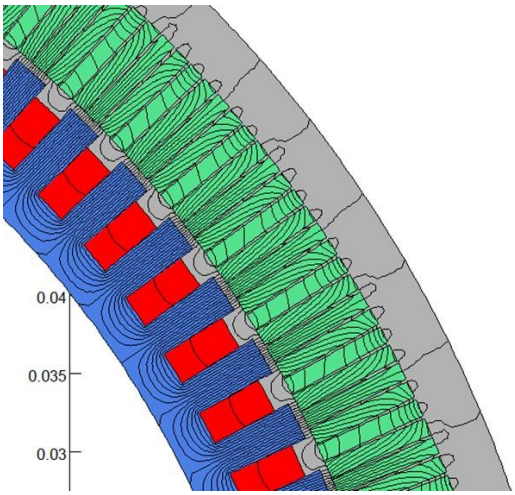

(d) Four pieces Halbach magnet array with non-magnetic frame

Figure 4.58 Open circuit flux distribution in two different Halbach magnet arrays

The output power versus DC load current characteristics for this series of Halbach array rotors with both magnetic and non-magnetic magnet frames are shown in Figure 4.59. These characteristics demonstrate that all four designs have similar performance, although the version with four magnet pieces per pole with the magnetic frame (labelled as h4p-magfra in Figure 4.59) has the highest maximum power capability of 115.5kW. As shown by Figure 4.59, all the machine designs have very similar performance at a 50kW operating point in terms of DC load current.

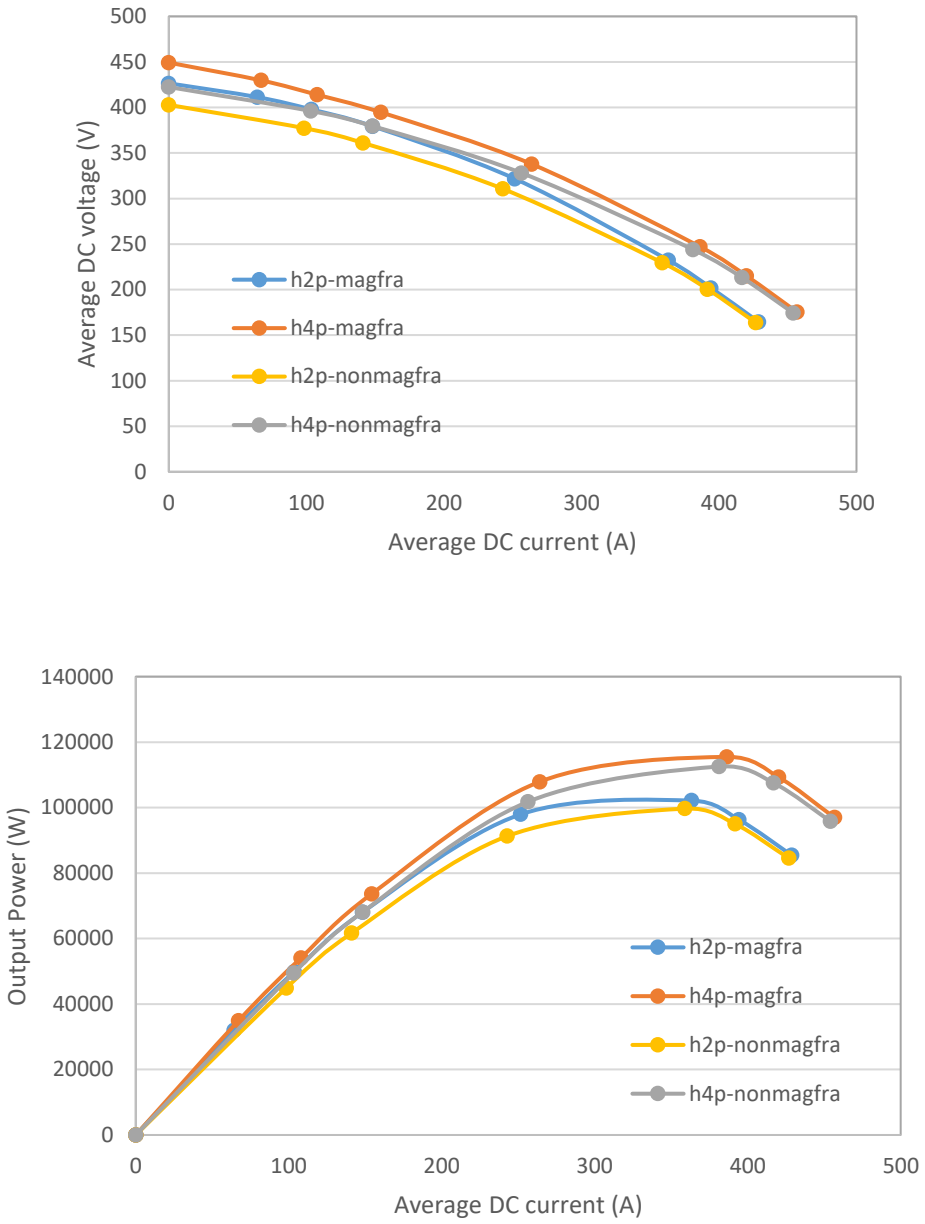

Figure 4.59 Finite element predicted variation in output voltage and power with current for a series of machine design with different Halbach arrays and magnet frame designs.

The stator core losses for these machines were again calculated using time-stepped two-dimensional finite element analysis in combination with the custom post-processor described previously in section 4.4.1. A summary of the losses is shown in Figure 4.60, in each case for the maximum power operating point.

Given the closeness in performance between the four designs, manufacturing and mechanical issues can be considered to establish the preferred option. A two-piece Halbach array involves half the number of individual magnet pieces and given the high number of magnets already involved in producing a 96 pole rotor, this is an important consideration. Furthermore, the potential to integrate the frame which locates individual magnets and the rotor containment into a single-piece structure makes the two piece Halbach array with a non-magnetic frame the preferred choice.

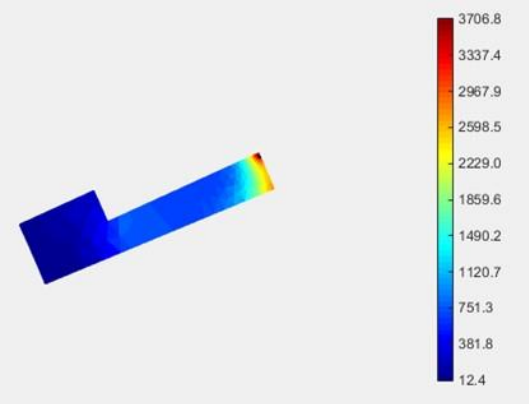

(a) Design 4.6.1 with 2 piece 96-pole Halbach array and magnetic frame with PCHF stator core at 102kW operating point (total machine loss of 464W)

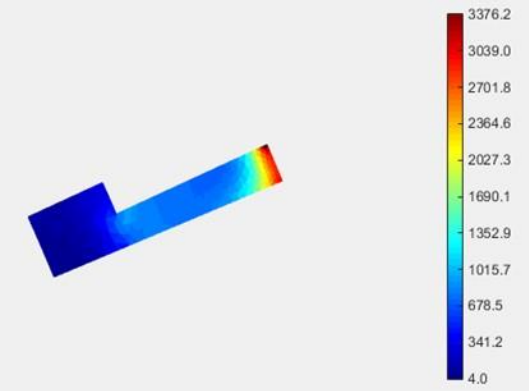

(b) Design 4.6.2 with 4 piece 96-pole Halbach array and magnetic frame with PCHF stator core at 115kW operating point (total machine loss of 518W)

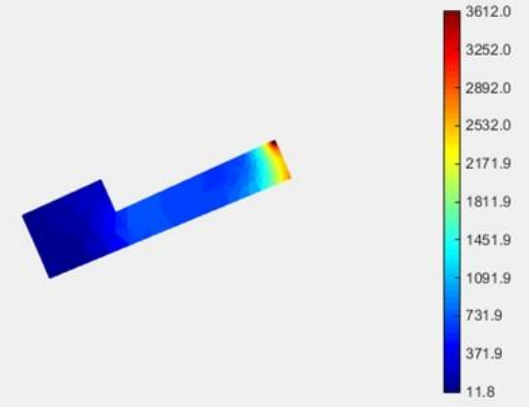

(c) Design 4.6.3 with 2 piece 96-pole Halbach array and non-magnetic frame with PCHF stator core at 99.7kW operating point (total machine loss of 447W)

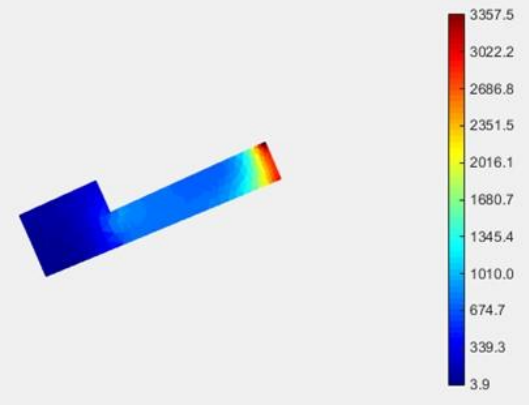

(d) Design 4.6.4 with 4 piece 96-pole Halbach array and non-magnetic frame with PCHF stator core at 113kW operating point (total machine loss of 509W)

Figure 4.60 Finite element predicted stator core loss distributions in a series of machine designs (scale bar in each case refers to W/kg loss). All machines have a stator hub ratio of 0.8.

In addition to the iron loss distribution at peak power point for this two-piece Halbach array non-magnetic frame machine (design 4.6.3), the iron loss distribution at a 50kW operating point (DC load current of 105A) was calculated. The iron loss post-processor output at this operating point is shown in Figure 4.61. As would be expected with the reduced stator current mmf opposing the magnet flux, the iron loss increases significantly at this 50kW operating point compared to the peak power working point. Specifically, at ~50kW, the loss increases to 735W as compared to 447W for the same machine at its maximum power operating point of 99.7kW. The losses and resulting heat flux per unit surface area of the three cases considered are compared in Table 4.12.

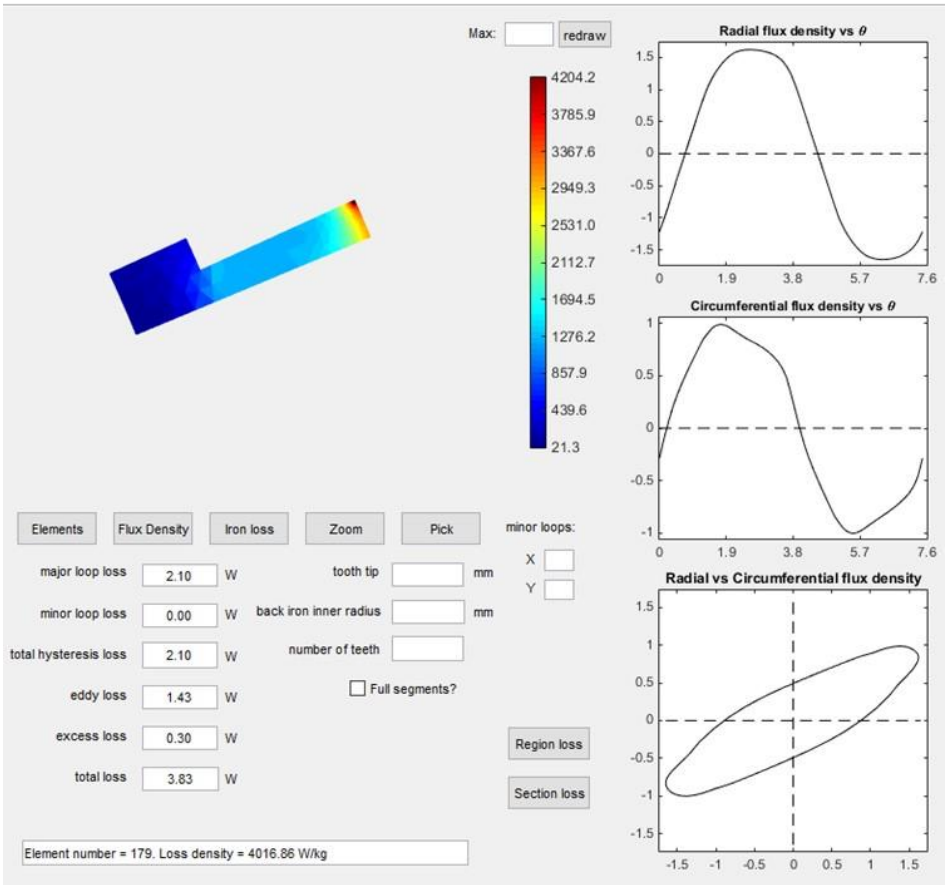

Figure 4.61 Output from iron loss post-processing tools for 50kW point (at 20,000rpm) for design 4.6.3 (h2p-nonmag) with core material PCHF (loss values shown are for half stator tooth and an axial length of 50mm). Total machine iron loss of 735W.

Table 4.12 compares the performance of design 4.6.3 (i.e. 2 piece Halbach magnet pole) with a stator hub ratio of 0.8 when operating at its maximum power point of 99.7 kW and at a 50kW operating point. It is worth noting that the maximum power point of 99.7kW is the peak of a relatively flat power versus current characteristic, e.g. a reduction in the

current to 242A (which would reduce the copper loss from 3.44kW to 1.57kW) would only reduce the output power to 91.3kW. As shown, reducing the operating point of this design to 50kW brings the heat flux close to 50kW/m^2. This could well be manageable with liquid jacket cooling, particular given that ~70% of this loss is in the core.

Table 4.12 Comparison of losses and stator bore heat flux for design 4.6.3 (assumes a copper packing factor of 0.8)

Stator hub ratio	Load power	Average DC load current	Stator Iron loss (W)	Conductor area for each slot (mm2)	Copper loss at 180°C (W)	Back iron area (m2)	Heat Flux from total loss (W/m2)
0.8	99.7kW	358	447	9.59	3444	0.02011	193,486
0.8	50kW	105	735	9.59	296	0.02011	51,268

A comparison between the predicted loss for the 96 pole machine (design 4.6.3) and the best 192 pole machine (design 4.4.3-H from section 4.4.1 of this chapter) is shown in Table 4.13 for a 50kW operating point. In both cases, the data presented is for the variant with a stator hub ratio of 0.8 and an assumed slot packing factor of 0.8.

Table 4.13 Comparison between 96 pole (design 4.6.3) and 192 pole (design 4.4.3-H) at a nominal 50kW operating point

Poles	Iron loss	Copper loss at 180°C	Total loss	Efficiency	Heat flux through core back
96	735 W	296W	1,031W	98.0%	51.3 kW/m2
192	1452W	188W	1,640W	96.8%	81.6kW/m2

As will be apparent, with the 96 pole design, there is a significant reduction of in the overall heat flux compared to the 192 pole design. Although the reduction in pole number has resulted in a significant reduction in the iron loss, it has only about halved. This reduction is less than would be expected on a simple like-for-like basis in which only the fundamental frequency changes. A simple scaling by frequency would have suggested a

reduction to a half (if the loss was dominated by hysteresis loss) and to quarter if eddy currents (which are proportional to the square of frequency were dominant). For these two designs, it is interesting to consider the contributions to the overall loss from the various components as shown in Table 4.14. As will be apparent from Table 4.14, the powdered nature of these cores means that even at these high frequencies, the hysteresis loss forms a significant fraction of the loss. It is also worth noting that there all several difference in some important aspects of the two design, e.g. use of Halbach arrays in 96 pole machine which will tend to increase the flux density, the 8% greater iron volume in the 96 pole machine. Despite not achieving a bigger reduction in the iron loss, it was concluded that the significantly lower heat flux of the 96 pole makes this the preferred option for a demonstrator machine.

Table 4.14 Breakdown of iron loss for 96 pole (design 4.6.3) and 192 pole (design 4.4.3-H) machines

Poles	Operating point	Hysteresis loss	Excess loss	Eddy current loss	Iron loss
96	50kW	403.2 W	57.6 W	274.6 W	735 W
192	50kW	552.9 W	122.8 W	779.5 W	1452 W

4.6 Conclusions

This chapter has considered a large number of single-phase machine designs including both 192 pole and 96 pole designs, numerous internal and external rotor designs and machines with Halbach and radially magnetised rotors. Many of these designs had electromagnetic power capability that greatly exceeded the output power that could be sustained thermally. However, with some optimisation of various features a highly competitive 96 pole design based on a PCHF core was established. This has an efficiency of 98% and a power density of 20.4kW/kg based on active mass only of 2.45kg (both at a 50kW operating point). The main features and leading dimensions of this design along with some key performance values are summarised in Table 4.15

Table 4.15 Features of the selected demonstrator design

Parameter	Value	Notes
Rotor configuration	External rotor	
Stator core material	PCHF 125u	
Pole and slot number	96	
Stator and rotor axial length	50	
Stator outer diameter	144	Corresponds to a split ratio of 0.9
Stator inner diameter	128	Corresponds to a stator hub ratio of 0.8
Stator slot width	2.2	
Stator slot radial depth	5.32	
Stator tooth width	2.51mm at airgap 2.16mm at back of slot	Trapezoidal shaped tooth to accommodate parallel slot
Rotor outer diameter	160	
Rotor magnet pole arrangement	Halbach array	
Number of magnet poles	96	
Number of magnet pieces per Pole	4	
Magnet radial depth	7mm	
Number of turns per slot	1	
Calculated active mass*		
Predicted rms current density at 50kW operating point*	128A	
Predicted copper loss at 50kW operating point*	296W	
Predicted iron loss at 50kW operating point	735W	
Efficiency at 50kW operating point	97.9%	

* - based on 0.8 coil packing factor

4.7 REFERENCES

[1] Y. Pang, Z.Q. Zhu, and D.Howe, "Analytical determination of optimal split ratio for permanent magnet brushless motors", IEE Proc. Electrical Power Applications, vol.153, no.1, pp.7-13, Jan 2006.

[2] R.Boll "Soft Magnetic Materials: Fundamentals, Alloys, Properties, Products, Applications: The Vacuumschmelze Handbook", Heyden 1979, ISBN: 3800912724.

[3] Vacuumschmelze GmbH & Co., "Rare-Earth Permanent Magnets," vol. 3, no. 1, 2010.

[4] Elektrisola Dr. Gerd Schildbach GmbH&Co. KG 'Technical basics and calculation of Litz products' 2018

[5] J J H Paulides, "High performance 1.5MW 20,000rpm permanent magnet generator with uncontrolled rectifier for 'more electric' ship applications", Thesis (Ph.D.) - University of Sheffield, Department of Electronic and Electrical Engineering, 2006.

[6] 'The Jet Engine', John Wiley and Sons Ltd, 2015, ISBN10: 1119065992.

[7] Vacuumschmelze GmbH & Co., "Soft magnetic Cobalt-iron Alloys:Vacoflux and Vacodur", 2016 Edition

[8] G.A.V. Sowter, "Soft magnetic materials for audio transformers: history, production and applications", J. Audio Eng. Soc. 35 (1987) 760–777.

[9] Y.G. GUO, J.G. ZHU, and W. WU. "Design and analysis of electric motors with soft magnetic composite core". Studies in Applied Electromagnetics and Mechanics, 15(1):93–99, 2004. Japan Society of Applied Electromagnetics and Mechanics.

[10] L. O. Hultman, and A. G. Jack, "Soft magnetic composites-materials and applications," in Electric Machines and Drives Conference, 2003, IEMDC'03, vol.1, 1-4 June 2003, pp. 516-522.

[11] F. Magnussen, D. Svechkarenko, P. Thelin, C. Sadarangani,'Analysis of a PM machine with concentrated fractional pitch windings Proceedings of Nordic Workshop on Power and Industrial Electronics (NORPIE), Trondheim, Norway, June 14–16 (2004)

[12] H. Shokrollahi, K. Janghorban, 'Soft magnetic composite materials (SMCs)', J. Mater. Process Tech., 189 (2007), pp. 1-12

[13] Somaloy Material Data, Höganäs AB, SE-263 83 Höganäs, Sweden, 2016

[14] Magnetic Powder Cores - E-Brochure, Changsung Corporation, Incheon, Korea, 2014

[15] K. Atallah, D. Howe, "The calculation of iron losses in brushless permanent magnet dc motors", Journal of Magnetism and Magnetic Materials, Vol. 133, Issues 1–3, 1994, pp. 578-582.

[16] R.L. Stoll, 'The analysis of eddy currents', Clarendon Press 1974.

[17] L.K. Rodrigues, "High temperature embedded electrical machines for aerospace turbine applications", Thesis (Ph.D.) - University of Sheffield, Department of Electronic and Electrical Engineering, 2014.

[18] Johannes J. H. Paulides, Geraint W. Jewell, & David Howe, "An Evaluation of Alternative Stator Lamination Materials for a High-Speed, 1.5 MW, Permanent Magnet Generator," IEEE Transactions on Magnetics. Vol. 40, No. 4, July 2004.

[19] J. D. Lavers, P. P. Biringer, and H. Hollitscher, "Simple Method of Estimating Minor Loop Hysteresis Loss in Thin Laminations," IEEE Transactions on Magnetics, vol. 14, pp. 386-388, 1978.

[20] J. Gieras, 'Advancements in electric machines', ser. Power Systems. Springer London.

[21] P. Ponomarev, 'Tooth-Coil Permanent Magnet Synchronous Machine Design for Special Applications', DSc Dissertation, Lappeenranta University of Technology, 2013, ISBN 978-952-265-470-

[22] A. Yu and G. W. Jewell, "Systematic design study into the influence of rotational speed on the torque density of surface-mounted permanent magnet machines," in The Journal of Engineering, vol. 2019, no. 17, pp. 4595-4600, 6 2019.

[23] Z. Q. Zhu, Z. P. Xia, K. Atallah, G. W. Jewell and D. Howe, "Powder alignment system for anisotropic bonded NdFeB Halbach cylinders," in IEEE Transactions on Magnetics, vol. 36, no. 5, pp. 3349-3352, Sept 2000.

[24] M. Marinescu and N. Marinescu, "New concept of permanent magnet excitation for electrical machines: analytical and numerical computation," in IEEE Transactions on Magnetics, vol. 28, no. 2, pp. 1390-1393, March 1992.

[25] K. Atallah and D. Howe, "The application of Halbach cylinders to brushless AC servo motors," in IEEE Transactions on Magnetics, vol. 34, no. 4, pp. 2060-2062, July 1998.

[26] K. Halbach, 'Design of permanent magnet multipole magnets with oriented rare earth cobalt material', Nucl. Instrum. Meth., 169, pp. 1-10, 1980.

[27] Z. Q. Zhu and D. Howe, "Halbach permanent magnet machines and applications: A review," IEE Proc.-Elect. Power Appl., vol. 148, no. 4, pp. 299–308, Jul. 2001.

[28] D. Mansson, "On the Optimization of Halbach Arrays as Energy Storage Media", Progress In Electromagnetics Research B, Vol. 62, 277–288, 2015.

Chapter 5 Prototype machine manufacture and testing

5.1 Introduction

This chapter describes the construction and testing of a prototype machine. The initial machine considered is design 4.6.3 from section 4.5 of chapter 4. Figure 5.1 shows a cross-section through the machine. This is 96 pole machine with a PCHF powdered iron core.

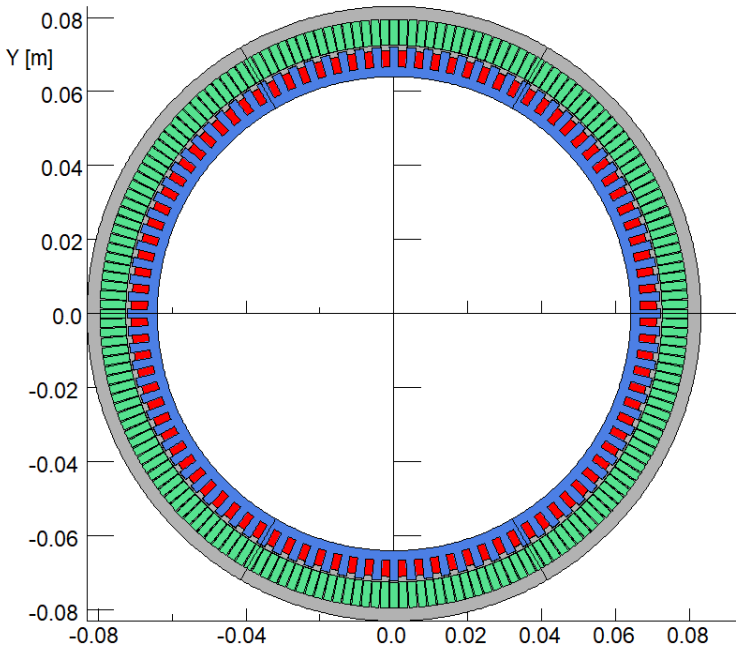

Figure 5.1. Design selected for manufacture

(Design 4.6.3 with dimensions shown previously in Table 4.15)

5.2 Manufacture of a stator core of iron powder core high flux (PCHF)

Magnetic components such as transformer and inductor cores which are made from powdered iron are normally pressed to their final shape in volume production although sometimes key surfaces are the precision ground. However, even for simple shapes, this requires expensive custom tooling. The narrow teeth in this stator could pose challenges for a pressed part and even if it was possible to press the part, this would probably only be possible in short axial length parts and several pressed cores would be needed to make up the 50mm stack length. Although in principle a press-tool could be manufactured to

press the stator core geometry shown previously in Figure 5.1, for one-off or low volume manufacture it is necessary to machine the stator core from a suitable plain ring.

In order to produce a stator core for the prototype machine, eight large toroid shaped PCHF cores were purchased, which included a number of spares for machining trials. The cores in their as-delivered conditions are shown in Figure 5.2(a). These cores have an inner diameter of 88.9mm, and outer diameter of 165mm and an axial length of 25.4mm, i.e. two machined cores would be required to make up the full axial length of 50mm. The rings were supplied with an insulating coating which is the green coating shown in Figure 5.2(a). The first stage in the manufacture involved the bore and the outer surface of the cores being turned to the correct diameters. Figure 5.2(b) shows the machined ring prior to machining of the individual slots.

(a) As delivered

(b) Turned rings prior to slot milling

Figure 5.2 PCHF cores during manufacture

The core was then clamped between two Aluminium end-plates, arranged on a rotary table and successive slots milled with a CNC milling machine. Although the first few machined without any damage to the core, a number of teeth became damaged as machining progressed as shown in Figure 5.3.

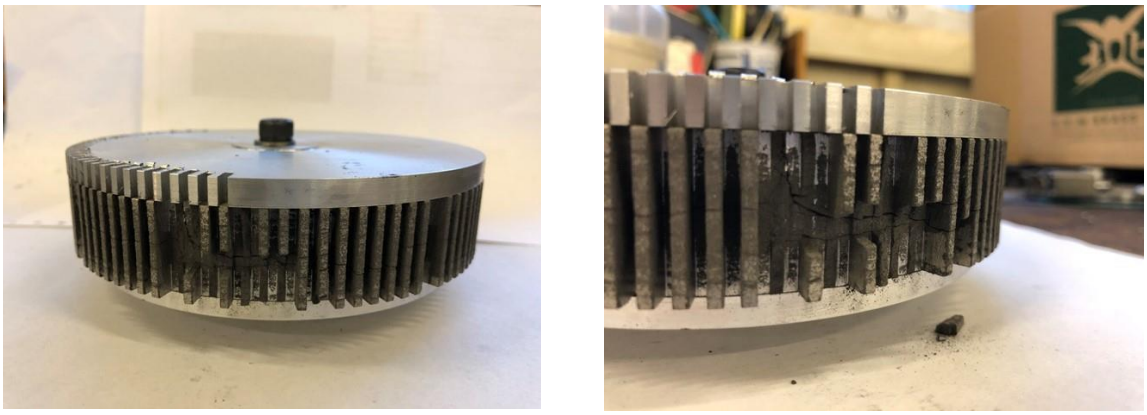

Figure 5.3 Damaged stator core teeth

After several attempts to machine a core with a range of different cutting parameters and the use of supporting PTFE strips into the other finished slots, it was concluded that these cores are too fragile and contain too many cracks (resulting from the original manufacturing process) to reliably machine a core from PCHF. Some of the subsequent cores contained large cracks even during the initial turning phase as shown by the example in Figure 5.4.

Figure 5.4 Cracked core following initial turning

Hence despite promising performance of this material in terms of machine performance (maximum power of 99.7kW at an efficiency of 96.1%) a one-off prototype stator core could not be machined and unfortunately this route to a prototype was abandoned. It may be possible to revisit this material if a geometry specific press-tool was manufactures to press the geometry of the stator as single piece and coat it, but the narrow teeth might be difficult to press and may still be too fragile to withstand the forces applied during coil winding. Alternatively, smaller block could well contain fewer flaws and it might be possible to build up a stator from a large number of small pieces.

5.3 Design of a laminated stator core

The failure to establish a method of stator manufacture for the PCHF required a re-appraisal of the option to produce a machine with a laminated core as opposed to a composite core. In order to manage eddy current losses at the high frequencies encountered in this type machine it is necessary to consider ultra-thin laminations. As was shown in chapter 4, the machine designs with 0.1mm thick Cobalt-iron laminations was not competitive in terms of iron loss even though it is regarded as a high performance and low loss material for many applications. The material whose mechanical properties are suitable for rolling into ultra-thin laminations is Nickel iron which, in available commercially down to 0.02mm, although at high cost [1]. There are many grades of magnetic Nickel iron with Nickel content between 36% and 80% with properties suited a wide variety of applications [2].

Nickel iron is not widely used in electrical machines due to a combination of lower saturation flux density (up to a maximum of 1.6T in the case of 48% NiFe) and cost. Of the various grades available, grades around 48-50% Nickel content offer the best option for electrical machines because of their higher saturation flux density. Although 49% Nickel iron since eddy current loss is likely to be the dominant loss mechanism at frequencies of a few tens of kHz, it is useful to simply compare candidate lamination materials in terms of their electrical resistivity and availability of lamination thickness. Table 4.3 shows a comparison for typical commercial grades of each category of alloy. Although 6.5% Silicon-iron has the highest electrical resistivity [3] [4], it is not available commercially in laminations thinner than 0.1mm. A useful comparator of the performance is the combination of electrical resistivity and thickness factors which comprise the eddy current loss coefficient of the overall iron loss, i.e. $1/(\rho d^2)$. The values of this quantity for the various materials are shown in Table 5.1 for 4 different lamination materials. As shown, the ability to produce very thin sheets of Nickel-iron make it by far the preferred material in terms of eddy current loss despite its resistivity being lower than 6.5% Silicon-iron.

Table 5.1 Comparison for typical commercial soft-magnetic materials

Material	Composition	Electrical resistivity, ρ, ($\mu\Omega$cm)	Minimum lamination thickness, d,*	$\frac{1}{\rho d^2}$	Source of data
3% Silicon Iron	3% Si, Bal. Fe	52	0.1mm	1.92	[5]
6.5% Silicon Iron	6.5% Si, Bal. Fe	82	0.1mm	1.22	[4]
Cobalt iron	49% Co, 2%V, Bal. Fe	40	0.1mm	2.50	[6]
Nickel Iron (Alloy 49)	0.02% C, 0.50% Mn, 0.35% Si, 48% Ni, Bal. Fe	48	0.02mm	52.08	[1] [2]

* - commercially available in some cases by special order with high set-up costs

5.3.1 Design revisions for Nickel Iron core

The starting point for the Nickel Iron demonstrator (designated as design 5.1.1) was a design which was identical in geometry and magnet arrangement to the final preferred design at the end of chapter 4 with a PCHF core and whose attempted manufacture was described previously in this chapter (design 4.6.3). With Nickel iron laminations, this machine produces the V-I curves and the power versus current characteristic shown in Figures 5.5 and 5.6 has a total active mass of 2.51kg (for the case of a coil packing factor of 0.8). As shown in Figure 5.6, the combination of a higher permeability results in a significant increase in power compared to the PCHF core, with a maximum power capability of 144kW. However, this is achieved at an average DC load current of 344A. The slot dimensions for this design is 2.2mm wide and 5.36mm deep and hence this DC load current of 344A corresponds to a rms current density of 49.8A/mm^2 at a coil packing factor of 0.8, increasing to 66.4A/mm^2 rms for a coil packing factor of 0.6 At the more sustainable current density of 10A/mm^2 with a 0.8 coil packing factor (corresponds to an average DC load output current of 69.3A), the load power is reduced to ~40.9kW. The corresponding output power at a current density of 10A/mm^2 rms for a coil packing factor of 0.6 (correspond to a DC load current of 52A) is only 30.9kW.

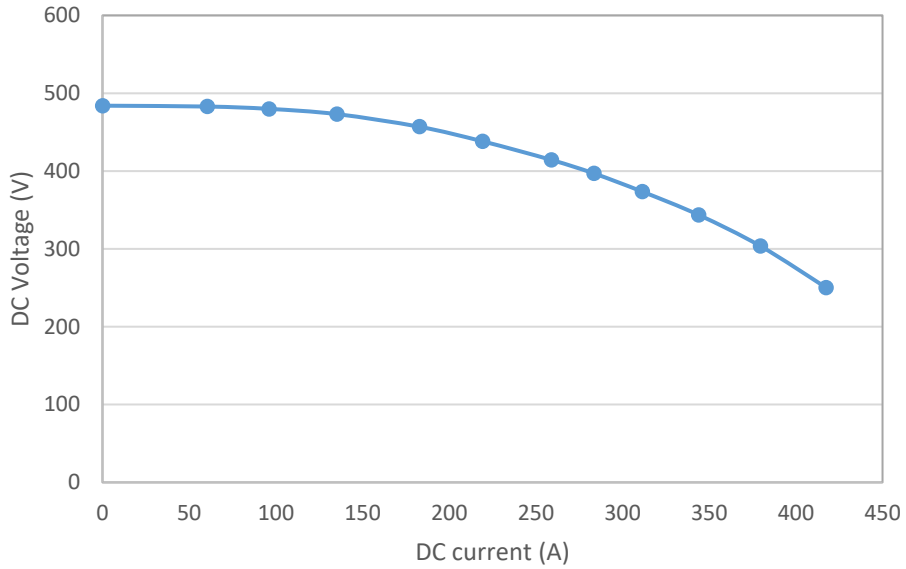

Figure 5.5 Finite element predicted output V-I curve of the Nickel iron machine (design 5.1.1)

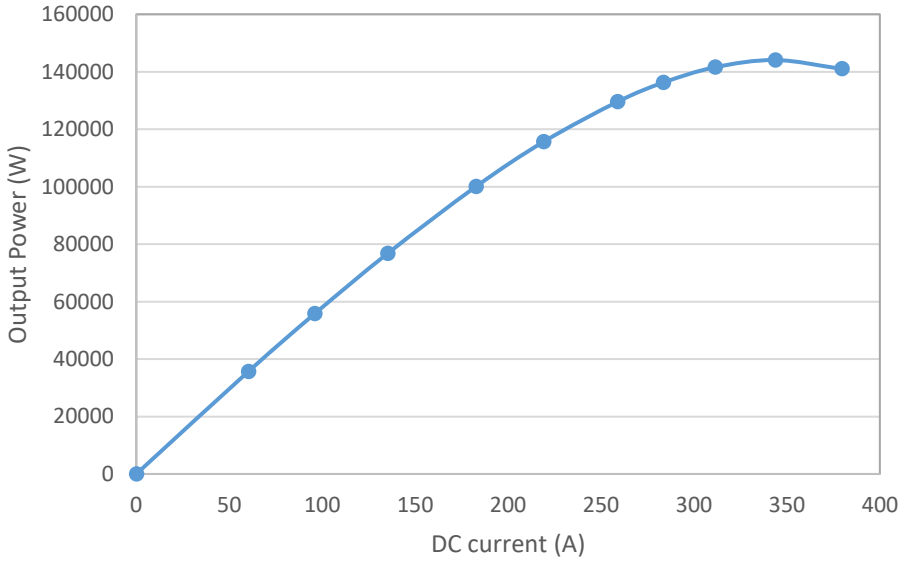

Figure 5.6 Finite element predicted variation in output power with DC load current for Nickel iron machine (design 5.1.1)

It is important to recognise that the slot depth was chosen for the PCHF machine at which a peak power of 99.7kW was achieved at a DC average load current of 358A (corresponds to 51.8A/mm^2 rms or 69.1A/mm^2 rms at coil packing factors of 0.8 and 0,6 respectively). Hence, in order to make use of the additional power capability of the Nickel iron machine, an increase in the slot depth of the Nickel iron machine was explored. Specifically, a further design (designated design 5.1.2) was analysed in which the slot depth was

increased by 2mm from 5.36mm to 7.36mm, A comparison between cross-sections between these two designs is shown in Figure 5.7.

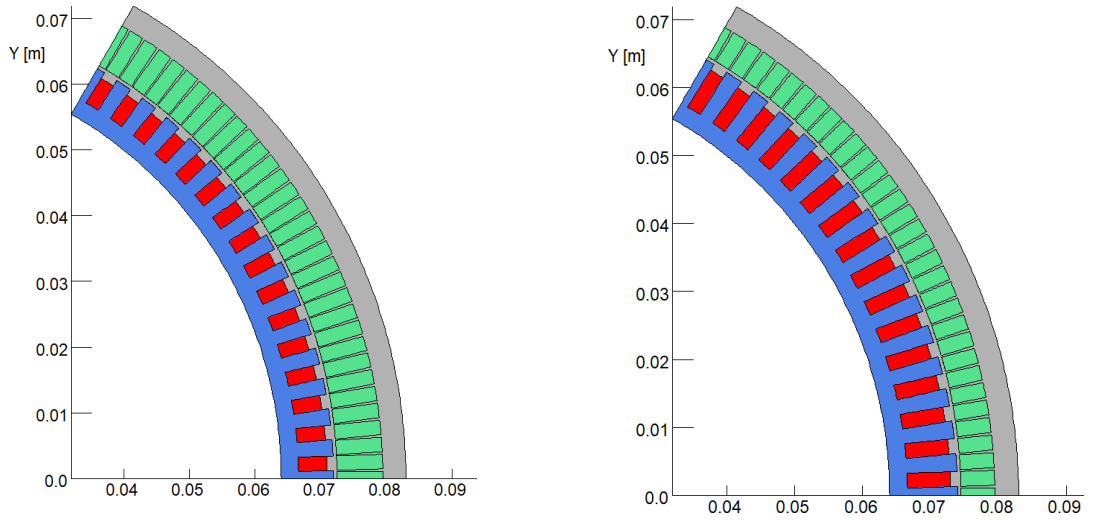

(a) Design 5.1.1 with 5.36mm deep slot (b) Design 5.1.2 with 7.36mm deep slot

Figure 5.7 Cross-sections through Nickel iron designs with different slot depths

The resulting predicted performance of this modified design with the increased slot depth is shown in Figures 5.8 and 5.9. As would be expected, this modified design has a lower maximum power capability (121kW compared to 144kW) due to the increased reactance resulting from the increased slot-depth. It is also worth noting that the DC load current at the maximum power point is 287A compared to 344A in design 5.1.1 with the shallower slots. Due to a reduced DC load current and an increased slot area, the current density at the maximum power operating point is reduced to 28.4A/mm^2 rms at a coil packing factor of 0.8 and 37.9A/mm^2 rms at a coil packing factor of 0.6. Another useful comparison of the benefits of increasing the slot depth is the power capability at a current density of 10A/mm^2 rms. At a coil packing factor of 0.8, the power capability at 10A/mm^2 rms for the 5.36mm slot depth was 40.9kW which increases to 57.5kW for the 7.36mm slot design. The corresponding values for a coil packing factor of 0.6 are 30.9kW and 44.1kW respectively.

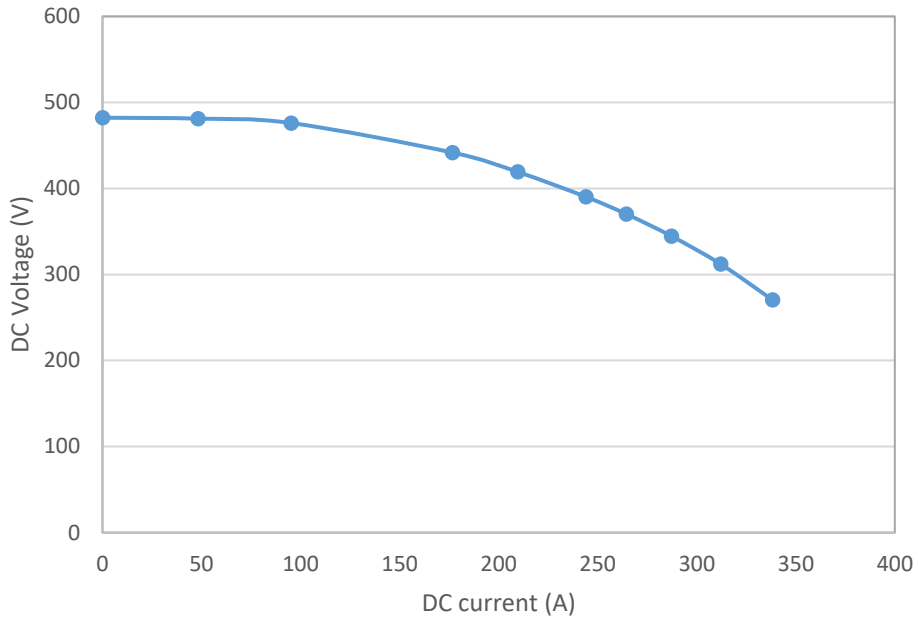

Figure 5.8 Finite element predicted output V-I curve of the Nickel iron design 5.1.2 (7.36mm deep stator slots)

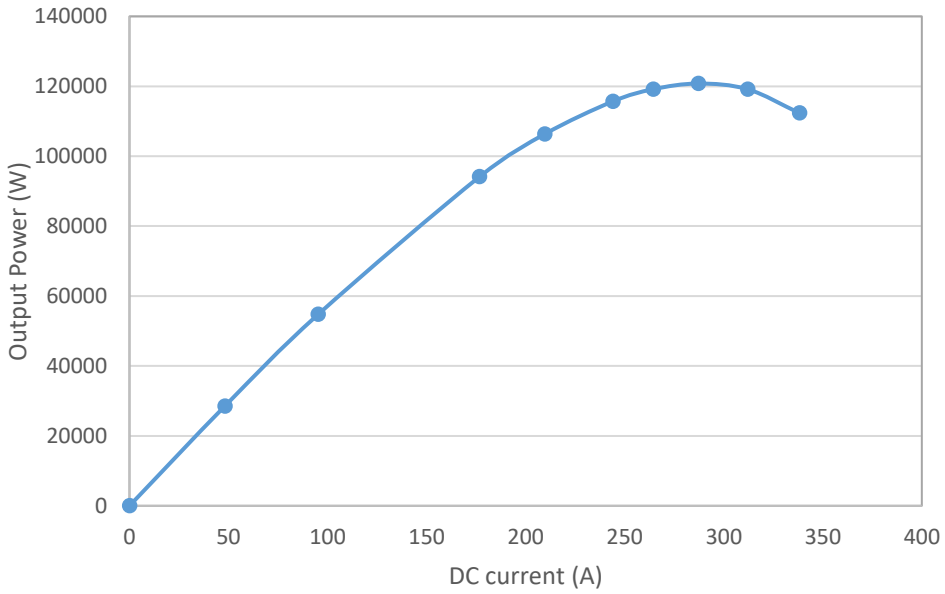

Figure 5.9 Finite element predicted variation in output power with average DC load current for Nickel iron design 5.1.2 (7.36mm deep stator slots)

A further 2mm increase in slot depth to 9.36mm was considered, but this resulted in a further reduction in power capability with a maximum power of 104.8kW at a DC average load current of 313A (corresponding to current densities of 23.6A/mm^2 and

31.5A/mm^2 at coil packing factors of 0.8 and 0.6 respectively). The predicted output power at a current density of 10A/mm^2 rms was 58.3kW and 44.9kW at coil packing factors of 0.8 and 0.6 respectively. Given that there are on benefits in terms of the power at a current density of 10A/mm^2 rms, this further increase in slot depth was not adopted and the slot depth of 7.36mm (design 5.1.2) was selected as the final Nickel Iron design.

5.3.2. Stator core segmentation

Most electrical machine stator cores are formed from a stack of laminations, each of which spans the full cross-section of the machine, i.e. the cross-section is made up of a single lamination. However, in some machines such as very large generators the stator core dimensions are several meters and it is necessary to make-up the stator core from many segments [7].

In the case of the prototype machine considered in this thesis, the stator outer diameter is well within the size that can be produced from commercially available Nickel iron strip. However, for larger stator hub ratios machines such as the designs shown previously in Figure 5.7, a single piece lamination leads to very poor utilisation of the expensive core material. For example, a single piece lamination of the design in Figure 5.7b would need to be cut (by laser, wire-erosion or stamping) from a square sheet for 180mm x 180mm (allowing 15mm residual edge width). This leads to a material utilisation of 8.58%. Hence even is volume production, there may be a case for using a segmented approach in which better utilisation of this high value material can be achieved. If the same stator lamination was made in 24 segments, this could be cut from a rectangular sheet of ~12.5mm x 20mm as shown in Figure 5.10. The utilisation of the material within this 12.5mm x 20mm rectangle is 53%.

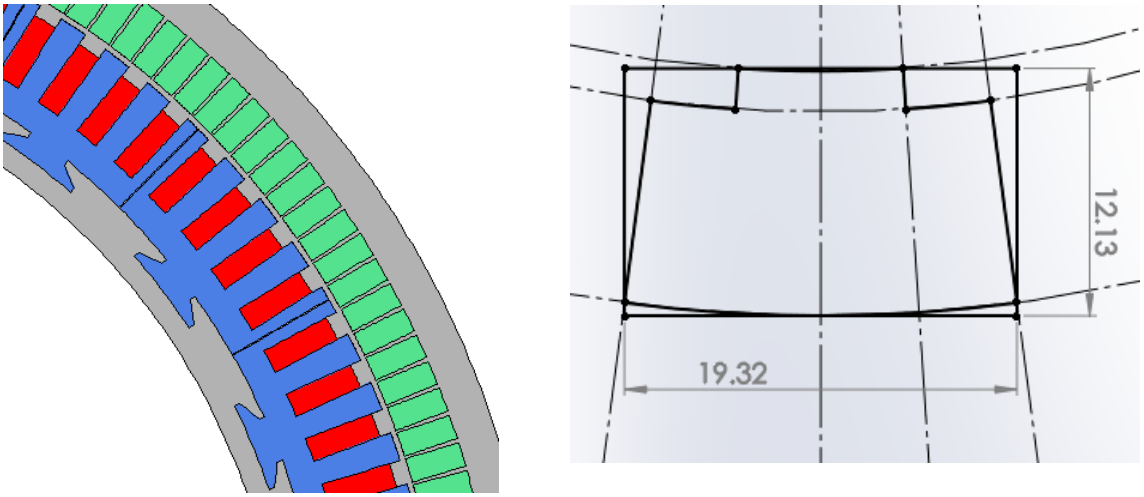

Figure 5.10 Segmented stator arrangement (24 segments) and material requirements

For the one-off prototype in this thesis, material availability in small quantities was also a constraining factor. Although 0.02mm thick material (0.007") is produced commercially by Arnold Magnetics this is manufactured to order with a minimum order of 40lbs (~20kg) at a cost of the order of £800/kg for such small volumes because of the set-up costs. This minimum order requirement made this option prohibitive in terms cost for a one-off prototype recalling that the stator core mass is only ~1kg. An in-stock quantity of 0.03mm thick Nickel iron laminations was identified following an extensive search. In the case of available thin sheets of Nickel Iron, the widest strip available in a small quantity was 170mm which would have allowed a single piece lamination, but unfortunately the total stock of material available was only ~11kg, which necessitated at least segmentation into four 90° (as shown in Figure 5.11) to get a full stator core from this stock.

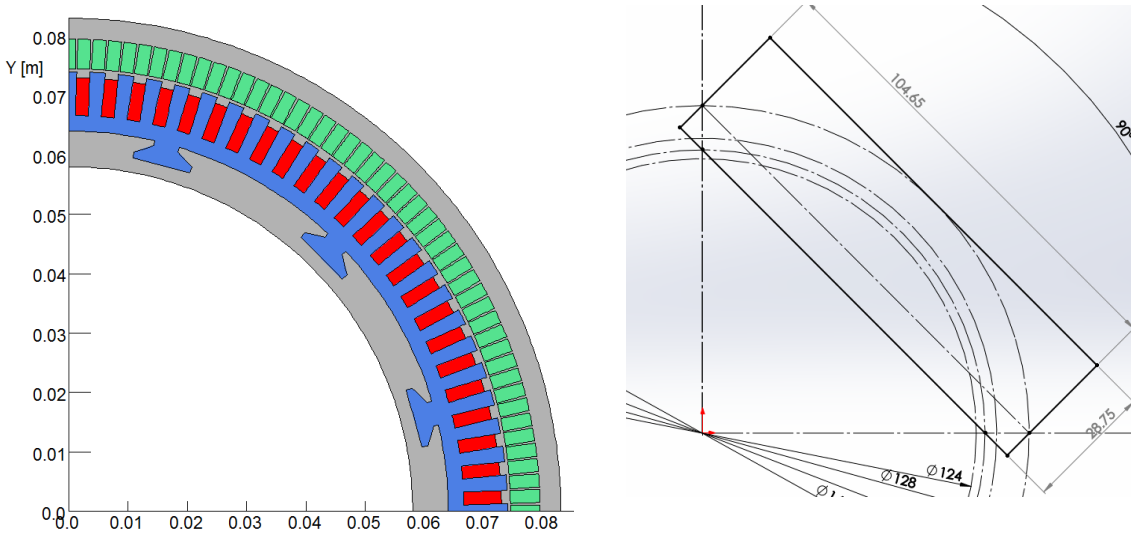

Figure 5.11 Segmented stator arrangement (4 segments) and material requirements

Segmenting a lamination introduces additional airgaps into the stator core which may influence electromagnetic performance, e.g. additional harmonics in the back emf and/or a change in power capability. In order to determine the influence of stator segmentation on machine performance, a series of different degrees of segmentation of the stator core cross-section were simulated. It is worth noting that segmentation requires the incorporation of some means of locating and retaining the stator core modules. In this study, dovetails were introduced on the stator core modules to engage with a stator hub and these were included in the electromagnetic model even though they were not expected to have a significant influence. The gap between segments was represented by a fixed 0.1mm gap in the finite element models.

Figures 5.12 and 5.13 show predicted V-I curves and power versus DC load current characteristics for machines with a single lamination (with no dovetail) and corresponding machine designs which are identical other than segmentation of the stator into 4 and 24 pieces, in both cases with the addition of dovetails for location into the stator hub as shown previously in Figure 5.10 and 5.11. As will be apparent, in terms of these measures of performance, there is no significant effect from segmentation, even with 24 segments. The gaps between segments was assumed to be 0.1mm in the finite element calculations.

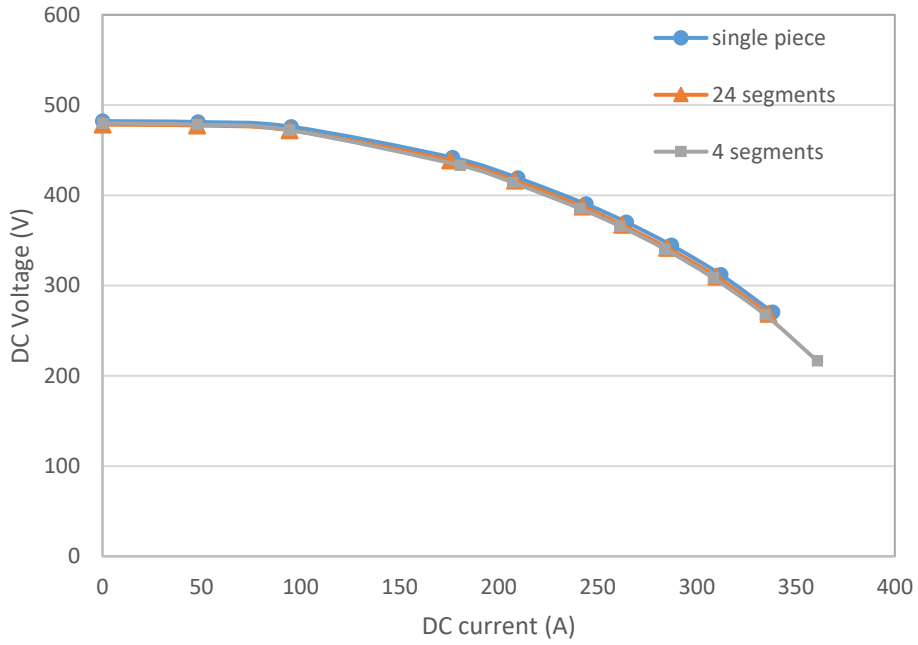

Figure 5.12 Average DC output voltage versus DC load current characteristics for different levels of stator lamination segmentation (single series turn)

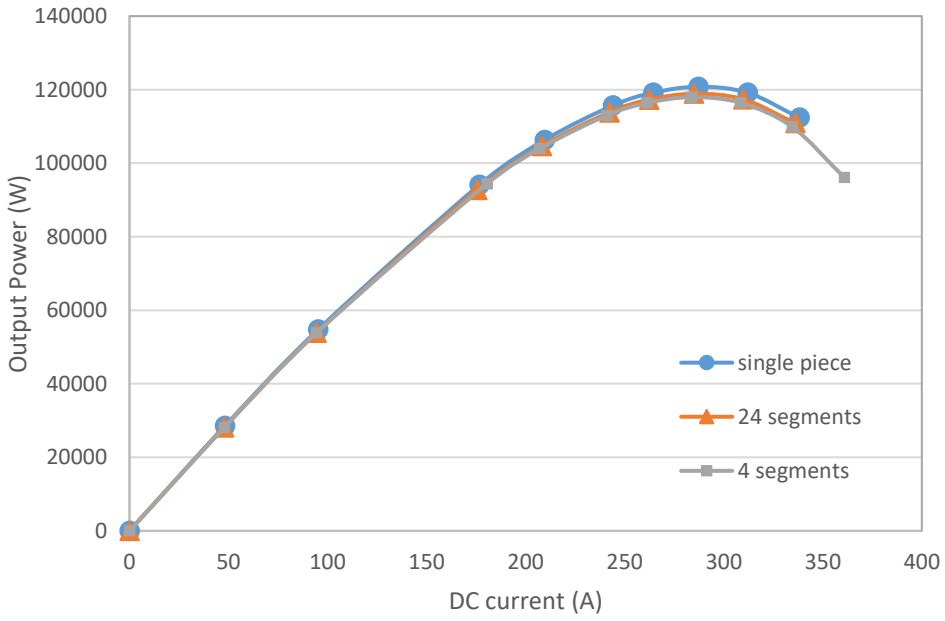

Figure 5.13 Average output power versus DC load current characteristics for different levels of stator lamination segmentationa (airgap 0.5mm in all cases)

On the basis of the characteristics in Figure 5.13 and the limited stock of material, a stator segmentation of four sections was adopted. The remaining dimensions and design features for the final machine selected for prototyping are summarised in Table 5.1.

Table 5.1 Design parameters of the prototype design

Stator Dimensions	
Number of stator segments	4
Number of stator teeth	96mm
Stator outer diameter	148mm
Stator core inner diameter	128mm
Stator dovetail depth	2.00mm
Stator core depth	2.64mm
Stator slot width	2.20mm
Stator slot depth	7.36mm
Stator coil depth	6.36mm
Turns per coil	1
Gaps assumed between segments for FE modelling	0.10mm
Machine active length	50.00mm
Airgap width	0.50mm
Rotor outer diameter	160mm
Magnet circumferential width	2.20mm
Rotor pole pairs	48
Rotor inner diameter	74.5mm
Magnet radial depth	5.00mm
Magnet pieces per pole pair	4
Magnet arrangement	Halbach Array
Angle between magnet	90°

5.3.3 Iron losses for Nickel iron design

The iron loss for this final Nickel-iron design was calculated using the time-stepped finite element method and post-processing tool described in chapter 4. The loss coefficients for 48% Nickel iron are shown in Table 5.2. These coefficients were derived from curve fitting of the published losses of a commercial grade of similar composition (VDM® Magnifer 50) to the material sourced for the demonstrator [8]. The classical eddy current term was established from the electrical resistivity and lamination thickness of 0.03mm for the sample. The finite element predicted iron for this set of material parameters were calculated at a rotational speed of 20,000rpm for the maximum power point of 118kW and a 50kW operating point. The finite element predicted loss distributions are shown in

Figure 5.14. It is interesting to note that for the direct comparison point of an output power of 50kW, the predicted iron loss with this particular Nickel-iron grade in a 0.03mm lamination thickness is lower than the PCHF core as well as offering a higher maximum power capability. Hence, this particular grade of Nickel iron would be a preferred option providing a competitive lamination stacking factor could be realised.

Table 5.2 Iron loss coefficient for 0.03mm thick 48% Nickel-iron laminations

Kh	0.025
α	1.430
β	0.06
Kloop	0.65
Electrical Conductivity (S/m)	2.22×106
Lamination thickness (mm)	0.03
Mass density (kg/m3)	8165
Kexc	0
Kcl	2.08x10-8

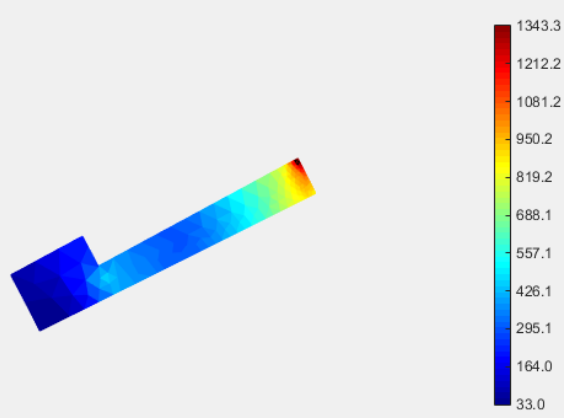

(a) At 118kW/20,000rpm with Nickel iron core – total loss of 394W

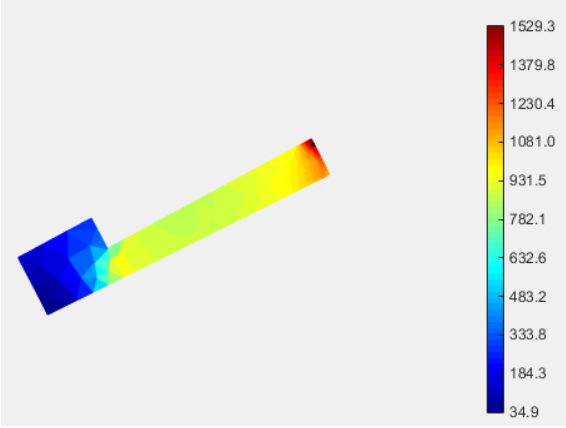

(b) At 50kW /20,000rpm with Nickel iron core – total loss of 739W

Figure 5.14 Predicted iron loss for the final demonstrator design

5.4 Manufacture of the demonstrator machine components

The general arrangement of the machine components is shown in the cross-section of Figure 5.15. In some external rotor machines, the load such as an EV wheel hub is mounted directly onto the rotor outer surface. However, for this machine it is proposed to still use a conventional shaft for coupling to the dynamometer for testing. Both the stator and rotor components are mounted on a central stator shaft. The right hand end of this stator shaft serves as the stationary connection surface for locating and mounting the machine onto a test-rig face-plate hub or rotor hub. In order to connect the machine to an external circuit, it is necessary to feed the ends of the stator winding though the hollow stator shaft.

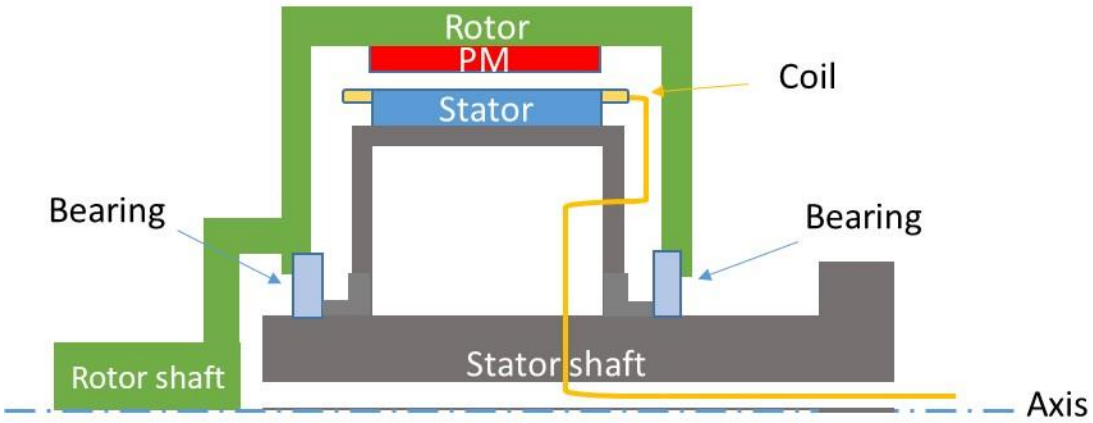

Figure 5.15 General arrangement schematic of machine structure

5.4.1 Stator core manufacture

The first component manufactured was the stator core segments. A 370mm wide roll of Nickel iron was guillotined into 370mm ×70mm rectangular strips and a ~50mm tall stack of these strips (~1515 strips each 0.03mm thick) was assembled and clamped along with a steel top and bottom plates for wire electro-discharge machining (EDM) as shown in Figure 5.16. This stack was welded at several locations around the edge to retain the clamping force during wire EDM and to ensure a good electrical contact between laminations during the EDM process (which is necessary for the current flow involved in the EDM process).

Figure 5.16 Stack of nickel iron materials

Following EDM cutting of each of the four segments, laser welding was used on the inner surface of the stator core segments to join the laminations before release of a clamp applied near the end of cutting (which maintains alignment and compression of the stack during welding). The welded segments are shown in Figure 5.17. There are four thin welding lines in each segment, which are all aligned with a tooth. The small bulging associated with the individual weld lines were removed with abrasive paper. The penetration of each of these precision laser welds was visually estimated to be 0.2-0.4mm in depth, which should not have a major effect on electromagnetic performance given that the stator core back iron is 2.64mm thick. When the clamping was released after welding the height of segments increased to ~53mm due to some spring-back of the stack.

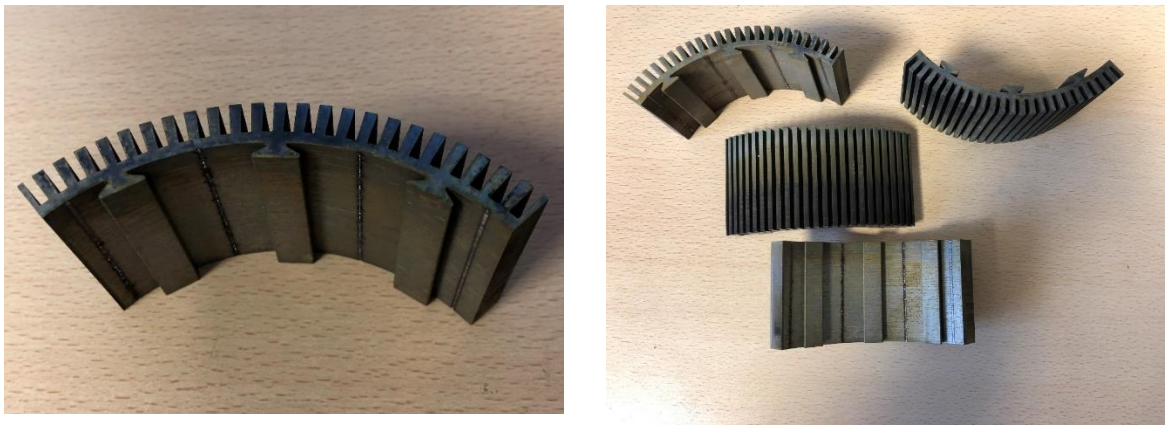

Figure 5.17 Wire eroded and welded stator core segments

5.4.2 Manufacture of the stator assembly

An exploded CAD drawing of the main structural parts are shown in Figure 5.18. The stator hub which locates and retains the stator core segments was manufactured in aluminium using a combination of machining and wire EDM. It incorporates a series of shaped slots which fit the 12 dovetails on the back of the stator core (3 dovetails in each of the 4 segments). These were dimensioned with a 0.1mm clearance relative to the dovetails. The manufactured stator Hub is shown in Figure 5.19. To clamp the stator core segments in place, the two stator end-plates shown in Figure 5.20 were manufactured in aluminium using standard machining methods. These end-caps incorporate bearing housings.

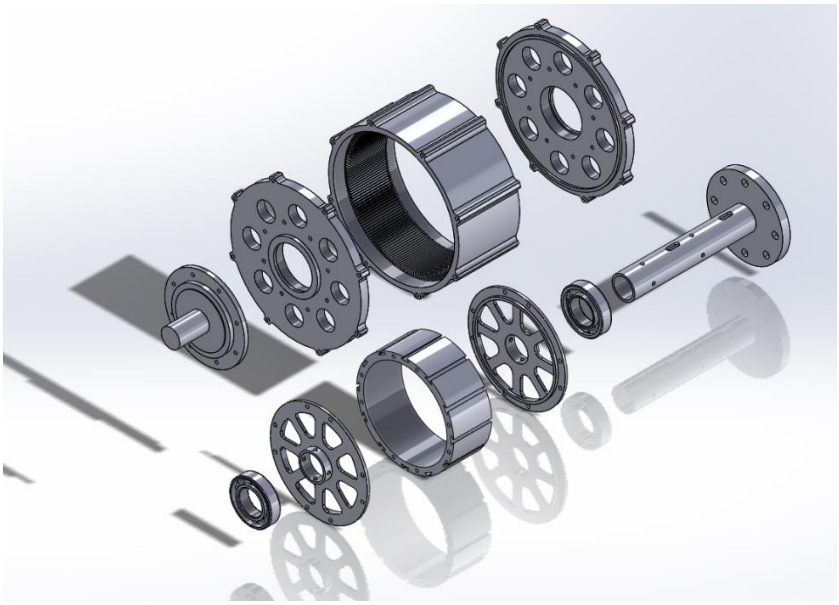

Figure 5.18 Exploded view CAD drawing of structural components

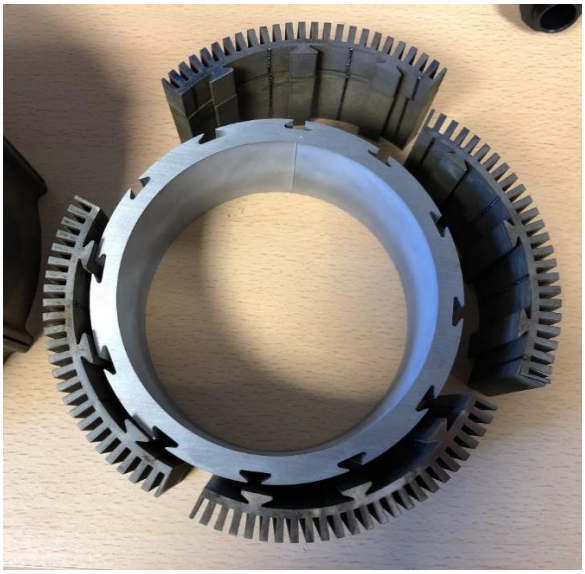

Figure 5.19 Manufactured stator hub prior to fitting of the stator core segments

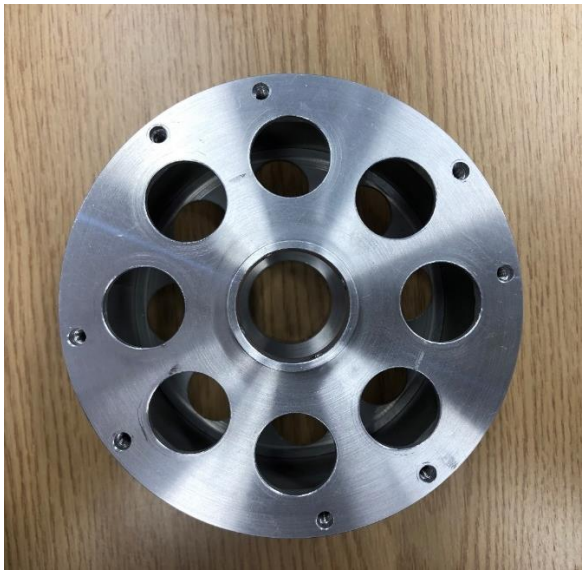

Figure 5.20 Manufactured stator end-caps

Prior to the assembly of the stator segments with in the hub and end-caps a thin (1mm) glass fibre reinforced board was CNC machined with the stator core profile to act as insulating end-plate for the stator core. This plate is useful in terms of avoiding damage to the coil insulation near the ends of the stator core. One of the insulating end-plates is shown in the close-up of Figure 5.21 while the assembled stator structure is shown in Figure 5.22.

Figure 5.21 Close-up of assembled stator with glass-fibre reinforced plates on the ends of the stator core

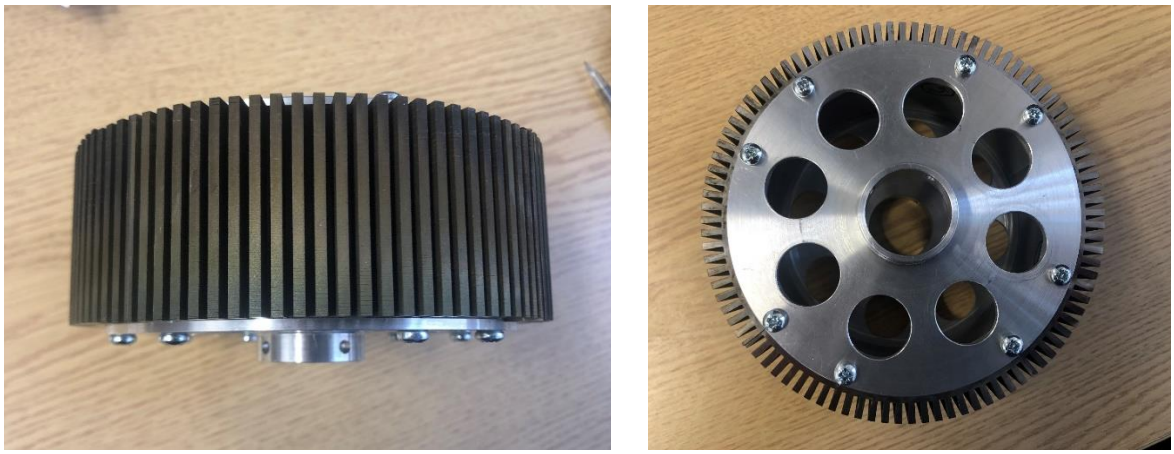

Figure 5.22 Assembled stator

5.4.3 Coil manufacture

As discussed in Chapter 4 preformed rectangular section Litz wire offers the possibility of achieving a good slot factor in a single-turn winding. As shown previously in Figure 4.7 Litz wire manufacturers predict slot fill factors up to 0.8 for tight fitting Litz wire, a condition that requires the manufacture of custom Litz wire. The manufacture of custom wire is often subject a minimum quantity order, usually in the hundreds of kg. Ideally, custom Litz wire would be sourced to suit the exact slot dimensions. However, for this

one-off prototype, it was necessary to select an existing Litz wire that was available in small quantities. The best fit that could be sourced commercially for the prototype was a rectangular formed Litz wire with a cross-section of 4.67mm x 1.57mm. This was made up of 10 strands of AWG 20 (0.812mm diameter) wire, yielding a copper cross-sectional area of 5.19mm^2. This is far from ideal as it gives an overall slot packing factor of only 0.37. Hence, this Litz wire would only allow testing at lower power or intermittent testing at higher powers. Moreover, the relatively large individual wire diameters could be problematic at high frequencies. Ideally, Litz wire of larger cross-section made up of finer strands would be used, but for the purposes of the testing in this chapter, the wire which was available commercially was purchased and used.

The Litz wire was wound by hand into the slots to produce a serpentine winding. However, since the width of the teeth is quite narrow (~2 mm) the resulting tight turn of Litz wire in the end-winding resulted in some splaying out of the individual strands in the Litz. This made forming of a tight end-winding with repeatable geometry difficult in practice. As shown in Figure 5.23, there was some inconsistency in the shape and dimension of the end-winding despite repeated attempts with different tools, including the use of 2mm thick PTFE formers around which the end-winding was formed. Despite these difficulties, eventually a pair of windings spanning 24 slots (i.e. one 90° stator segment) were successfully wound. After the winding was formed, the slot liner was trimmed back and the winding was varnish manually using RS 199-1480 insulating varnish. Figure 5.24 shows the wound stator.

Deformed from bending in the end

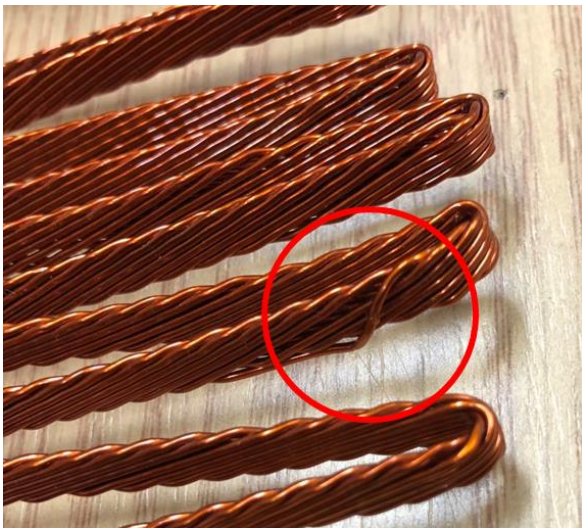

Single strands deform

Figure 5.23 Litz wire end-winding deformation

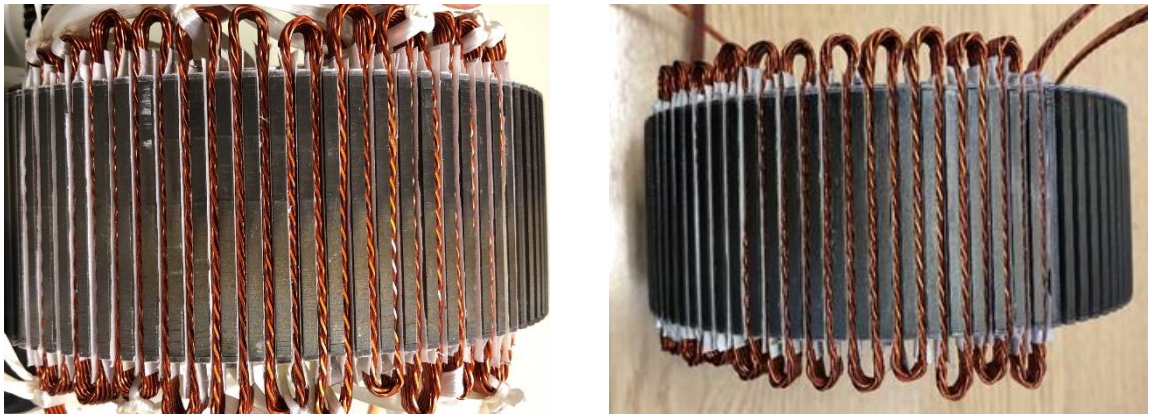

Prior to varnishing After varnishing

Figure 5.24 Wound stator

5.4.4 Rotor manufacture

The rotor hub is a component that is required to rotate at high speed while retaining the magnets against centrifugal forces. It is also worth noting that the hub will include locating features to allow the precise construction of the very high pole number magnet array. The Halbach array used for the rotor hub means that a non-magnetic hub can be used. The following mechanical properties are the most important in terms of selecting the preferred material for the hub

- Low mass density – this will help in terms of both the overall machine mass the centrifugal self-loading of the hub.
- High Young modulus and hence stiffness to avoid excessive strain of the rotor and hence a change in magnetic airgap.
- High yield stress – It is common in design practice to set the maximum component stress to some fraction of the material yield stress (usually the 0.2% yield stress point). Hence, a high yield stress allows a thinner hub to be employed.

As a non-magnetic component in electrical machine, there are two main material options for the rotor hub: Aluminium and Titanium. A summary of key physical properties for these materials are shown in Table 5.2 along with the properties of the Sm_2Co_{17} magnets. As shown, although Titanium has a higher density than Aluminium and hence will have a greater self-loading due to centrifugal forces, it has a significantly higher yield stress.

Another important factor in material selection is the potential for thermal expansion mis-match between different elements of the rotor. As shown by the date in Table 5.2, Titanium is a much close match to the rotor magnets which have a typical coefficient of thermal expansion of 8-12 μm/m.K.

Table 5.2 physical properties of materials used in the prototype

	Density (kg/m3)	Young's modulus (GPa)	0.2% Yield Stress (MPa)	Ultimate Tensile Strength (MPa)	Thermal expansion (μm/m.K)
Aluminium 7000 Series (7075-T60)	2820	70	503	572	21.4-22.5
Titanium Grade 5	4430	113.8	880	950	9.2

Taking a worst case assumption that the magnets act as a dead-weight on the containment sleeve (i.e. neglecting the effect of an adhesive bond between the individual magnets and the rotor core) then the maximum stress in a containment sleeve at a rotational speed of ω is given by the following equations [9] which were used previously in Chapter 4 for calculating containment sleeve thickness for an internal rotor machine:

$$\sigma_{\max} = \frac{\delta_c \omega^2}{8}\left[(3+\nu_c)\left(\frac{d_{co}^2}{2}+\frac{d_{ci}^2}{4}\right)-(1+3\nu_c)\frac{d_{ci}^2}{4}\right]+\left(\frac{d_{ci}^2+d_{co}^2}{d_{co}^2-d_{ci}^2}\right)\left(\frac{m_{eq} r_{meq} \omega^2}{\pi\, d_{mo}}\right) \tag{5.1}$$

Where the effective mass and radius of the arc shaped magnet pieces (which are a reasonable mechanical representation of the Halbach array) are given by:

$$m_{eq} = \frac{\pi}{4}\left(d_{mo}^2 - d_{mi}^2\right)\left(\frac{\alpha\delta_m}{180}+\left(1-\frac{\alpha}{180}\right)\delta_{ip}\right)$$

$$r_{meq} = \frac{\sqrt{2}}{2}\sqrt{\frac{(d_{mo}^4 - d_{mi}^4)}{4(d_{mo}^2 - d_{mi}^2)}}$$

These analytical formulae were used to calculate the stress in various designs of rotor hub in both Aluminium and Titanium with the full magnet array acting as a uniformly distributed dead-weight on the hub. Figure 5.25 shows the analytically predicted hoop

stress in the hub as a function of rotor hub wall thicknesses at 20,000rpm. It is common design practice to operate a metal at some proportion of its yield stress, typically 50-60% to allow some margin to account for fatigue etc [10]. Applying a 50% yield stress design criterion gives maximum operating stress levels of 250 MPa and 440MPa for Aluminium and Titanium respectively. As shown by Figure 5.25, a 4 mm thick Titanium hub can meet this stress criteria while a 9mm thick Aluminium hub would be required.

Although the hoop stress in the Titanium hub is higher at a given thickness than an Aluminium hub, the higher stiffness of Titanium means that the growth in airgap for a particular hub thickness is smaller with a Titanium hub as shown in Figure 5.26. The combination of a much thinner hub, greater stiffness and improved thermal expansion match with the rotor magnets, make Titanium the preferred material for this application. However, rather than adopt the 4mm hub thickness to limit the stress to 50% of the yield, the Titanium hub thickness was increased to 6mm to limit the change in airgap to <0.25mm.

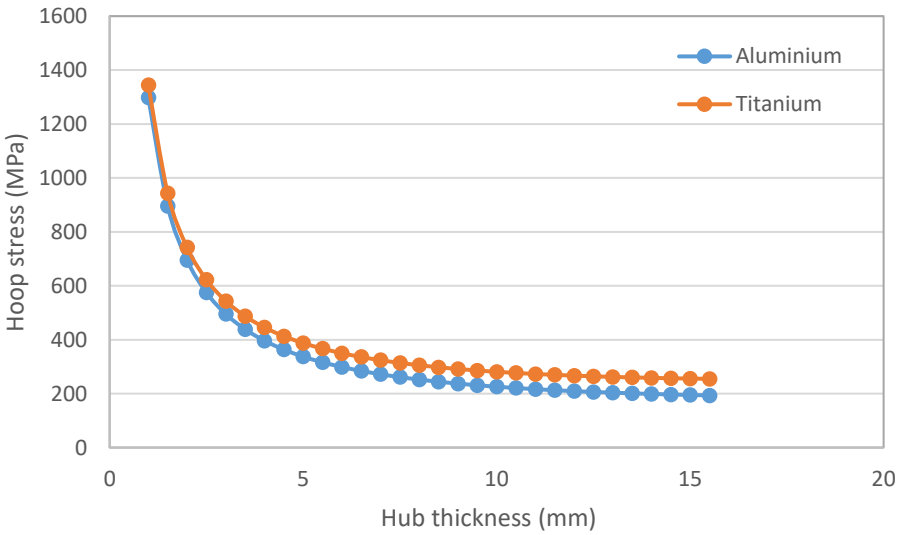

Figure 5.25 Hoop stress in two material rotor hub at 20,000 rpm

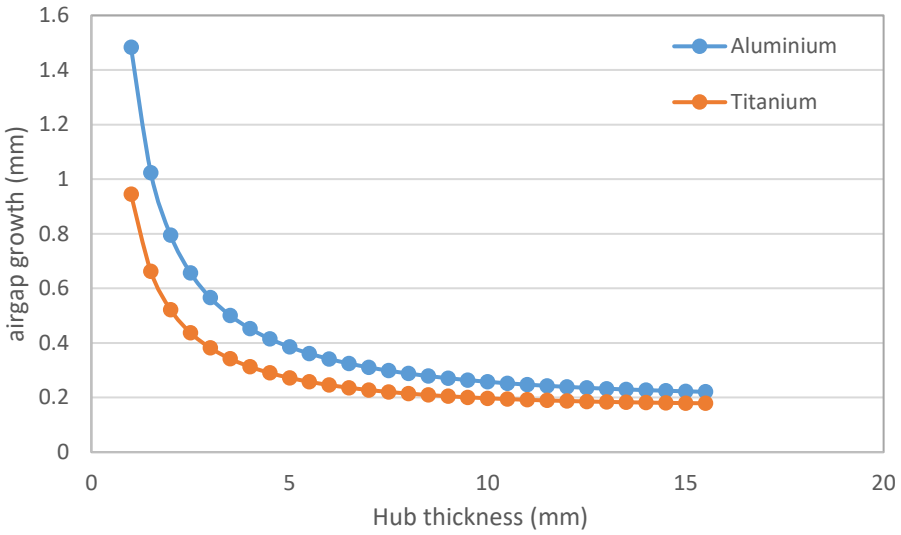

Figure 5.26 Airgap growth from hoop stress in two material rotor hub at 20,000 rpm

Figure 5.27 shows the Titanium rotor hub used to hold the individual magnet poles. This was manufactured by wire electro-discharge machining from a solid Titanium billet. The initial internal bore was first cut by EDM and then the first 15mm from each end was turned out to form a step which corresponds with the end of the frame which locate the magnet pieces. A series of 192 thin ribs were subsequently cut to hold the magnets. These were dimensioned taking into account the manufacturer specified tolerance of ±0.2mm. Finally, the outer profile, which includes a series of bosses for tie-rods, was cut by wire EDM.

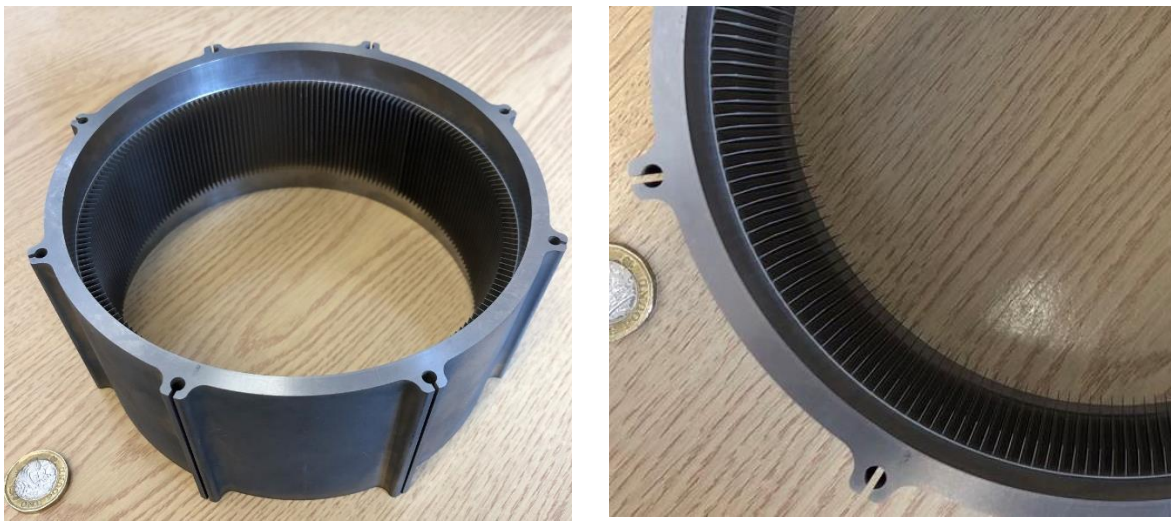

Figure 5.27 Titanium rotor hub

One feature of the wire EDM process is that internal corners are left with a small radius in the corner (order of 0.16mm in the case of the 0.25mm wire used). To allow for this and to prevent the magnets from sitting proud of the specified rotor bore, and additional 0.2mm was added to the slot depth. Following several trial methods, eventually a method for inserting and gluing the magnets was established which used a series of specifically sized PTFE spacers and a series of miniature clamps to define precisely the location of the magnet to be inserted. This still posed challenges in terms of the force exerted on the magnets during manual assembly.

Figure 5.28 shows a typical arrangement of the spacers and the rotor assembly with one of the four magnet pieces per pole inserted in all poles. The first pass shown in Figure 5.28 in which a quarter of the magnet pieces were inserted was more straightforward, both in terms of the forces on the magnets during assembly and the fit of the magnets into the Titanium frame. Whereas each of these first set of magnets fitted into the slots in the Titanium rotor housing, it did result in some flexure of the thin-walled Titanium separators between adjacent poles. When it came to inserting the remaining pieces, many of these did not fit into the remaining slots. An attempt was made to thin down the magnet pieces by ~0.2mm using a holding jig and a wire-eroder, in which the wire made a pass along the surface of an array of magnets to erode a thin layer. The set-up used is shown in Figure 5.29. Unfortunately, this did not result in a sufficient consistent thinning down and resulted in considerable agglomeration of magnetised powder on the magnets. Hence, it was concluded that a new set of slightly narrower magnet pieces were required to complete the third and fourth passes of the rotor magnets. Unfortunately, a second set of narrower Sm_2Co_{17} magnets were only available on a very long lead-time while a set of NdFeB of similar remanence and energy product were available from stock. Specifically, the Sm_2Co_{17} used in the rotor had a manufacturer quoted remanence of 1.10T while the N35 grade NdFeB has a remanence of 1.17-1.22T. Hence, the rotor was finished with a mixture of Sm_2Co_{17} and NdFeB. Although not directly comparable in terms of elevated temperature performance etc., this substitution was deemed appropriate for the testing which was scheduled to be undertaken.

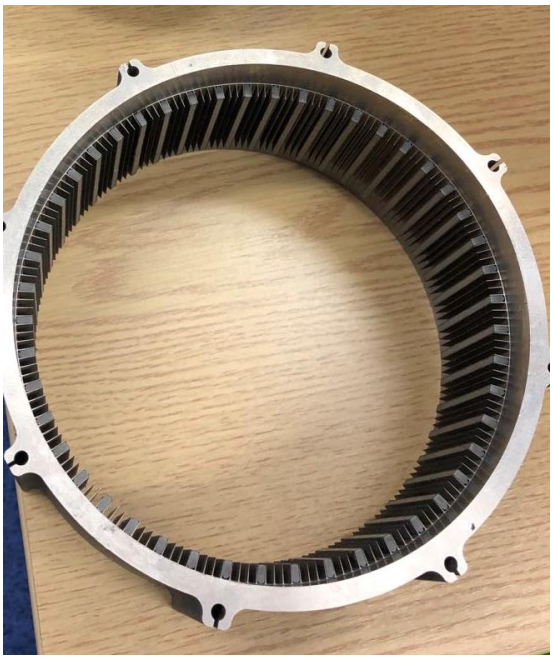

Figure 5.28 Rotor magnet assembly – first pass of one piece in each pole pair

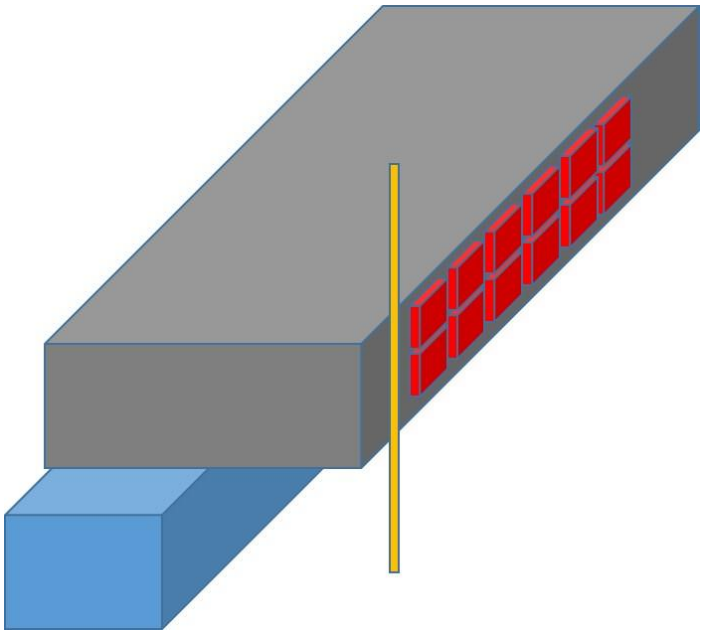

Figure 5.29 Schematic of wire-eroder arrangement used to attempt to thin-down the Sm_2Co_{17} magnets

Figure 5.30 shows the rotor following insertion of all 1920 magnet pieces (10 magnets in each of 192 slots). Inspection of this rotor revealed a small number instances of the magnet pieces being proud of the nominal bore. Hence, a finishing cut using wire EDM was used to produce a smooth bore. The effect of this finishing cut is shown in Figure

5.30, in which it can be seen that only a proportion of the magnets were cut-back (shown by the absence of the Nickel coating applied to the magnets).

Figure 5.30 Rotor frame fully populated with rotor magnets

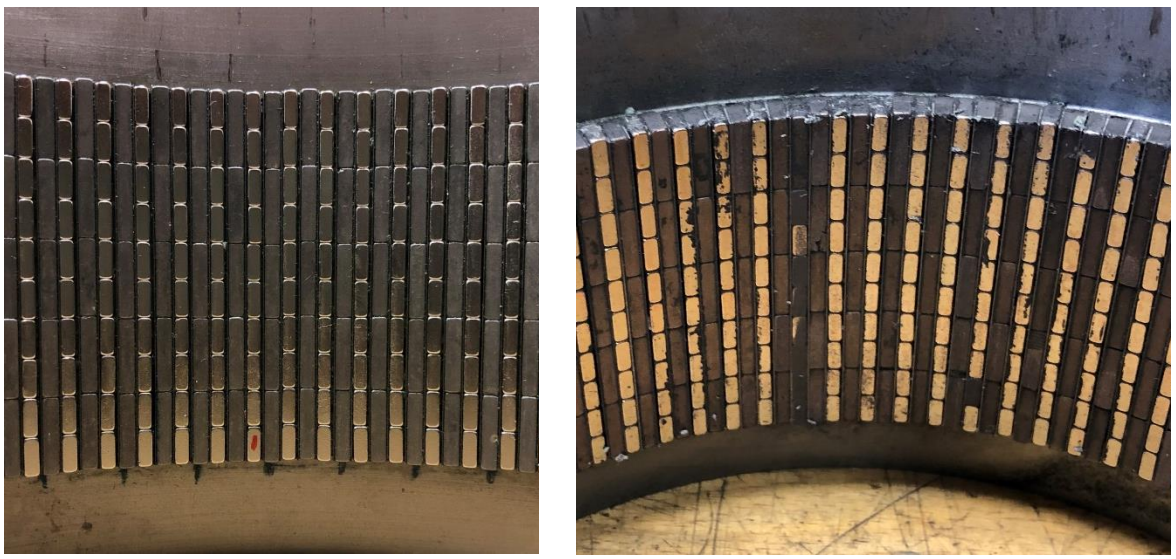

Figure 5.31 Section of the rotor showing the effect of a finishing cut using EDM

The remaining mechanical components of the rotor, which are shown in Figures 5.32 were manufactured in Aluminium by a combination of CNC machining and wire EDM. In order accommodate the irregular end-winding shown previously in Figure 5.24, it proved necessary to adapt the rotor end-plate to incorporate a recess to accommodate the extra overhang compared to that assumed in the design stage.

(a) Rotor end-plate inward-facing face

(b) Rotor end-plate inward-facing face

(c) Rotor shaft

(d) Rotor shaft

Figure 5.32 Rotor mechanical components

5.4.5 Final assembly

The fully assembled machine is shown in Figure 5.33. The first attempt at assembly resulted in some asymmetry in the final airgap to the extent that the rotor and stator were in contact at some points around the periphery. The full set of sub-assemblies were checked for dimensional tolerance and concentricity. The rotor, as noted previously in this chapter was skimmed using a wire eroder and was found to be circular to within ±0.064mm and with a measured bore diameter of 148.946mm. The assembled stator was

measured using a clock and found to be circular within ±0.10mm with a measured diameter of 148.09mm. The concentricity of the rotor endcap locating shoulders and bearing housing were checked with a clock. Hence, in principle with a working airgap of 0.5mm, the entire machine should have come together with a clear airgap all round. However, when assembled, the rotor was binding on the stator bore and 0.25mm shims could not be inserted down the airgap at some locations around the periphery. It was concluded that the process of assembling itself was causing some degree of asymmetry in the rotor / stator alignment, e.g. radial displacement of the stator sections due to magnetic attraction forces.

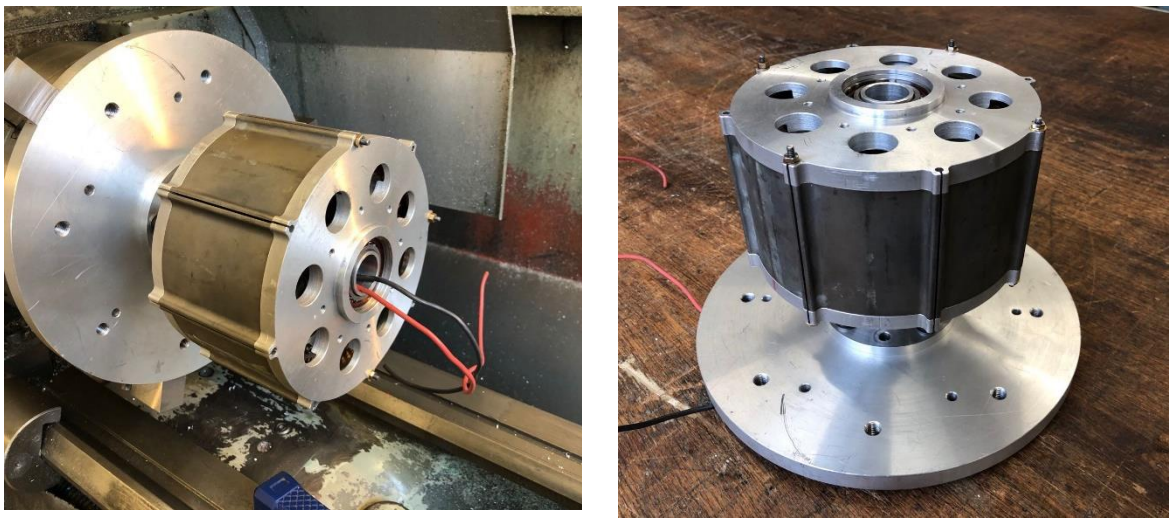

Figure 5.33 Assembled machine

The machine was dis-assembled on several occasions and many measurements and checks performed but it did not provide possible to retain a clearance around the full airgap. The two un-wound stator core segments were removed and this showed up a small amount of radial play in the dovetail joints which secure the segments to stator hub which may be a contributing factor to a closing of the gap at some locations given the large radial magnetic force in the airgap. There is also the possibility that the central stator shaft and end-caps are not sufficiently stiff to resist unbalanced magnetic pull resulting in deformation on the scale of a few tenths of millimetres. Ultimately it was concluded that although significant progress had been made in manufacturing a demonstrator machine, the numerous challenges in manufacturing such a novel and different topology could not be resolved within the time-frame of this research

programme (see several suggestions for future work in this field in Chapter 6) and hence no testing was performed on the demonstrator machine.

5.5 Conclusions

This chapter has described two attempts at manufacturing a demonstrator machine for testing. It has shown the complexity of manufacturing such a high pole number machine, particularly with it being an external rotor topology, has led to several challenges which could not be resolved within the time-frame of this project. Several potential modifications and further areas of work to overcome these challenges are described in chapter 6.

5.6 References

[1] 'Nickel Irons and Soft Magnetics Specification Sheet'. Arnold Magnetic Technologies, 2017.

[2] B. Gehrmann, 'Nickel–iron alloys with special soft magnetic properties for specific applications', Journal of Magnetism and Magnetic Materials, Volumes 290–291, Part 2, April 2005, Pages 1419-1422.

[3] G. Ouyang, X. Chen, Y.Liang, C. Macziewskia, J. Cui, 'Review of Fe-6.5 wt%Si high silicon steel—A promising soft magnetic material for sub-kHz application', Journal of Magnetism and Magnetic Materials, Volume 481, 1 July 2019, Pages 234-250.

[4] 'Super Core TM - Electrical steel sheets for high-frequency application', JFE Steel Corporation, Cat.No.F1E-002-02.

[5] Non-oriented electrical steel - Typical data. Cogent Surahammars Bruks AB, Surahammar, Sweden, 2016

[6] Hiperco 50 alloy data Carpenter Technology Corporation, US, 2005 Vacoflux50 (0.025mm 280mm/width) P248

[7] M. Znidarich, "Hydro generator stator cores part 1- constructional features and core losses," in Proc. Australasian Univ. Power Eng. Conf., Sydney, Australia, 2008, pp. 1–8.

[8] VDM Metals, 'VDM® Magnifer 50', Material Data Sheet No. 9002, 2002.

[9] J. J. H Paulides, "High performance 1.5MW 20,000rpm permanent magnet generator with uncontrolled rectifier for 'more electric' ship applications", Thesis (Ph.D.) - University of Sheffield, Department of Electronic and Electrical Engineering, 2006.

[10] J.M. Gere, S.P. Timoshenko, 'Mechanics of materials', Third SI Edition, Chapman & Hall, 1991

Chapter 6 Conclusions

6.1 Introduction

This thesis has described a comprehensive investigation into a novel type of permanent magnet machine to produce a very high output frequency as the direct input to a soft-switched pulse density modulation converter. The thesis has focussed on the electromagnetic design of machines capable of meeting the very unusual performance specification of this application. This performance specification, in particular the high output frequency, has resulted in several novel aspects in this thesis compared to mainstream permanent magnet machines covering topology, material selection and winding configuration. One important factor in this respect is the overriding importance of iron loss in selecting the preferred topology and core material, including consideration of several powder based and ultra-thin laminated core materials which are not normally considered for mainstream high performance electrical machines. This chapter discusses the key outcomes from the research and identifies several aspects for future research.

6.2 Key conclusions

Each individual chapter in this thesis has drawn chapter-specific conclusions. This discussion of key conclusions is not intended to repeat these individual chapter level conclusions. This discussion will instead focus on some key outcomes which provide useful guidance for any future design or research on very high output frequency permanent magnet machines.

Chapter 2 developed a simplified model of a PDM converter and demonstrated the benefits of a higher generator output frequency in terms of minimising converter output voltage distortion and filter requirements. A generator output frequency of 32kHz allowed the THD specification to be met while also allowing a gap between the natural frequency of the second-order filter and the 400Hz fundamental of a AC system. Whereas an output frequency of 16kHz can meet THD requirements under some circumstances, the resulting filter natural frequency is far closer to the fundamental than would normally be considered as good filter design practice with some risk of resonant behaviour. The need for such high generator frequencies in order to produce an acceptable voltage waveform is also partly due to the 400Hz fundamental required for aircraft. A 50Hz

fundamental in a non-aerospace application would have been easier to accommodate with a 16kHz or possibly even an 8kHz output.

The numerous flux-switching and flux-modulation machines considered in chapter 3 were only capable of producing very modest output power levels although they were able to produce the required output frequency with a low number of conventional coils. This poor performance was due to a combination of significant inter-pole leakage which is inevitable with very fine magnet pole-pitches and the high machine reactance which limited the electromagnetic power capability.

Single-phase surface mounted permanent magnet machines with a serpentine winding of the type adopted as the preferred solution in chapter 4 of this thesis are able to achieve very high electromagnetic power limits of >100kW, though often at excessive current densities and hence unsustainable copper loss. In the case of very fine pole pitches considered (2.36mm with 192 rotor poles) predicted performance is very sensitive to the length of the magnetic airgap, which required a shift to an external rotor machine in which the magnet retaining structure is not in the working airgap.

Several different powder based soft magnetic materials were evaluated in chapter 4. These spanned a range of permeabilities and loss coefficient. At 32kHz, the lowest permeability material (PCHF powdered iron) offered the best performance in terms of minimising loss while retaining sufficient power capability. However, for 192 pole machines (32kHz AC output frequency) considered in chapter 4, the iron losses were extremely high and unsustainable and it proved necessary to move to a 16kHz generator (96 poles). Not only did this change in frequency considerably reduce the machine core loss but it also resulted in a useful increase in the electromagnetic power capability. Chapter 4 contains numerous predictions of electromagnetic power and losses, but the basic electromagnetic potential of the adopted machine topology is shown by the predicted performance of the final design at the end of chapter 4. For this machine (detailed in Table 4.15) the power density (based on active mass only) is 20.4kW/kg at an efficiency of 98.0% at a 50kW operating point of 50kW and 40.7kW/kg at 96.2% for the maximum electromagnetic power operating point of 99.7kW. Other important outcomes included the benefits of a Halbach array and the significant influence of stator slot depth on the reactance in such narrow slots and hence the limitations on electromagnetic power capability.

The manufacture of a demonstrator machine was reported in chapter 5. Initially, many attempts were made to produce a PCHF powdered iron core but ultimately this route was not successful. The manufacturing route selected attempted to produce a single piece core from a large ring but this proved not possible due to a combination of cracks, material flaws and residual stress within the large rings and the poor mechanical strength of narrow teeth. The cracks and residual stresses are likely to be more of a concern in very large rings because of the greater stresses induced during heating and cooling. An alternative approach which could be considered in future attempts would be to manufacture a modular stator in which a number of smaller stator segments are machined or, even better, pressed in custom tooling. These stator modules could then be combined into a full stator core. The problems with the manufacture of a powder core required a change to using ultra-thin Nickel iron laminations. Although predictions of performance in terms of electromagnetic power capability and core loss for ultra-thin Nickel iron laminations were promising, the availability of material in small quantities and at reasonable cost was problematic. It is difficult to extrapolate small batch prices (such as the £1000/kg quoted for custom manufacture of ~20kg which include significant set-up costs) with production volume costs, but it is inevitable that very thin laminations of Nickel Iron will be an expensive material option (likely £100s per kg). In this regard, is worth recognising that the demonstrator in Chapter 5 only contains 1kg of Nickel Iron.

The high frequency, small slot dimensions and the need for a single turn per slot for the performance specification in this study offered scope to produce a precise winding with a good slot packing factor. Although some Litz wire was sourced from the stock range of a manufacturer this did not result in an adequate slot packing factor. Furthermore, the low number of strands limited the flexibility of the overall wire and resulted in some challenges in producing neat and consistent end-windings, with individual conductors tending to come out of the bundle on sharp turns. The manufacture of a custom Litz wire (typical minimum orders being ~300kg) would result in a profile which would be a better fit to the stator slot and a more flexible wire with many more strands of smaller individual diameter.

The problems encountered in building the components of the prototype machine and the assembly of the full machine demonstrated the many manufacturing challenges involved in this unusual machine. Several of the arising issues are discussed in the future research section later in this chapter. The most likely cause of the difficulty is the limited stiffness

of the central stator supporting shaft and its ability to resist deflection and hence lead to some loss of concentricity.

Finally, despite the numerous difficulties encountered in the manufacture of a prototype machines, the designs developed in this thesis have resulted in very competitive predicted power densities, e.g. 25.5kW/kg for the final Nickel-iron design in chapter 5 at a predicted efficiency of 98.2% at 50kW and 60.2kW/kg and 98.5% at its maximum power point of 118kW. Hence, this study has demonstrated, at least from an electromagnetic perspective, the promise of this type of machine, both for the specific application considered in this thesis, but also more widely as a high power density single-phase generator.

6.3 Suggestions for future work

There are several aspects of the research undertaken in thesis which have identified future opportunities for research. Many of these relate to mechanical design and manufacturing issues. The following are specific issues that would drive-forward the realisation of state-of-the-art high frequency and power dense permanent magnet machines:

Mechanical re-design of demonstrator machine - The main limitation of the research reported in this thesis was the failure to produce a working prototype for testing. This was despite effort on two different stators and the manufacture of several high precision components. It is worth noting that even if a prototype which could maintain an airgap clearance had been successfully manufactured, a risk assessment would have limited the operation of this prototype to no more than ¼ of the rated speed of 20,000rpm because of simplifications in mechanical attachment of the rotor end-plates to the rotor hub and the uncertainty over the bonding of each and every individual magnet. The key to realising a robust demonstrator machine would be to develop a full mechanical model of the stator and rotor structural parts to ensure that designs they can resist deformation from any unbalanced magnetic forces and provide the necessary rotor-dynamic stiffness.

Manufacturing process development for serpentine winding of Litz wire – The various attempts at manual coil winding of the serpentine coils in chapter 5 demonstrated the challenges of winding a rectangular Litz wire (~2mm wide) around a semi-circular path of similar diameter. The automation of this process with tooling to produce a more repeatable coil would be beneficial in terms of adopting this type of winding.

Use of amorphous soft magnetic materials for stator core – The results presented in chapter 5 showed the benefits of ultra-thin laminations in reducing losses. One class of materials that was not investigated because of the lack of availability in a form suitable for manufacture of a prototype was amorphous material. These are produced directly as very thin (~20μm) foils but are very difficult to process into sheets and stator components. The development of a reliable and cost-effective method for processing amorphous materials into complex geometry core parts would make this type of material attractive in this application.

Improved converter model - The converter model developed and investigated in Chapter 2 contained many simplifications such as no closed loop controller, open-circuit only considerations of output voltage THD and ideal representation of the generator output voltage. This was adequate in order to establish a frequency specification for the generator voltage but could be expanded to provide a full-closed loop model of the controller with a more detailed representation of a particular generator design and a series of load models. This would provide system level evaluation of the proposed generation system.

Appendix A Design designation system used in chapter 4 and 5

Table A Numbering system of machine designs through chapter 4 and 5

Design number	Stator core material	Machine frequency	Description
4.1.1	Cobalt iron	32kHz	Surface mounted PM Machine (SPM)
4.1.2	Cobalt iron	32kHz	SPM without tips
4.1.1-ag	Cobalt iron	32kHz	Enhance airgap from 4.1.1 with sp=0.9
4.2.1	Cobalt iron	32kHz	interior permanent magnet (IPM) machines
4.2.2	Cobalt iron	32kHz	IPM machine with magnet bridge
4.2.1-ag	Cobalt iron	32kHz	Enhance airgap from 4.2.1
4.2.3	Cobalt iron	32kHz	Trapezoid magnet IPM
4.3.1	Cobalt iron	32kHz	External rotor machine (ERM) with rotor type A
4.3.2	Cobalt iron	32kHz	External rotor machine (ERM) with rotor type B
4.3.3	Cobalt iron	32kHz	External rotor machine (ERM) with rotor type C
4.3.4	Cobalt iron	32kHz	External rotor machine (ERM) with rotor type D
4.4.1	Cobalt iron	32kHz	ERM 433 with a parallel sided stator slot
4.4.2	Cobalt iron	32kHz	Increased stator hub ratio (0.75) from 4.4.1
4.4.3	Cobalt iron	32kHz	Increased stator hub ratio (0.8) from 4.4.1
4.4.2-S	Somaloy	32kHz	Somaloy based on 4.4.2
4.4.3-S	Somaloy	32kHz	Somaloy based on 4.4.3
4.4.2-M	PCMF	32kHz	PCMF 4.4.2
4.4.3-M	PCMF	32kHz	PCMF 4.4.3
4.4.2-H	PCHF	32kHz	PCHF 4.4.2
4.4.3-H	PCHF	32kHz	PCHF 4.4.3
4.5.1	PCHF	16kHz	16 kHz design with stator hub ratio (0.8)
4.5.2	PCHF	16kHz	Increase airgap to 0.5mm (sh=0.8)
4.6.1	PCHF	16kHz	Two pieces per pole Halbach array/magnetic pole frame
4.6.2	PCHF	16kHz	Four pieces per pole Halbach array/magnetic pole frame
4.6.3	PCHF	16kHz	Two pieces per pole Halbach array/non-magnetic pole frame
4.6.4	PCHF	16kHz	Four pieces per pole Halbach array/non-magnetic pole frame
5.1.1	Nickel iron	16kHz	Nickel iron design based on 4.6.3 design
5.1.2	Nickel iron	16kHz	Increase airgap radius to 76mm (sh=0.8)

Appendix B PDM Simulink model explore in chapter 2

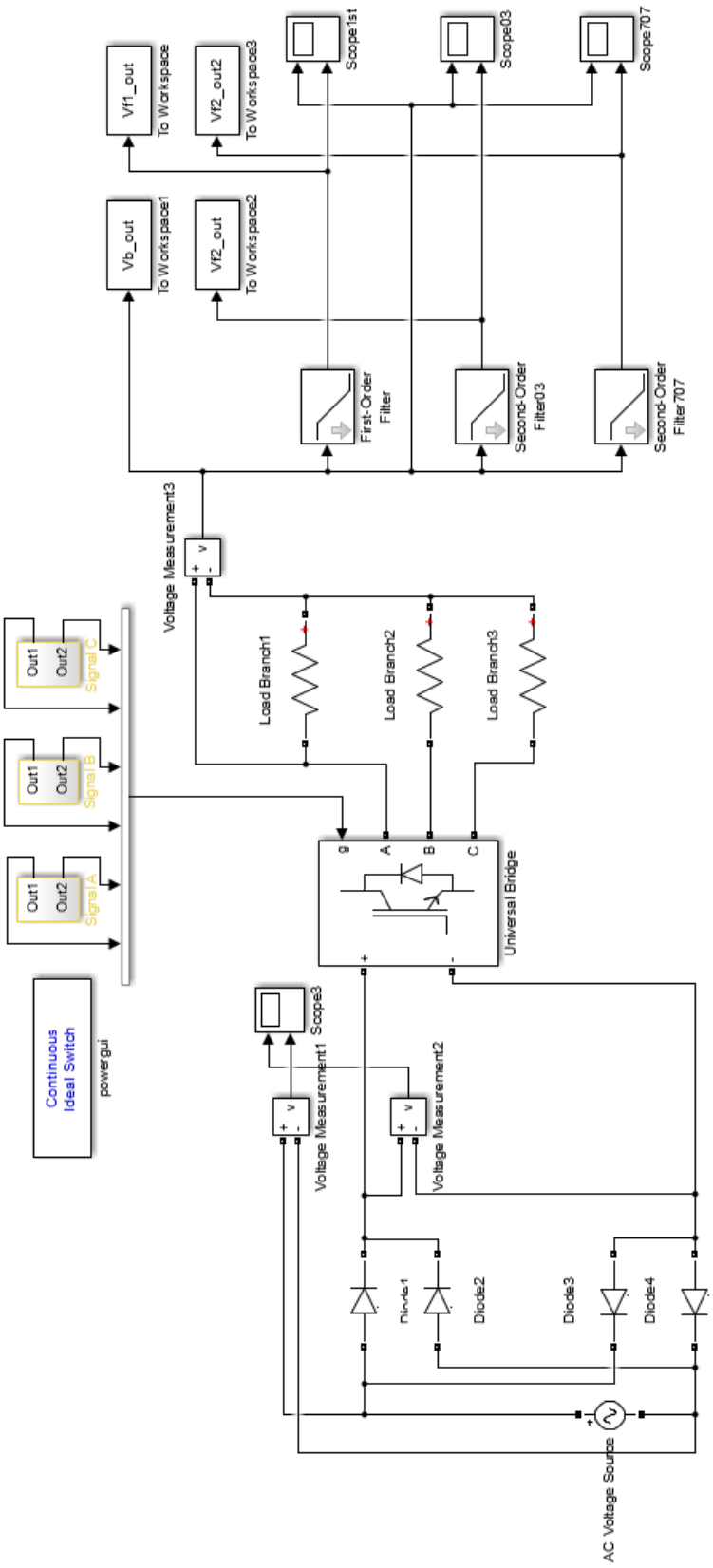

Figure B PDM Simulink model explore in chapter 2

Appendix C Example script of Opera 2D on final design

```
$COMI | reco
///editor: Bo Jiang
$constant #vn 1.1
//clear all the regions and circuits in the model before modelling
Erase reg1=1 reg2=* erase=yes
external
delete c1=1 c2=* |quit

//////////////
$constant #m 1 description='phase number'
$constant #r_ro 80e-3 description='rotor outer radius in m'
$constant #r_so 74e-3 description='stator outer radius in m'
$constant #r_si 64e-3 description='stator inner radius in m'
$constant #W_ag 0.5e-3 description='air gap width'
$constant #W_sg 0.1e-3 description='stator gap width'
$constant #num_Ts 96 description='stator teeth number'
$constant #num_Tr 48 description='rotor pole pairs number'
////////////////////////////////////////////////////////////////////////////

$constant #c_rt 2.5
$constant #w_br 0.5e-3 description='bridge thickness'
$constant #r_ri #r_so+#W_ag description='rotor inner radius in m'
$constant #r_st #r_so-#W_ag description='stator tips radius in m'
$constant #r_stt #r_st-#W_ag description='stator teeth tips ends radius in m'
$constant #r_rb #r_ro+(3e-3) description='rotor outside air radius in m'
$constant #ang_rt 360/#num_Ts description='rotor pole pitch'

$constant #r_sit 63.2e-3
$constant #r_skt 61.5e-3
```

```
$constant #r_sk 60.5e-3
$constant #r_sbg 58e-3 description='stator bg'

/$constant #ang_stt 0.8*#ang_rt description='stator teeth angle'
$constant #w_cb 2.2e-3 description='stator coil body width'
/$constant #w_cb 0.8*pi*#r_so*#ang_rt/360 description='stator coil body width'
$constant #r_ag 0.5*(#r_so+#r_ri) description='airgap radius for calculating the torque'
/$constant #r_sy #r_st+(0.5*#w_tb) description='stator main teeth inner radius'
$constant #w_bi 1.2*#w_cb description='back iron width'
$constant #r_cy #r_si+#w_bi description='conductor inners radius'

$constant #ang_stt 2*asin(#w_cb/2/#r_stt)*180/pi description='stator teeth angle'

//////////mesh size
$constant #Esize_air pi*#r_ag/#num_Tr/36
$constant #Esize_mt 2*#Esize_air
$constant #Esize_tt 2*#Esize_mt
$constant #Esize_iron 4*#Esize_mt
$constant #Esize_bg 12*#Esize_mt

//outer radius of airlayer on stator side
/$constant #r_air_s #r_ag
$constant #r_air_s #r_ag-#Esize_air/2
//inner radius of airlayer on rotor side
/$constant #r_air_r #r_ag
$constant #r_air_r #r_ag+0.5*#Esize_air
////////////////////
$constant #num_sym #num_Tr/12
/// tolerance for calculations
$constant #tole 1e-8
////////////////////////////////////////////////
$constant #al 50e-3
```

```
$constant #Irms 0

$constant #phaseA #Irms

$constant #Num_turn 1


$const #speed_mec 2e4

$const #freq_elec #num_Tr*#speed_mec/60

$const #ts 1/#freq_elec/60

$const #endtime 1/#freq_elec


//////////stator teeth/////////////

draw shape=poly mat=4 perm=4500 den=0 cond=0 n=0 sym=0 vel=0 xcen=0 ycen=0 angle=0 nx=1 ny=1 dx=0 dy=0 tmirr=0 mirr=no rotation=0 trotation=0 TMIRROR=0 rotation=0 trotation=0

quitdraw

polygon data=yes option=text polar=yes radius=(#r_so) theta=0.5*(#ang_rt)-atan(#w_cb/2/#r_so)*180/pi

polygon data=no size=yes esize=#Esize_air bias=0.5 line=straight f=no

polygon data=yes option=text polar=yes radius=(#r_st) theta=0.5*(#ang_rt)-atan(#w_cb/2/#r_st)*180/pi

polygon data=no size=yes esize=#Esize_mt bias=0.5 line=straight f=no

polygon data=yes option=text polar=yes radius=(#r_stt) theta=0.5*(#ang_rt)-atan(#w_cb/2/#r_stt)*180/pi

polygon data=no size=yes esize=#Esize_tt bias=0.5 line=straight f=no


polygon data=yes option=text polar=yes radius=(#r_cy) theta=0.5*(#ang_rt)-atan(#w_cb/2/#r_cy)*180/pi

polygon data=no size=yes esize=#Esize_tt bias=0.5 line=curvature curvature=-1/(#r_cy) f=no

polygon data=yes option=text polar=yes radius=(#r_cy) theta=0.5*#ang_rt

polygon data=no size=yes esize=#Esize_iron bias=0.5 line=straight f=no

polygon data=yes option=text polar=yes radius=(#r_si) theta=0.5*#ang_rt

polygon data=no size=yes esize=#Esize_tt bias=0.5 line=curvature curvature=1/(#r_si) f=no

polygon data=yes option=text polar=yes radius=(#r_si) theta=atan(#w_sg/2/#r_si)*180/pi
```

polygon data=no size=yes esize=#Esize_tt bias=0.5 line=straight f=no

polygon data=yes option=text polar=yes radius=(#r_cy) theta=atan(#w_sg/2/#r_cy)*180/pi

polygon data=no size=yes esize=#Esize_mt bias=0.5 line=straight f=no

polygon data=yes option=text polar=yes radius=(#r_stt) theta=atan(#w_sg/2/#r_stt)*180/pi

polygon data=no size=yes esize=#Esize_mt bias=0.5 line=straight f=no

polygon data=yes option=text polar=yes radius=(#r_st) theta=atan(#w_sg/2/#r_st)*180/pi

polygon data=no size=yes esize=#Esize_air bias=0.5 line=straight f=no

polygon data=yes option=text polar=yes radius=(#r_so) theta=atan(#w_sg/2/#r_so)*180/pi

polygon data=no size=yes esize=#Esize_air bias=0.5 line=curvature curvature=-1/(#r_si) f=no

polygon option=close

draw shape=poly mat=4 perm=4500 den=0 cond=0 n=0 sym=0 vel=0 xcen=0 ycen=0 angle=0 nx=1 ny=1 dx=0 dy=0 tmirr=0 mirr=no rotation=0 trotation=0 TMIRROR=0 rotation=0 trotation=0

quitdraw

polygon data=yes option=text polar=yes radius=(#r_so) theta=0.5*(#ang_rt)+atan(#w_cb/2/#r_so)*180/pi

polygon data=no size=yes esize=#Esize_air bias=0.5 line=straight f=no

polygon data=yes option=text polar=yes radius=(#r_st) theta=0.5*(#ang_rt)+atan(#w_cb/2/#r_st)*180/pi

polygon data=no size=yes esize=#Esize_mt bias=0.5 line=straight f=no

polygon data=yes option=text polar=yes radius=(#r_stt) theta=0.5*(#ang_rt)+atan(#w_cb/2/#r_stt)*180/pi

polygon data=no size=yes esize=#Esize_tt bias=0.5 line=straight f=no

polygon data=yes option=text polar=yes radius=(#r_cy) theta=0.5*(#ang_rt)+atan(#w_cb/2/#r_cy)*180/pi

polygon data=no size=yes esize=#Esize_tt bias=0.5 line=curvature curvature=1/(#r_cy) f=no

polygon data=yes option=text polar=yes radius=(#r_cy) theta=0.5*#ang_rt

```
polygon data=no size=yes esize=#Esize_iron bias=0.5 line=straight f=no
polygon data=yes option=text polar=yes radius=(#r_si) theta=0.5*#ang_rt
polygon data=no size=yes esize=#Esize_iron bias=0.5 line=curvature curvature=-1/(#r_si) f=no
polygon data=yes option=text polar=yes radius=(#r_si) theta=#ang_rt
polygon data=no size=yes esize=#Esize_iron bias=0.5 line=straight f=no
polygon data=yes option=text polar=yes radius=(#r_cy) theta=#ang_rt
polygon data=no size=yes esize=#Esize_tt bias=0.5 line=straight f=no
polygon data=yes option=text polar=yes radius=(#r_stt) theta=#ang_rt
polygon data=no size=yes esize=#Esize_mt bias=0.5 line=straight f=no
polygon data=yes option=text polar=yes radius=(#r_st) theta=#ang_rt
polygon data=no size=yes esize=#Esize_air bias=0.5 line=straight f=no
polygon data=yes option=text polar=yes radius=(#r_so) theta=#ang_rt
polygon data=no size=yes esize=#Esize_air bias=0.5 line=curvature curvature=1/(#r_si) f=no
polygon option=close

COPY REG1=2 REG2=2 DX=0 DY=0 MIRROR=yes THETA=#ang_rt

//COPY REG1=2 REG2=2 DX=0 DY=0 MIRROR=no THETA=#ang_rt

$DO #cloop 1 22 1
COPY REG1=2 REG2=3 DX=0 DY=0 MIRROR=no THETA=#ang_rt*#cloop
$end do
COPY REG1=1 REG2=1 DX=0 DY=0 MIRROR=yes THETA=45

////////////////////////////////////
///////air in stator//////////
////////////////////////////////////////

draw shape=poly mat=0 perm=1 den=0 cond=0 n=0 sym=0 vel=0 xcen=0 ycen=0 angle=0 nx=1 ny=1 dx=0 dy=0 tmirr=0 mirr=no rotation=0 trotation=0 TMIRROR=0 rotation=0 trotation=0
```

quitdraw

polygon data=yes option=text polar=yes radius=(#r_so) theta=0.5*(#ang_rt)-atan(#w_cb/2/#r_so)*180/pi

polygon data=no size=yes esize=#Esize_air bias=0.5 line=straight f=no

polygon data=yes option=text polar=yes radius=(#r_st) theta=0.5*(#ang_rt)-atan(#w_cb/2/#r_st)*180/pi

polygon data=no size=yes esize=#Esize_mt bias=0.5 line=straight f=no

polygon data=yes option=text polar=yes radius=(#r_stt) theta=0.5*(#ang_rt)-atan(#w_cb/2/#r_stt)*180/pi

polygon data=no size=yes esize=#Esize_mt bias=0.5 line=curvature curvature=-1/(#r_stt) f=no

polygon data=yes option=text polar=yes radius=(#r_stt) theta=0.5*#ang_rt

polygon data=yes option=text polar=yes radius=(#r_stt) theta=0.5*(#ang_rt)+atan(#w_cb/2/#r_stt)*180/pi

polygon data=no size=yes esize=#Esize_mt bias=0.5 line=straight f=no

polygon data=yes option=text polar=yes radius=(#r_st) theta=0.5*(#ang_rt)+atan(#w_cb/2/#r_st)*180/pi

polygon data=no size=yes esize=#Esize_air bias=0.5 line=straight f=no

polygon data=yes option=text polar=yes radius=(#r_so) theta=0.5*(#ang_rt)+atan(#w_cb/2/#r_so)*180/pi

polygon data=no size=yes esize=#Esize_air bias=0.5 line=curvature curvature=1/(#r_si) f=no

polygon option=close

$DO #cloop 1 23 1

COPY REG1=49 REG2=49 DX=0 DY=0 MIRROR=no THETA=#ang_rt*#cloop

$end do

/COPY REG1=49 REG2=49 DX=0 DY=0 MIRROR=yes THETA=#ang_rt

//

///////air gap on stator side//

//

draw shape=poly mat=0 perm=1 den=0 cond=0 n=0 sym=0 vel=0 xcen=0 ycen=0 angle=0 nx=1 ny=1 dx=0 dy=0 tmirr=0 mirr=no rotation=0 trotation=0 TMIRROR=0 rotation=0 trotation=0

quitdraw

polygon data=yes option=text polar=yes radius=(#r_so) theta=#ang_rt

polygon data=no size=yes esize=#Esize_air bias=0.5 line=curvature curvature=1/(#r_so) f=no

polygon data=yes option=text polar=yes radius=(#r_so) theta=(0.5*#ang_rt+atan(#w_cb/2/#r_so)*180/pi)

polygon data=yes option=text polar=yes radius=(#r_so) theta=(0.5*#ang_rt-atan(#w_cb/2/#r_so)*180/pi)

polygon data=yes option=text polar=yes radius=(#r_so) theta=atan(#w_sg/2/#r_so)*180/pi

polygon data=yes option=text polar=yes radius=(#r_so) theta=0

polygon data=no size=yes esize=#Esize_air bias=0.5 line=straight f=no

polygon data=yes option=text polar=yes radius=(#r_air_s) theta=0

polygon data=no size=yes esize=#Esize_air bias=0.5 line=curvature curvature=-1/(#r_air_s) f=no

polygon data=yes option=text polar=yes radius=(#r_air_s) theta=#ang_rt

polygon data=no size=yes esize=#Esize_air bias=0.5 line=straight f=no

polygon option=close

draw shape=poly mat=0 perm=1 den=0 cond=0 n=0 sym=0 vel=0 xcen=0 ycen=0 angle=0 nx=1 ny=1 dx=0 dy=0 tmirr=0 mirr=no rotation=0 trotation=0 TMIRROR=0 rotation=0 trotation=0

quitdraw

polygon data=yes option=text polar=yes radius=(#r_so) theta=2*#ang_rt

polygon data=no size=yes esize=#Esize_air bias=0.5 line=curvature curvature=1/(#r_so) f=no

polygon data=yes option=text polar=yes radius=(#r_so) theta=(1.5*#ang_rt+atan(#w_cb/2/#r_so)*180/pi)

polygon data=yes option=text polar=yes radius=(#r_so) theta=(1.5*#ang_rt-atan(#w_cb/2/#r_so)*180/pi)

polygon data=yes option=text polar=yes radius=(#r_so) theta=#ang_rt

polygon data=no size=yes esize=#Esize_air bias=0.5 line=straight f=no

polygon data=yes option=text polar=yes radius=(#r_air_s) theta=#ang_rt

polygon data=no size=yes esize=#Esize_air bias=0.5 line=curvature curvature=-1/(#r_air_s) f=no

```
polygon data=yes option=text polar=yes radius=(#r_air_s) theta=2*#ang_rt
polygon data=no size=yes esize=#Esize_air bias=0.5 line=straight f=no
polygon option=close


/COPY REG1=74 REG2=74 DX=0 DY=0 MIRROR=yes THETA=2*#ang_rt

$DO #cloop 1 21 1
COPY REG1=74 REG2=74 DX=0 DY=0 MIRROR=no THETA=#ang_rt*#cloop
$end do

COPY REG1=73 REG2=73 DX=0 DY=0 MIRROR=yes THETA=45
////////////////////////////////////////////////////////////////////////////////////////////////////////////////////
//////////////////
////////////////////////////////////////////////////////////////////////////////////////
/////////////// draw of conductor, number 1, material 1//////////////////
////////////////////////////////////////////////////////////////////////////////

draw shape=poly mat=1 perm=1 den=0 cond=0 n=1 sym=0 vel=0 xcen=0 ycen=0
angle=0 nx=1 ny=1 dx=0 dy=0 tmirr=0 mirr=no rotation=0 trotation=0
quitdraw

polygon data=yes option=text polar=yes radius=(#r_stt) theta=0.5*(#ang_rt)-
atan(#w_cb/2/#r_stt)*180/pi
polygon data=no size=yes esize=#Esize_tt bias=0.5 line=straight f=no
polygon data=yes option=text polar=yes radius=(#r_cy) theta=0.5*(#ang_rt)-
atan(#w_cb/2/#r_cy)*180/pi
polygon data=no size=yes esize=#Esize_tt bias=0.5 line=curvature curvature=-1/(#r_cy)
f=no
polygon data=yes option=text polar=yes radius=(#r_cy) theta=(0.5*#ang_rt)
polygon data=yes option=text polar=yes radius=(#r_cy)
theta=0.5*(#ang_rt)+atan(#w_cb/2/#r_cy)*180/pi
polygon data=no size=yes esize=#Esize_tt bias=0.5 line=straight f=no
```

polygon data=yes option=text polar=yes radius=(#r_stt) theta=0.5*(#ang_rt)+atan(#w_cb/2/#r_stt)*180/pi

polygon data=no size=yes esize=#Esize_mt bias=0.5 line=curvature curvature=1/(#r_stt) f=no

polygon data=yes option=text polar=yes radius=(#r_stt) theta=(0.5*#ang_rt)

polygon option=close

/MODIFY REG1=1 REG2=1 N=1 ERASE=YES

$DO #cloop 1 23 1

COPY REG1=121-24 REG2=121-24 DX=0 DY=0 MIRROR=no THETA=#ang_rt*#cloop

MODIFY REG1=121-24+#cloop REG2=121-24+#cloop N=1+#cloop ERASE=YES

$end do

//////////////////gap between segment//////////

draw shape=poly mat=0 perm=1 den=0 cond=0 n=0 sym=0 vel=0 xcen=0 ycen=0 angle=0 nx=1 ny=1 dx=0 dy=0 tmirr=0 mirr=no rotation=0 trotation=0 TMIRROR=0 rotation=0 trotation=0

quitdraw

polygon data=yes option=text polar=yes radius=(#r_si) theta=atan(#w_sg/2/#r_si)*180/pi

polygon data=no size=yes esize=#Esize_tt bias=0.5 line=straight f=no

polygon data=yes option=text polar=yes radius=(#r_cy) theta=atan(#w_sg/2/#r_cy)*180/pi

polygon data=no size=yes esize=#Esize_mt bias=0.5 line=straight f=no

polygon data=yes option=text polar=yes radius=(#r_stt) theta=atan(#w_sg/2/#r_stt)*180/pi

polygon data=no size=yes esize=#Esize_mt bias=0.5 line=straight f=no

polygon data=yes option=text polar=yes radius=(#r_st) theta=atan(#w_sg/2/#r_st)*180/pi

polygon data=no size=yes esize=#Esize_air bias=0.5 line=straight f=no

polygon data=yes option=text polar=yes radius=(#r_so) theta=atan(#w_sg/2/#r_so)*180/pi

polygon data=no size=yes esize=#Esize_air bias=0.5 line=curvature curvature=1/(#r_so) f=no

polygon data=yes option=text polar=yes radius=(#r_so) theta=0

polygon data=no size=yes esize=#Esize_air bias=0.5 line=straight f=no

polygon data=yes option=text polar=yes radius=(#r_st) theta=0

polygon data=no size=yes esize=#Esize_mt bias=0.5 line=straight f=no

polygon data=yes option=text polar=yes radius=(#r_cy) theta=0

polygon data=no size=yes esize=#Esize_tt bias=0.5 line=straight f=no

polygon data=yes option=text polar=yes radius=(#r_si) theta=0

polygon data=no size=yes esize=#Esize_tt bias=0.5 line=curvature curvature=-1/(#r_si) f=no

polygon option=close

COPY REG1=145-24 REG2=145-24 DX=0 DY=0 MIRROR=yes THETA=45

/++ $DO #cloop 1 3 1

/++ COPY REG1=81 REG2=82 DX=0 DY=0 MIRROR=no THETA=#ang_rt*4*#cloop

/++ $end do

//////////////////stator key/////

draw shape=poly mat=4 perm=4500 den=0 cond=0 n=0 sym=0 vel=0 xcen=0 ycen=0 angle=0 nx=1 ny=1 dx=0 dy=0 tmirr=0 mirr=no rotation=0 trotation=0 TMIRROR=0 rotation=0 trotation=0

quitdraw

polygon data=yes option=text polar=yes radius=(#r_si) theta=45+0.5*#ang_rt

polygon data=no size=yes esize=#Esize_iron bias=0.5 line=straight f=no

polygon data=yes option=text polar=yes radius=(#r_sit) theta=45+0.5*#ang_rt

polygon data=yes option=text polar=yes radius=(#r_skt) theta=45+4.7

polygon data=yes option=text polar=yes radius=(#r_sk) theta=45+4.7

polygon data=no size=yes esize=#Esize_iron bias=0.5 line=straight f=no

polygon data=yes option=text polar=yes radius=(#r_sk) theta=45-4.7

polygon data=no size=yes esize=#Esize_iron bias=0.5 line=straight f=no

polygon data=yes option=text polar=yes radius=(#r_skt) theta=45-4.7

```
polygon data=yes option=text polar=yes radius=(#r_sit) theta=45-0.5*#ang_rt

polygon data=yes option=text polar=yes radius=(#r_si) theta=45-0.5*#ang_rt

polygon data=no size=yes esize=#Esize_iron bias=0.5 line=curvature curvature=-1/(#r_si) f=no

polygon data=yes option=text polar=yes radius=(#r_si) theta=45

polygon option=close


COPY REG1=147-24 REG2=147-24 DX=0 DY=0 MIRROR=no THETA=-30

COPY REG1=147-24 REG2=147-24 DX=0 DY=0 MIRROR=no THETA=30


/////background of stator//////////////////


draw shape=poly mat=0 perm=1 den=0 cond=0 n=0 sym=0 vel=0 xcen=0 ycen=0 angle=0 nx=1 ny=1 dx=0 dy=0 tmirr=0 mirr=no rotation=0 trotation=0 TMIRROR=0 rotation=0 trotation=0

quitdraw

polygon data=yes option=text polar=yes radius=(#r_si) theta=45+0.5*#ang_rt

polygon data=no size=yes esize=#Esize_iron bias=0.5 line=straight f=no

polygon data=yes option=text polar=yes radius=(#r_sit) theta=45+0.5*#ang_rt

polygon data=yes option=text polar=yes radius=(#r_skt) theta=45+4.7

polygon data=yes option=text polar=yes radius=(#r_sk) theta=45+4.7

polygon data=no size=yes esize=#Esize_iron bias=0.5 line=straight f=no

polygon data=yes option=text polar=yes radius=(#r_sk) theta=45-4.7

polygon data=no size=yes esize=#Esize_iron bias=0.5 line=straight f=no

polygon data=yes option=text polar=yes radius=(#r_skt) theta=45-4.7

polygon data=yes option=text polar=yes radius=(#r_sit) theta=45-0.5*#ang_rt

polygon data=yes option=text polar=yes radius=(#r_si) theta=45-0.5*#ang_rt

polygon data=no size=yes esize=#Esize_iron bias=0.5 line=curvature curvature=1/(#r_si) f=no


$DO #cloop 2 8 1

polygon data=yes option=text polar=yes radius=(#r_si) theta=45-0.5*#ang_rt*#cloop

$end do
```

```
polygon data=no size=yes esize=#Esize_iron bias=0.5 line=straight f=no
polygon data=yes option=text polar=yes radius=(#r_sbg) theta=30
polygon data=no size=yes esize=#Esize_iron bias=0.5 line=curvature curvature=-1/(#r_sbg) f=v
polygon data=yes option=text polar=yes radius=(#r_sbg) theta=60
polygon data=no size=yes esize=#Esize_iron bias=0.5 line=straight f=no
polygon data=yes option=text polar=yes radius=(#r_si) theta=60
polygon data=no size=yes esize=#Esize_iron bias=0.5 line=curvature curvature=1/(#r_si) f=no

$DO #cloop 1 6 1
polygon data=yes option=text polar=yes radius=(#r_si) theta=60-0.5*#ang_rt*#cloop
$end do
polygon option=close


polygon data=yes option=text polar=yes radius=(#r_si) theta=15+0.5*#ang_rt
polygon data=no size=yes esize=#Esize_iron bias=0.5 line=straight f=no
polygon data=yes option=text polar=yes radius=(#r_sit) theta=15+0.5*#ang_rt
polygon data=yes option=text polar=yes radius=(#r_skt) theta=15+4.7
polygon data=yes option=text polar=yes radius=(#r_sk) theta=15+4.7
polygon data=no size=yes esize=#Esize_iron bias=0.5 line=straight f=no
polygon data=yes option=text polar=yes radius=(#r_sk) theta=15-4.7
polygon data=no size=yes esize=#Esize_iron bias=0.5 line=straight f=no
polygon data=yes option=text polar=yes radius=(#r_skt) theta=15-4.7
polygon data=yes option=text polar=yes radius=(#r_sit) theta=15-0.5*#ang_rt
polygon data=yes option=text polar=yes radius=(#r_si) theta=15-0.5*#ang_rt
polygon data=no size=yes esize=#Esize_iron bias=0.5 line=curvature curvature=1/(#r_si) f=no

$DO #cloop 2 7 1
polygon data=yes option=text polar=yes radius=(#r_si) theta=15-0.5*#ang_rt*#cloop
```

```
$end do
polygon data=yes option=text polar=yes radius=(#r_si) theta=atan(#w_sg/2/#r_si)*180/pi
polygon data=yes option=text polar=yes radius=(#r_si) theta=0
polygon data=no size=yes esize=#Esize_iron bias=0.5 line=straight f=no
polygon data=yes option=text polar=yes radius=(#r_sbg) theta=0
polygon data=no size=yes esize=#Esize_iron bias=0.5 line=curvature curvature=-1/(#r_sbg) f=v
polygon data=yes option=text polar=yes radius=(#r_sbg) theta=30
polygon data=no size=yes esize=#Esize_iron bias=0.5 line=straight f=no
polygon data=yes option=text polar=yes radius=(#r_si) theta=30
polygon data=no size=yes esize=#Esize_iron bias=0.5 line=curvature curvature=1/(#r_si) f=no

$DO #cloop 1 6 1
polygon data=yes option=text polar=yes radius=(#r_si) theta=30-0.5*#ang_rt*#cloop
$end do
polygon option=close

COPY REG1=151-24 REG2=151-24 DX=0 DY=0 MIRROR=yes THETA=45

////////////////////////////////////
/////////rotor///////////////
////////////////////////////////////

////////rotor pm////////////
////////////////////////////////

Draw shape=poly mat=6 perm=1.05 CONDUCTIVITY=0 PERM=1 DENSITY=0 VELOCITY=0 MIRROR=no ROTATIONS=0, DX=0 DY=0 NX=1 NY=1 TMIRROR=0 rotation=0 TROTATION=0, XCENTRE=0 YCENTRE=0 ANGLE=0
```

```
QUITDRAW

polygon data=yes option=text polar=yes radius=(#r_ri) theta=0

polygon data=no size=yes esize=#Esize_air bias=0.5 line=curvature curvature=-1/(#r_ri) f=no

polygon data=yes option=text polar=yes radius=(#r_ri) theta=(atan(#w_cb/2/#r_ri)*180/pi)

polygon data=no size=yes esize=#Esize_mt bias=0.5 line=straight f=no

polygon data=yes option=text polar=yes radius=(#r_ro-#w_br) theta=(atan(#w_cb/2/(#r_ro-#w_br))*180/pi)

polygon data=no size=yes esize=#Esize_tt bias=0.5 line=curvature curvature=1/(#r_ro-#w_br) f=no

polygon data=yes option=text polar=yes radius=(#r_ro-#w_br) theta=0

polygon data=no size=yes esize=#Esize_tt bias=0.5 line=straight f=no

polygon option=close


COPY REG1=153-24 REG2=153-24 DX=0 DY=0 MIRROR=yes THETA=0.25*#ang_rt

COPY REG1=153-24 REG2=154-24 DX=0 DY=0 MIRROR=no THETA=0.5*#ang_rt


$DO #cloop 1 23 1

COPY REG1=153-24 REG2=156-24 DX=0 DY=0 MIRROR=no THETA=#ang_rt*#cloop

$end do


$DO #cloop 0 88 8

MODIFY REG1=153-24+#cloop REG2=153-24+#cloop PHASE=0.25*#cloop*#ang_rt+180 ERASE=no

$end do


$DO #cloop 0 88 8

MODIFY REG1=154-24+#cloop REG2=155-24+#cloop PHASE=0.5*#ang_rt+0.25*#cloop*#ang_rt-90 ERASE=no

$end do


$DO #cloop 0 88 8
```

MODIFY REG1=156-24+#cloop REG2=157-24+#cloop PHASE=#ang_rt+0.25*#cloop*#ang_rt ERASE=no

$end do

$DO #cloop 0 88 8

MODIFY REG1=158-24+#cloop REG2=159-24+#cloop PHASE=1.5*#ang_rt+0.25*#cloop*#ang_rt+90 ERASE=no

$end do

$DO #cloop 0 88 8

MODIFY REG1=160-24+#cloop REG2=160-24+#cloop PHASE=2*#ang_rt+0.25*#cloop*#ang_rt+180 ERASE=no

$end do

////////rotor core////////////

////////////////////////////////

draw shape=poly mat=0 perm=1 den=0 cond=0 n=0 sym=0 vel=0 xcen=0 ycen=0 angle=0 nx=1 ny=1 dx=0 dy=0 tmirr=0 mirr=no rotation=0 trotation=0 TMIRROR=0 rotation=0 trotation=0

quitdraw

polygon data=yes option=text polar=yes radius=(#r_ri) theta=0.25*#ang_rt

polygon data=no size=yes esize=#Esize_air bias=0.5 line=curvature curvature=-1/(#r_ri) f=no

polygon data=yes option=text polar=yes radius=(#r_ri) theta=(0.5*#ang_rt-atan(#w_cb/2/#r_ri)*180/pi)

polygon data=no size=yes esize=#Esize_tt bias=0.5 line=straight f=no

polygon data=yes option=text polar=yes radius=(#r_ro-#w_br) theta=(0.5*#ang_rt-atan(#w_cb/2/(#r_ro-#w_br))*180/pi)

polygon data=no size=yes esize=#Esize_tt bias=0.5 line=curvature curvature=-1/(#r_ro-#w_br) f=no

polygon data=yes option=text polar=yes radius=(#r_ro-#w_br) theta=0.5*#ang_rt

polygon data=no size=yes esize=#Esize_tt bias=0.5 line=straight f=no

polygon data=yes option=text polar=yes radius=(#r_ro) theta=0.5*#ang_rt

polygon data=no size=yes esize=#Esize_tt bias=0.5 line=curvature curvature=1/(#r_ro) f=no

polygon data=yes option=text polar=yes radius=(#r_ro) theta=0.25*#ang_rt

polygon data=no size=yes esize=#Esize_tt bias=0.5 line=straight f=no

polygon data=yes option=text polar=yes radius=(#r_ri+#w_br) theta=0.25*#ang_rt

polygon data=no size=yes esize=#Esize_mt bias=0.5 line=straight f=no

polygon option=close

COPY REG1=249-24 REG2=249-24 DX=0 DY=0 MIRROR=YES THETA=0.25*#ang_rt

/MODIFY REG1=13 REG2=13 PHASE=#ang_rt+180 ERASE=no

//////////////air gap in rotor side//

draw shape=poly mat=0 perm=1 den=0 cond=0 n=0 sym=0 vel=0 xcen=0 ycen=0 angle=0 nx=1 ny=1 dx=0 dy=0 tmirr=0 mirr=no rotation=0 trotation=0 TMIRROR=0 rotation=0 trotation=0

quitdraw

polygon data=yes option=text polar=yes radius=(#r_ri) theta=0

polygon data=no size=yes esize=#Esize_air bias=0.5 line=curvature curvature=-1/(#r_ri) f=no

polygon data=yes option=text polar=yes radius=(#r_ri) theta=(atan(#w_cb/2/#r_ri)*180/pi)

polygon data=yes option=text polar=yes radius=(#r_ri) theta=0.25*#ang_rt

polygon data=yes option=text polar=yes radius=(#r_ri) theta=(0.5*#ang_rt-atan(#w_cb/2/#r_ri)*180/pi)

polygon data=yes option=text polar=yes radius=(#r_ri) theta=0.5*#ang_rt

polygon data=no size=yes esize=#Esize_air bias=0.5 line=straight f=no

polygon data=yes option=text polar=yes radius=(#r_air_r) theta=0.5*#ang_rt

polygon data=no size=yes esize=#Esize_air bias=0.5 line=curvature curvature=1/(#r_air_r) f=no

polygon data=yes option=text polar=yes radius=(#r_air_r) theta=0

```
polygon data=no size=yes esize=#Esize_air bias=0.5 line=straight f=no

polygon option=close

/COPY REG1=147 REG2=147 DX=0 DY=0 MIRROR=YES THETA=#ang_rt



//////////////rotor outside air////////////

draw shape=poly mat=0 perm=1 den=0 cond=0 n=0 sym=0 vel=0 xcen=0 ycen=0 angle=0 nx=1 ny=1 dx=0 dy=0 tmirr=0 mirr=no rotation=0 trotation=0 TMIRROR=0 rotation=0 trotation=0

quitdraw


polygon data=yes option=text polar=yes radius=(#r_ro) theta=0

polygon data=no size=yes esize=#Esize_tt bias=0.5 line=curvature curvature=-1/(#r_ro) f=no

polygon data=yes option=text polar=yes radius=(#r_ro) theta=0.25*#ang_rt

polygon data=yes option=text polar=yes radius=(#r_ro) theta=0.5*#ang_rt

polygon data=no size=yes esize=#Esize_iron bias=0.5 line=straight f=no

polygon data=yes option=text polar=yes radius=(#r_rb) theta=0.5*#ang_rt

polygon data=no size=yes esize=#Esize_iron bias=0.5 line=curvature curvature=1/(#r_rb) f=v

polygon data=yes option=text polar=yes radius=(#r_rb) theta=0

polygon data=no size=yes esize=#Esize_iron bias=0.5 line=straight f=no

polygon option=close



$DO #cloop 1 47 1

COPY REG1=249-24 REG2=252-24 DX=0 DY=0 MIRROR=no THETA=0.5*#cloop*#ang_rt

$end do


////////////////////////////////////////////////////////////////////////////////////////////

// end of geometry draw

////////////////////////////////////////////////////////////////////////////////////////////
```

```
GAP include=one RADIUS=#r_ag SYMMETRY=#num_sym
mesh tol=#tole dis=no

////////////////////////////////////////////////////////////////////////////////////////////////////

BHDATA MATERIAL=4 TYPE=ISOTROPIC PHASE=0 PACK=1
DELETEBH N1=1 N2=*
LOADBH FILE='E:\Opera backup programming\nife.bh'
DEMAGQUAD COMMAND=CLEAR
QUIT

// rotor laminations
BHDATA MATERIAL=5 TYPE=ISOTROPIC PHASE=0 PACK=1
DELETEBH N1=1 N2=*
LOADBH FILE='E:\Opera backup programming\Sura NO20.bh'
DEMAGQUAD COMMAND=CLEAR
QUIT

/// permanent magnets

$constant #num_BH 10
BHDATA MATERIAL=6 TYPE=ISOTROPIC PHASE=0 PACK=1
DELETEBH N1=1 N2=*
$do #m 0 #num_BH 1
ADD BVALUE=1.075*#m/#num_BH HVALUE=-(1-#m/#num_BH)*740e3
$end do
DEMAGQUAD COMMAND=CLEAR
QUIT



//////////////////////////////////////////////////////
///$string filename 'IPM_1turns_40_%int(#w_br*100000)br'
```

```
////////////////////////////////////

$const #i 0
$do #i 1 4*int(#endtime/#ts)
SOLVE TYPE=RM
CASE COMM=ADD POSITION=#i VALUE=#ts*#i |QUIT
$end do

SOLVE TYPE=RM
LOGFILE LOGGING=SOLUTION COL1=TTIME COL2=R1_I COL3=R1_V
/COL4=W1_V COL5=W2_V COL6=W3_V COL7=W4_V COL8=W5_V COL9=W6_V COL10=W7_V COL11=W8_V COL12=W9_V COL13=W10_V COL14=W11_V COL15=W12_V COL16=W13_V COL17=W14_V COL18=W15_V COL19=W16_V
DATA LINEAR=no TSTYPE=FIXED TSTEP=#ts MOTIONTYPE=FIXED RMVEL=2e4 |QUIT

CEDITOR OPTION=load FILENAME='E:\Opera backup programming\Opera 2D\Part_9\9.1.3_nife_seg_h2p_870_64_74_80\2_999k.vfc'
OPTION=update

SET FIELD=MAGNETIC SYMMETRY=XY AUTOMATIC=YES ELEMENT=LINEAR

$string path 'E:\Opera backup programming\Opera 2D\Part_9\9.1.3_nife_seg_h2p_870_64_74_80'
$cd directory='&path&'
$string filename 'ORM_1turns_999k_test'
WRITE FILE='&filename&.op2'
$OS OPERAANL rm '&filename&.op2' BACK

CEDITOR OPTION=clear
```

```
CEDITOR OPTION=load FILENAME='E:\Opera backup programming\Opera 2D\Part_9\9.1.3_nife_seg_h2p_870_64_74_80\R1_10.vfc'

OPTION=update


SET FIELD=MAGNETIC SYMMETRY=XY AUTOMATIC=YES ELEMENT=LINEAR


$string path 'E:\Opera backup programming\Opera 2D\Part_9\9.1.3_nife_seg_h2p_870_64_74_80'

$cd directory='&path&'

$string filename 'ORM_1turns_1_10'

WRITE FILE='&filename&.op2'

$OS OPERAANL rm '&filename&.op2' BACK


CEDITOR OPTION=clear



$DO #ld 1 1 -5

CEDITOR OPTION=load FILENAME='E:\Opera backup programming\Opera 2D\Part_9\9.1.3_nife_seg_h2p_870_64_74_80\2_00.vfc'

ceditor option=modify COMPONENTNAME=r1 PROPERTYNAME=resistance VALUE=#ld

OPTION=update


SET FIELD=MAGNETIC SYMMETRY=XY AUTOMATIC=YES ELEMENT=LINEAR


$string path 'E:\Opera backup programming\Opera 2D\Part_9\9.1.3_nife_seg_h2p_870_64_74_80'

$cd directory='&path&'

$string filename 'ORM_1turns_%int(#ld*100)_100_test'

WRITE FILE='&filename&.op2'

$OS OPERAANL rm '&filename&.op2' BACK
```

```
CEDITOR OPTION=clear

$end do
```